Impact of space weather on the polar atmosphere

Jone Edvartsen

16.06.2020

Master Thesis in Space Physics

Supervisors: Dr. Hilde Nesse Tyssøy and Dr. Ville Maliniemi

Department of Physics and Technology
University of Bergen

Acknowledgement

A special thanks to Dr. Hilde Nesse Tyssøy and Dr. Ville Maliniemi for helping me with this project by giving me the necessary guidance and positive encouragement. You have helped to open my mind to a new way of thinking, which has been really motivating for me. I could not have done this without you two. I would also like to thank the University of Bergen, and especially Birkeland Centre for Space Science, for giving me this opportunity, which I have really enjoyed all the way through. Lastly, I would like to thank my family and friends for their support throughout this year. I really appreciate the understanding of my absence while I have been digging deep into this project. I'll be back.

Abstract

Evidence are pointing to two potential links between solar wind forcing and atmospheric dynamics in polar regions. The Chemical-Dynamical link follows from energetic particle precipitation (EPP) ionizing the upper atmosphere (>50km), leading to a production of nitrogen and hydrogen oxides (NO_x and HO_x), which later on participate in ozone destruction. This can lead to changes in the radiative balance of the atmosphere, followed by related changes in winds. The physical link, called the Mansurov effect, is related to the interplanetary magnetic field (IMF) and its ability to modulate the global electric circuit (GEC), which further is assumed to impact the polar troposphere through cloud generation processes. By use of ERA-5 reanalysis data and OMNI near Earth solar wind magnetic field and plasma parameter data, we investigate these hypotheses through superposed epoch analyses, where the internal atmospheric variability is taken into account. The analyses are done over the data period 1979-2017.

Results concerning the Chemical-Dynamical link show statistically significant negative correlations between EPP (geomagnetic activity index A_p used as a proxy) and geo-potential height anomalies in the local winter inside the polar vortex. The results indicate a greater response in the NH compared to the SH. In the NH for the early winter, anomalies are significant through all atmospheric levels observed (1-1000 hPa level). In particular, the period 15.Dec-15.Jan shows a consistent pattern of negative anomalies centered at polar latitudes for multiple different atmospheric states. Analyses attributing the mechanism for this anomalous period are needed for determination of an actual EPP driven response. The possibility of an aliasing effect exists, as the volcanic eruption of Mount Pinatubo in 1991 is shown to play a major role in one of the results exhibiting significance in the period 15.Dec-15.Jan. However, significance in the same period is obtained when the pre-volcanic conditions are excluded. The results also show significant correlations at the surface level in the late winter, without obtained significance at higher atmospheric levels.

For the Mansurov effect, a significant correlation is seen between the IMF horizontal (B_y) component and lower tropospheric pressure in the SH over the whole time period when a -2 day lag is added between the driver and the response. Such a relationship is unphysical and not in line with the current theory. This result indicates a lack of understanding of the Mansurov effect. A possible aliasing mechanism operating through atmospheric- and ocean-tidal forcing driven by the lunar orbit is suggested. Highly significant correlations between the lunar orbit and polar pressure are observed in both hemisphere. The analyses are not ideally set up for a measure of this forcing, and definite evidence of an aliasing mechanism are not provided. However, while previous studies have highlighted the Mansurov effect for the period 1998-2002, the lunar orbit also suggest increased impact on the polar surface pressure in this period. This encourages further investigation and revision of the hypothesized physical link.

Contents

1 Introduction

Since ancient times the vast effect of the Sun on the Earth has been recognized. The presence creates the day, the absence takes it away. Throughout the ages of humanity this has made the Sun into an object of worship and praise. It has been the precursor of countless legends and myths, as well as the inspiration of numerous gods and goddesses representing power and strength. Something of such an immense perceived power and capability of controlling the passing of days couldn't possibly be of a natural origin, or could it?

The intrinsic curiosity, which inhabits all of us, have driven the understanding of the Sun and its effects from tale to science. Many great minds have refused to believe what they were told and instead pondered both philosophically and scientifically about the deeper truth concerning the driving forces behind such a seemingly immense glowing object in the sky.

Greek philosopher Anaxagoras (510–428BC) was one of the first people to offer a scientific explanation for the Sun. He proposed that the Sun itself was not a mythological object, but rather a giant burning ball of metal, and that the perceived luminosity of the Moon is solely the reflected light of the Sun. Claims opposing the current belief system were not accepted kindly in ancient times, and Anaxagoras was originally sentenced to death for his theory.

A less risky activity was, however, pure observational studies. It exists continuous data of observations of dim spots on the sun, known as sunspots, tracked by Chinese astronomers during the Han Dynasty (206BC–220AD). Observational studies of the motion of the Sun itself can be dated back even further than the time of Anaxagoras. Astronomers at around 1000 BC had noted that the Sun's movement was not uniform, but changed speed along the path, which they could not explain. At these times the assumption of Earth as the center of the universe with the Sun revolving around it was widely accepted.

The conclusion of a heliocentric system is one of the most revolutionizing breakthroughs when talking about space-science and astronomy. The idea that all the planets including the Earth is orbiting the Sun, was first proposed as early as the 3rd century BC. It still took over seventeen centuries, mixed with the genius and bold mind of Nicolas Copernicus (1473-1543), for the scientific community to accept and apply such an idea. He proposed a detailed mathematical model of the Heliocentric system, which was an idea in great opposition to the current religiously influenced belief of the Earth as the center of it all. According to history, Copernicus was very anxious about publishing his new theory, and waited until his final years before doing so to avoid any unpleasant criticisms or consequences.

Since then the planetary motions has been established, the chemical composition of the Sun, and the role of nuclear fusion as the Sun's engine has been

unravelled. Nonetheless, the Sun is still subject to ongoing research for solar physicists, space scientists, and climate researchers. And still to this day, new ideas that might appear fairly controversial to the scientific community are launched. It is common knowledge that the Sun regulates the climate and weather. As a first approximation, Earths climate depends upon the energy it receives from the Sun, which is mostly determined by the distance between the Earth and the Sun. What is not common knowledge, and a cause of controversy, is the idea that the day to day and year to year variability of the Sun and how its different forms of energy output can modulate everything from chemical composition in the upper atmosphere to changed wind patterns at sea level. New research are suggesting that different mechanisms operating through solar wind parameters such as strength of the magnetic field of the solar wind, the speed and density of the solar wind driving ionized particles into the atmosphere, can effectively change weather patterns in the polar regions. It is proposed that these changes could possibly induce a non-linear increasing change in the larger scale weather patterns potentially affecting a larger area than just the polar regions. This is a relatively new field of research, where the mechanisms of such links are still under development. To further our knowledge surrounding the Sun and all its possible effects, determining the solar dependence of the weather and climate variability is of great importance. Research in this field has the potential to improve our scientific models which could deepen our understanding of how the future may look like in terms of climate and weather.

The overarching goal of this thesis is to increase the understanding of the possible links between the solar variability and the related polar weather anomalies.

1.1 Motivation

The link between the energetic particle precipitation (EEP) and the production of nitrogen and hydrogen oxides (NO_x and HO_x) in the polar regions is well established (Rozanov et al. 2005; Randall et al. 2005; 2015; Turunen et al. 2009; Sinnhuber et al. 2012; Smith-Johnsen et al. 2017). Smith-Johnsen et al. (2017) show direct EPP impact on NO_x down to 55 km altitude. These molecules are known to be catalytic ozone destroyers. (Bates et al. 1950; Crutzen 1971; Johnston 1971). A study by Seppala et al. (2009) received considerable attention in the HEPPA (High Energy Particle Precipitation in the Atmosphere) community, after the authors found a significant temperature change in the polar surface air at winter time correlated with the geomagnetic index A_p which can be used as a rough proxy for the EPP. These findings introduce a hypothesis for a chemical-dynamical coupling between geomagnetic activity and polar surface air temperature variability which is observable on a monthly and interannual scale:

Hypothesis 1: **A chemical dynamical coupling**

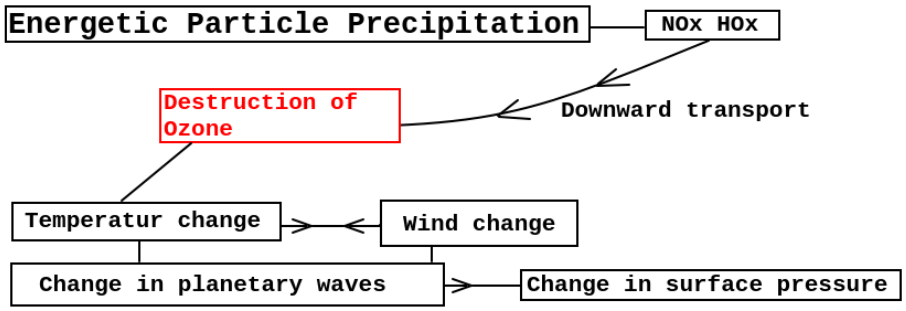

Already in the 1970s studies revealed a significant correlation between the changes in the B_y component of the Interplanetary magnetic field (IMF) and changes in the polar surface pressure, which is known in the literature as the Mansurov Effect (Mansurov et al. 1974; Burns et al. 2007; Burns et al. 2008, Lam et al. 2013). Later studies have also confirmed a significant temperature change (Freeman and Lam 2019) for the period 99-02, correlated to the B_y component. There also exist evidence of significant perturbations in the ionospheric potential related to the same change in B_y (Tinsley 2000; 2008; Frank-Kamenetsky et al. 2001; Kabin et al. 2003; Pettigrew et al. 2010; Lam et al. 2013). A potential physical mechanism involving the Global Electric Circuit (GEC) modulating cloud generation processes, has been suggested (Lam and Tinsley 2016). These findings introduce a hypothesis of a physical coupling between solar wind variability and polar surface air temperature variability which is estimated to be immediate, evident on a day-to-day basis.

Hypothesis 2: **The Mansurov Effect**

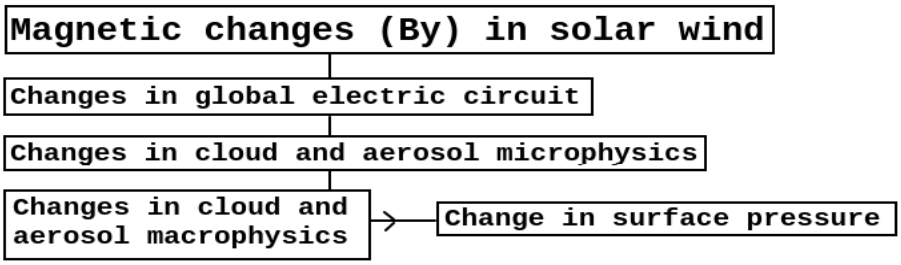

1.2 Objectives

With the use of European Center for Medium-range Weather Forecast Re-Analysis weather data (ERA-5) and OMNI near-Earth solar wind magnetic field and plasma parameter data, the objective of this thesis is to investigate **Hypothesis 1** and **Hypothesis 2** taken into account the natural variability of the atmosphere over the period 1979-2017. Judging by the relevant literature, this is the first time both hypothesis are compared in the same analysis. The investigation will aim at answering three key questions.

Key questions
1. Is there a statistical significant correlation between polar surface pressure and the geomagnetic activity index A_p and/or the IMF B_y?
2. Are there deviations between the hypotheses and the findings (e.g. unphysical relationship, dependence on season, atmospheric state etc.)?
3. Are there any potential aliasing effects associated with the two mechanisms?

Structure of thesis
The first section presents the relevant theory needed to understand the individual processes included in the hypotheses. Secondly, the data and method are described in detail before the results are presented. The results are further discussed in terms of validity and how they compare to recent publications. The last sections are attributed to a conclusion in terms of answers to the key questions, and recommendations for future work.

2 Theory

This chapter examines relevant theory regarding the Sun, the solar wind, the interplanetary magnetic field, the magnetosphere and the atmosphere. Further, it describes how solar forcing may affect the polar regional climate. Special focus is dedicated to both the chemical-dynamical coupling and the Mansurov effect along with supporting evidence from recent studies.

2.1 The Sun

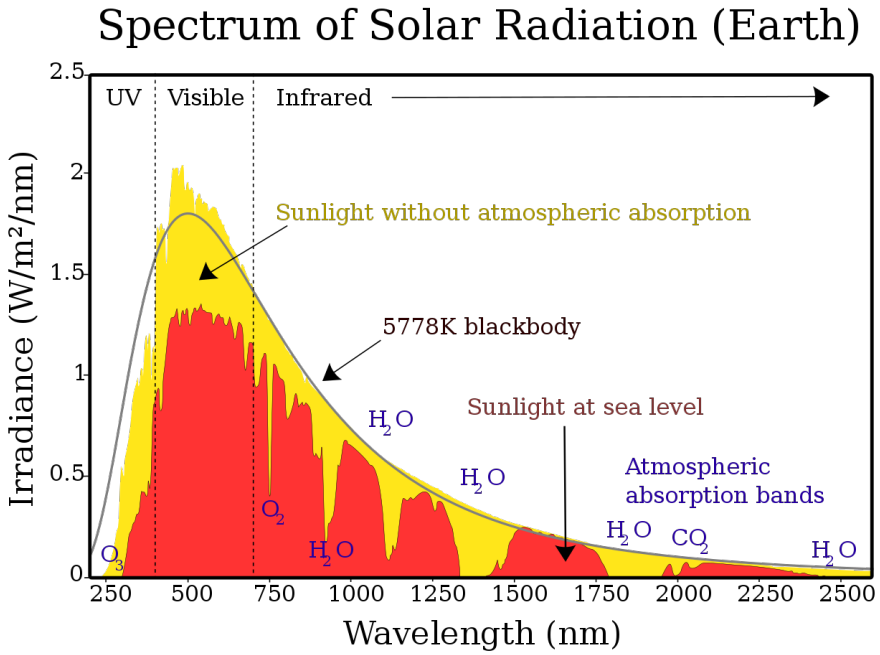

Figure 1: The graph represents the solar radiation spectrum for direct sunlight at both the top of the Earth's atmosphere (yellow area) and at sea level (red area). The sun produces light with a distribution similar to what would be expected from a 5778 K (5505 °C) blackbody, which is approximately the Sun's surface temperature. As light passes through the atmosphere, some is absorbed by gases with specific absorption bands. (Figure and description are taken from commons.wikimedia.org)

The Sun is the star at the center of our Solar System, located roughly 150 million kilometers (**1 AU**: 1 astronomical unit) from the Earth at any given time. It takes the shape of sphere measuring roughly 700 000 km in radius. Nearly all the energy needed for life on Earth is provided by the Sun, through the process of nuclear fusion inside the core where the dominating process is

when 4 protons create a helium nucleus. A major portion of the Sun's mass is made up of hydrogen, with a smaller portion of helium, and heavier elements including oxygen, carbon, neon and iron. The Sun can be divided up in multiple parts, starting from the center known as the core, followed by the radiative zone, the convection zone, the photosphere, the chromosphere and the outermost layer, the corona. The Sun also has an inherent magnetic field.

Energy transport from the core and outwards happens through radiation and convective processes of hot plasma rising due to density differences. This convection of plasma also participate in generating the solar magnetic field. The Sun's influence on Earth is mainly due to radiation. A spectrum of solar radiation received by Earth is given in Figure 1. The vast majority of the radiation received is shortwave radiation, which accounts for the input in the radiation budget of the Earth. The radiation budget is defined as the balance between incoming radiation from the Sun and the outgoing and reflected radiation from the Earth. Some radiation is reflected back as shortwave radiation, while a major part is absorbed and contribute to heating of the Earth, corresponding to longwave (thermal) radiation sent from Earth back to space as Earth cools. The average temperature of the Earth depends on the equilibrium state of the radiation budget, which can be modulated by higher amounts of incoming radiation, as well as changes in atmospheric opacity regarding both longwave and shortwave radiation.

2.1.1 Solar cycle

The Sun possesses different kinds of cyclic behaviour. It rotates around its own axis with a period ranging from approximately 25 days near the equator and 36 days near the poles. Viewed from the Earth, a fixed feature on the Sun will rotate to the same apparent position in approximately 27 days. The dominating cycle, known as the solar cycle, refers to the reversal of the Sun's magnetic field which have a periodicity of about 11 years. With each occurring cycle, the Sun's magnetic poles flip. The level of solar radiation emitted, the amount of ejected solar material, solar flares, and sunspot number, all fluctuate with this 11 year periodicity. The number of dark spots, seen in the visible spectra on the solar surface, may be the most prominent feature of the solar cycle, with continuous records dating back to 1750 (Tribble 2003). The sunspot number is defined as a quantity measuring the number of sunspots and groups of sunspots at any given time. Sunspots are accompanied by a brighter area around them called penumbra. Together the superposed effect is a small but notable enhancement in the total solar flux. Figure 2 shows the sunspot number plotted together with the spectral solar flux at 10.7 cm wavelength, also known as the F10.7 cm index. The F10.7 cm correlates well with the sunspot number, making it a suitable proxy for measuring solar activity.

Another phenomena correlating with the solar cycle is the galactic cosmic ray (GCR) flux, where GCR is defined as high energy particles originating from out-

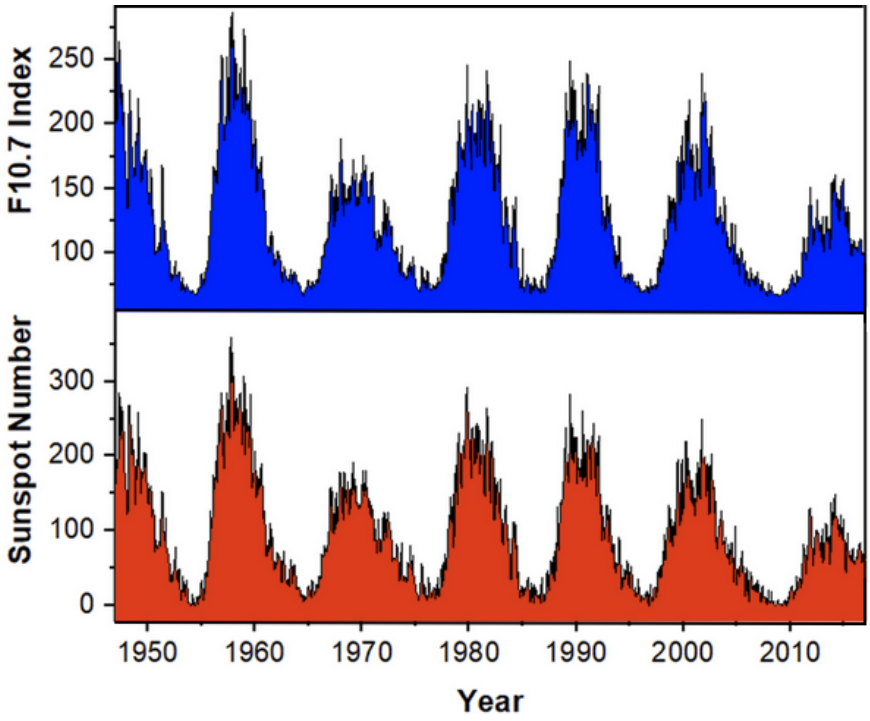

Figure 2: F10.7 cm radio emissions (blue) and sunspot number (red). (Singh et al. 2019)

side our solar system. Figure 3 shows that it is an inverse relationship between the two. Stronger solar activity implies less incoming cosmic rays as higher interplanetary magnetic field strength shields more cosmic particles from entering our solar system (Potgieter 2008). GCR may have an impact on weather and climate through ionization of molecules in the troposphere affecting cloud generation processes (Ormes 2018).

2.1.2 Solar sources of geomagnetic activity

Coronal holes

Through the study of individual 27-day recurrences in geomagnetic activity, Bartels (1932) identified persistent active areas on the Sun's surface which in many cases could not be coordinated to any visual phenomena observable by the current astrophysical methods. The regions, which Bartels named M-regions, appeared seemingly independent of the sunspot cycle (Allen 1944; 1964). Later, they were identified to be coronal holes, defined in simple terms as areas on

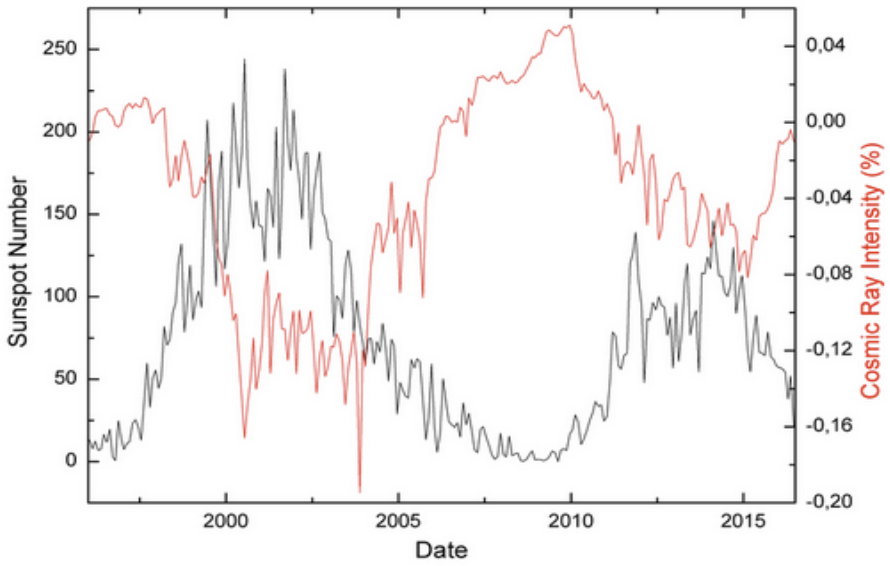

Figure 3: Black line showing monthly averaged sunspot number from 1997-2016. Red line showing monthly averaged cosmic ray intensity. As one can see from the graph, there exists an inverse relationship between the solar cycle and galactic cosmic ray flux. (Lingri et al. 2016)

the Sun with open magnetic field lines, contributing to the release of the Sun's particles in the form of high speed solar wind streams (HSSWS) as shown in Figure 4 (Billings and Roberts 1964; Krieger et al. 1973; Zirker 1977; Lindblad 1990).

Corotating interaction region

As HSSWS originating from coronal holes accelerate outwards from the Sun, it will overtake and interact with the slow speed solar wind streams, creating a region of compressed plasma and magnetic field at the interfaces, as seen in Figure 5 (Tsurutani 2006). The structure formed in the region of interaction is known as the corotating interaction region (CIR), characterized by enhanced magnetic field magnitudes and plasma temperatures (Tsurutani 2006). CIRs may persist for many solar rotations (Richardson 2018), and are the potentially geoeffective structure. About 33% of all CIRs are capable of causing moderate/intense geomagnetic storms (Alves 2006).

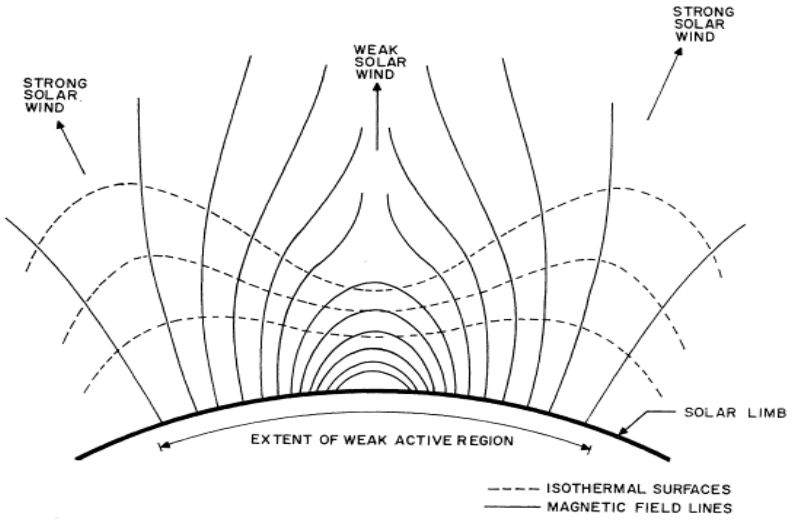

Figure 4: Temperature and density gradient significantly decrease along open magnetic field lines as outward transport of solar particles increase. (Billings and Roberts 1964).

Coronal mass ejections

Magnetic field lines stemming from extended arch's, like the ones originating from sunspots (see Appendix A.1), can participate in a magnetic reconnective process where field lines of opposite magnetic polarity can connect to each other. This releases large doses of energy through radiation, ejected particles and ejected magnetic fields, known as a coronal mass ejection (CME) (Lin et al. 2010; Webb and Howard 2012). CMEs are responsible for the most intense geomagnetic storms, with potentially devastating effects for electronic equipment (Cliver et al. 2013; MacAlester et al. 2014). CMEs partake in accelerating protons capable of precipitating directly into the lower atmosphere (Torsti et al. 1999; Belov 2017; Wang et al. 2019). These events are also known as solar proton events (SPE). CME-related structures account for ∼50% of the geomagnetic disturbances in the maximum phase of the solar cycle, and <10% in the declining phase. In contrast, HSSWS/CIR account for ∼30% of all disturbances in the maximum phase, and ∼70% during the declining phase. Slow solar wind contributes ∼20% throughout the solar cycle (Richardson 2000).

2.1.3 Solar wind and the interplanetary magnetic field

The solar wind is made up of ions and electrons continuously moving away from the Sun, originating from the outermost layer called the corona. It is characterized by its velocity, composition, particle density, dynamic pressure and magnetic field strength. Richardson and Cane (2012) divides the solar wind

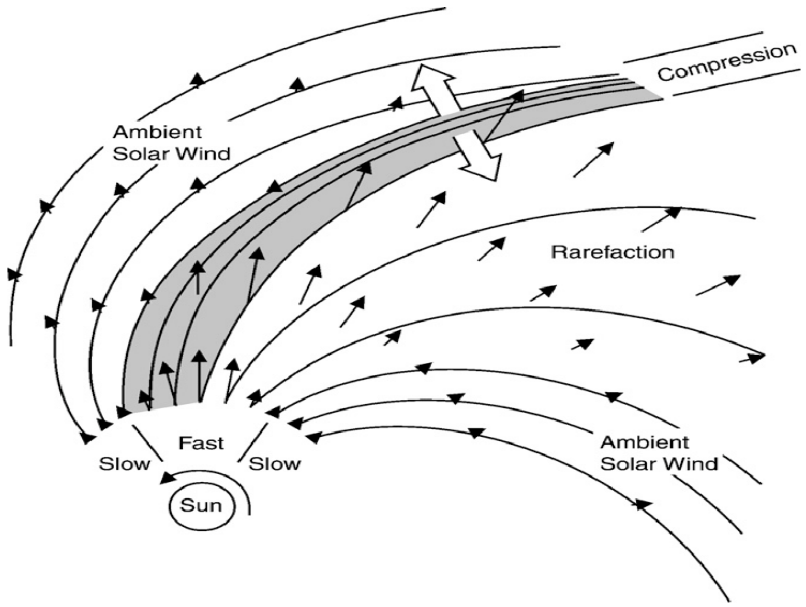

Figure 5: Fast solar wind overtaking the slow solar wind, thereby creating a region of compression. The structure formed in the region of interaction is known as CIR (Picture from Russell and Jian 2008).

into three main categories; Corotating high-speed streams, typically with solar wind speed $>\sim$450 km/s, originating from coronal holes, transient flows originating from CMEs, and slower interstream solar wind, typically associated with the streamer belt at the Sun (Feldman et al. 1981). (Antiochos et al. (2011) offers a detailed description of the sources of the slow solar wind). Differences extend beyond velocity, with fast solar wind being hotter and less dense than the slow solar wind (Suess 1999). Evidence exists showing how the distinct types of solar wind increase and decrease in correlation with the 11-year solar cycle, with the fast solar wind reaching maximum as the solar cycle reaches its minimum (Tokumaru et al. 2010).

The solar wind can be treated as a plasma with an inherent magnetic field. With certain restrictions (not valid for particles of high energy or in cases of magnetic reconnection), the magnetic field can be approximated to be frozen-into the plasma, meaning that the magnetic field and plasma moves together. The solar magnetic field is dragged out from the solar corona by the flow of the solar wind constructing an interplanetary magnetic field (IMF). Due to the rotational motion of the Sun, a field line connected to the Sun will continuously move in a specific angular direction. Figure 6a and b show the spiraling structure of the IMF originating from this motion. The structure of the IMF is known as the Parker Spiral (Parker 1965). The magnetic polarity of the spi-

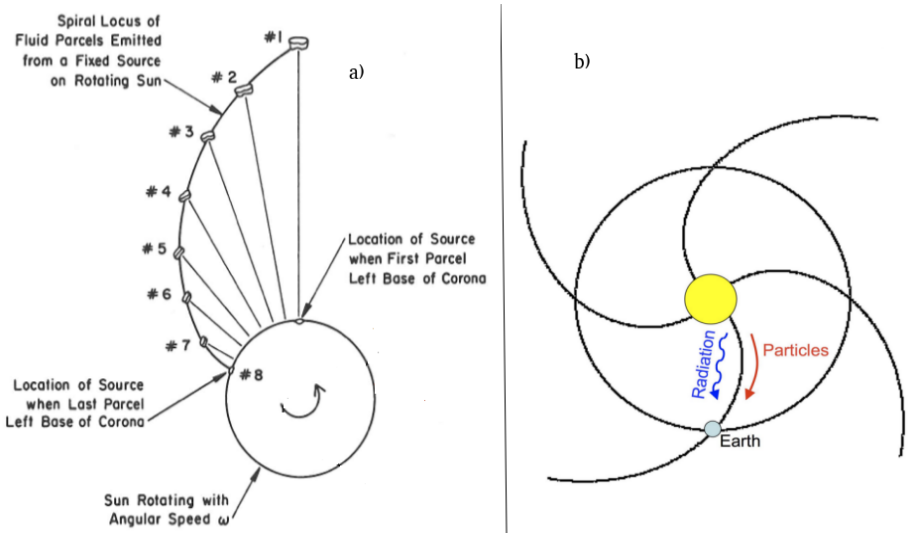

Figure 6: a) Shows the different plasma parcels continuously moving outwards from the Sun together with the magnetic field line connected to the Sun. b) Shows the structure of the Parker spiral at Earth's orbit. One can see how emitted charged particles follows the trajectory of the magnetic field lines, while radiation follows a straight line path. (Figure taken from PHYS 251 compendium)

raling arms of the IMF depends upon the magnetic polarity of the source point on the Sun. One can then define a surface boundary encircling the Sun that separates the opposing magnetic polarities, called the heliospheric current sheet (HCS) (Hoeksema et al. 1983; Smith 2001). An illustrative depiction of the HCS is given in Figure 7. In simple terms, by crossing the HCS, the magnetic

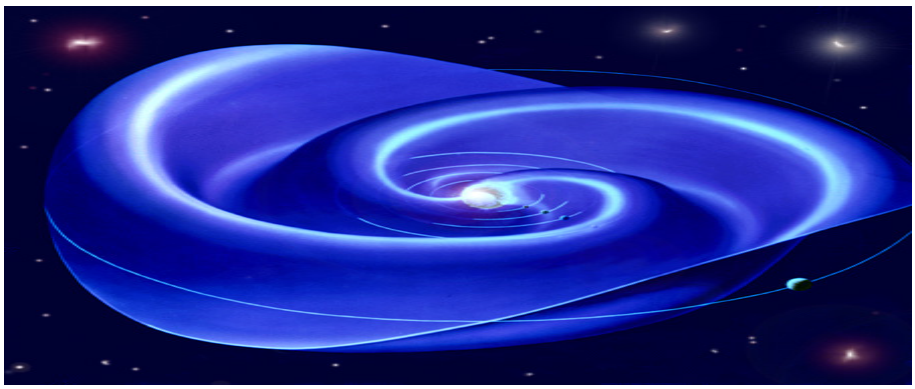

Figure 7: An artistic illustration of the heliospheric current sheet (HCS). (www.sciencephoto.com)

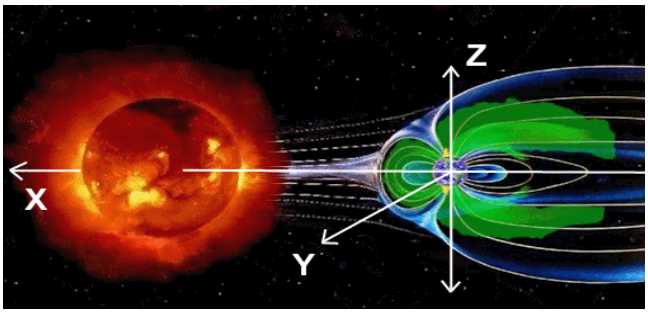

Figure 8: GSM coordinate system illustrated. X-axis aligns with the Earth-Sun line, Z-axis align with the dipole axis of the magnetic field, and Y-axis perpendicular to both X and Z, thereby completing the coordinate system. (poleshift.ning.com)

polarity of the IMF changes. The shape of the current sheet is in constant dynamical evolution. It follows the rotation of the Sun, with an average rotational period of about 27 days as viewed from Earth. Additional changes in shape and structure depends on changes in the solar wind and the solar magnetic field. It is observed substantial structural changes during the 11-year solar cycle (Hoeksema et al. 1983), as the Sun's magnetic field reverses during one cycle. The HCS in itself represents the magnetic equator of the global heliosphere (Smith 2001).

In this thesis, the important parameters deduced from the solar wind are the bulk velocity of the solar wind, and the magnetic field strength of the IMF. The bulk velocity is defined as the averaged outward radial velocity of the solar wind. Both parameters can be decomposed into three orthogonal components, one for each spatial dimension, according to a reference coordinate system. The geocentric solar magnetic (GSM) coordinate system, depicted in Figure 8, is used for the solar wind parameters in this thesis.

2.2 The Magnetosphere

The magnetosphere is defined as the area where the Earth's internal magnetic field dominates. Figure 9a illustrates the shape of the magnetosphere. Without the influence of the IMF, Earth's magnetic field can be approximated by a dipole illustrated in Figure 9b. The deviations from the dipole approximation arises from the interactions between Earth's magnetic field and the IMF. This interaction gives rise to a compressed area in the day-side due to pressure balance between the solar wind and Earth's magnetic field. At the night-side the magnetosphere is stretched out due to the solar wind impact. Hence, the geomagnetic field is a superposition of all the major contributions to the field, Earth's inner core, permanent magnetization of Earth's crust, and electric currents in the ionosphere and magnetosphere originating from the interaction with

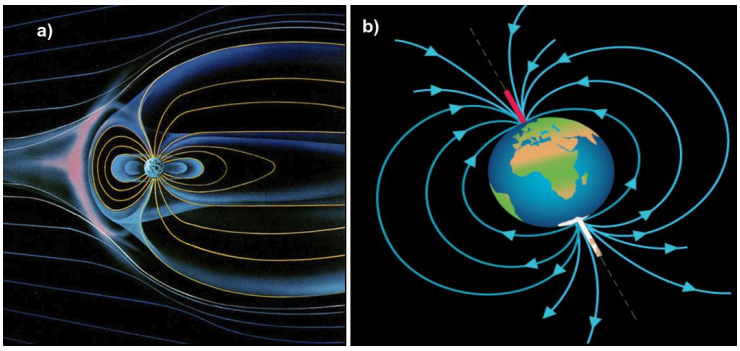

Figure 9: a) Earth's magnetic field. b) Earth's magnetic field approximated by a dipole field. (www.shutterstock.com & wwww.forcetoknow.com)

the solar wind and solar radiation.

Both hypotheses in this thesis have mechanisms depending on the solar wind's (IMF) ability to transfer energy into the atmospheric system.

2.2.1 Geomagnetic storms

A geomagnetic storm is defined as a temporal disturbance in Earths magnetosphere, caused by drivers in the solar wind. CMEs and CIRs are identified as the main sources of geomagnetic storms (Richardson 2012). These solar wind structures produce enhancements in the different magneto- and ionospheric current systems, manifesting itself as measurable magnetic disturbances in the geomagnetic field. Geomagnetic storms are classified according to the strength of the negative perturbation in the horizontal component of the terrestrial magnetic field, known as the Dst-index. Table 1 shows the classification of geomagnetic storms. Geomagnetic storms are often identified by an initial phase, a main phase and a recovery phase. In the initial phase, increased solar wind dynamic pressure compresses the dayside magnetosphere, forcing the magnetopause currents closer to the Earth, thereby increasing the strength of the horizontal com-

Table 1: Classification of geomagnetic storms (Loewe and Prölss 1997)

Storm Type	*Dst* Range [nT]
Great	< -350
Severe	[-200,-350]
Strong	[-100,-200]
Moderate	[-50,-100]
Weak	[-30,-50]

ponent of the magnetic field. In the main phase, as a response to the unstable conditions, plasma is injected towards the nightside from the magnetotail, resulting in a deflection in the horizontal component as the newly injected plasma increases the ring current (See Appendix A.2 for motion of charged particles). In the recovery phase, the newly injected plasma is slowly drained through loss processes into the atmosphere or outer edge of the magnetosphere, eventually restoring the geomagnetic field to pre-storm conditions (Akasofu 1977).

2.2.2 Reconnection

Magnetic reconnection implies that magnetic field lines of opposite polarities can connect to each other, rearranging the magnetic topology, converting magnetic energy to kinetic and/or thermal energy, along with acceleration of particles inside the plasma. Dungey (1961; 1963) was the first to propose a coupling between the IMF and the terrestrial magnetic field with magnetic reconnection acting as the driving mechanism. Figure 10a illustrates the Dungey cycle. The IMF (yellow lines) with a negative B_z (pointing N-S) component reconnects with field lines of opposite polarity (green lines; pointing S-N), originating from the terrestrial field. After the reconnetive process the field lines are defined as open field lines (purple lines), with one end connected to the Earth, and the other connected to the flowing solar wind. As the open field lines in both hemispheres are dragged by the solar wind they can reconnect in the magnetotail. After the reconnection on the night-side the magnetic field lines flow back to the day-side ending the cycle, where they are now ready interact with the IMF again.

The cycle can also be followed from the perspective of the ionospheric polar cap (Figure 10b), where flow of plasma caused by the Dungey cycle start at the day-side before entering the polar cap as open field lines, ultimately ending

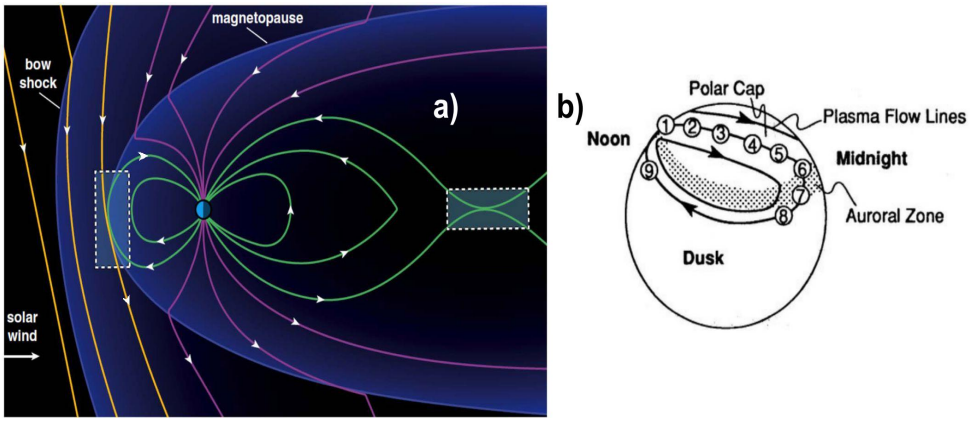

Figure 10: a) The Dungey cycle seen from space. b) The motion of plasma through the ionospheric cap originating from the Dungey cycle. (Case 2014)

up at the night-side where the reconnection of field lines occur. After reconnection the plasma flows at lower latitudes back to the day-side. As can be seen in the figure, the plasma flows clockwise and anticlockwise depending if its on the dusk or dawn side of the Earth, creating disturbances of opposite polarity in the ionosphere.

Based on the geometry of the geomagnetic field and IMF, reconnection will also happen with a positive B_z component, but at a slower rate. The rate is also dependent on the radial bulk speed of the solar wind, V_x (Kessel et al. 1996; Kabin et al 2003; Richardson 2013). As the reconnection in the magnetotail occurs, particles bounded and gyrating along magnetic field lines can be accelerated and eventually lost to the atmosphere, which are of great importance for hypothesis 1.

2.2.3 Magnetosphere-Ionosphere coupling

The ionosphere is defined as the layer of the atmosphere which is ionized due to solar- and cosmic radiation, giving it the properties of a plasma. It is divided into distinct layers depending on the electron density. As day-side and night-side have different rates of ionization, the electron density has distinct diurnal changes. Phenomena like strong particle precipitation at night-side can ionize the lower ionospheric regions, resulting in unusually high electron densities compared to quiet conditions. Figure 11 illustrates the layers called D-, E-, F1- and F2-layer, and their respective regions. The coupling between the magnetosphere and ionosphere is a complex process depending on a reciprocal relationship. This section will give a short and qualitative description of the underlying processes of energy transfer involved in the coupling.

Blanc (1988) divides the coupling into three basic processes, which operate along the same magnetic field lines. Firstly, is the transmission of electric fields between the magnetosphere and ionosphere. This can happen via propagation of Alfvén waves (approximately) along the magnetic field lines. Alfvén waves are essentially plasma oscillation of ions in response to a restoring force provided by an effective tension on the magnetic field line (Alfvén 1942). With some exceptions, these waves propagate in the direction of the magnetic field. Transmission of electric fields can also occur as a result of potential difference established across field lines in the ionosphere (with respect to the magnetosphere). The potential difference will then be mapped to the magnetosphere (with respect to the ionosphere) along the conducting magnetic field lines. Secondly, is the coupling process occurring from the exchange of particles, which happens in both directions between the magnetosphere and ionosphere. Particle precipitation from the magnetosphere to the ionosphere acts as a loss process for the ion-electron population in the magnetosphere, while the outflow of ionospheric plasma into the magnetosphere is the counterpart. Finally, is the exchange of electric charges, known as Birkeland currents (field-aligned currents). These are currents running along the magnetic field lines in certain regions.

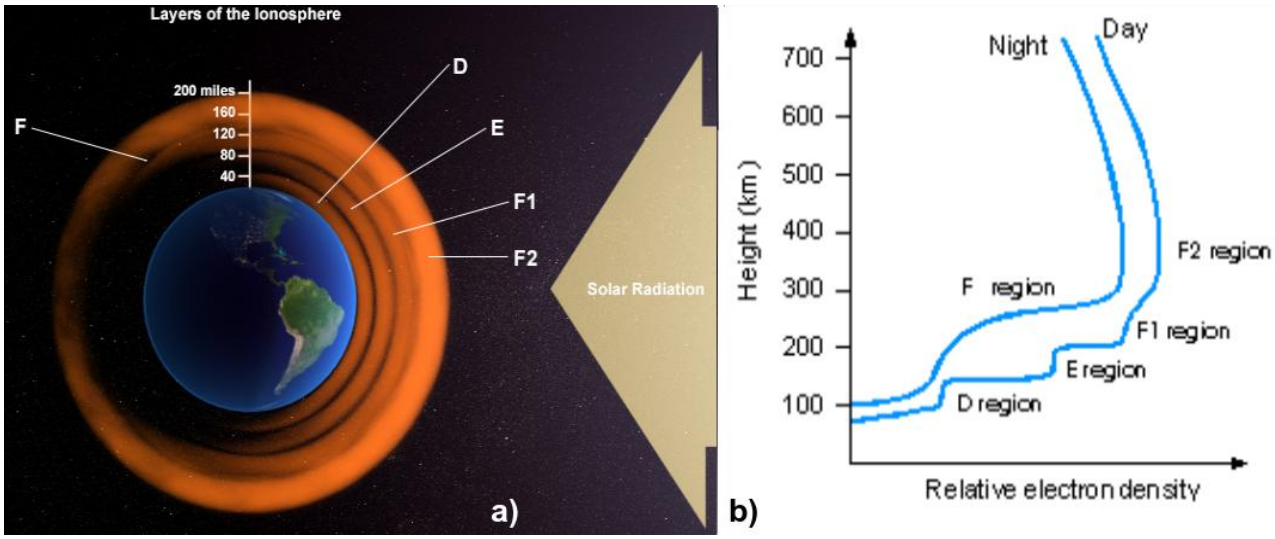

Figure 11: a) The ionosphere with its distinct layers at both day-side and night-side. Radiation from the Sun ionizes the ionosphere, making the day-side ion population denser (Ionosphere not to scale compared to Earth, in reality it's only a fraction of the thickness of Earth's radius). b) Relative electron density vs. height in the ionosphere for both day- and night-side. (The COMET® Program & www.astrosurf.com)

2.2.4 The radiation belts, particle acceleration and loss mechanisms

Van Allen belts

The radiation belts were first discovered in 1958 by James Van Allen and his Geiger–Müller tube instruments on multiple satellites. They are made of trapped ions and electrons in the magnetosphere bouncing off mirror points (see Appendix A.3 for definition of mirror points). The main structure takes

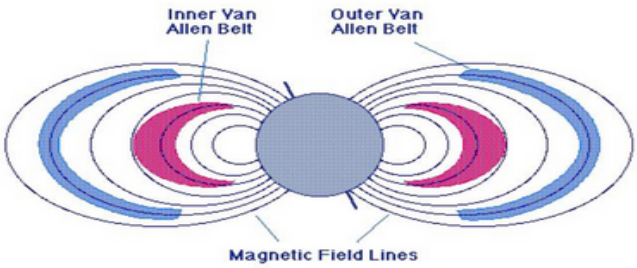

Figure 12: Drawing showing the inner and outer Van Allen belts

the form of an inner (L = 1.5-2.5 (See Appendix A.5 for definition of L-value)) and outer belt (L = 4-6), with the majority of high energy electrons found in the outer belt (0.1-10 MeV). The solar wind and the ionosphere are the main sources of charged particles in the Van Allen belts.

Accelerating mechanisms in the Van Allen belts

Solar wind electrons and ionospheric electrons have typically low energies compared to the relativistic electrons seen in the Van Allen belts. This paves the way for an accelerating mechanism to explain the observed energy gap. Reeves et al. (2013) defines two classes of accelerating processes for electrons: transport and acceleration of electrons from a source population located outside the radiation belts (radial acceleration) or acceleration of lower-energy electrons to relativistic energies in situ in the heart of the radiation belts (local acceleration).

Radial acceleration, through radial diffusion, requires the presence of fluctuating magnetospheric fields on the time scale of a drift period. Such fluctuations can be caused by pressure instabilities, electromagnetic waves generated in the magnetosphere (ULF waves), or to changes in the electromagnetic fields driven by geomagnetic storms. (Walt 1971; Hudson et al. 2000; Li and Temerin 2001). For it to be effective, an already hot source population of electrons from outside the magnetosphere is needed. As the particles are moved toward the Earth, the magnetic field strength increases, which increases the electron energy if the first and second adiabatic invariants are conserved (See Appendix A.4 for definition of adiabatic invariants) (Reeves et al. 2013).

Local acceleration, by breaking the first adiabatic invariant, increases the energy of the electrons in situ from wave-particle-interactions (WPI). Lower energy electrons in the magnetosphere generate waves, which happens to resonate with the electrons, potentially accelerating them to relativistic speeds if the temporal scale of the interaction operates within a gyro period. Both naturally occurring electromagnetic very low frequency (VLF $\geq$1 kHz) waves and ultra low frequency (ULF 300 Hz-3 kHz) are candidates for such interactions (Reeves et al. 2013). Recent studies have shown that chorus waves (VLF) alone can efficiently accelerate electrons, increasing the phase space density between 4.5<L<6.5 by up to three orders of magnitude (Thorne et al. 2013; Turner et al. 2014; Chaston et al. 2017; Hiraga and Omura 2020).

Loss mechanisms in the Van Allen belts

There exists a strong variability in radiation belt fluxes in association with geomagnetic storms. Known as electron flux drop-outs, the outer electron radiation belt fluxes decreases rapidly (dropout) at the early stages of a storm, with a later rapid return (recovery). (Reeves et al. 2003; Borovsky and Denton 2009; Hudson et al. 2014). Initially, it was thought that the dropouts were fully adiabatic and thereby reversible changes in the system. Known as the 'Dst effect',

as fresh particles are injected into the radiation belts the ring current increases. This leads to perturbations in the terrestrial field, ultimately decreasing the horizontal component. As a response through conservation of the first and third adiabatic invariant, electrons move radially outwards, resulting in energy loss. At the onset of the recovery phase of the storm, when the horizontal magnetic perturbation diminishes, this effect would reverse. This leads to a temporal 'dropout' in electron fluxes without any true particle loss to either the atmosphere or magnetosphere (Turner et al. 2012). It was later shown that after a storm, trapped electron fluxes could both increase and decrease compared to pre-storm levels, indicating that non-adiabatic true loss processes also played a role in competition with the acceleration processes (Reeves et al. 2003). Turner et al. (2012) list the loss processes to the magnetosphere as magnetopause shadowing and outward radial transport originating from WPI interactions. The loss processes to the atmosphere are listed as pitch-angle scattering through WPI with magnetospheric plasma waves and violation of the first adiabatic invariant due to highly stretched magnetotail fields.

Magnetopause shadowing occurs when the dynamic pressure of the solar wind moves the magnetosphere inward, resulting in the opening of closed drift paths from where electrons are lost to the outer magnetosphere (Ukhorskiy et al. 2006; Turner et al. 2012). Radial diffusion through WPI and the violation of the third adiabatic invariant of the drifting electrons can push them both inward and outward, which, depending on the conditions, could effectively enhance the loss to the outer edge of the magnetosphere (Shprits et al. 2006). For a particular case study, it was shown that sudden electron depletion observed during the storm's main phase was primarily a result of outward transport rather than loss to the atmosphere (Turner et al. 2012)

Loss to the atmosphere are of great importance for the thesis, as this defines the linkage between the magnetosphere and the atmosphere in hypothesis 1. Appendix A.3 gives supplementary theory on the definition of pitch angle, mirror point and loss cone, crucial to the understanding of particle precipitation. In the case of reconnection between the IMF and the magnetosphere, particles can be injected into the magnetosphere following paths of magnetic field lines. Some freshly injected particles will have pitch angles falling into the loss cone, leading to direct particle precipitation, presumable of low energies. Under disturbed conditions, high energy particles in trapped orbits can interact with waves in the plasma, effectively scattering them into the loss cone. This pitch angle scattering (loss) competes in an intricate process with acceleration processes (gain) through WPI of different waves. Electromagnetic ion cyclotron waves (EMIC waves), defined as pulsations in the 0.1-5 Hz frequency range, are shown to resonate with relativistic electrons, leading to pitch angle diffusion followed by atmospheric precipitation (Millan et al. 2007; Turner et al. 2014; Zhu et al. 2020). Chorus waves, while highly correlating with ongoing local acceleration of relativistic outer belt electrons (Thorne et al. 2013; Turner et al. 2014), are found to be the dominant cause of the most intense diffuse auroral precipita-

tion (Thorne et al. 2010), emphasizing the competing nature of wave-particle interactions.

2.3 The Atmosphere

The atmosphere is the layer of gases (air) retained by Earth's gravity. The specific components making up the mass of the air at ground level are Nitrogen (78.09%), Oxygen (20.95%), Argon (0.93%) and small amounts of trace gases such as Helium, Hydrogen and Carbon Dioxide (<0.1%). The composition is almost constant below ∼90km in what is known as the homosphere. In the heterosphere, which is above ∼90 km, collisions between particles become less important and the composition changes with height. It is common to subdivide the atmosphere into different layers depending on the temperature gradient. The temperature profile depends on the latitude and season, as illustrated in the left panel in Figure 13. From the ground upwards, the temperature decreases,

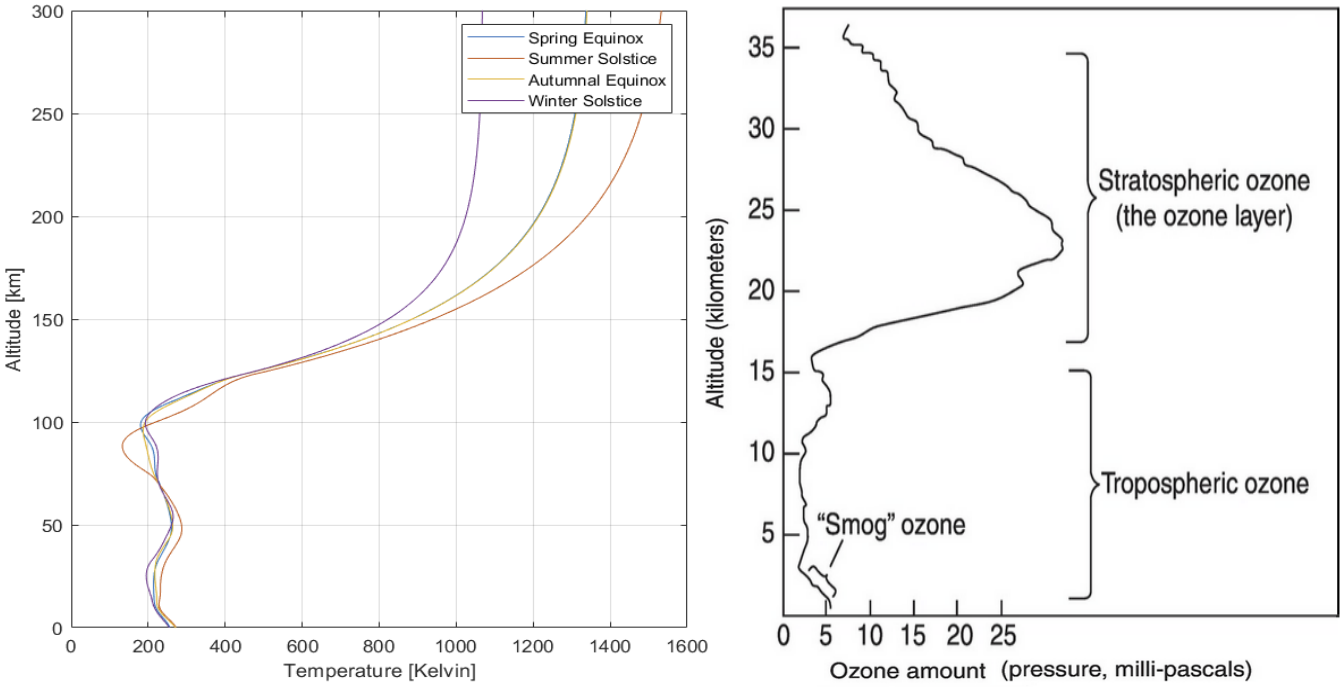

Figure 13: **Left panel:** Seasonal temperature profile (70°-80° N) for four different seasons. (Courtesy of Eldho Midhun Babu). **Right panel:** Ozone distribution versus altitude (Brasseur and Jacob 2017).

defining the troposphere. The tropopause is the height region where this tem-

perature gradient changes sign. As the temperature increases again, this defines the stratosphere, with the local stratopause defined by the temperature gradient switching back to negative. The mesosphere and the local mesopause is defined in the same fashion. The region above the mesopause is known as the thermosphere. As a consequence of the seasonal dependence, the winter mesopause ($\sim$98 km), is rather warm, compared to the summer mesopause ($\sim$85 km).

Ozone, which is responsible for the absorption of high energy UV radiation, is an important atmospheric trace gas. The right panel in Figure 13 shows the distribution of ozone versus height. A small peak in the ozone density can be seen in the lower troposphere, due to industrial human activities (Brasseur and Jacob 2017). The main layer extends from the tropopause till the upper stratosphere, with the maximum ozone concentration occurring between 20-30 km. The geographical distribution show higher concentration over polar latitudes, with trace amounts of found up to the mesopause boundary. In the stratosphere, ozone is formed by chemical reactions involving solar UV radiation and oxygen. In the troposhere, ozone forms by chemical reactions involving both naturally occurring and pollutive sources of gases. Ozone has two main effects on the thermal balance of the Earth coming from its absorptive properties. It absorbs solar UV radiation, contributing to heating of the stratosphere. It also absorbs IR radiation emitted by the Earth, effectively trapping heat in the troposphere. Substantial temperature changes have been shown to correlate with the depletion of ozone over the Antarctic plateau in the late 20-century (Ivy et. al 2016). Ozone's emissive properties can also affect the thermal balance. This emission is in terms of IR radiation, which is emitted from all bodies as they cool. In the winter hemisphere, when less solar radiation is present, more radiation can be emitted than absorbed, leading to what is called radiative cooling. The immediate surrounding atmosphere is then cooled as ozone has a net loss of heat by thermal radiation. The radiative change associated with ozone destruction acts as one of the main links between EPP and polar surface pressure variations in hypothesis 1.

The atmosphere can also be divided into levels depending on the altitude of a distinct pressure. This type of division of different atmospheric levels will be used throughout the thesis. In this method an atmospheric level is defined by a constant pressure given in hecto pascal (hPa). Since the pressure is constant, the altitude of the chosen pressure level is a variable which can be readily measured. This altitude depends on the atmospheric conditions. To clarify with an example, if the 1000 hPa level (approximately at ground level) is chosen for any given measurements, an increasing pressure at ground level will increase the height, defined as geopotential height (measured in meters), of this specific pressure level. In the same way a decreasing pressure will decrease the geopotential height of the same specific pressure level.

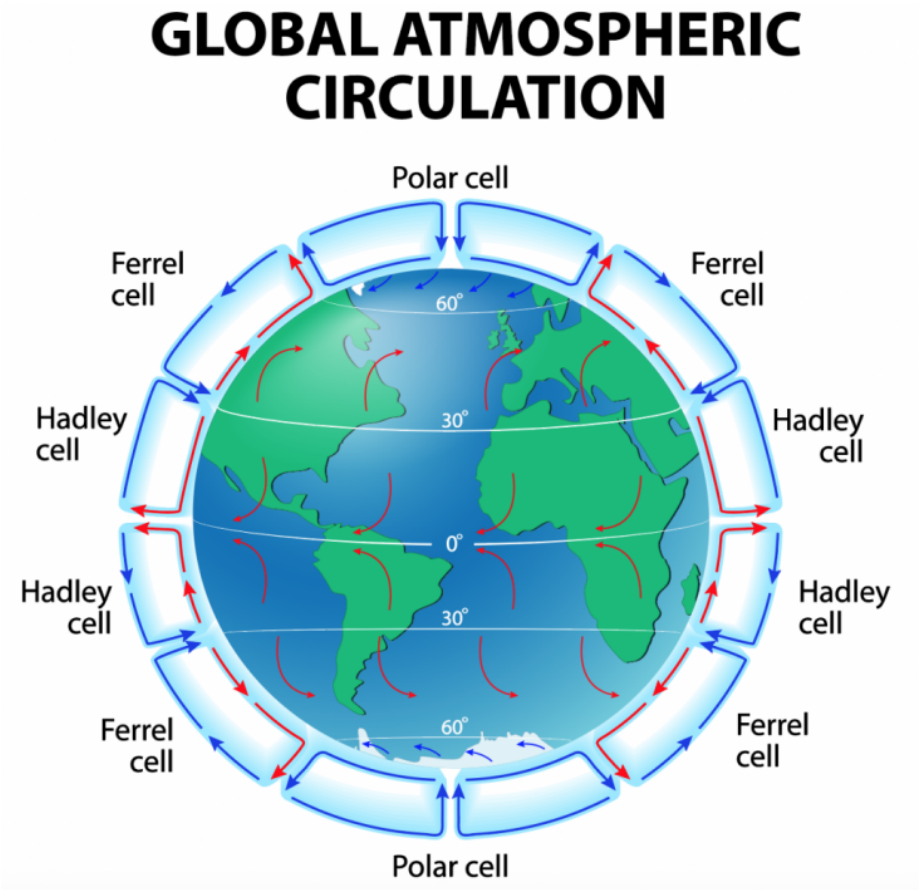

Figure 14: Latitudinal cells in the troposphere. The Hadley cell is active from approximately the equatorial region to around 30° in both latitudinal directions. The Ferrel cell and the Polar cell is active from 30°- 60° and 60°- 90° in both latitudinal directions, respectively. (Figure taken from https://www.internetgeography.net)

2.3.1 General circulation

The general circulation in the troposphere can be seen as a consequence of the radiation from the Sun, and the laws of thermodynamics acting on the atmosphere. The equatorial region positioned closest to the Sun absorbs most of the energy. The heated air rises and redistributes the energy towards the poles.

At spatial distances of a few to tens of kilometers, the atmospheric circulation can seem chaotic and unorganised, but at larger scales, distances of hundreds and thousands of kilometers, different patterns arise. These larger scale patterns

remain relatively constant due to fundamental properties of the Earth such as size, heating, rotation rate and atmospheric composition. From the ground up to the tropopause there are three distinct circulation cells in the latitudinal direction as illustrated in Figure 14 called the Hadley cell, the Ferrel cell and the Polar cell. The cells act as approximately closed loops of circulating air, where some mixing occurs at the junctions, especially between the Ferrel and Polar cell. The Hadley cell is caused by warm air rising at the equatorial region due to heating from the surface, where it could flow either north- or south-wards. As the warm air moves towards the poles and cools, it becomes denser, where it descends around 30° latitude in both directions. The cooler air then travels along the surface in the equator-ward direction to replace the air ascending from the equatorial region, which closes the loop. The Polar cell works in the same fashion, while the Ferrel cell is, however, a secondary circulation feature occurring as a consequence of the existence of the Hadley cell and Polar cell. Also shown in Figure 14 is the longitudinal vector component of the wind direction. The Coriolis effect, originating from the rotation of Earth, causes the latitudinal winds to be displaced in the longitudinal direction. This causes the winds in the Northern Hemisphere (NH) to blow from southwest as opposed to just blowing from south. In the Southern Hemisphere (SH) the same pattern occurs.

Airflow in 'closed' circulation cells are also found in the longitudinal direction in the troposphere. As with the latitudinal cells, these cells also arise due to differences in surface temperature, but in a different manner. The differences in heat capacity and absorptivity of water and land masses implies that land masses needs to absorb less heat than water does, for the same temperature

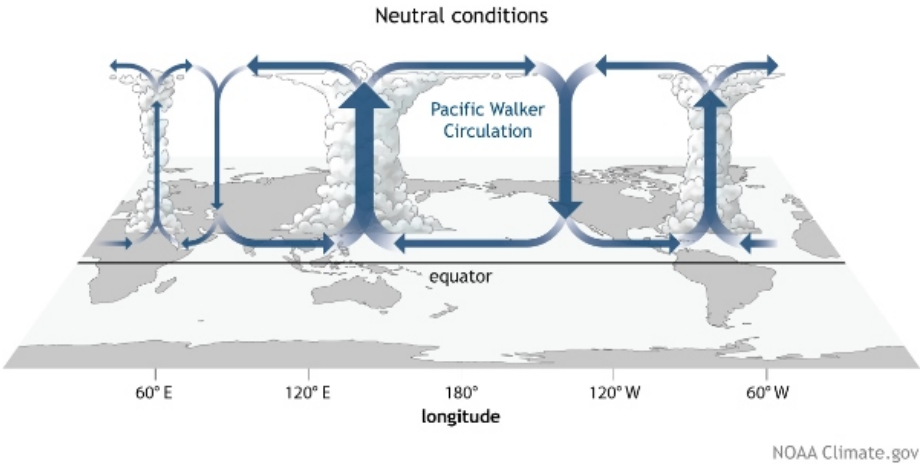

Figure 15: The Walker circulation under neutral conditions. Longitudinal circulation driven by temperature differences between land masses and sea. (Figure taken from www.climate.gov)

increase. This results in larger temperature increases at land then at sea, giving rise to temperature differences in the longitudinal direction. One example of this kind of circulation is the Walker Circulation. As can be seen in Figure 15, this circulation pattern is composed of many longitudinal cells approximately parallel with the equator. The Walker Cell plays a key role in the El Niño-Southern Oscillation phenomenon, which will be discussed later.

Above the tropopause the drivers of the circulation becomes less intuitive. Figure 16 shows the Brewer-Dobsen meridional circulation pattern. This model explains the geographical distribution of e.g. ozone. While most of the ozone is produced in the equatorial region, the highest concentration is found at polar latitudes. In general, the model describes how masses of air from the tropical stratosphere is distributed pole-wards in both directions, where the airflow is stronger towards the winter pole (Rosenlof 1995). Above the stratopause, a pole to pole circulation leads to rising (descending) motions over the summer (winter) pole with associated adiabatic cooling (heating). This adiabatic mo-

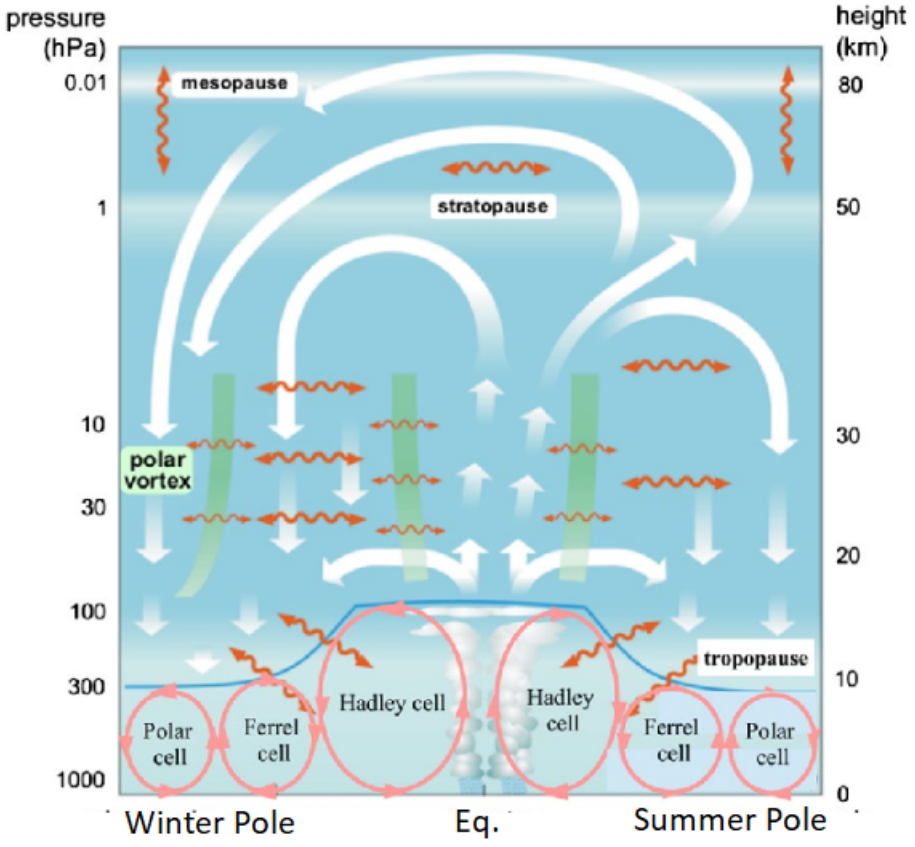

Figure 16: Brewer-Dobson circulation (Schmidt et al. 2001)

tion produces the coldest temperature at Earth, reaching as low as 120° K at the mesospheric summer pole (Vincent 2015). The main physical driving mechanism of the Brewer-Dobson circulation is the deposition of momentum in the stratosphere due to breaking of planetary waves. The wave breaking produces a body force resulting in a pole-ward mass flow. Mass continuity in an atmosphere with density decreasing with height requires that the pole-ward flow be accompanied by up-welling in the tropics and down-welling at higher latitudes. Gravity wave breaking and dissipation drives the summer to winter pole circulation in the mesosphere (Holton et al. 1995; Haynes et al. 1991; Ossó et al. 2015; Vincent 2015). The deposition of momentum originating from Rossby waves and gravity waves will be discussed in the following section.

The Brewer-Dobson circulation will be of great importance for hypothesis 1. The NO_x (HO_x has to short lifetime for significant downward transport) created by EPP needs a downward propagation mechanism traversing the mesosphere and stratopause for it to impact the upper stratospheric ozone distribution. The signal produced from this destructive interaction also has to propagate downward for it to be detectable at the surface.

2.3.2 Atmospheric waves

Gravity waves are driven by buoyancy where parcels of air are pushed to another region of different density, mainly from irregularities like mountains or thunderclouds. The scale size varies over a wide spectrum from meters to several hundreds of kilometers, with the temporal scales varying between five minutes and several hours. A vertically propagating gravity wave will be absorbed (filtered) through a 'critical level' if the component of background wind in the direction of wave propagation is equal to the wave's horizontal phase speed. For gravity waves generated directly by topography (zero phase speed relative to ground), a critical level will occur when the background wind direction is perpendicular to the wave's propagation direction (Whiteway and Duck 1996). For the mesosphere, evidence show a filtering favouring westward gravity waves in the winter and eastward in the summer (Holton and Alexander 2000). As gravity waves propagate in the vertical direction, the amplitude increase as the density of the atmosphere decrease with vertical height. At some point in the higher atmosphere these waves will break and release their energy and momentum. This momentum deposition will then affect the atmospheric circulation at the deposit altitude. This allows for transport of energy and momentum from the troposphere to the stratosphere and mesosphere (Carmen 2002; Fritts 2003, Espy et al. 2004).

Rossby waves results from the conservation of potential vorticity, which is analogous to conservation of angular momentum in mechanics. They occur as parcels of air are influenced by pressure gradients, with the Coriolis force (originating from Earth's rotation) acting as the restoring agent (Rossby et al. 1939). Rossby waves in the middle atmosphere are larger than gravity waves in spatial extent,

reaching thousands of kilometers which earns them the name planetary waves. The waves can be characterized by its phase velocity always having a westward component relative to the mean flow. A study by Kleinknecht et al. (2014) of zonal wave numbers 1 and 2 indicates vertical coupling throughout the middle atmosphere around autumn and during winter when sudden stratospheric warming (SSW) events occur frequently in the NH. These events are caused by Rossby waves themselves. The Rossby waves decelerate the polar night jet, leading to distortion and temporarily breakdown of the polar vortex (SSW events are discussed in more detail in section 2.3.4). After such an event, the conditions are favourable for further propagation of stratospheric planetary waves into the mesosphere-lower-thermosphere (MLT). Further, the observed planetary wave amplitudes in the winter where approximately halved between the stratosphere and the MLT, indicating significant dissipation in the middle atmosphere (Kleinknecht et al. 2014). In the SH, SSW events are rarely seen. This is a consequence of the low continent-ocean contrast, which makes unfavorable conditions for the generation of zonal wave numbers 1 and 2. Rossby waves have a dominating role in the positioning of high and low pressure zones, as well as significantly affecting the distribution of atmospheric composites (Rhines 2002; Rodas et al. 2017; Zhang et al. 2019; Jing et al. 2019).

2.3.3 Dynamical coupling between atmospheric layers

Both the planetary and gravity waves are crucial in the coupling between atmospheric layers. This section will focus on the dynamical coupling between atmospheric layers, with an increased focus on the polar regions, as this is most relevant for the thesis.

In both polar regions a particular circulation phenomenon occur, known as the stratospheric polar vortex. It is mainly driven by the Coriolis effect and manifests as a large low pressure area circulating anti-clockwise in the North and clockwise in the South, centered approximately at the poles. The tropospheric counterpart is known as the tropospheric polar jet. It is driven by temperature differences between high latitudes and mid-latitudes, with the boundary winds forming the polar jet stream. The edge between the cold air in the low pressure area and the warmer air at lower latitudes is known as the polar front. Figure 17 shows the behaviour of the northern polar vortex under stable (positive AO) and disturbed conditions (negative AO). In the vertical direction, both polar vortices are located from the middle troposphere, extending into the stratosphere, thereby providing a coupling between the troposphere and stratosphere for the exchange of masses of air, as well as waves carrying energy.

The chemical dynamical coupling is dependent on the coupling from the mesosphere, down to the surface. A model proposed by Holton (1983) shows how the structure of the mesospheric circulation is determined by the deposition of momentum by gravity waves, driving a slow summer to winter pole circulation. Kidston et al. (2015) states how pure weather systems are inhibited from pene-

trating the tropopause, as the stratosphere with its strong winds cannot support the dynamics characterizing a weather system. Nonetheless, the stratosphere has a significant downward influence on the polar surface weather pattern. Coupled simulations have compared an artificially perturbed stratosphere to observations and unforced coupled simulations, with a similar tropospheric response (Norton 2003; Haig et al. 2005; Scaife et al. 2005; Hardiman et al. 2008; Scaife et al. 2008). Kidston et al. (2015) also proposes a model called stratospheric downward influence. The principle is that the mean westerly momentum transported across latitudes and vertically acts to conserve angular momentum and maintain mass continuity. The steady state solution causes a steady stratospheric circumpolar jet. If wave breaking of Rossby or gravity waves into the polar jet significantly decreases, the circumpolar jet speeds up, accompanied by equatorward momentum transport. By maintaining the mass continuity in this situation, upward transport is induced over the polar cap, with sinking at lower latitude, causing near instantaneously induced pressure anomalies extending down into the troposphere (Hartley et al. 1998; Haynes et al. 2005). The situation reverses if wave breaking increases, with weakening of the circumpolar jet, inducing downward transport over the polar cap, and up welling at lower latitudes. Feedbacks from tropospheric eddies or weather systems induced by the downward influence are also crucial to the surface response (Kidston et al. 2015).

Observational evidence support a stronger downward influence in the polar region from the stratosphere when the polar vortex in the stratosphere is disturbed (Osprey 2010; Kidston et al. 2015). Also, changes in total ozone at high latitudes, accompanied by coherent changes of opposite sign at lower latitude support this model (Salby et al. 2002). According to an analysis done by Baldwin et al. (2001), by using the AO-index (discussed in next section), which is a proxy of the strength of the polar vortex, the signal of a weak polar vortex (negative AO-index) originating in the stratosphere propagates to the tropopause in about 10 days, while the signal originating from a strong polar vortex (positive AO-index) takes some days longer. Furthermore, the analysis states that only the strongest anomalies of either sign connects to the surface, with weaker anomalies typically remaining within the stratosphere.

2.3.4 Internal variability of the atmosphere and its consequences for measurements and analysis

As stated by The International Panel on Climate Change (IPCC), "Climate variability refers to variations in the mean state and other statistics (such as standard deviations, the occurrence of extremes, etc.) of the climate on all spatial and temporal scales beyond that of individual weather events. Variability may be due to natural internal processes within the climate system (internal variability), or to variations in natural or anthropogenic external forcing (external variability)." This section will focus on the internal modes of variability in the troposhere and stratosphere including the El Niño–Southern Oscillation

(ENSO), the quasi-biennial oscillation (QBO), the North Atlantic Oscillation (NAO), the Arctic Oscillation (AO), the Antarctic Oscillation (AAO) and Sudden Stratospheric Warmings (SSW).

ENSO is a cyclic climate pattern concerning temperature changes of waters in the central and eastern tropical Pacific Ocean. With an irregular period ranging from 2-8 years (Rasmusson et al. 1982), large areas of the surface waters either cools or warms, depending on the phase of the ENSO, compared to averaged conditions. This cycle directly influences rainfall distribution in the tropics, and can also have a strong influence on weather across other parts of the world (Davey et al. 2014; Pavia 2017). Some evidence also suggest linkages between the warming phase of ENSO and a weakening of the polar vortex (Li et al. 2013).

QBO is a quasi-periodic variation between downward propagating east-ward and west-ward wind happening in the equatorial stratosphere driven by the vertical transfer of momentum by equatorial waves (Holton et al. 1972). The downward propagation switches direction between easterly and westerly with a phase of $\sim$28 months. Even though the QBO happens in the equatorial region, it affects the stream of stratospheric air going pole-wards. Statistical studies show that QBO in the easterly phase is associated with a weakening of the polar vortex, which in turn can lead to enhanced cooling over Northern Europe (Marshall et al. 2009; Gray et al. 2018). Observations also support an opposite relation between the QBO and the southern polar vortex (Ford et al. 2009).

NAO is an irregular cyclic large-scale redistribution of atmospheric mass between the Arctic and the subtropical Atlantic, often measured as the difference of atmospheric pressure at sea level between Iceland and the Azores which constitutes to the NAO index (Hurrell et al. 2013). A negative NAO index refers to a higher pressure in the polar regions, with a positive index referring to a lower pressure in the polar regions (relative to the Azores). According to Hurrel et al. (2013), large changes in the mean wind speed and direction over the Atlantic can be seen in the swings from one phase to another, along with changes in heat and moisture transport. Storm tracks and intensity also vary with the phase of the NAO. Further, because it arises primarily from stochastic interactions between atmospheric storms, climatological stationary eddies and the time mean jet stream, the year-to-year changes in the phase and amplitude of the NAO can be difficult to predict (Hurrel et al. 2013).

AO (AAO in south) is phenomenon closely related to the NAO in the north. It is a weather phenomenon occurring above 20° latitude. In simple terms it can be defined as a qualitative measure of the strength of the polar vortex, or the strength of the pressure surrounding the polar region. As with the NAO, AO is also quantified by an index. A positive AO phase constitutes a stronger and more symmetrical polar vortex, thereby enclosing the polar air to the polar region, which in turn prevents cold air from escaping. A negative AO phase is defined as a disturbed polar vortex, which can lead to cold polar air leaking

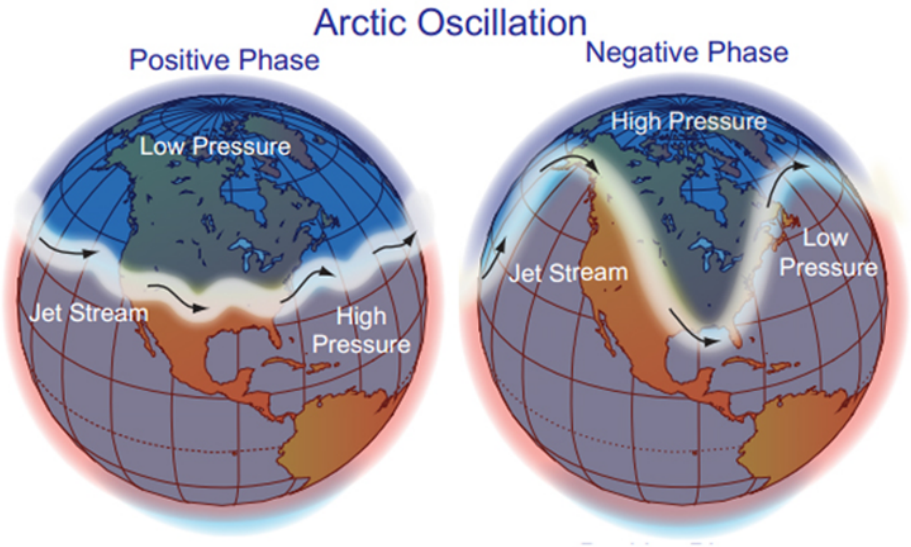

Figure 17: Illustrative depictions of positive and negative phase of the AO (blog.northgeorgiawx.com)

to lower latitudes. Leakage of cold polar air in the negative AO phase is often associated with colder over northern Eurasia (Jovanović et al. 2008; Shen et al. 2012). An illustrative depiction of both phases of the AO is given in Figure 17. As the AO is closely related to the NAO, with closely correlating phases, it is argued about which one is more fundamentally descriptive of the atmospheric dynamics. As the NAO may be associated with more physically meaningful parameters, it may carry more impact on measurable atmospheric changes (Ambaum et al. 2001).

SSW is an event where the stratospheric temperature rapidly increases (tens of Kelvin) within a short period of time (days), happening roughly every second year in the North. In the south, only two SSW events are ever recorded. This type of event is strongly associated with a disruption of the polar vortex, leading to either a weaker polar vortex, a displacement of the vortex, a split of the vortex, or even a complete temporarily breakdown of the vortex. It is caused by upwards propagating planetary waves (Rossby waves) that decelerate the polar night jet, leading to distortion and breakdown of the polar vortex. By further intensification the westerly jet completely shifts to easterly wind patterns. As the polar vortex weakens or breaks down, polar stratospheric temperatures increases abruptly. Even though SSW is a stratospheric phenomenon, there is a confirmed link between these events and surface weather, which resembles the weather anomalies following the negative phase of the AO (Baldwin et al. 2001; O'Callaghan et al. 2014) in compliance with effects following disturbances of

the polar vortex.

Different modes of internal variability affects different areas and constituents of the atmospheric system, ranging from changes in ocean temperature to stratospheric wind disturbances. Several of the modes of variability affect each other, making it a large intertwined dynamical system without a clear reference point in terms of an absolute atmospheric state. This can easily cause problems for an atmospheric researcher analysing cause and effect. If not chosen carefully, data can yield significant results, when in reality the results stem from the internal variability of the atmosphere, and not the cause in question. The key to a solid analysis depends on the sorting process of the data.

2.4 Solar Forcing

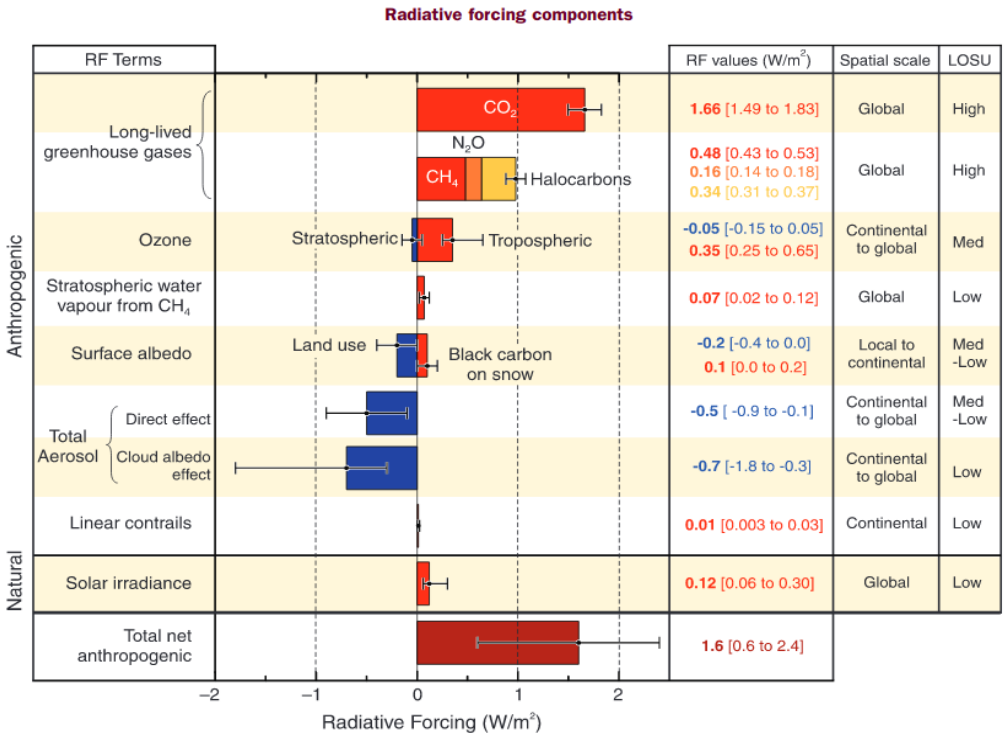

Figure 18: Global average radiative forcing in 2005 (best estimates and 5 to 95 uncertainty ranges) with respect to 1750 for anthropogenic sources and other important agents and mechanisms like solar forcing, together with the typical geographical extent (spatial scale) of the forcing and the assessed level of scientific understanding (LOSU) (IPPC 2007 Climate report).

The Sun radiates over a wide spectrum from X-ray to infrared as shown in Figure 1. Positive radiative forcing means Earth is absorbing more radiation than it radiates out to space, with a reversed situation for a negative radiative forcing. It is a measurable quantity defined as Watt per square meter (W/m^2). Figure 18 shows the different contributions to the total radiative forcing given in IPCC's climate report of 2007. As one can see, the contribution from the Sun is fairly low compared to the different anthropogenic sources as of the scientific understanding in 2007, but still maintains a low level of scientific understanding. It should be emphasized that the report only states the contribution from the Sun as solar irradiance, and does not include solar wind interaction.

2.4.1 Total solar irradiance

Total solar irradiance (TSI) is a measure of the total radiative power incident on the Earth's upper atmosphere over the whole wavelength spectrum per square meter (W/m^2). By integrating the graph in Figure 1 over all wavelengths one would get the TSI, which has an average value of roughly 1361 W/m^2. TSI follows the solar cycle, but the variations have only been measured to around 0.1% from maximum to minimum (Willson et al. 1991). The short term variations in TSI and its effects on the surface temperature variability is relatively well established (Solanki et al. 2013), with only a minor global influence attributed to about 10% of the total temperature rise seen in later years (Seppälä et al. 2014). However, the discussion about the variations in TSI and its effects over larger temporal scales is still going on. A bottom-up mechanism is proposed for the impact of TSI. It involves a direct surface impact from solar radiation being absorbed over the oceans. This leads to enhanced evaporation, ultimately leading to changes in the precipitation patterns and vertical motions, strengthening the Hadley cell and the Walker circulation associated with colder sea surface temperatures for solar maximum (Seppälä et al. 2014, and references therein, Misios et al. 2016).

2.4.2 Spectral solar irradiance

Spectral solar irradiance (SSI) is a measure of the wavelength dependent radiative power incident on the Earth's upper atmosphere per square meter (W/m^2). The impact of SSI is proposed through a top-down mechanism. Different wavelengths affect the Earth's atmosphere differently, particularly the UV spectrum, which is absorbed by ozone. This absorption contributes to heating of the stratosphere. At the same time there is a direct effect on the ozone production from the UV photolysis of oxygen, creating an additional feedback mechanism for more heating. Some evidence are pointing to a linkage between the temperature gradient created in this increased heating and zonal wind changes affecting the pole-ward wind circulation (Seppälä et al. 2014).

It is known that different wavelengths vary at different rates throughout the solar cycle, as illustrated by Figure 19. Variations of up to 6% can be seen near

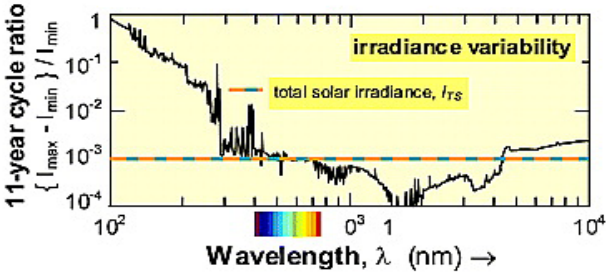

Figure 19: Spectral variability of the irradiance, defined as the difference between the S_{max} and S_{min} values, as a ratio of the S_{min} value, based on the last two solar cycles. The horizontal dashed line gives the corresponding value for the total solar irradiance, I_{TS}, i.e., the integral over all wavelengths. (Figure and description taken from Gray et al. 2010).

200 nm. Up to 4% variation can be seen in the region 240-320 nm. The former is the region where oxygen dissociate and ozone production occur, and the latter where absorption by stratospheric ozone is prevalent (Gray et al. 2010). Other measurements have found the UV flux to decrease by a much larger factor than indicated by Figure 19 (factor of 4-6) (Harder et al. 2009; Gray et al. 2010). Such a large variability in the SSI is quite controversial and not in compliance with the current understanding of solar physics. By comparing different models to observation, there exists persistent discrepancies between them (Marchenko et al. 2016). Lean et al. (2012) recommends that SORCE SIM observations (observations where the large UV decrease is found) should be used with extreme caution in studies of climate and atmospheric change until additional validation and uncertainty estimates are available. More research is needed in this area to understand the variations in SSI over time, with the most significant challenges being the difficulty of accessing the instrument degradation corrections (Woods et al. 2015).

2.5 The chemical dynamical coupling

This chapter will elaborate on the important physical principles underlying the chemical dynamical coupling. The first section will give an overview of the origin of the forcing, and its pathways into the atmosphere. The following section will cover the hypothesized mechanisms of the atmospheric response, ending with an update of recent publications.

2.5.1 Energetic particle precipitation

CMEs and HSSWS/CIR are the main drivers behind geomagnetic disturbances, which ultimately cause particles to precipitate into the atmosphere (Asikainen and Ruopsa 2016). EPP includes freshly injected particles having a pitch angle

inside the loss cone, trapped radiation belt particles interacting with plasma waves under disturbed conditions, as well as high energy solar proton events and GCRs which precipitates directly into the atmosphere. Figure 20 illustrates the ionization rates of the different particle species, along with the dominant zones of precipitation. Particles mainly enter the atmosphere in the geomagnetic polar regions, with the radiation belt electrons being lost at the geomagnetic latitudes 55°-72° (Andersson et al. 2014a). As the charged incoming particles impact, the atmospheric neutrals, dissociate, ionize or get excited, leading to a change in the rate of chemical reactions in the atmosphere.

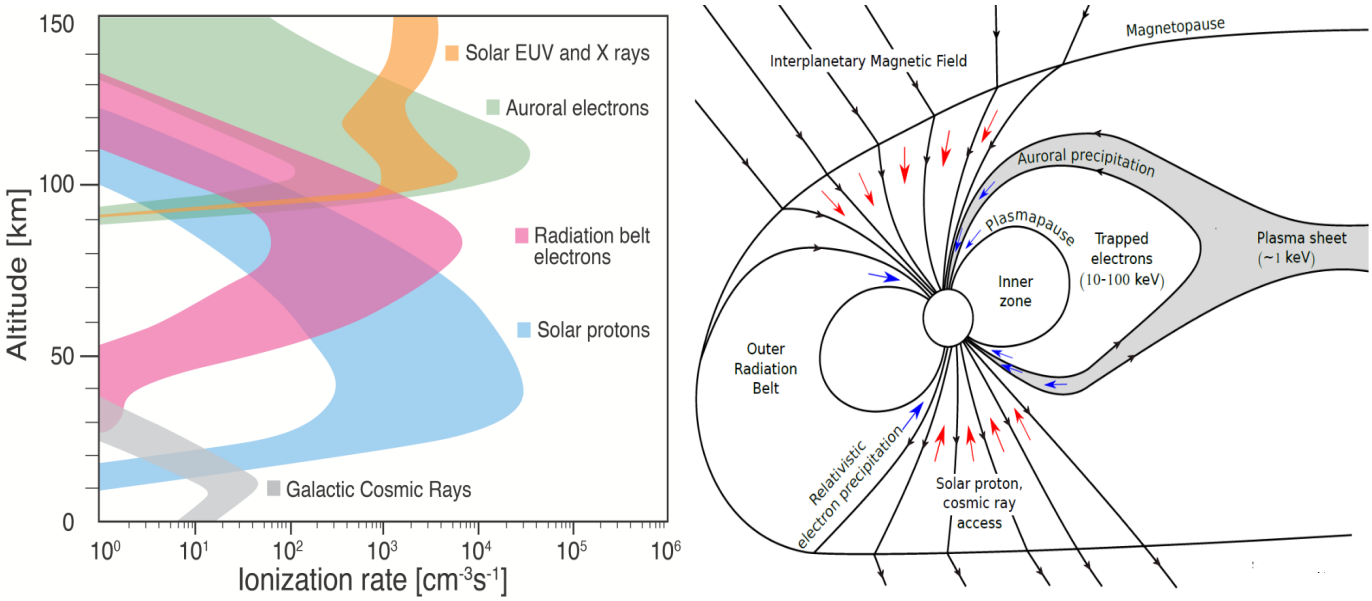

Figure 20: **Left panel:** Instantaneous ionization rates of EPP, Solar EUV and X-ray of the Earth's atmospheric layers (Baker et al. 2012). **Rigth panel:** The dominant zones of particle precipitation (Thorne 1980).

2.5.2 Mechanism: The chemical dynamical coupling

The Chemical-Dynamical coupling can be summarized as a polar surface temperature/pressure response from incoming energetic particle precipitation (EPP). Studies show that EPP correlate well with the production of NO_x and HO_x gases down to the upper stratosphere (Rozanov et al. 2005; 2015; Randall et al. 2005; Turunen et al. 2009; Smith-Johnson et al. 2017). Already in the 70s evidence of the destructive influences of these gases on ozone was emerging (Bates et al. 1950; Crutzen 1971; Johnston 1971) via catalytic cycles of the form (Portmann et al. 2012):

$$X + O_3 \rightarrow XO + O_2 \tag{1}$$

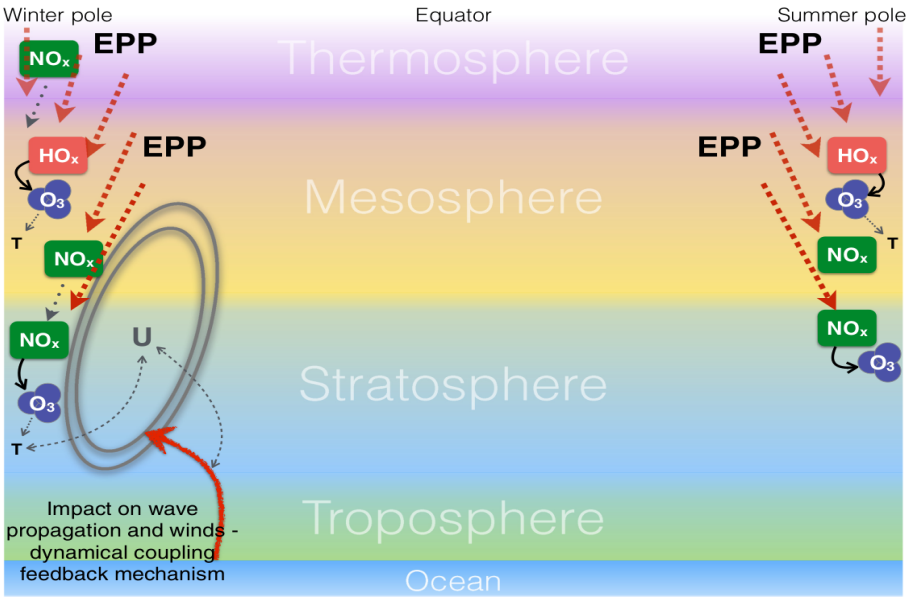

Figure 21: Energetic particle precipitation (EPP) impact on the atmosphere. Main direct and indirect impacts from EPP (including EEP and SPE). EPP ionisation is focused on the polar regions leading to production of HO_x and NO_x shown in the figure. Transport processes are shown with grey dotted lines, while coupling mechanisms are indicated with grey dashed lines. Direct chemical impacts are shown with black arrows. (Figure and description taken from Seppälä et al. 2014)

$$XO + O \rightarrow X + O_2 \tag{2}$$

With X = {NO_x,HO_x}, giving a net:

$$O_3 + O \rightarrow 2O_2 \tag{3}$$

The recycling of the X-molecule makes the reaction even more destructive as one X-molecule can destroy many orders of magnitudes of ozone molecules before it is converted to a less reactive molecule (Lary 1997). After production HO_x quickly dissociate or react in the area of production, as it has a lifetime of only hours in the mesosphere. NO_x has a mean lifetime ∼1 day, before it is photodissociated. This lifetime can be greatly increased by the absence of sunlight, which is part of the reason why the mechanism only operates in the local winter polar hemisphere. The effects of EPP are usually classified as direct or indirect effects. Direct effects are the local production of NO_x and HO_x (Andersson et al. 2014b), whereas the indirect effect are the effects of the down welling of NO_x from the production area to the stratosphere (Randall et al. 2009).

The mechanism being investigated in this thesis depend on the indirect effects,

even though a combination of the occurrences of both cannot be ruled out. As the NO_x molecules are transported downwards, a present polar vortex confine the molecules to the polar region on their downward path, thereby enhancing the effect in this region. NO_x will then destroy ozone along the trajectory of the downward path (Bates et al. 1950; Crutzen 1971; Johnston 1971; Sinnhuber et al. 2018). Ozone absorbs UV-radiation, and emit thermal long wave radiation, which increases and decreases temperature, respectively. During winter polar night with less UV, the radiative cooling is the dominant effect. A reduction in the ozone will then moderately decreases the emission of long wave radiation resulting in a net stratospheric warming (Graf et al. 1998; Langematz et al. 2003).

This temperature increase can induce zonal wind changes, ultimately affecting the surface through wave-mean flow coupling and wave refraction (Seppälä et al. 2014). In the scientific literature, two different coupling mechanisms are used to explain the surface response. Seppälä et al. (2013) proposes an indirect interaction between NO_x and stratospheric dynamics through wave-mean flow interactions. The interaction requires stable initial vortex conditions (associated with QBO-W conditions), where the wave-mean flow interaction acts to refract planetary waves into the low latitude upper stratosphere during the early winter. This result in the dynamic response seen during the late winter (January-March). The other proposed coupling mechanism have a reversed pattern. Here, the wave-mean flow interactions between NO_x and the stratospheric dynamics are enhanced under disturbed vortex conditions (QBO-E). Higher winter polar concentrations of ozone, as well as a generally warmer polar stratosphere under these conditions makes the polar vortex more susceptible to wave-mean-flow interactions. This allows the EPP-induced dynamical effect to propagate downward more efficiently (Salminen 2019; Asikainen et al. 2020). Figure 21 represents all the steps in the mechanism.

2.5.3 Recent publications

Seppälä et al. (2009) used reanalysis data to show significant winter surface air temperature anomalies resembling the AO pattern when years are divided depending on the geomagnetic activity. Higher geomagnetic activity resembled an intensification of the polar vortex. Figure 22 shows the surface air temperature anomalies when sorting the years into high and low A_p ($\pm 5\%$ of the average A_p values), excluding the years with SSW events. The same paper includes a case with the inclusion of years with a SSW event, where the effect diminishes.

Simulations done by Baumgaertner et al. (2011) and (Rozanov et al. 2012) both found the same effect, with higher geomagnetic activity followed by ozone depletion and cooling in the lower stratosphere, leading to an intensification of the northern polar vortex and warming over Europe. Studies by Baumgaertner et al. (2011) and Rozanov et al. (2012) have shown warming of higher altitude regions where the ozone depletion occur, alongside a cooling of the lower altitudes and an enhanced polar vortex following EPP. The warming can be

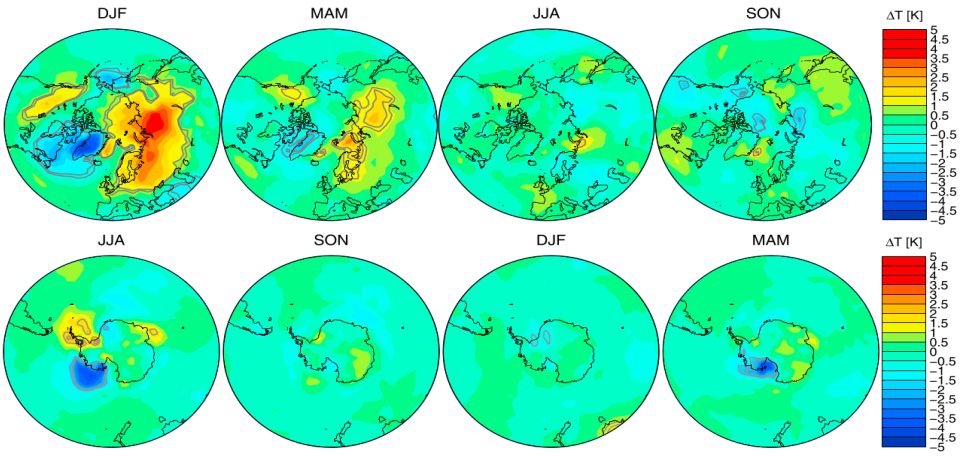

Figure 22: Northern and southern hemisphere seasonal differences in ∇T = High A_p - Low A_p. (Full details about the analysis can be found in Seppälä et al. 2009)

explained by ozone's radiative properties. The cooling at lower altitudes can be explained by a weakening of the winter-poleward Brewer-Dobson circulation as the zonal winds and wave breaking changes due to the changing temperature, leading to adiabatic cooling when the down welling decreases. Results from Baumgaertner et al. (2011) can be seen in Figure 23.

Studies on the mechanism have pointed to somewhat contradictory responses of the polar vortex to geomagnetic activity when the phase of the QBO is taken

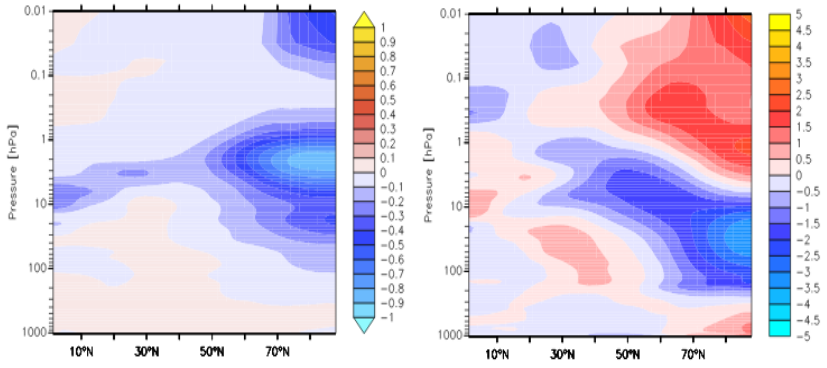

Figure 23: Left panel: Ozone depletion stemming from EPP. Right panel: Pressure change related to the ozone depletion. (Full details about the analysis can be found in Baumgaertner et al. 2011)

into account. Recent studies by Maliniemi et al. (2016) and Salminen et al. (2019) show a larger polar vortex response to geomagnetic activity during the easterly phase of the QBO, while studies by Lu et al. (2008) and Seppälä et al. (2013) show a larger response during westerly QBO. There is no conclusive evidence of the time lag of the effect, or its dependence on early and late winter.

2.6 The Mansurov effect

This sub-chapter elaborates on the important physical principles underlying the Mansurov effect. The first two sections will give a detailed overview of the origin of the forcing, and its pathways into the atmosphere. The following sections will cover the hypothesized mechanisms of the atmospheric response for the forcing, ending with an update of recent publications.

2.6.1 Global Electric Circuit

Before discussing solar influence through the magnetic and electric fields in the IMF, the Global Electric Circuit (GEC) must be introduced. GEC links the electric fields and currents flowing in the lower atmosphere, ionosphere and magnetosphere forming a giant spherical condenser (Siingh et al. 2007) as shown in Figure 24a. The GEC has upward driven currents originating from the worlds thunderstorms and electrified clouds which helps maintain a potential difference V_i between the ground and the ionosphere at around 250 kV (Williams 2005; Tinsley 2000). These current systems spread around the globe through the ionosphere and magnetosphere following geomagnetic field lines to the opposite hemisphere (Siingh et al. 2007). In fair weather regions a return current is set up from the ionosphere to the ground completing the circuit of the GEC. The vertical current density J_z in clear weather is in the range 1-4 pA m^{-2} (Tinsley 2000).

Figure 24b presents a simpler model of the GEC. The thunderstorms which acts as the generators of the electric potential is highly concentrated in the low latitude tropics as shown in the figure. By definition of Ohm's law we have to introduce the resistance of the vertical earth-ionosphere column which the vertical current density J_z passes through. We note that the conductivity of this column increases rapidly with altitude in clear air, thereby dividing the resistance into a tropospheric part (R_T) and stratospheric part (R_S). In the upper stratosphere and mesosphere the conductivity is so high compared to the lower levels of the atmosphere, that the ionospheric potential effectively extends down to mid-stratospheric levels (Tinsley 2000).

2.6.2 Solar influence on the GEC

The current density, J_z, of the GEC can be modulated by changing the conductivity and/or the ionospheric potential. The conductivity of the troposphere

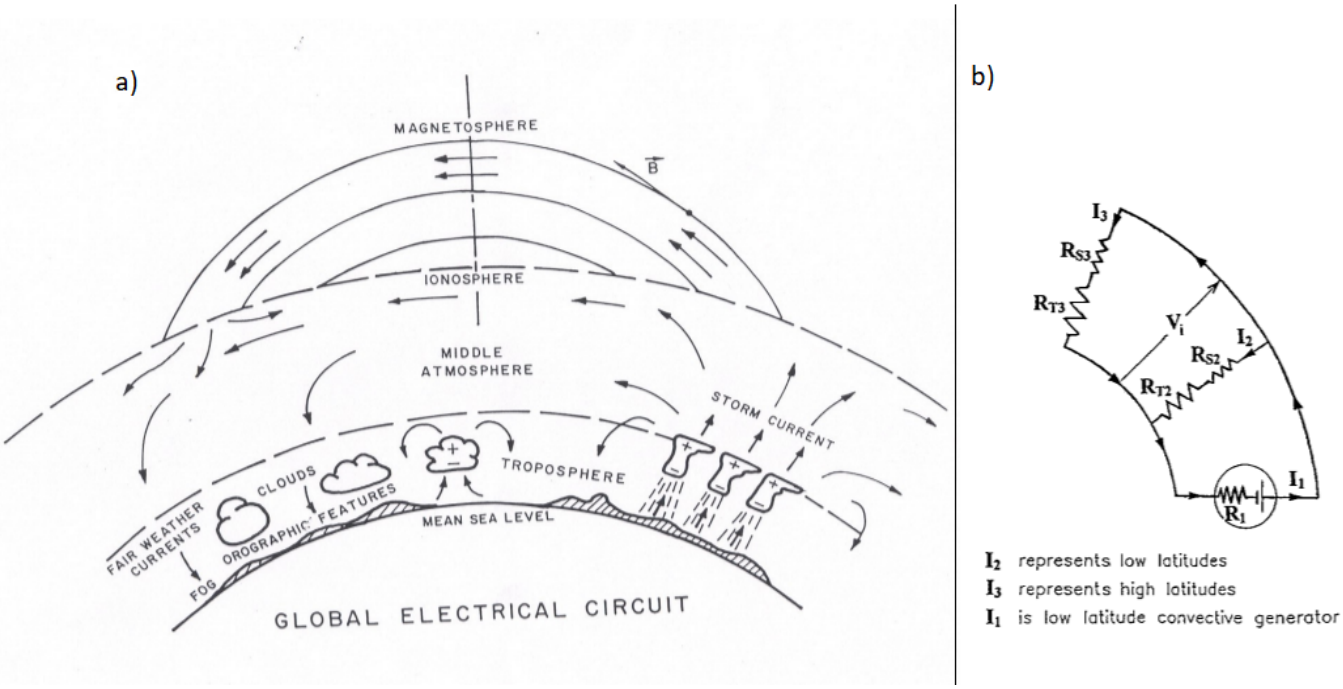

Figure 24: a) Drawing of the GEC. (Siingh et al. 2007) b) A simple illustration of the GEC. Subscript **S** and **T** represents the stratosphere and troposphere, respectively. (Tinsley 2000)

and/or stratosphere can be affected by changes in ionization of the neutral atmosphere, with sources of ionization being GCR, deeply penetrating solar particles, as well as radioactive materials in the ground at Earth. Modulating J_z, through the change of the ionospheric potential V_i, is the focus of this section. Research shows that the solar wind, through different magnetic orientations of its field, has the ability to significantly affect the ionospheric potential, which is the pathway of the Mansurov effect.

A brief explanation of the physical principles of this mechanism starts by following the Dungey cycle discussed earlier in section 2.2.2. When reconnection occurs, the polar cap magnetic field lines connect to the solar wind. As the solar wind with its frozen in magnetic field is in motion, an electric field is induced as seen by an observer at Earth, known as the motional electric field (Dungey 1961; Borovsky 2016):

$$\mathrm{E} = \frac{-[\mathbf{V}\mathrm{x}\mathbf{B}]}{c} \tag{4}$$

As discussed in section 2.2.3, the transmission of electric fields can occur along magnetic field lines, essentially transporting the electric potential associated with the electric field in the solar wind to the polar cap ionosphere, causing

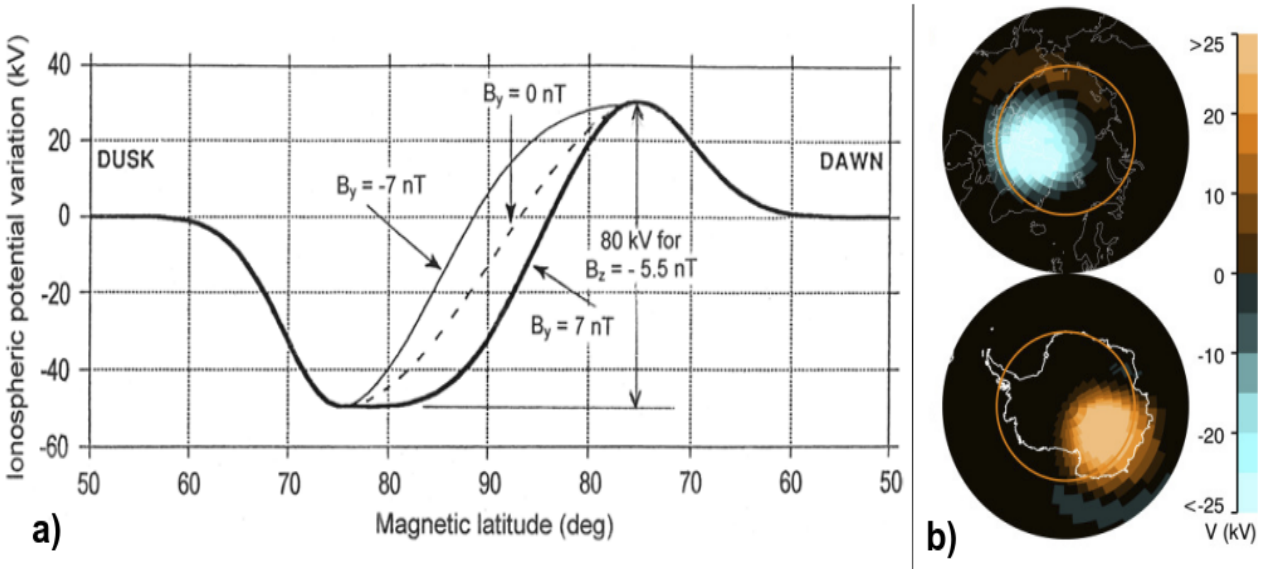

Figure 25: a) Ionospheric potential deviation from the 'global' value in the dawn–dusk magnetic meridian in the NH with B_z negative; for an 80 kV total horizontal 'dawn–dusk' potential difference, and for three B_y values. In the SH the variations correspond to those in the NH but with the curves for positive and negative B_y interchanged (Tinsley 2008). b) Superimposed plot for ionospheric potential for B_y oriented in opposite directions for both hemispheres (days with B_y high ($>$ 3 nT) subtracted days with B_y low ($<$ -3 nT). The orange circle represents the 70° parallel (Lam et al. (2013) for full analysis).

an additional potential to be superimposed on the global ionospheric potential V_i (Tinsley 2008). From Equation 4, the electric field set up by the moving solar wind is determined by the cross product between the velocity vector of the solar wind, and the magnetic field vector. The cross product between the B_z component and the V_x components gives rise to an electric field parallel to the dusk-dawn direction in the GSM-coordinate system. Figure 25a shows that for $B_y = 0$ nT, the overall dusk-dawn effect of a negative B_z is negligible as the negative and positive perturbation averages out over the whole polar cap. Different values of B_y changes the symmetry of the dusk-dawn potential differences at a specified hemisphere, with an interchangeable symmetry between the North and South for opposing signs of B_y. This results from the fact that the cross product between the B_y component and the V_x components gives rise to an electric field parallel to the North-South direction in the GSM-coordinate system, where this additional electric field will affect the North and South ionospheric cap with oppositely signs when superimposed. The asymmetry in the ionospheric potential arising from the value of the B_y component shows a linear dependence (Frank-Kamenetsky et al. 2001; Pettigrew et al. 2010). Larger

absolute values of B_y represent larger asymmetries in the ionospheric potential in the dusk-dawn plane, causing a larger total perturbation when averaged over the whole polar cap. The effects of the B_y component can also be seen in Figure 25b for both polar caps. The plot represents a superimposed plot of the average ionospheric potential for the days with positive B_y, minus the average ionospheric potential for the days with negative B_y (B_y (pos) - B_y (neg) = ∇kV). In the north, the total perturbation is negative, while it is positive in the South for the same values of B_y (Tinsley 2000; 2008; Burns 2008; Lam et al. 2013).

Early studies by Svalgaard (1968), Mansurov (1969) and Heppner (1972) were the first to give evidence of geomagnetic disturbances in the polar regions correlating with the orientation of the IMF. Later studies (Tinsley 2000; 2008; Frank-Kamenetsky et al. 2001; Kabin et al. 2003; Pettigrew et al. 2010; Lam et al. 2013) have shown a wide variety of different patterns of polar cap ionospheric disturbances as the orientation of the IMF and the different angles of incidence of the solar wind changes, where the largest asymmetry is seen between the states $+B_y$/$-B_y$. Several studies have shown a high significant correlation including only the B_y component, where a coupled V_xB_y is expected to yield even higher correlations.

2.6.3 Mechanism: The Mansurov effect

The physical case can be summarized as a polar surface temperature/pressure response from the modulation of the solar magnetic field via the route of the GEC. What is still controversial and not fully supported yet, is the GEC's part in determining the weather. Since the 70s empirical studies have shown significant correlations between changes in the IMF B_y component and polar surface pressure (Mansurov et al. 1974; Burns et al. 2007; Burns et al. 2008). As the significant correlation has been demonstrated in a fair amount of data sets, together with findings of vastly changing electrical conditions between different weather conditions (Harrison 2011), it has paved the way for a mechanism involving the GEC to explain the related surface anomaly.

Figure 26 shows a diagram depicting all the different forcing acting on the GEC. Pathway A in the figure represents the Mansurov effect. The mechanism proposes that changes in the GEC changes cloud and aerosol microphysics, in turn affecting the macro physics of the clouds resulting in weather and climate effects reaching the surface. Many theories have tried to explain how a change in current density J_z affect the cloud generation processes, but none have been fully accepted or reproduced in experiments (Tinsley 2008)

2.6.4 Recent publications

As discussed, many individual papers have confirmed the significance of the Mansurov effect. The effect found is a positive (negative) pressure correlating with a negative (positive) B_y-component in the north, with the opposite effect

in the south which happens with a time lag of just a few days. The pressure variations related to the variation of B_y have a maximum of around 3 hPa, which can be seen in Figure 27 (Burns et al. 2008; Lam et al. 2013). All recent papers finds the highest significant correlation for the period 95-05, with the highest correlation found in Antarctica.

Burns et al. (2008) finds a -2 day lag from the pressure response to the driver, counterintuitive to a cause-and-effect relationship. This discrepancy is partly explained by being within the realms of statistical error margin.

Recent papers have also calculated the temperature anomaly related to the Mansurov effect (for the period 99-02 in Antarctica), finding a seasonal dependence with a total peak amplitude of 3.2 C in the autumn (Freeman and Lam 2019). The most recent study from Freeman and Lam (2019) finds seasonal differences for the period 99-02, with the strongest temperature anomalies in March-April-May.

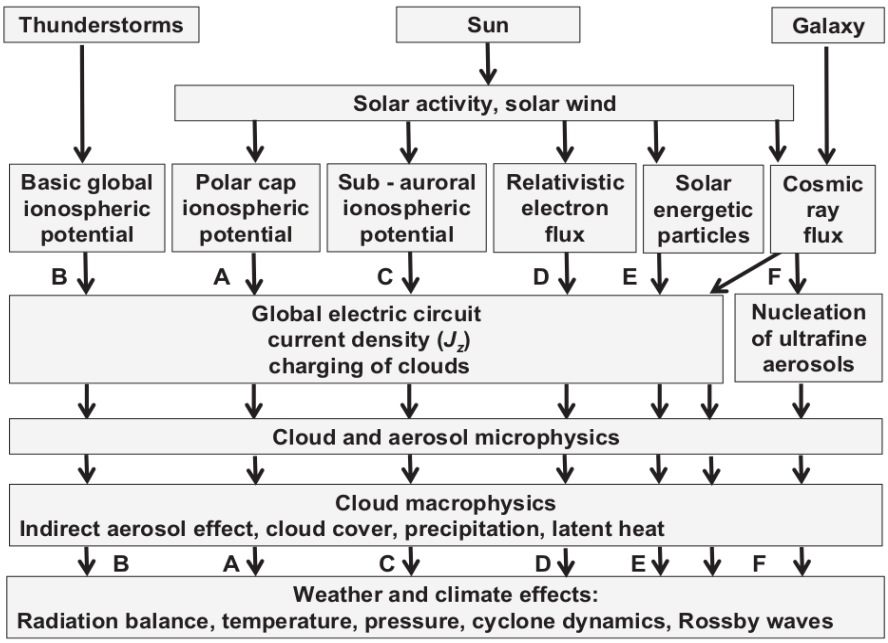

Figure 26: A-F are all individual forcings on the atmospheric system. This mechanism includes forcing through pathway A. (Tinsley et al. 2016)

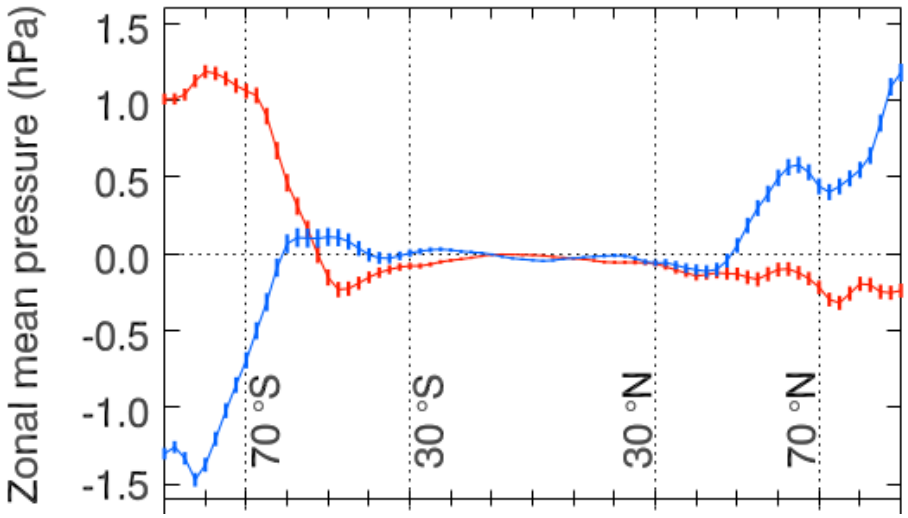

Figure 27: Red (blue) line represents the average over days with $+B_y$ ($-B_y$) subtracted the total climatology. Analysis done for the period 1999–2002. [Lam et al. 2013]

3 Data and method

This chapter will describe the data used in this thesis, followed by a discussion of the methods of sorting data in an atmosphere with an intrinsic variability. The statistical methods used to evaluate the significance of the results are examined. Further, a critical look into the Super Epoch method and its possible limitations is explored. At last, an elaboration of the different ways to obtain the climatology, which is used as a reference frame for the atmosphere, is presented.

3.1 Data

3.1.1 Atmospheric weather data

The atmospheric weather data used in this thesis are reanalysis data. Shortly described, it is created from data assimilation where observations are combined with output from a numerical model. As data coverage and new observational methods advance, the raw data input also changes over the time period in the reanalysis data. Reanalysis products may produce artificial variability and false trends, but has proven useful when used with caution.

This main source of atmospheric data in this thesis comes from the European Center for Medium-Range Weather Forecast Re-Analysis[1] (ERA5), which is the latest climate reanalysis produced by ECMWF. It provides hourly estimates of many atmospheric and ocean variables. The data cover the Earth on a 30 km grid, with a height resolution of 137 levels from the surface up to 80 km, which are interpolated to 37 pressure levels [2]. The current version covers the period from 1979. The parameters extracted from ERA5 for further analyses are geopotential height for 1 hPa, 5 hPa, 10 hPa, 50 hPa, 100 hPa, 250 hPa, 500 hPa, 750 hPa and 1000 hPa pressure level. Geo-potential height is estimated based on temperature and pressure data and can be understood roughly as the height above sea level of a pressure level.

Data on the occurrences of SSW events comes from the Sudden Stratospheric warming compendium by Butler et al. (2017). It consists of data from six different reanalysis products, where SSW events are listed for each product. This thesis defines an SSW event if it is apparent in 3 or more of the reanalyses.

Data on the QBO are obtained from the National Oceanic and Atmospheric Administration (NOAA) [3]. The phases are defined by the monthly averaged equatorial wind direction given as either positive (westerly) or negative (easterly). This thesis will use the QBO-phases at the 30 hPa level, as it is concluded

[1] Copernicus Climate Change Service (C3S) (2017): ERA5: Fifth generation of ECMWF atmospheric reanalyses of the global climate. Copernicus Climate Change Service Climate Data Store (CDS), date of access

[2] https://confluence.ecmwf.int/display/CKB/ERA5%3A+data+documentation

[3] https://www.cpc.ncep.noaa.gov/data/indices/qbo.u30.index

by Maliniemi et al. (2016) to be significant in respect to the modulation of the EEP-NAM relation.

3.1.2 Solar wind data

The solar wind parameters are provided by OMNI space weather data [4]. They are deduced from satellite measurements located approximately 230 Earth radii upstream at the L1 Lagrange point, as illustrated by Figure 28. After esti-

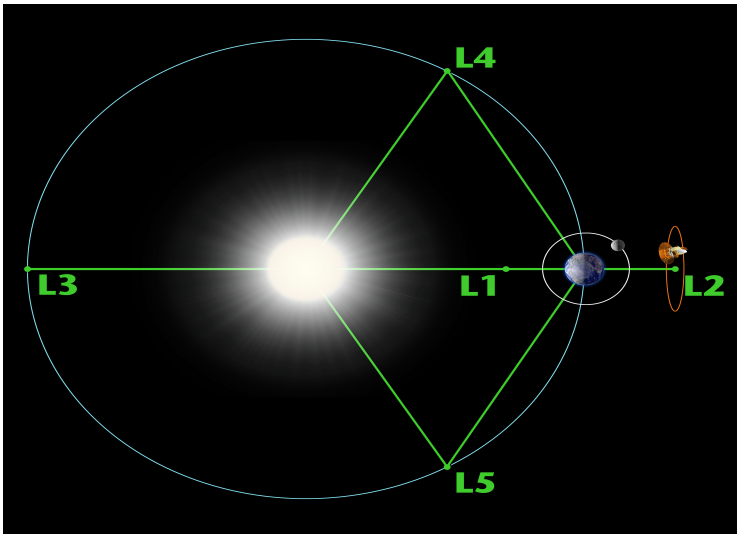

Figure 28: [https://solarsystem.nasa.gov/]

mating the solar wind phase front orientations and propagation, the data are recomputed to simulate the values at the interface between the solar wind and the magnetosphere at approximately 14 Earth radii. This thesis use the IMF B_y-component and the radial solar wind speed (v_x) for further analyses.

Vokhmyanin et al. (2019) offers a critical view of the OMNI space weather data. As the dayside magnetopause extends to roughly ∼10 Earth radii, it is suggested that the solar wind measured at 230 Earth radii may miss the magnetosphere. By comparison to independent measurements closer to the magnetopause the paper concludes that ∼10% of the data have correct variability but wrong absolute value, ∼15% of the data being poor, and the rest being very or relatively good. This suggests caution when handling the solar wind parameters.

Figure 29 shows the power spectrum for B_y and V_xB_y coupled. It is calculated through Fourier transformation analysis. Both indices show dominant peaks at approximately 27 days per cycle.

[4] https://omniweb.gsfc.nasa.gov/

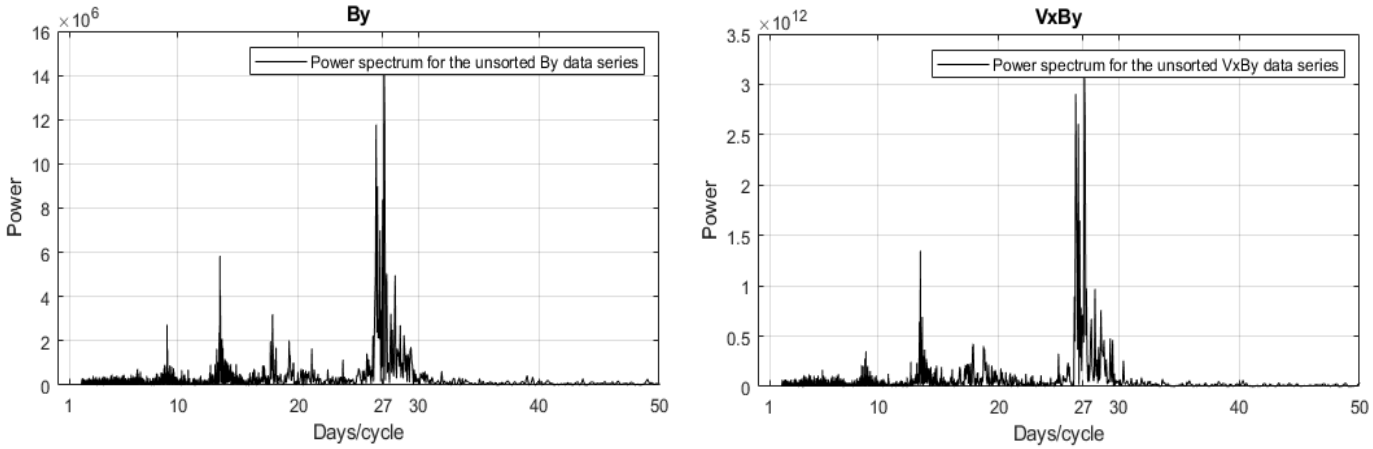

Figure 29: **Left panel:** Power spectrum of the raw By data series. **Right panel:** Power spectrum of the raw coupled VxBy data series. Both show a dominant periodicity of approximately 27 days. This periodicity is greatly enhanced when Vx is coupled to By.

3.1.3 Index of magnetic disturbance: A_p

Transport of energy via charged particles and magnetic and/or electric fields from the solar wind through the magnetosphere and the ionosphere results in disturbances in the geomagnetic field. A number of indices have been derived from magnetic measurements to classify the general level and/or type of disturbance. This section will give a short description of the A_p-index.

The A_p-index is in fact derived from another index, the K_p-index, which in turn is derived from the K_s-index, ultimately derived from the K-index. The K-index is derived from the geomagnetic field measurements at 13 observatories[5], which measure the strength of two components of the magnetic field (Declination, Horizontal), and assig a value from ranging from 0 (low) - 9 (high) to each three hour interval depending on the strength of the disturbance after diurnal variations have been subtracted. The 0-9 values follow a near logarithmic scale, with K=9 being around 100 times greater than K=0. By correcting for seasonal variations, and the fact that observatories near magnetic midnight tend to have higher K-indices, all observatories are transformed to the K_s-index. By combining the K_s-index as an average from all observatories for each three hour interval one get the K_p-index, which represents the level of geomagnetic disturbance on a global scale. Finally, by deriving a linear representation of the logarithmic K-scale from the K_p-index, the A_p index is determined.

In general, it is easier to handle the linear A_p-index compared to the logarithmic

[5]List of observatories: http://isgi.unistra.fr/indices_kp.php

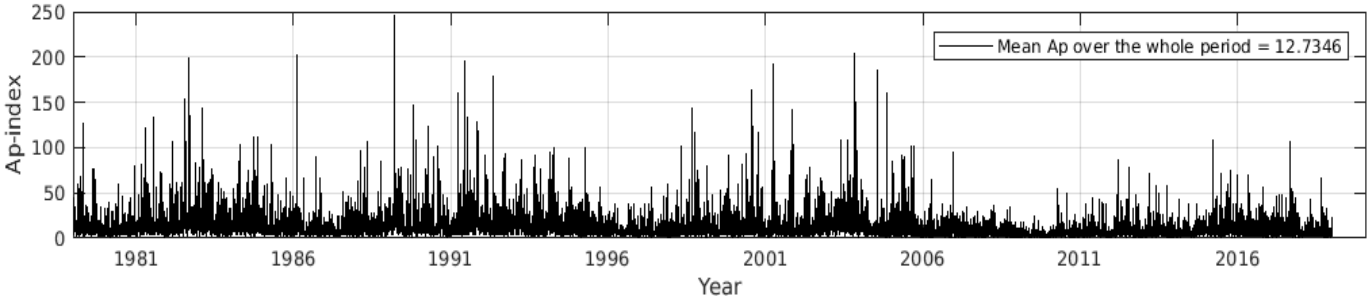

Figure 30: Variations in the A_p-index. The mean A_p equal 12.7346 over the period 1979-2018.

K_p-index when analysing data. Since the A_p-index is derived straight forward from the K_p-index, both have a long history of records (K_p since 1930), which is valuable for e.g. climate analyses. The A_p-index is used as a general measure of the global scale geomagnetic disturbances, where major disturbances reflects a higher probability for EPP. Figure 30 shows the variations in the A_p-index over the whole data period for the thesis (1979-2018). The A_p-index is provided by the OMNI space weather data.

3.2 Data sorting: Internal atmospheric variability

When looking at cause and effect between an external forcing and atmospheric response, it is crucial that the compared data points have a matching internal atmospheric state. As an example, Table 2 list the internal state of 10 data points. The goal is to find out if the external forcing (EF) changes the pressure.

Table 2

Nr	**EF**	**QBO phase**	**NAO phase**	**SSW occuring**	**Volcanic year**	**ENSO**
1	Yes	West	Neg	Yes	No	Neg
2	Yes	West	Neg	Yes	No	Neg
3	No	West	Neg	No	No	Neg
4	No	West	Neg	No	No	Neg
5	Yes	West	Neg	No	Yes	Pos
6	Yes	East	Neg	No	No	Neg
7	No	East	Neg	No	No	Neg
8	Yes	East	Neg	No	No	Pos
9	No	West	Pos	No	No	Pos
10	Yes	East	Neg	No	No	Pos

Exemplified data points (1-10) with coinciding atmospheric internal state defined by the modes of internal variability described in this section. [**EF**: External Forcing]

Sorting the first four data points based on the EF, the pressure difference would be:

$$\nabla \mathrm{P} = \frac{\mathrm{Pressure}(1) + \mathrm{Pressure}(2)}{2} - \frac{\mathrm{Pressure}(3) + \mathrm{Pressure}(4)}{2} \tag{5}$$

Despite that most the atmospheric states parameters are similar, the positive external forcing bins are aliased with a SSW event. SSWs will strongly impact the stratospheric temperature, which would also affect the pressure profile. A comparison of these bins would yield what is called an 'aliasing effect', where it is impossible to distinguish the contribution from the EF, to the contribution of the SSW events.

By a second look at Table 2, one can see more difficulties arising. Because of all the different modes of variation, it can be hard to find comparable atmospheric states sorted by the strength of an external force. This opens up a situation of gain and sacrifice. To gain the most similar atmospheric state contained in the data set one would have to sacrifice the amount of data points. The situation at hand makes it clear that a perfect analysis in a dynamical atmospheric system is impossible. In the following analyses, data containing modes of internal variability causing major atmospheric changes like SSWs and years following volcanic eruptions are treated with caution, and excluded when possible. Data containing modes following cyclic behavior are also treated carefully, and sorted into categories defined by each cycle (ex. west or east phase of QBO) if possible depending on the amount of data points.

3.3 Statistical tools

When analysing and correlating data, minimizing statistical errors is of high priority. This section describes the statistical methods used to account for both the spatial and temporal auto-correlation, which is not accounted for by the commonly used t-test.

For the spatial auto-correlation, False Detection Rate (FDR) by Wilks (2016) is used. Wilks (2016) states that a statistical test used to measure the significance of each individual gridpoint (when plotting maps) is not enough to act as an indicator of a physically meaningful result. A global null hypothesis encompassing all the local null hypothesis (individual tests) is needed. It is further stated that if the global null hypothesis cannot be rejected, one cannot conclude with adequate confidence that any of the individual local tests show meaningful violations of their respective null hypotheses. According to Wilks method, the p-value with students (two-sample) t-test is calculated for each individual gridpoint. The p-values are then sorted in ascending order, matching the set $i = 1,..,\mathrm{N}$, where N represents the total sample size. The new global p-value, $\mathrm{p_{FDR}}$, is then calculated according to equation 6, where α_{FDR} is set equal 0.1, to achieve a significance of 0.05 (Wilks 2016).

$$p_{\mathrm{FDR}} = \max[p(i) : p(i) \leq (i/\mathrm{N})\alpha_{\mathrm{FDR}}],\ i = 1, .., \mathrm{N} \tag{6}$$

For the temporal auto-correlation, a Monte Carlo method is used. After obtaining a result, n number of the same analysis with are run, where some parameters are randomly selected. For the monthly analyses, the years contributing to each bin will be randomly shuffled, while for the daily analyses, both years and days will be picked at random. Other variables such as time lag, map location, which time period daily values are selected from, etc. are kept constant and equal to the original analysis. From n analyses, a distribution is made containing all outcomes. For a map plot, a distribution is made for every individual grid point. The original result of the analysis is then assigned a p-value depending

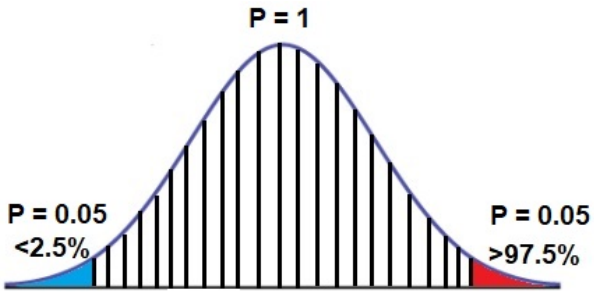

Figure 31: Significance at different regions in the normal distribution.

on its placement according to the different percentiles of the distribution at the matching grid point. If pn defines the percentile level (pn = 1,2,3,..,100), the p-value is calculated according to:

$$\text{P-value} = \frac{2pn}{100} \ (pn <= 50) \tag{7}$$

$$\text{P-value} = \frac{100 - pn}{100} \cdot 2 \ (pn > 50) \tag{8}$$

To obtain statistical significance, the original results have to be in the lower 2.5 percentile or higher 97.5 percentile of the Monte Carlo distribution, which is equal to a p-value of < 0.05. The confidence in the Monte-Carlo method increases with increasing number of random simulations (n). A range of n = {300,2500} will be used in this thesis.

For all map plots containing multiple grid points, the Monte Carlo approach combined with the False Detection Rate are used to account for the spatial and temporal auto-correlation. Comparisons to the two sample t-test combined with FDR are also done to get insight into the necessity of the method.

3.4 The Superposed Epoch method

The main analysis tool used throughout this thesis is a variant of the Super Epoch method. In essence, the occurrence of an event is marked as the zero epoch time. All events are superposed on each other with the key time synchronized. As an example, evaluating IMF B_y as the external force, periods of high $B_y(+)$ are marked as key times. Subsets from the pressure data are then picked out around the key time, super imposed, and synchronized. The idea behind the method is that noise interferes incoherently, while a signal will add up. For most parts of the thesis, opposite extremes e.g. the maximum and minimum values of B_y, is selected as key times. The superimposed and synchronized time series from one criterion will be subtracted from the other, giving an estimate of the amplitude value between two different states of the forcing.

Throughout the analyses, a weakness with the method emerged. As a hypothetical example, a time series of length **L** is used to look for an effect from a forcing that occur with a 30 days periodicity. If the forcing occurs at the first day (day 1) of the time series, the next occurrence will happen at day 30. This can be written as:

$$O_1, O_2, O_3, O_4, O_5, ..., O_N \text{ ,N is an integer} <= \frac{\mathbf{L}}{30} \tag{9}$$

O stands for occurrence, the subscript defines which occurrence it is in chronological order, and there is always 30 days between each O. Every O now defines a key time. By looking at a different data set, P, all key times can be written as:

$$P_{O_1}, P_{O_2}, P_{O_3}, P_{O_4}, P_{O_5}, ..., P_{O_N} \tag{10}$$

The super epoch analysis will now superimpose all subset $P_{1\rightarrow N}$ at day zero (key date). At day +30 in the super epoch, which is the periodicity of the occurrences, P_{O_1} has now become P_{O_2}, P_{O_2} has become P_{O_3}, and so on. The superimposed value at day +30 can be written as:

$$+1 \text{ period: } \; P_{O_2} + P_{O_3} + P_{O_4} + P_{O_5} + P_{O_6} +, ..., +P_{O_{N+1}} \tag{11}$$

One can see that the same will happen for -1 period as well, only in the reversed direction. This implies that values at periodicity lengths from day zero are made up from the same values as the ones making up day zero, minus two values which will differ. An artificial periodicity found in such a hypothetical example will then be created as the signal found at day zero replicates itself to day ± (1,2,3,4,5,..,N) periodicity's. The further from day 0 in terms of periods, the smaller the replicating effect.

Figure 32 shows an artificial periodicity occurring as a consequence of this specific way of selecting data points. The plot is made by first generating a data series representing 14600 days, where a value between 1-300 is chosen for each day. A periodicity of 29 is then selected. Data points chosen as keytime

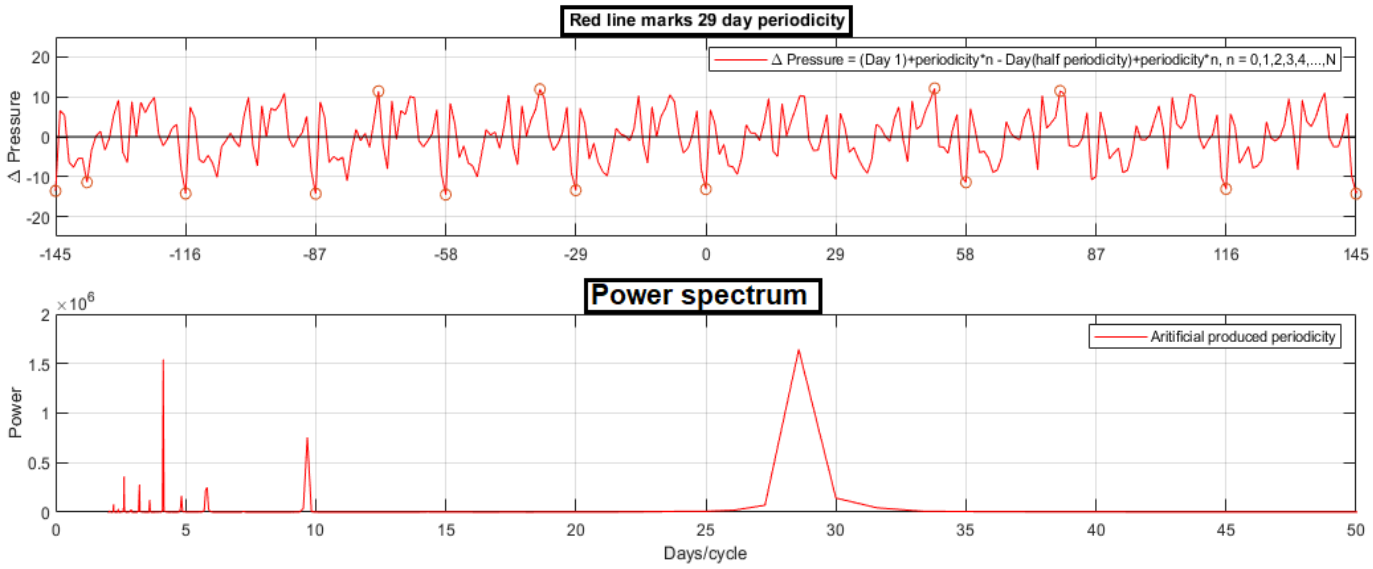

Figure 32: Artificially produced periodicity of 29. The data are generated as random numbers between 1-300.

are then picked out from the random data series at n = periodicity intervals with the surrounding subset of data spanning -300:300 days, and put in the first bin. The same process is done again for a second bin, with the keytime picked with the same interval between them, but 180° out of phase from the first bin (for a 29 periodicity this equates to ≈14 days). By synchronizing all data, and plotting the averaged first bin − averaged second bin, the resulting plot occur. As can be seen in the figure, the closer to the keytime (day 0), the more identical the periodic pattern look, which is a consequence of the self replication. The t-test is applied to both bins, with significance marked by the orange markers. This highlights the weakness of the t-test, as many significant anomalies appear in this randomly generated data series.

The same sorting can also be applied to the real geopotential height data. Figure 33 illustrates the artificial periodicity's of 12 and 19. The top and middle panels represents the response and power spectrum, when sorted according to the 12 and 19 days, respectively. The bottom panel represents the power spectrum of the raw geopotential height data. At periodicity's of 12 and 19, no peaks are found in this power spectrum, underlining the insincere periodicity's produced by the sorting method. The smothering of the response seen in the top panel compared to the random data in Figure 32 can be attributed to the temporal auto correlation of the geopotential height data.

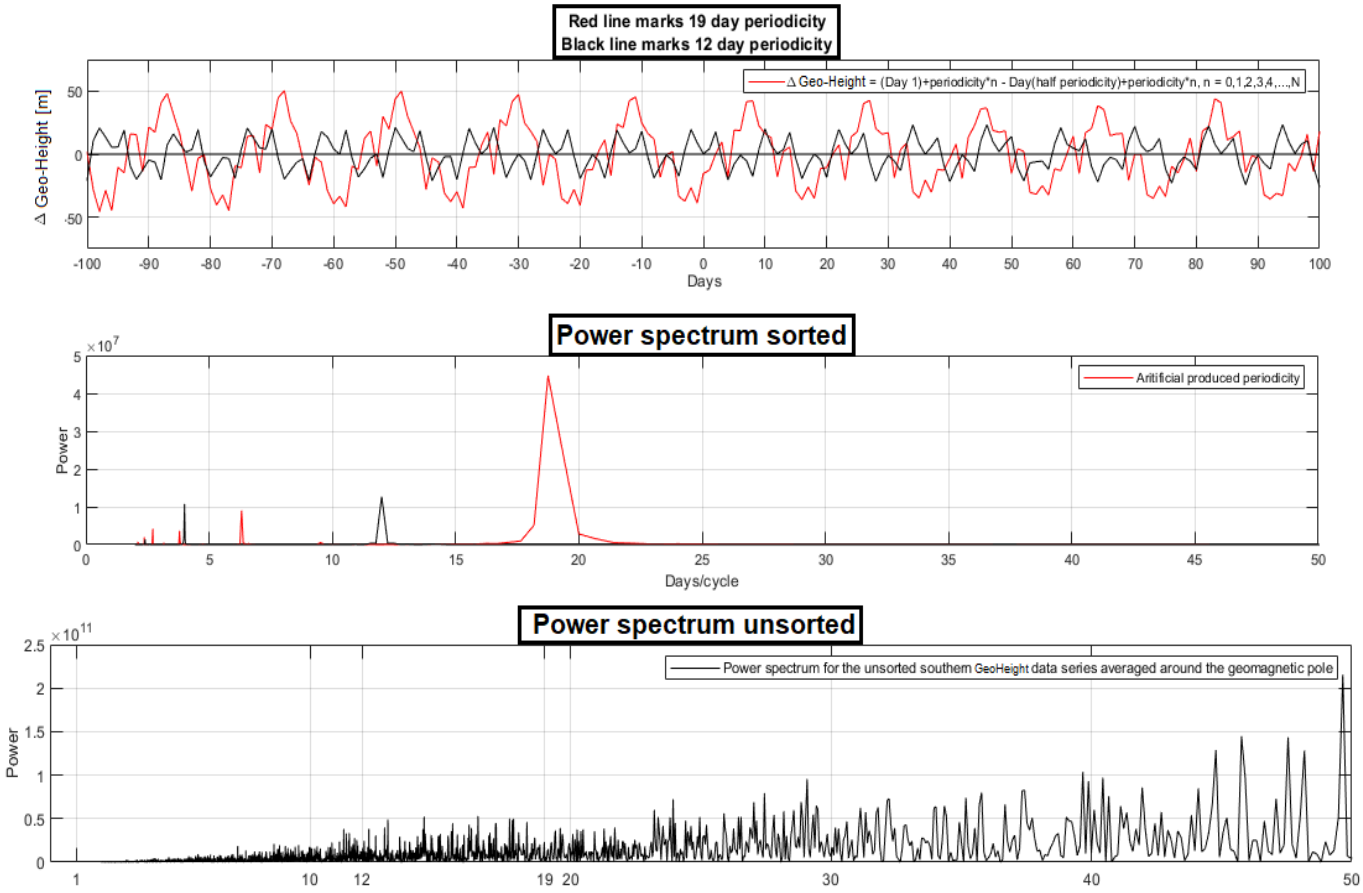

Figure 33: **Top panel:** Artificially produced periodicity of 12 and 19 as consequence of the sorting method. **Middle panel:** Power spectrum made by Fourier transformation of the data producing the top panel. **Bottom panel:** Power spectrum of the raw unsorted geopotential height data. All data are real geopotential height data for the 1000 hPa level in the SH, averaged around the geomagnetic pole.

3.5 Climatology

3.5.1 Total climatology

Total climatology represents the average climate over the data period. It is made by averaging the weather parameters of every ith (i = 1,2,3,...,365) day from each year. This becomes a data set of 365 days which ought to act as an average year for the whole data period (79-17).

3.5.2 Climatology frame of reference

For cases where total climatology is not a valid frame of reference, a specific climatology frame of reference (CLIMREF-spec) will be used. As an example, investigating the effects of high EPP on the polar pressure for the winters without a sudden stratospheric warming (SSW), SSW events would have to be excluded from the analysis as a whole. In a superimposed plot defined as ΔPressure = High A_p winters $-$ Climatology, both the High A_p winters bin and the climatology will have to exclude the same occurrences of SSW. The climatology with the SSW events excluded becomes the CLIMREF-spec for this case.

If a super imposed plot span multiple days, it is important that the data composing the climatology will follow the same consecutive logic in terms of days. To illustrate, a case includes a plot on the form ΔPressure = High A_p winters $-$ Climatology, spanning 1.Nov-1.Feb. Once again the aim is to analyse the effect of EPP on the polar pressure in the winters without a SSW event. If a SSW event happens in mid January, the whole period from 1.Nov-1.Feb has to be excluded from the climatology, not just the isolated event happening inside January. By only excluding isolated events from the climatology (CLIMREF-spec), it would still include contributions from the days leading up to the event, with no coherent matching days in the High A_p winters bin (or any other bin where the criterion is no SSW for the period 1.Nov-1.Feb). This will be taken into account in all of the different variants of climatology to minimize uncertainty and errors.

3.5.3 Weighted climatology

Table 3: Total amount of datapoints: **25**

Year	**Month**	**Data points (days)**	**Contribution to total as % (n/N)**
2010	Oct	4	16%
2011	Oct	10	40%
2012	Oct	3	12%
2013	Oct	1	4%
2014	Oct	1	4%
2015	Oct	6	24%

Exemplified distribution of data points with the criteria A_p-index > 50 in the period 2010-2015 for October.

When looking at cause and effect at a daily scale, certain years can have a higher contribution of days within a specific criterion. A comparison of such a data bin against a climatology made from equal contributions from each year could potentially affect the results. To illustrate, Table 3 shows the number of days with A_p-index > 50 for October in the period 2010-2015. The different years contribute differently in percentage to the average. By making a total climatology for the period 2010-2015, each year would contribute evenly. With

an analysis defined through ΔPressure = Bin($A_p > 50$) − Climatology, this would yield an uneven comparison. The year 2011 make up 40% of the Bin($A_p > 50$), while only contributing 20% to the climatology, meaning that any unrelated atmospheric phenomena happening in October 2011 will have a doubled impact in the analysis. The distribution of data points can be given as:

$$\text{Bin}(A_p > 50) = 2010(4)+2011(10)+2012(3)+2013(1)+2014(1)+2015(6) \quad (12)$$

$$\text{Climatology} = 2010(1)+2011(1)+2012(1)+2013(1)+2014(1)+2015(1) \quad (13)$$

To get around the problem, the concept of weighted climatology is introduced. It is defined as a climatology reflecting an equal contribution of years as the case of the analysis (can only be done if multiple days are chosen within the same year). The weighted climatology can then be given as:

$$\text{Weighted climatology} = 2010(4)+2011(10)+2012(3)+2013(1)+2014(1)+2015(6) \quad (14)$$

This will ensure that any time periods dominating a data set also will dominate the climatology, at the exact same fraction. Figure 34 gives a semi mathematical approach to the workings of weighted climatology, with the presumption that a cause and effect is present. From the ideal model, a strong enough effect taking x days to manifest itself as a measurable signal should show up as the largest anomaly in a plot at day x.

3.5.4 Removing seasonal variations

In all analyses where days from different seasons are compared against each other, the seasonal variations of the data have to be accounted for. Firstly, the mean of the Total Climatology is calculated. Secondly, a value representing the difference from this mean to the actual value of the specific day in the Total Climatology is calculated for each individual day. Finally, for all the days in the original data set, the specific value is subtracted from the coherent day, effectively removing the seasonal variations in the data set.

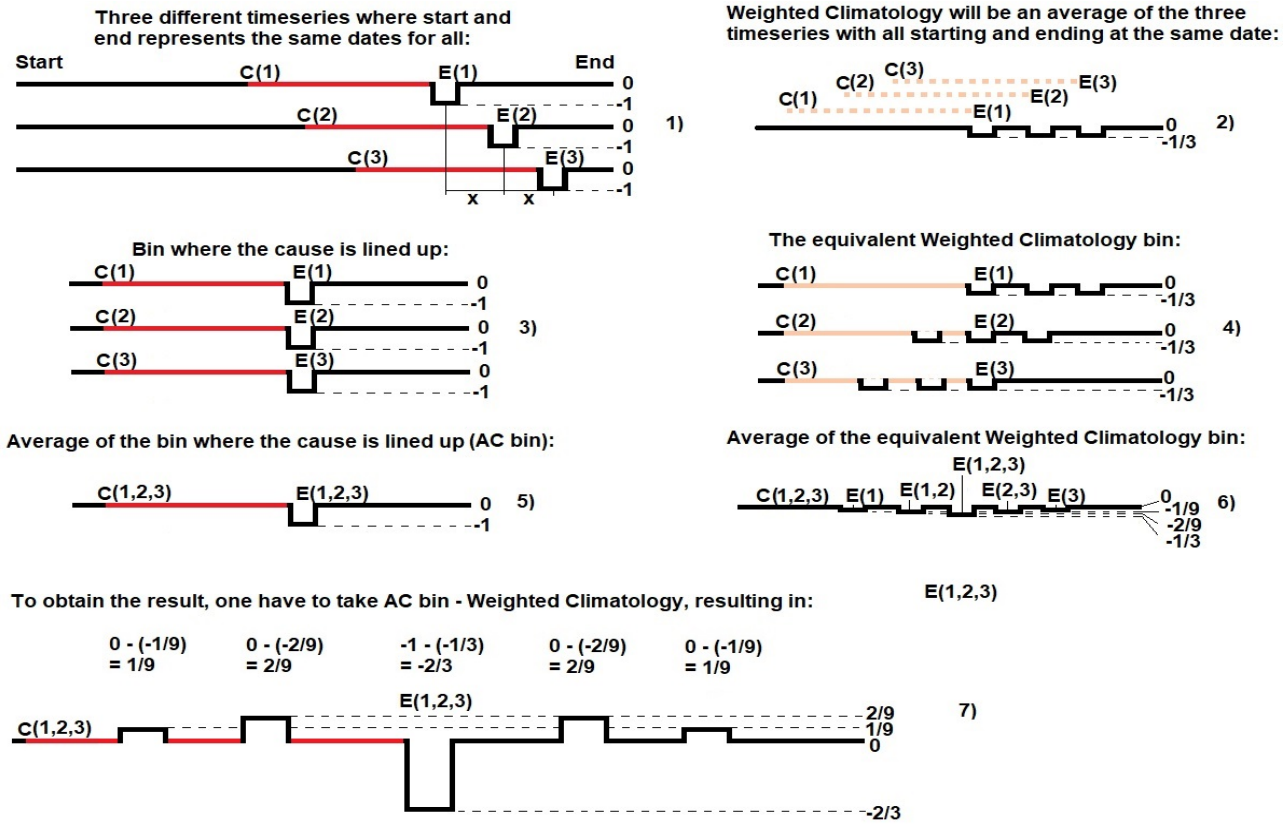

Figure 34: C defines cause, E defines effect. The effect reveals itself as the largest anomaly at x days from the cause when plotting AC bin - Weighted Climatology in an ideal case.

4 Results: The Chemical-Dynamical Coupling

Table 4 summarizes the analyses done for the Chemical-Dynamical coupling, together with the scientific goals. The main theme for this chapter is the investigation of the A_p - winter polar pressure relation through multiple different methods of sorting. The next chapters will go through each one explaining how the analyses are done in terms of data binning and important parameters. Each subsection ends with the result of the specific case.

Table 4: Summary of the different EPP analyses

Name	**Hemisphere**	**Timescale**	**A_p vs geopotential height**
A1N/S	North/South	Months	All winters
A1N: SSW	North	Months	SSW events excluded
A1N/S: QBO	North/South	Months	Sorted by QBO_{30} phases
A2N/S	North/South	Daily	Day to day basis, SSW events excluded
A2N: Peaks Excluded	North	Daily	Day to day, SSW events and maximum geomagnetic activity periods excluded
A2N: QBO	North	Daily	Day to day, sorted by QBO_{30} phases.
A3N	North	Daily	The potential time lag, weighted climatology

4.1 A1N/S: A_p-index vs geopotential height, all winters

For A1N and A1S, the A_p-index is averaged over two months from 14.Oct-14.Dec and 14.Apr-14.Jun, respectively. The years are then placed in either of two bins according to its value being in the lower (low A_p bin) or higher (high A_p bin) 50 percentile of all the averaged values obtained. For the Northern Hemisphere (NH), the winters of 84/85 and 03/04 will be excluded from the A1N case as both winters had a major SSW event. Maliniemi et al. (2013) found higher correlation between EPP and NAO when these unprecedentedly strong events were excluded. For this reason, the only SSW event in the Southern Hemisphere (SH) in the data period, occurring in 02 (Eguchi et al. 2007), is also excluded for the A1S case. Table 5 and 6 describes the distribution of the winters (years) into each bin for the NH and SH, respectively. Both tables also lists all the smaller SSW events and the QBO phases contained inside each of the bins, where the QBO phase is defined by the average QBO_{30hPa} value over the period Sep-Mar (May-Sep) for the NH (SH). The output variable of interest is geopotential height [m] of a distinct pressure level, where a lower geopotential height for a

Table 5: A1N

A_p(high) bin
80/81(W) 81/82(E) 82/83(W) 83/84(E) 85/86(W) 87/88(W) 89/90(E) 91/92(E) 92/93(W) 93/94(E) 94/95(W) 98/99(E) 99/00(W) 00/01(E) 01/02(E) 02/03(W) 04/05(W) 16/17(W)
Percentage of SSW in the high bin
44.44%
Ratio E:W in the high bin
8:10
A_p(low) bin
79/80(E) 86/87(E) 88/89(W) 90/91(W) 95/96(W) 96/97(E) 97/98(W) 05/06(E) 06/07(W) 07/08(E) 08/09(W) 09/10(E) 10/11(W) 11/12(E) 12/13(E) 13/14(W) 14/15(E) 15/16(W) 17/18(E)
Percentage of SSW in the low bin
47.36%
Ratio E:W in the low bin
10:9

SSW years are marked with red. E and W denotes QBO easterly and westerly.

specific level is consequence of lower pressure. It is defined from the equations:

$$\Delta\text{Geo-Height[m]} = \text{A}_\text{p}(\text{high}) - \text{CLIMREF-spec} \tag{15}$$

$$\Delta\text{Geo-Height[m]} = \text{A}_\text{p}(\text{high}) - \text{A}_\text{p}(\text{low}) \tag{16}$$

From the period 14.Oct-14.Nov (14.Apr-14.May) and onward a running mean (spanning 30 days) of the pressure for each pressure level will be calculated to capture the dynamics of the changes over the whole local winter time. As

Table 6: A1S

A_p(high) bin
80(W) 81(W) 82(E) 83(W) 84(E) 85(W) 89(E) 90(W) 91(W) 92(E) 93(W) 94(E) 95(W) 98(E) 00(W) 01(E) 03(E) 05(E)
Ratio E:W in the high bin
9:9
A_p(low) bin
86(W) 87(E) 88(W) 96(E) 97(W) 99(W) 04(W) 06(W) 07(E) 08(W) 09(W) 10(E) 11(W) 12(E) 13(W) 14(E) 15(E) 16(W) 17(W) 18(E)
Ratio E:W in the low bin
8:12

E and W denotes QBO easterly and westerly.

CLIMREF-spec is defined as the total climatology excluding the specific major SSW events, it is evident that both equations will capture the same signal, with equation 16 enhancing it.

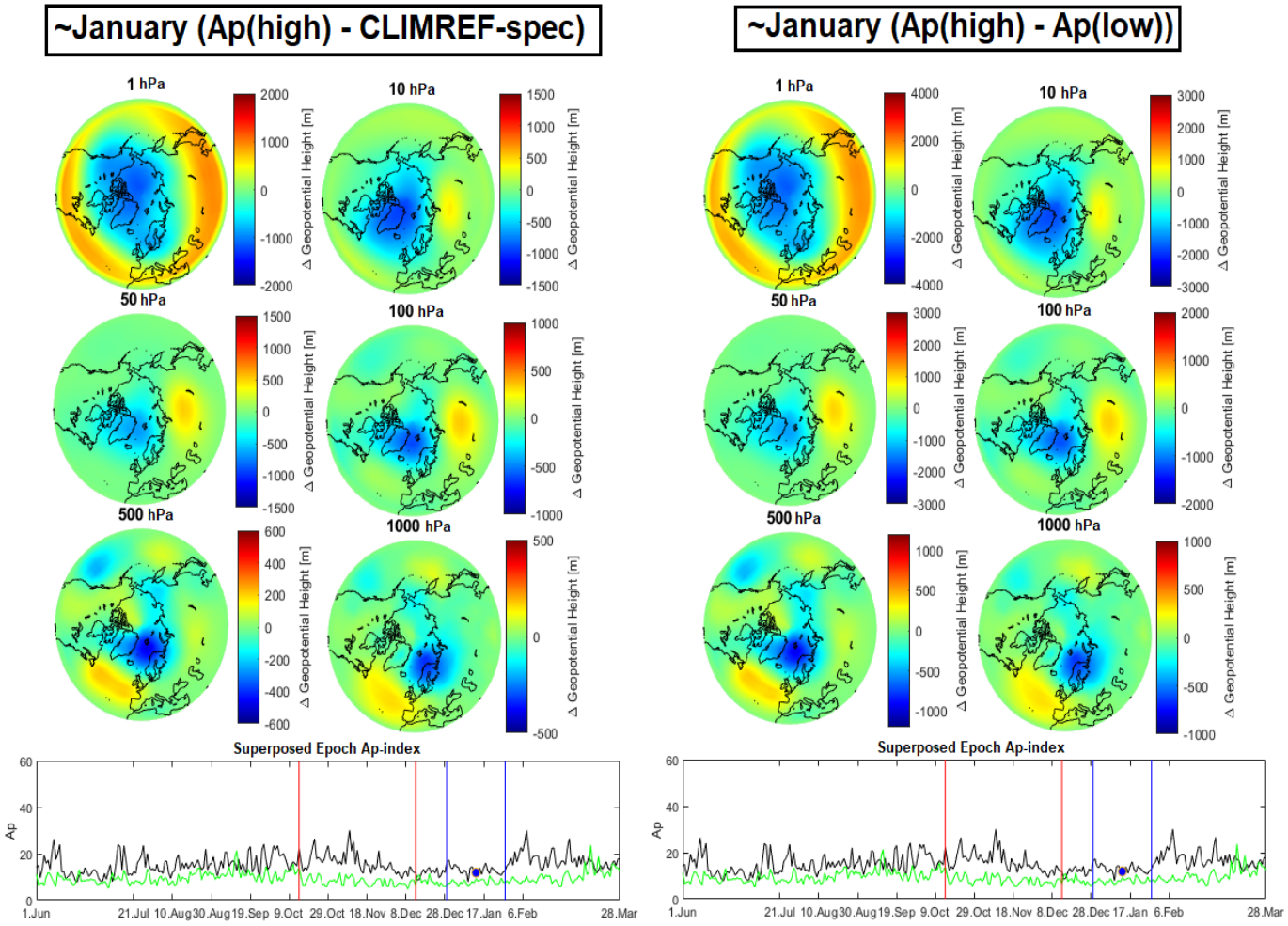

Figure 35: **Left panel:** Δ Geo-Height[m] = A_p (high)−CLIMREF-spec for January at 6 different pressure levels in the range 1-1000 hPa (A1N). Scale vary for each pressure level. **Right panel:** Equivalent plot through Δ Geo-Height[m] = A_p (high)−A_p (low). Notice how the scale is doubled, indicating that this plot enhances anomalies by 100%. **Bottom panels:** Black (green) solid line: A super imposed plot of the A_p-index from the A_p(high)−A_p(low) bin. Red lines: Defines the time period when the A_p-index is averaged (span 60 days). Blue lines: Defines the time period when the geopotential height is averaged (span 30 days).

Figure 35 shows the geopotential height anomaly at 6 different pressure levels in the range 1-1000 hPa for the running mean covering January (A1N) through both equations. The color scale is covering half of the range in the CLIMREF-spec plots compared to the A_p(low) plots. As the pattern itself is indistinguishable between the two, the following analysis focus on the A_p(high)$-A_p$(low) anomaly. From the figure, a low pressure anomaly can be seen over the po-

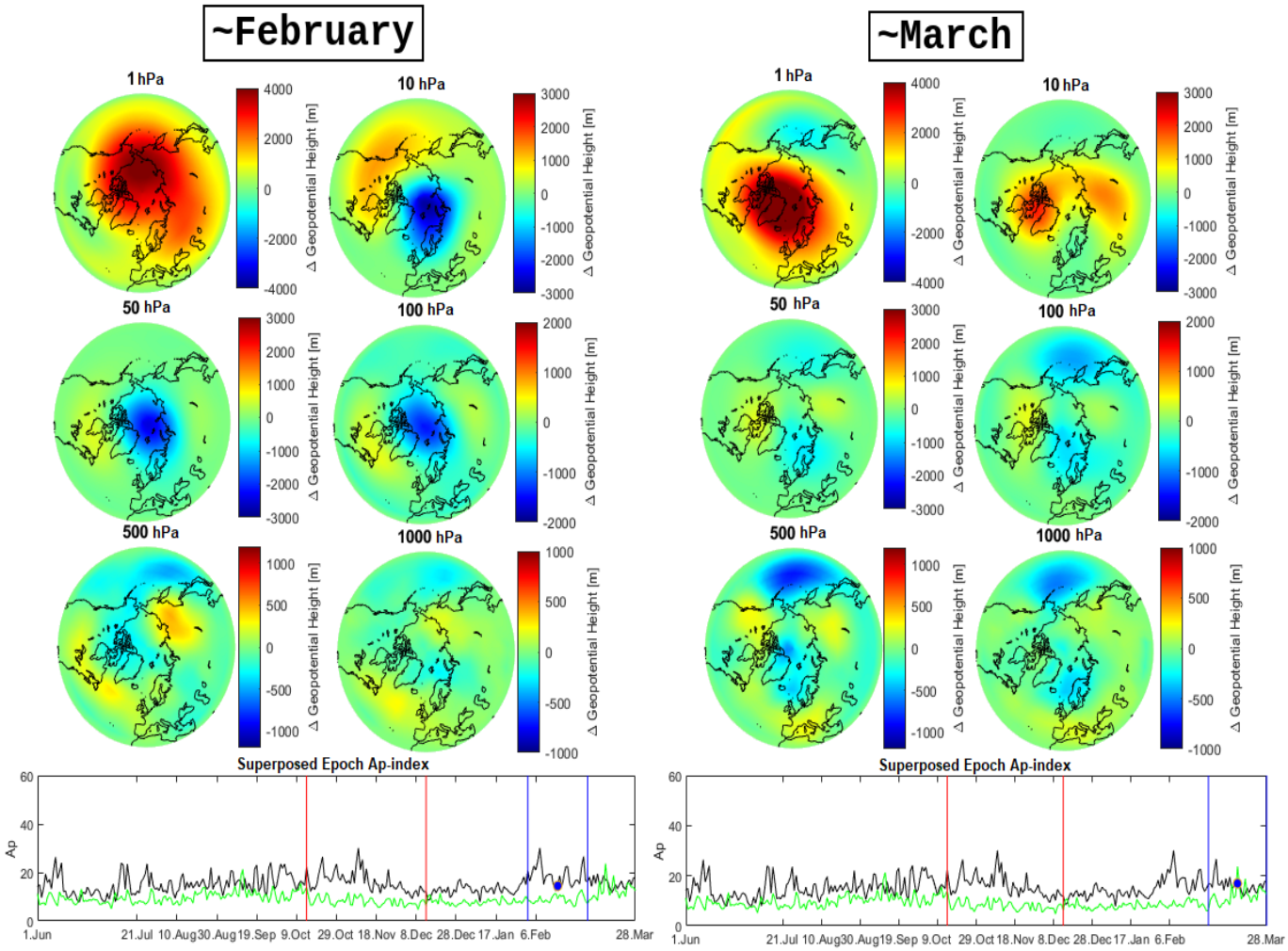

Figure 36: **Top panels:** Δ Geo-Height[m] = A_p (high)$-A_p$ (low) for February and March (A1N). Scale vary for each pressure level. No significance is found at any level. **Bottom panels:** Black (green) solid line represents a super imposed plot of the A_p-index from the high (low) bin.

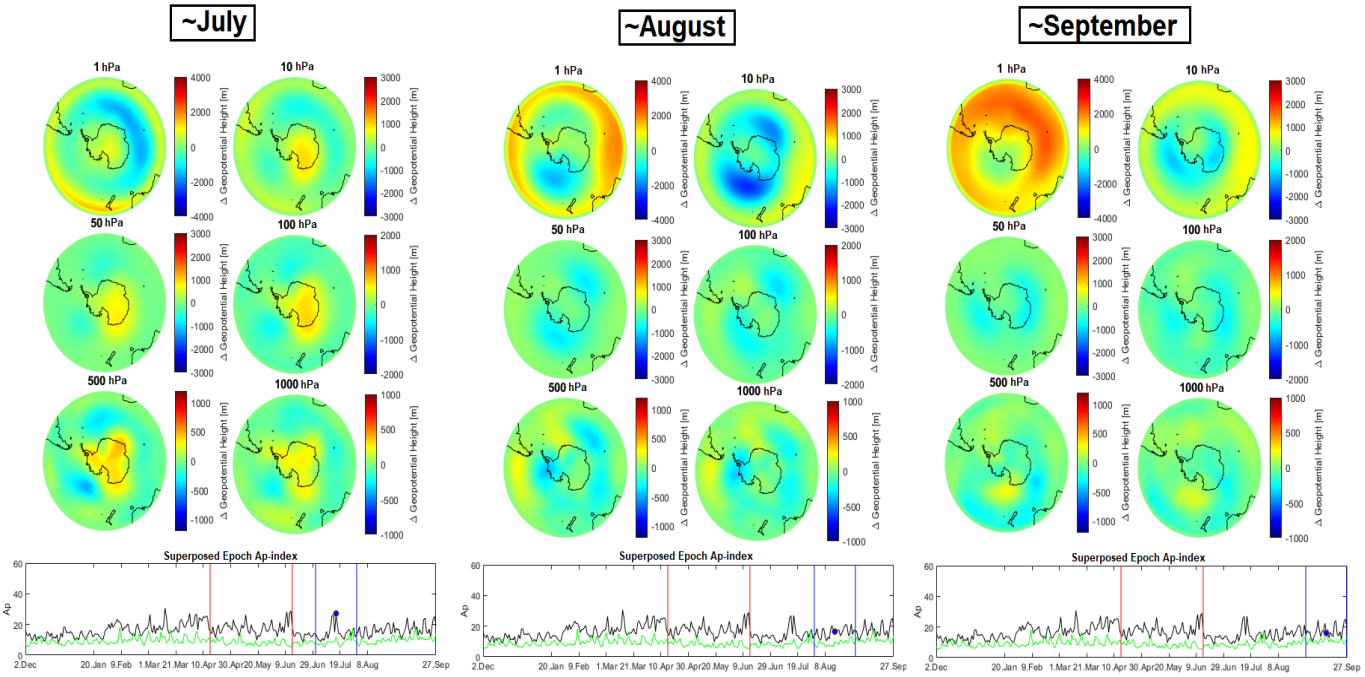

Figure 37: Δ Geo-Height[m] = A_p (high) - A_p (low) for July, August and September (A1S). No significance is found at any level.

lar latitudes for all six pressure levels, but not at a statistical significant level. 1000 Monte Carlo simulations are done together with FDR, which will be used as evaluation in all map plots. Figure 36 shows the equivalent plots when the running mean covers February and March. No statistical significance is found in either of the plots. The negative anomaly is still persistent at the 10 hPa, 50 hPa and 100 hPa level over the polar latitudes in February. A slight negative anomaly over the polar latitudes at the 500 hPa and 1000 hPa level occurring together with a positive anomaly at lower latitudes is seen in March, but not at a significant level. The distribution of SSW events and QBO phases are similar between both bins compared. Figure 37 shows the plots when the running mean covers July, August and September for the SH. No statistical significance is found. Though not significant, the anomalies appear weaker than in the plots for the NH.

4.2 A1N: SSW: A_p-index vs geopotential height, SSW events excluded

Table 7: A1N: SSW

A_p(high) bin	**A_p(low) bin**
82/83(W) 85/86(W) 89/90(E) 91/92(E) 92/93(W) 93/94(E) 94/95(W) 01/02(E) 04/05(W) 16/17(W)	90/91(W) 95/96(W) 96/97(E) 97/98(W) 10/11(W) 11/12(E) 13/14(W) 14/15(E) 15/16(W) 17/18(E)
Ratio E:W in the high bin	**Ratio E:W in the low bin**
4:6	4:6

This analysis focuses on the NH, which has regular occurrences of SSW events. It is defined in the same way as A1N, with the only difference being the exclusion of all SSW event, and is calculated based on equation 16. The remaining winters binned according to the 50th percentile A_p averaged value are listed in Table 7.

Figure 38 shows two of the same plots when the running mean is placed over January. When a students t-test is applied together with FDR, a statistical significant negative pressure anomaly appears at the 500 hPa and 1000 hPa level at high latitudes. The significance disappears when applying the Monte Carlo method together with FDR. By comparing to the A1N case, the amplitude of the anomalies are slightly strengthened when the SSW events are removed. No significance is found when the running mean is placed over February and March, or any intermediate period. The plots for February and March can be found in Appendix B Figure 74.

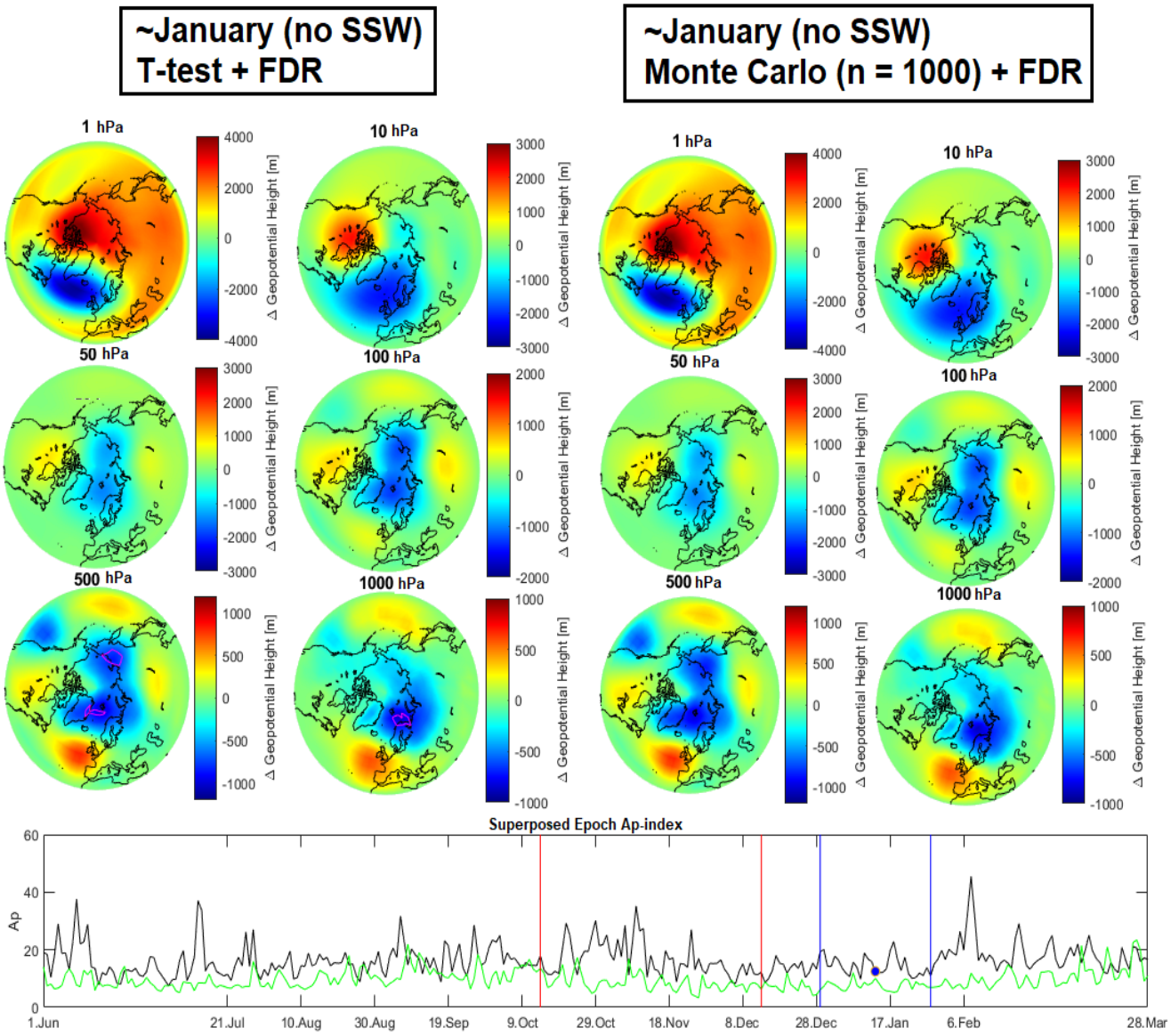

Figure 38: **Right panel:** Δ Geo-Height[m] = A_p (high)−A_p (low) for January (A1N: SSW). Purple lines indicate statistical significance. Students t-test and FDR are applied. **Left panel:** Same plot, only with Monte Carlo simulations and FDR applied to calculate the significance. With this method, where both temporal and spatial auto-correlation is accounted for, no statistical significance is found.

4.3 A1N/S: QBO: A_p-index vs geopotential height, sorted by QBO_{30} phases

This analysis targets the geomagnetic response of the atmosphere in the different QBO_{30hp} phases. It is defined in the same way as A1N/S and A1N: SSW, where the change in geopotential height will be plotted as:

$$\Delta\text{Geo-Height[m]} = \text{A}_\text{p}\ \text{QBO-(W or E) (high)} - \text{A}_\text{p}\ \text{QBO-(W or E) (low)} \quad (17)$$

Table 8 and 9 summarizes the division of the winters/years into the QBO-phases and the A_p bins. The QBO-phase is defined as either westward or eastward depending on the average QBO over the span Sep-Mar (NH) and May-Sep (SH), with the A_p bins divided into high (>50th percentile) and low (<50th percentile) depending on the average A_p value in the period 14.Oct-14.Dec (NH) and 14.Apr-14.Jun (SH). The two major SSW events happening in 84/85 and 03/04 in the NH and 02 in the SH are still excluded.

All results for six pressure levels for A1N/S: QBO when the running mean is placed over January, February and March in the NH, and July, August, September in the SH, can be found in Appendix B Figure 75 - 86. Figure 39 shows the plots for the 500 hPa and 1000 hPa level for the A1N: QBO case, as the main interest is the lower atmospheric effect of EPP. Significant negative pressure anomalies appear at the 500 hPa level in the QBO-E phase in March over Greenland, south of the Bering Strait and mid-latitude Eurasia. For the rest of the middle and upper atmospheric levels, no significant areas are found. No statistical significance is found in the A1S: QBO case.

Table 8: A1N: QBO

QBO-E		QBO-W	
A_p(high)	A_p(low)	A_p(high)	A_p(low)
81/82	79/80	80/81	88/89
83/84	05/06	82/83	90/91
86/87	07/08	85/86	95/96
89/90	09/10	87/88	97/98
91/92	11/12	92/93	06/07
93/94	12/13	94/95	08/09
96/97	14/15	99/00	10/11
98/99	17/18	01/02	13/14
00/01		02/03	15/16
		04/05	16/17
SSW %		SSW %	
55%	63%	40%	30%

SSW winters are marked in red

Table 9: A1S: QBO

QBO-E		QBO-W	
A_p(high)	A_p(low)	A_p(high)	A_p(low)
79	87	80	86
82	96	81	97
84	01	83	99
89	07	85	04
92	10	88	06
94	12	90	08
98	14	91	09
00	15	93	11
03	18	95	13
05		16	17

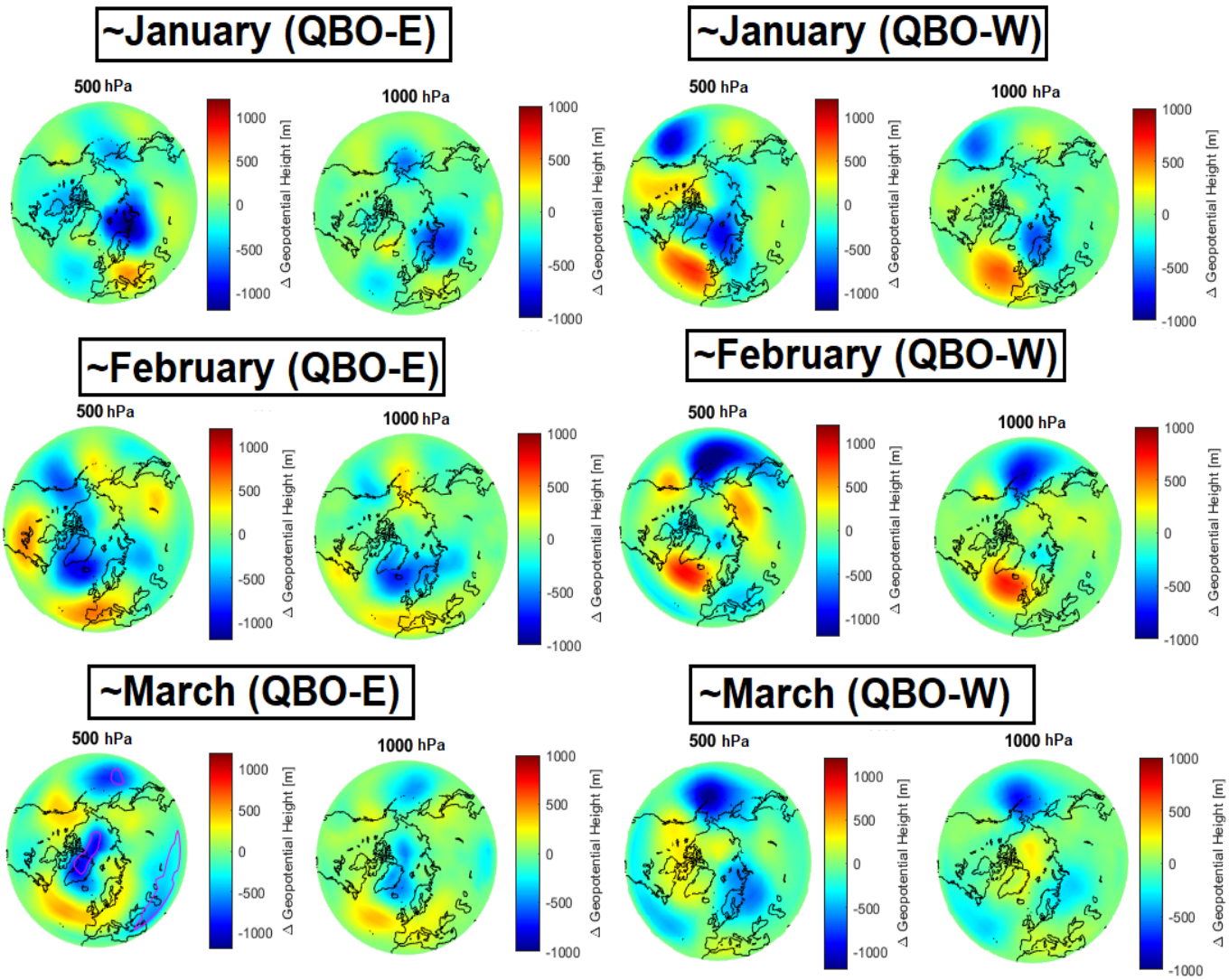

Figure 39: Δ Geo-Height[m] = A_p QBO-(phase)(high)$-A_p$ QBO-(phase)(low) for January, February and March at the 500 hPa and 1000 hPa level (A1N: QBO). A clear negative anomaly showing statistical significance is seen in March QBO-E at the 500 hPa level over the polar latitudes, southern Russia, and south of the Bering Strait.

4.4 A2N/S: A_p-index vs geopotential height, daily, SSW events excluded

This analysis looks at the EPP-surface signal from a different temporal perspective. Instead of selecting the time period with high averaged A_p-index, single days with A_p-index above a certain level will now be chosen as the keydate. The averaged atmospheric responses are then shown from the keydate and 150 days onward with the CLIMREF-spec subtracted from the plot, given by the equation:

$$\Delta\text{Geo-Height[m]} = A_p(\text{Daily high}) - (\text{CLIMREF-spec}) \tag{18}$$

Every month (Sep-Jan for A2N and Mar-Jul for A2S) will have a separate analysis, where the keydate is restricted to be chosen inside the specific month. All SSW events will be excluded from both cases, giving the same remaining winters for A2N as listed in both columns in Table 7. For the A2S case, this means only the removal of the year 02. CLIMREF-spec excludes the years for each hemisphere according to the same criteria. In the A2N case, the criteria for the keydate is A_p >40 for September, October and November, A_p >20 for December and A_p >25 January. This yields an approximately even amount of data points in each month, as December and January have fewer days with high A_p index. In A2S, the criteria is set to A_p >40 for all months.

Table 10 summarizes all statistically significant anomalies found at the surface level after applying the Monte Carlo method (n = 1000) together with False Detection Rate. In the A2N case, September, October, November and December show significant anomalies in the time period 22.Dec-05.Jan. Figure

Table 10: A2N/S, significant time periods

A2N				
SEP	**OCT**	**NOV**	**DEC**	**JAN**
∼23.Dec-05.Jan (99-112 days)	∼29.Dec (76 days)	∼22.Dec-25.Dec (38-41 days)	∼02. Jan (15 days)	∼11.Apr (86 days)
∼18.Jan (125 days)			∼10.Mar-13.Mar (82-85 days)	
			∼05.Apr-06.Apr (108-109 days)	
A2S				
MAR	**APR**	**MAY**	**JUN**	**JUL**
∼06.Aug-09.Aug (144-147 days)	No sig	∼20.Jul-21.Jul (66-67 days)	∼11.Oct-18.Oct (119-126 days)	No sig
		∼17.Sep-21.Sep (125-129 days)		

40 compares the associated plots. All plots show a very similar pattern at the 500 hPa and 1000 hPa. Areas of negative pressure are seen over Greenland and polar latitudes, while positive pressure anomalies are seen over Scandinavia extending down to middle Europe. The similar periods of significance despite different key dates, makes it challenging evaluating potential time lag dependencies over the winter.

Figure 41 shows ΔA_p calculated through A_p(high)− CLIMREF-spec and averaged at 20-day intervals for all months used in the A2N case. For September, December and January, ΔA_p remains roughly constant and positive both before and after the time period of the specific keydate. From this perspective, the pressure response seen from the different analyses could likely be the contribution of accumulated EPP from the whole winter season, and not the result of synchronized stockpiling of all days with high A_p. Every individual analysis also contain the same years, which further complicates the process of distinguishing between the specific months and the response. For October and November clear positive peaks in ΔA_p are seen around the keydate, with smaller ΔA_p in the time period before and after. These reflect more ideal circumstances for associating an effect with a cause. Figure 42 shows significant anomalies occurring in early April from keydate set in December and January. The uncertainties in determining the origin of the response are once more illustrated by the similarities of the plots. From the plot with keydate set inside December, a large positive pressure anomaly is seen at 1000 hPa at the Bering Strait and stretching to higher latitudes. A smaller region of positive anomaly is seen west of Portugal. Negative pressure anomalies are seen at the same pressure level over Scandinavia and at lower latitudes in the Pacific Ocean and east Russia. In the plot for January, the features of the anomalies are similar, but slightly shifted towards Europe.

The two remaining significant anomalies for the A2N case can be found in Appendix B Figure 87-88. As a general trend, all results for the early winter (Dec-Jan) show an approximately polar centered negative anomaly at the 1000 hPa level. This pattern is also reflected at multiple atmospheric levels in most of the plots, depending on the month limiting the keydate. In the late winter (Feb-Apr), no negative significant anomalies are found in the upper atmosphere. Anomalies at the 500 hPa and 1000 hPa level still remains significant, but more diffuse than in the early winter.

For the A2S case, the responses are lacking the circular symmetry seen in many of the A2N results. Figure 43 represents an anomaly seen in late July when keydate is set in May, and an anomaly seen in middle October when keydate is set in June. In the first plot (early winter), negative anomalies dominate the four lower atmospheric levels, positioned over parts of the South-Pacific and South-Atlantic Ocean. In the second plot (late winter), the 500 hPa and 1000 hPa level show a similar, but opposite signal, with positive anomalies in the same areas. At the upper levels, further intensification of the positive anoma-

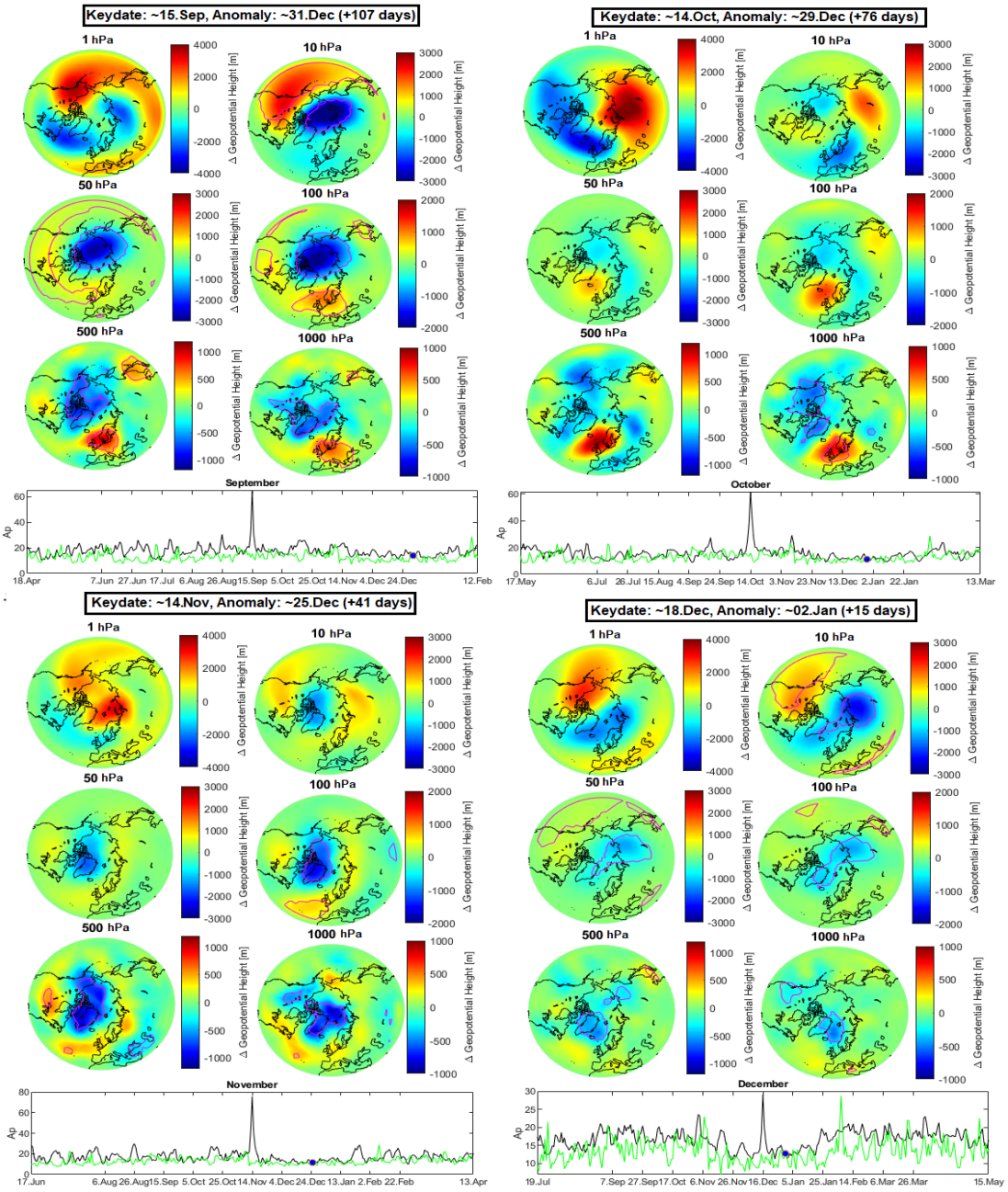

Figure 40: Anomaly happening in late December for keydate inside September, October, November and December for the A2N case. Purple lines indicate statistical significance. All small panels represents the superposed Epoch of the A_p-index with black (green) line representing the high (CLIMREF-spec) bin.

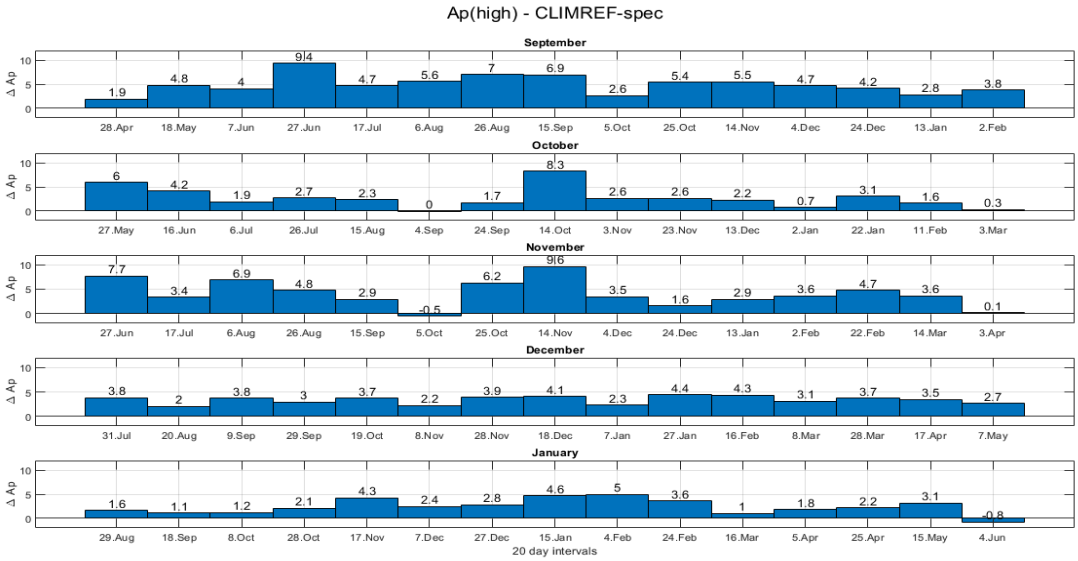

Figure 41: ΔA_p calculated through A_p(high)-CLIMREF-spec at 20 day intervals from the data series used in the A2N-case.

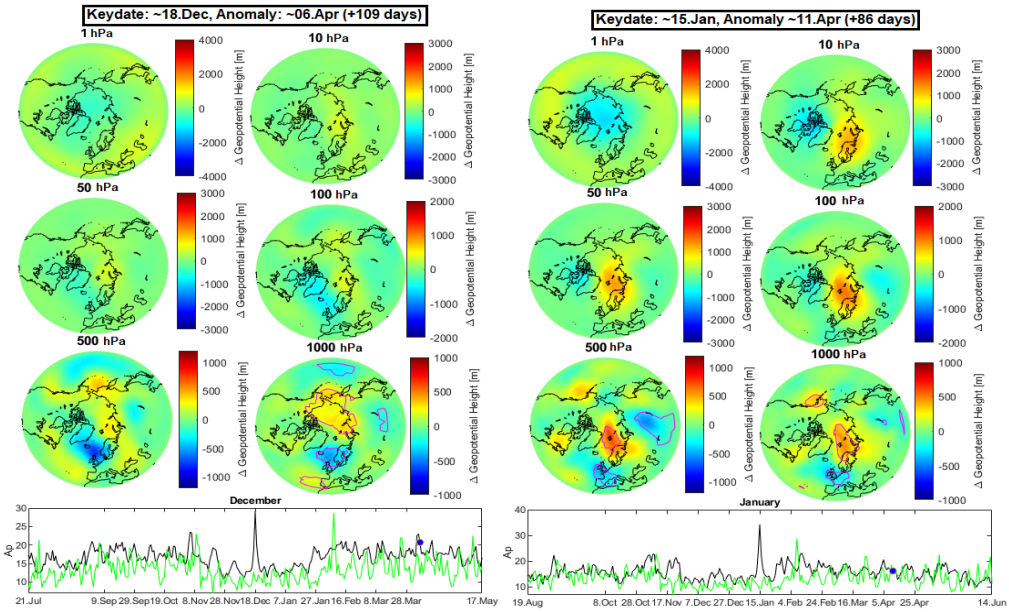

Figure 42: Anomaly occurring in early April for keydate inside December and January for the A2N case. Purple lines indicate statistical significance.

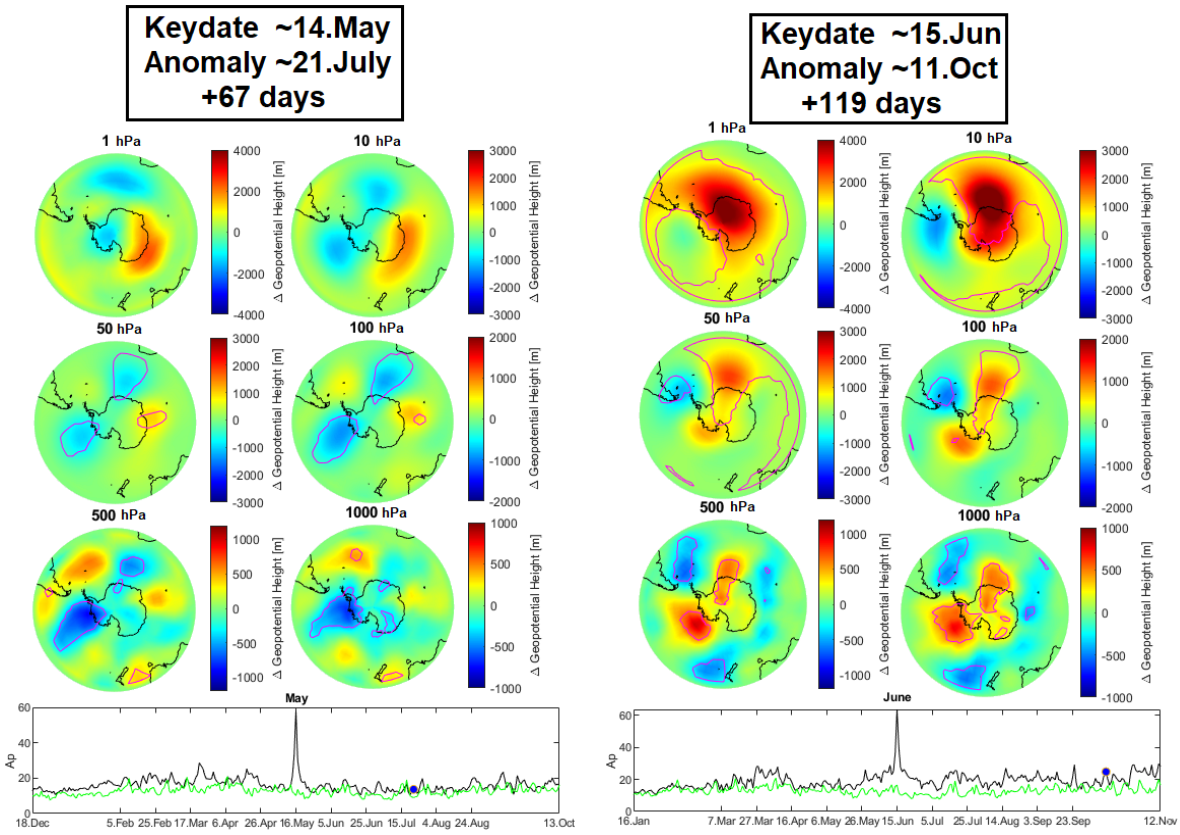

Figure 43: **Left panel:** Anomaly occurring in late July for keydate inside May for the A2S case. **Right panel:** Anomaly occurring in middle October for keydate inside June.

lies are seen. The two remaining anomalies for the A2S case can be found in Appendix B Figure 89-90. When comparing all the A2S results, the responses seen are diffuse and irregular. Keydate set inside April and July produces no statistical significance after applying the Monte Carlo method and FDR. For the four time periods that are significant, the negative anomalies seem to weaken over the extent of the winter, being replaced by positive anomalies later on. An investigation into the data series (ΔA_p) (Appendix B Figure 91), shows a relatively stable and positive ΔA_p for all months before and after the keydate.

4.5 A2N: Peaks Excluded: A_p-index vs geopotential height, daily, SSW events and maximum geomagnetic activity periods excluded

As the A2N case show a relatively consistent pattern in the anomalies, a further investigation in the NH at a daily scale is done. In addition to the exclusion of SSW events, years with very high geomagnetic activity are excluded. The aim of this sorting is to look at the pressure response when the EPP-fluxes are effectively reduced, as well as if there exists a dependency on the maximum activity years for the mechanism to operate. Periods are defined as peak years for each individual analysis (month defining the keydate is termed 'keymonth') according to the criteria:

- **Average A_p >23 in any of the 4 months prior to the 'keymonth', the 'keymonth', or in any of the 3 months after the 'keymonth'**

Table 11 summarizes the anomalies found when peak years are excluded. The analyses are carried out in the same manner as the A2N case, plotting from day 1 to day 150 from the keydate for each individual month. The A_p criteria for the keydate inside each month is adjusted to A_p >35 for September and October, A_p >25 for November, and A_p >20 for December and January. This ensures an approximately equal amount of data points for each analysis, while maximizing the A_p value at the keydate.

After applying the Monte Carlo method and FDR, the same pattern arise with statistical surface anomalies occurring around the same time period for each month, in late December and early January. A slight deviation is seen for keydate set in November, which also shows significance in early February. All anomalies are comparable to the A2N results, manifesting themselves as negative pressure areas over polar latitudes at the 1000 hPa level and warming over middle Europe. Significant negative polar centered pressure areas are also seen at the higher atmospheric levels for keydate set in September and December. The plots are summarized in Appendix B Figure 92-97.

Table 11: A2N: Peak years excluded, significant time periods

SEP	**OCT**	**NOV**	**DEC**	**JAN**
∼26.Dec-30.Dec (103-107 days)	∼03.Jan (79 days)	∼07.Jan (54 days)	∼31.Dec-01.Jan (14-15 days)	No significance
∼04.Jan (112 days)		∼06.Feb (84 days)		

4.6 A2N: QBO: A_p-index vs geopotential height, daily, sorted by QBO_{30} phases

The next analysis focuses on the QBO phasing on a daily scale. It is debated which phase carries most significance for the enhancement of the atmospheric response to EPP. This analysis will investigate both phases in the NH on a daily scale to see if there is any atmospheric state dependence on the significance of the response. The analysis is done similarly as the rest of this section, with a different analysis for the keydate restricted to different months. The years are first divided according to the QBO phases in Table 8 in Section 4.3. For an approximately equal distribution of years for each month, the A_p criteria is set to $A_p > 40$ for September, October and November, and $A_p > 25$ for December and January. Figure 44 shows ΔA_p calculated for both phases through A_p(high) - CLIMREF-spec. When selecting data points in this manner, the figure show a clear trend of a generally higher ΔA_p for the whole autumn/winter season for all the months in QBO-E compared to QBO-W. Only September has an approximately equal ΔA_p in both phases. NO_x will in general not be transported downwards in the NH this early. Still, the A2N case show high significance when September is selected to restrict the keydate, which indicates that the analysis might be dependent on ΔA_p between the high bin and CLIMREF-spec for the whole period leading up to the winter. The data points selected when September is set as keydate produces an approximately equal ΔA_p between both phases, making it an ideal target for comparing the responses between the easterly and westerly QBO.

Figure 45 shows the results for the 500 hPa and 1000 hPa level for both QBO phases for keydate set in September. For the extended period of 1:150 days lag from the keydate, the time between 23. Dec and 15. Jan is the only period producing anomalies at a significant level at the surface for any of the QBO-phases. In the easterly QBO phase, higher significance is found at the 500 hPa and 1000 hPa level, compared to the westerly QBO phase. The response manifests as negative anomalies at polar latitudes. However, significance is still found for the westerly QBO-phase at the 500 hPa and 1000 hPa level, but in a more sporadic manner. All plots including 6 pressure levels can be found in Appendix B Figure 98-101. In the upper atmospheric levels, a near continuously polar centered negative anomaly can be seen in both phases, with higher significance attributed to the westerly QBO-phase.

Figure 44: ΔA_p calculated through A_p(high)-CLIMREF-spec for both QBO phases at 20 day intervals from the data series used.

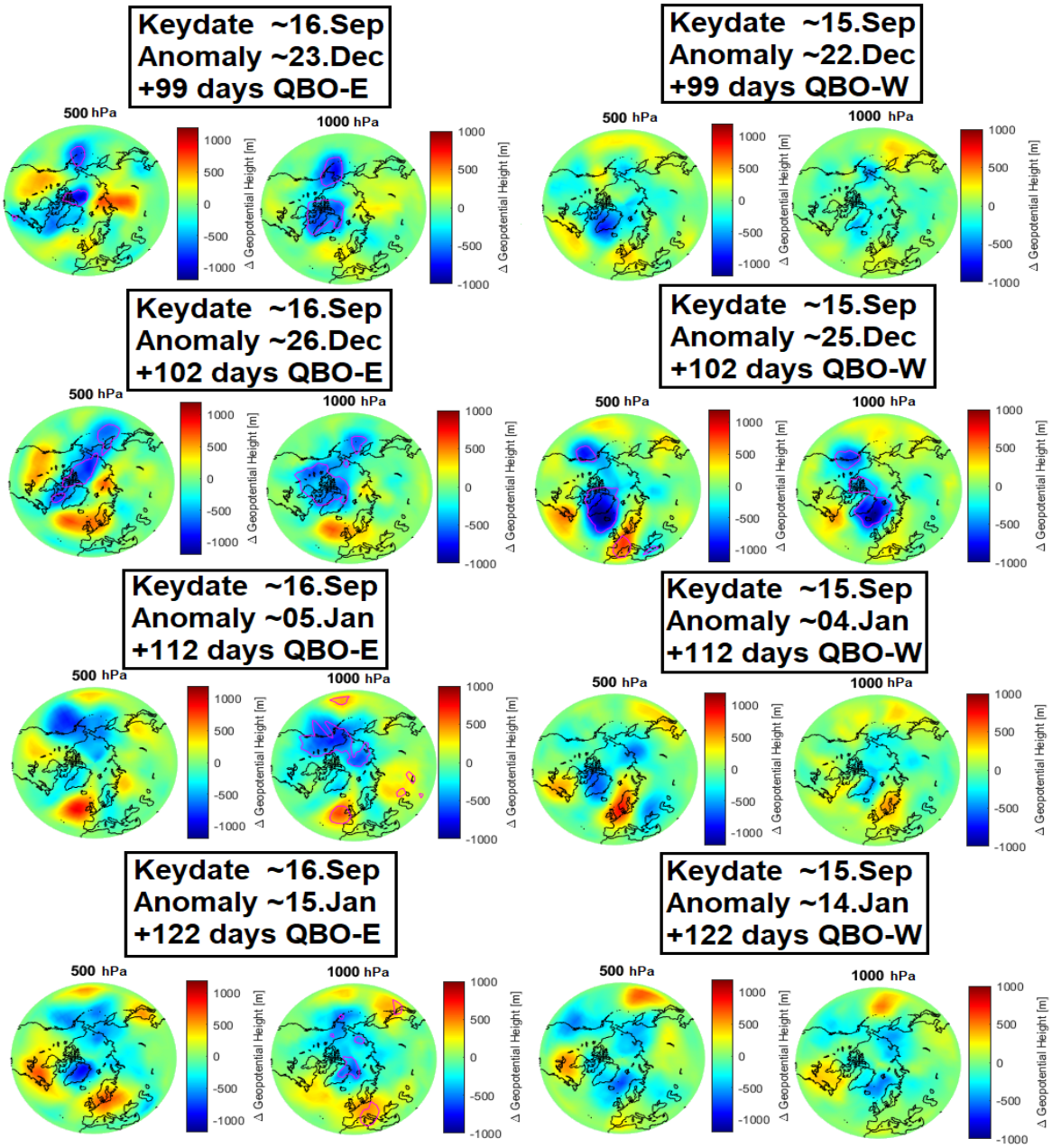

Figure 45: The 500 hPa and 1000 hPa level for both QBO-phases at different times in the middle winter for the A2N: QBO case. Times are chosen over a period where QBO-E show high significance.

4.7 A3N: A_p-index vs geopotential height, potential time lag, weighted climatology

If it was true that high EPP could alter the polar atmospheric pressure, could a single day with highly elevated EPP affect the pressure significantly later on? This analysis involves the method of weighted climatology, designed to detect such a response as the largest amplitude anomaly at day x. The analysis will only be done for the NH, as it shows the largest and most significant anomalies in the former analyses. Days with $A_p > 50$ inside a specific month are chosen as the keydate (day 0). The geopotential height for 1000 hPa, 750 hPa, 500 hPa, 250 hPa, 100 hPa, 50 hPa, 10 hPa, 5 hPa and 1 hPa are first averaged around the polar latitudes (70°-90°), then plotted through the equation:

$$\Delta\text{Geo-Height [m]} = A_p\text{high} - \text{Weighted Climatology} \tag{19}$$

The analysis captures -150:150 days, with levels being interpolated upwards (1000 hPa to 750 hPa = 1000 hPa, 750 hPa to 500 hPa = 750 hPa etc.). Figure 46 shows the plot when October is set to keydate. Mostly negative anomalies are seen at approximately +100 to +140 days from the keydate. By applying the Monte Carlo method at the 0.01 significance level, some areas of statistical significance is seen both before and after the keydate, with the highest amplitude anomaly being the negative area at the 100 hPa, 50 hPa and 10 hPa level in middle February.

Further investigation into the other months reveals uncertainties about the method. The keydate is set inside March, a month when occurrences of high A_p are hypothesized to have minor effects on the polar atmosphere in the coming spring/summer time. In this case, illustrated in Figure 47, multiple anomalies at a significant level are seen before the keydate in the whole winter season. The anomalies are sporadic, of generally high amplitudes and with no specific preference for a negative or positive sign. This indicates that the higher atmospheric pressure variability happening in the winter time compared to the rest of the year are able to create false signals of high significance. The results for the month of October should then be treated cautiously, as the random variability of the atmosphere may be the cause of the significant amplitudes seen. Investigation into different modes of data binning like the exclusion of SSW events have also been done. In all cases anomalies arise at a significant level for days before the keydate in the month of March, ultimately making the weighted climatology unsuited for determining a time lag of the response of the atmosphere to elevated EPP fluxes.

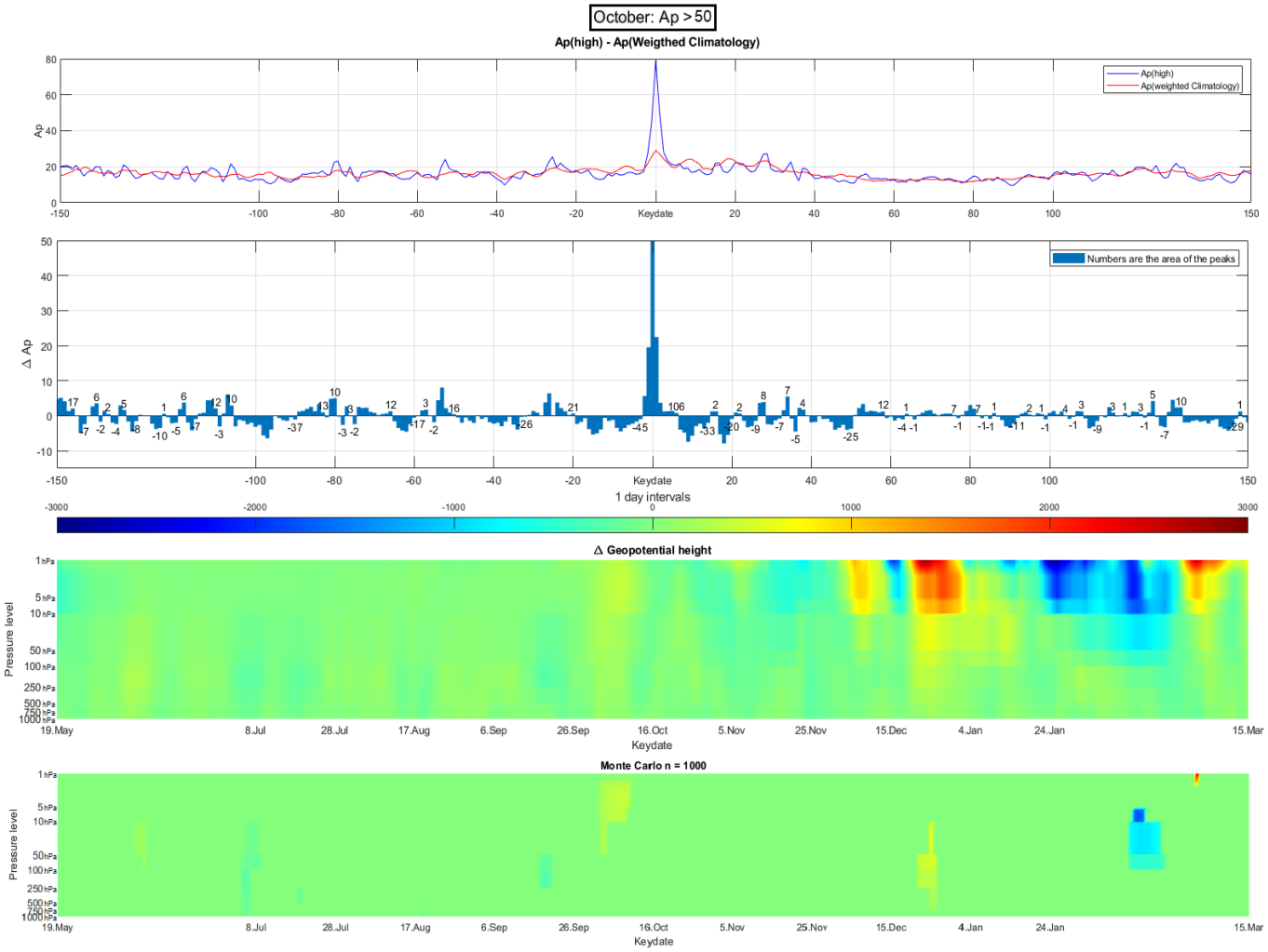

Figure 46: **First panel:** Blue (red) line represents the averaged Ap-index from the high (Weighted Climatology) bin. **Second panel:** The numbers represent the integrated ΔA_p for each peak. **Third panel:** Δ Geo-Height[m] = A_p(high)−Weighted Climatology for October set as keydate (A3N). **Bottom Panel:** Colored areas represent statistical significance after 1000 Monte Carlo simulations. The keydate for the A_p(high) bin is picked at random, with the years kept the same.

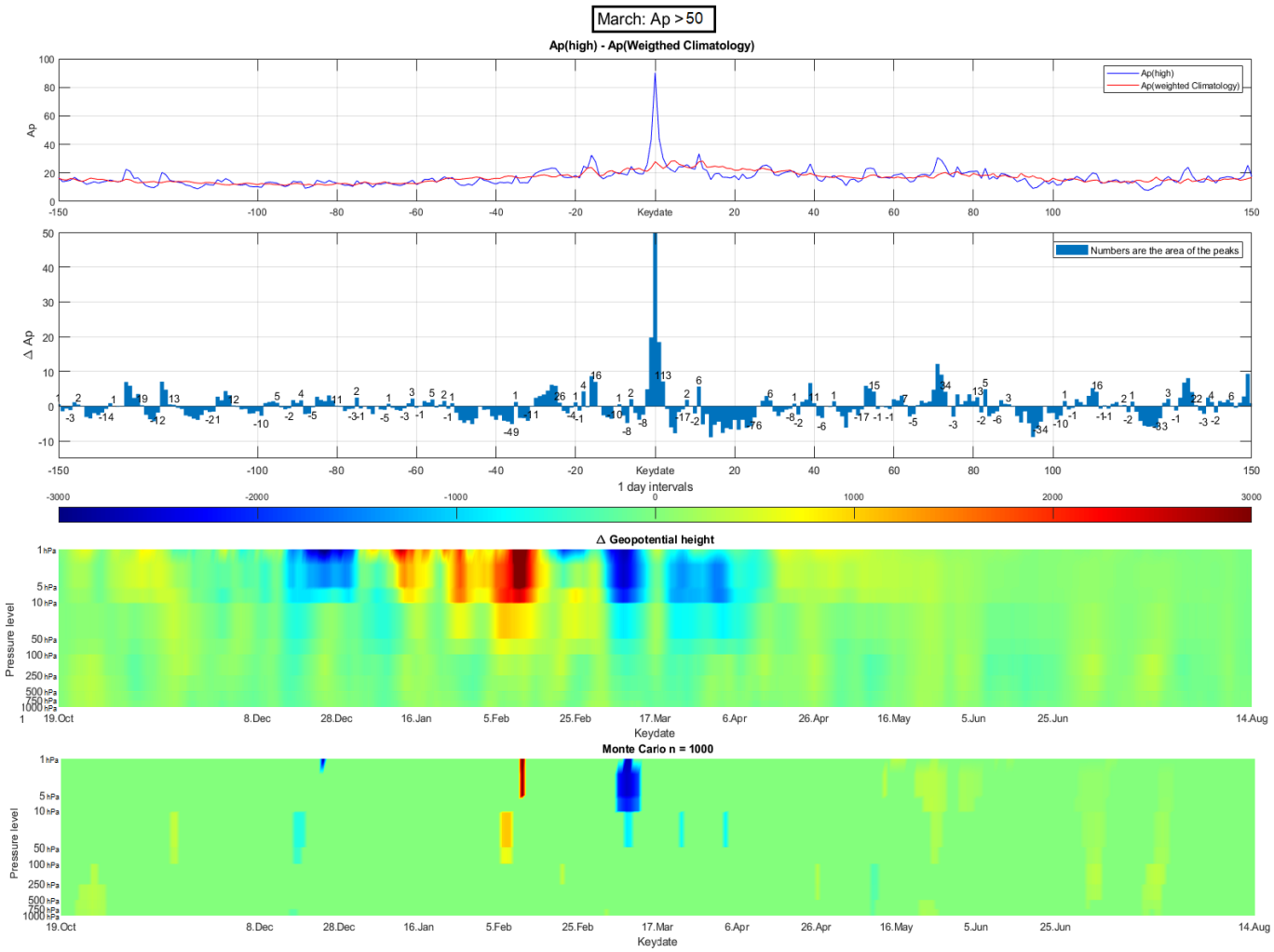

Figure 47: **First panel:** Blue (red) line represents the averaged Ap-index from the high (Weighted Climatology) bin. **Second panel:** The numbers represent the integrated ΔA_p for each peak. **Third panel:** Δ Geo-Height[m] = A_p(high)−Weighted Climatology for October set as keydate (A3N). **Bottom Panel:** Colored areas represent statistical significance after 1000 Monte Carlo simulations. The keydate for the A_p(high) bin is picked at random, with the years kept the same.

5 Results: The Mansurov Effect

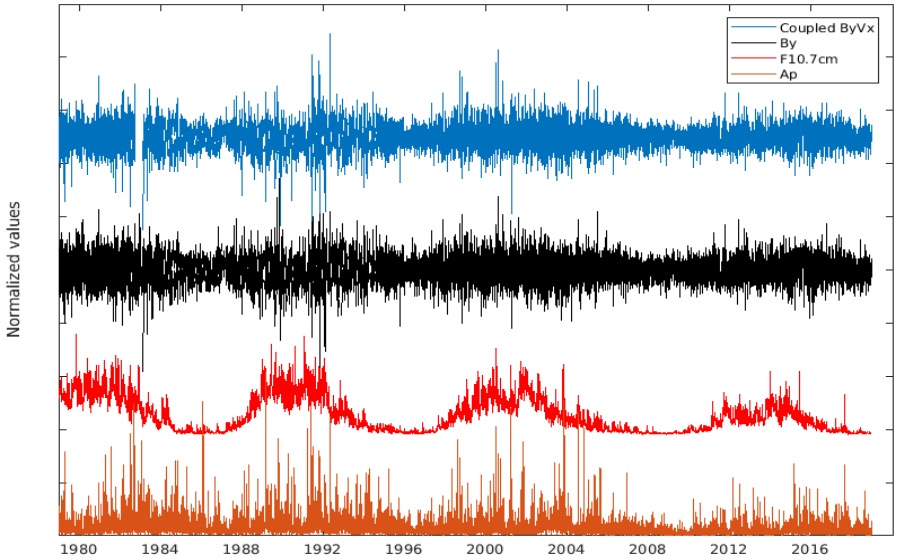

Figure 48: Coupled V_xB_y, B_y, F10.7cm and A_p index from 1979 to 2017. Values are normalized for visual comparison. The plot reveals how extreme maximum values of B_y and A_p follow the solar cycle, occurring with higher frequency near solar maximum.

Table 12 summarizes the analyses done for the Mansurov effect, together with the scientific goals. The overall theme for this chapter is the investigation of the pressure response in the polar regions correlating with the V_xB_y value, as well as the possibility of an aliasing mechanism. Figure 48 illustrates how

Table 12: Summary of the different analyses regarding the Mansurov effect.

Name	**Hemisphere**	**Timescale**	**Short description**
B1N/S	North/South	Daily	Spatial and temporal responses
B2N/S	North/South	Daily	Time evolution of responses
B3N/S	North/South	Daily	Aliasing through the gravitational pull of the Moon and the Sun

the V_xB_y, B_y, F10.7cm and A_p behave in the data period 1979-2017. V_xB_y and B_y are seen to have the majority of maximum absolute values occurring close to solar maximum, which is defined by the peaks in the F10.7cm index.

5.1 B1N/S: Spatial and temporal responses

This analysis investigates the polar pressure response of the Mansurov effect at 6 atmospheric levels ranging from 1-1000 hPa in both hemispheres. The results are shown as map plots to examine the spatial extent of the response. Superposed epoch analyses on the geopotential height data are performed, with the zero epoch times chosen based on the percentiles of the V_xB_y. The high (low) bin contains all days from the whole data period (79-17) in the >90th (<10th) percentile. The seasonality in the geopotential height is first removed, before it is plotted through the equation:

$$\Delta\text{Geo-Height [m]} = \text{High bin} - \text{Low bin} \tag{20}$$

Figure 49 shows the results for both hemispheres at six different pressure levels. Due to the extensive computing power needed for Monte Carlo simulations applying the significance limits, the method is only applied for 1000 hPa together with FDR. At other levels t-test is used together with FDR. Figure 49 shows no significance at any atmospheric levels over the whole time period. Further, the same analysis is performed for individual months for the whole data period to unravel potential seasonal dependencies. Significant anomalies over the period 1979-2017 are only found when the analysis is restricted to January in the SH, as illustrated by Figure 50. The response manifests itself as positive anomalies are over the Antarctic plateau, and at lower latitudes near South America and in the South Indian Ocean at the 1000 hPa level. Significant negative anomalies are also seen at lower latitudes in the South Pacific Ocean. The same pattern of anomalies are seen up to the 250 hPa level. A significant positive anomaly is also seen at the 100 hPa level. Note, however, that the Monte Carlo method has only been applied at the 1000 hPa level.

Figure 51 shows the distribution of data points from the >90th and <10th percentile of the V_xB_y values. The majority of the extreme values are seen to occur in the maximum/declining phase of the solar cycle. Previous studies suggest that the link between V_xB_y and surface pressure is most likely limited to the solar maximum periods (Burns 2008, Lam et al. 2013) exemplified with the period 1998-2002. Hence, the superposed epoch are performed for the solar-maximum periods 1980-1984, 1991-1995, 1998-2002 and 2012-2016. The high and low data points are binned according to the >90th/<10th percentiles, and the >75th/<25th percentiles. Statistical significant results are only found in the period 1998-2002, as shown in Figure 52. Both the NH and the SH show significant anomalies mainly at polar latitudes. For the NH, significance is found for both percentile criteria. The response manifests itself as a negative anomaly over Greenland, accompanied by positive anomalies over eastern Russia and the

North American continent at the 1000 hPa level. This pattern is seen through multiple atmospheric layers. At the 1 hPa level, a large polar centered negative anomaly occur. For the SH, significance is only found for the >75th/<25th percentile sorting. A positive response is seen over the Antarctic mainland and in the South Pacific. Significant negative anomalies also occur at lower latitudes. The response is seen up to the 500 hPa level, even though this should be treated with caution as the Monte Carlo method is only applied to the 1000 hPa for all plots. Appendix C Figure 102 - 104 summarizes the results for the other solar maximum periods.

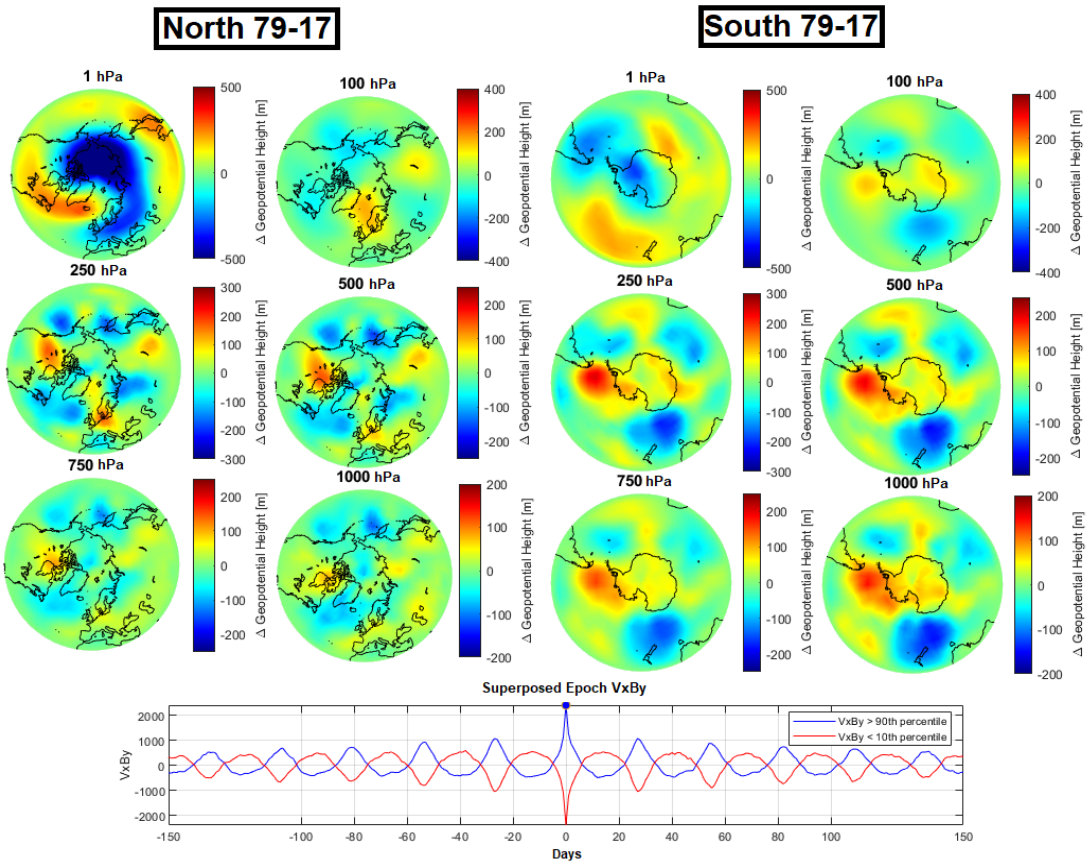

Figure 49: **Top left panel:** Six pressure levels for the B1N case. Binning according to the >90th/<10th percentiles of the V_xB_y values over the period 1979-2017. No statistical significance found. **Top right panel:** Six pressure levels for B1S case. No statistical significance found. The Monte Carlo method and FDR are applied for the 1000 hPa level. **Bottom panel:** Superposed epoch analysis of the V_xB_y data obtained from the percentile criteria.

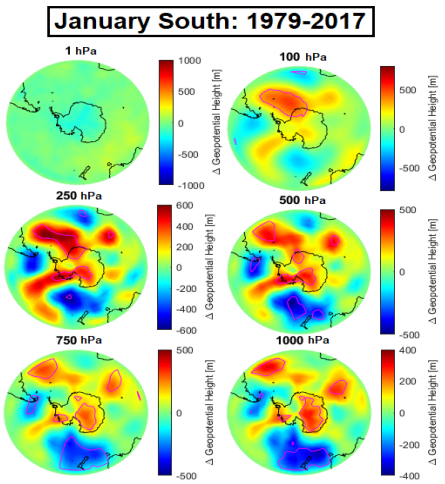

Figure 50: Same as Figure 49 restricted to January over the period 1979-2017. The Monte Carlo method combined with FDR is only applied to the 1000 hPa level. Significance for the other levels are calculated applying the t-test combined with FDR.

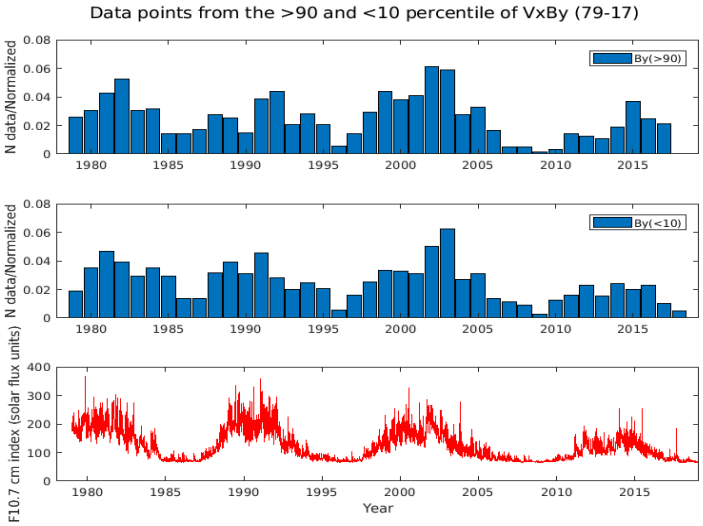

Figure 51: **Top panel:** Yearly distribution of data points from the >90 percentile bin of V_xB_y. **Middle Panel**: Yearly distribution of data points from the <10 percentile bin of V_xB_y. **Bottom panel:** The F10.7 cm index representing the solar cycle. A large fraction of the extreme V_xB_y values come from the maximum phase in the solar cycle.

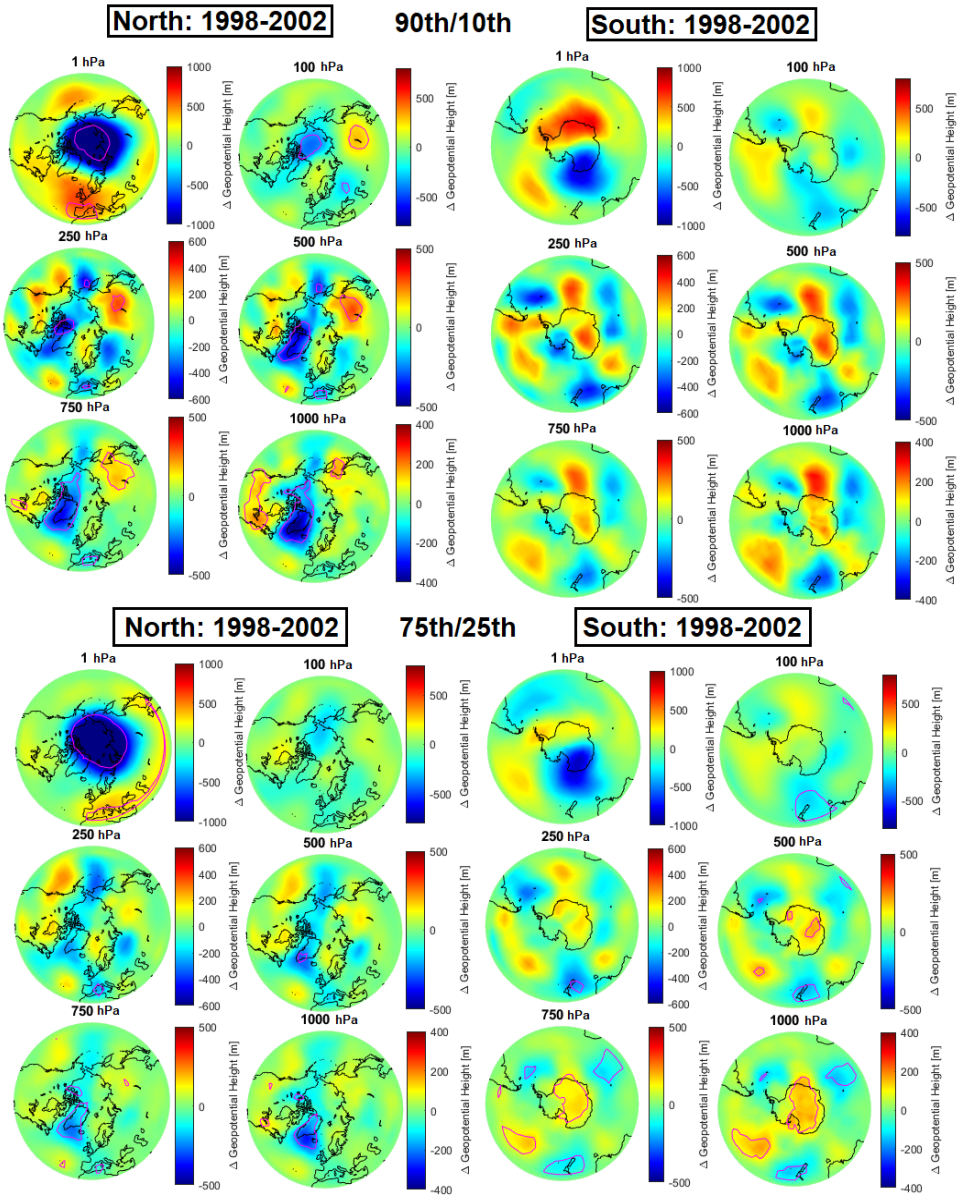

Figure 52: Solar maximum period 1998-2002. Binning according to the >90th/<10th and >75th/<25th percentiles of the V_xB_y values are shown. Significance in the SH is only seen for the latter, while the NH show significance for both percentile criteria.

5.2 B2N/S: Time evolution of responses

The following analysis investigates the time evolution of the Mansurov Effect. The theory predicts the largest response near the surface, which is partially seen in Figure 52. Hence, the analysis is limited to the 1000 hPa level. The geopotential height are averaged over the geomagnetic poles, with a radius of approximately 20° in latitude (approx. mlat ±70°), as this is the region where the strongest perturbations in the ionosphere from B_y fluctuations are expected. ΔGeo-Height[m] are plotted through equation 20 with the >90th/<10th percentile binning of the V_xB_y values. Figure 53 shows the results for the whole data period, and the period of the highest significance, 1998-2002.

As described in section 3.4, the responses seen at ± 1 periodicity of the V_xB_y driver includes some of the same data points as day 0. Hence, only ± half periodicity should be treated as valid.

For the whole data period, significance in the SH can be seen as a positive anomaly extending from day -8 till day 0. This is in contrast to Figure 49, which show no significance after the Monte Carlo method and FDR are applied for the same time period and sorting at day 0. Hence, it suggests a possible weakness in the t-test, and caution has to be made when interpreting. The whole data period also shows a -2 day lag for the peak in the geopotential height in response to the peak in the V_xB_y driver in the SH. This contradicts the expected cause-effect relationship. Burns et al. (2008) found the same -2 lag response for the Mansurov effect. They concluded that the offset was within In the paper

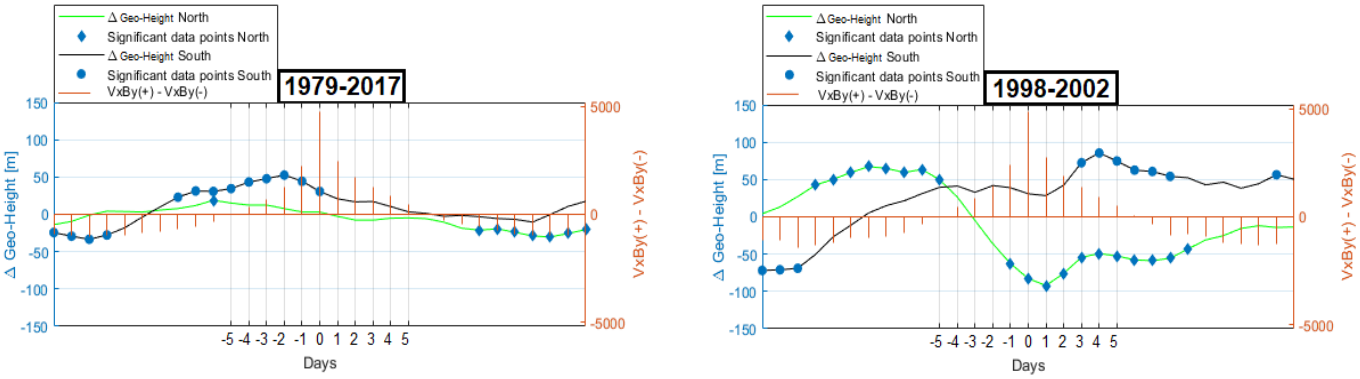

Figure 53: **Left panel:** ΔGeo-Height[m] = high bin(>90th percentile V_xB_y) - low bin(<10th percentile V_xB_y) for the period 1979-2017. **Right panel**: ΔGeo-Height[m] = high bin(>90th percentile V_xB_y) - low bin(<10th percentile V_xB_y) for the period 1998-2002. Significance is calculated through the t-test.

it is explained the statistical uncertainty of a 0-day lag. They also noted how the pressure shows a cyclic behaviour in accordance to the periodicity of the B_y-index. Here we question this cyclic behaviour with reference to section 3.4, as it may be artificially produced by the binning method. For the NH response, significant data points are seen at +8 days, manifesting as negative anomalies. For both hemispheres, the geopotential height responses are approximately in phase over the whole data period.

For the period 1998-2002, strong anomalies of opposing signs are seen between the hemispheres at day 0 in accordance with the theory. Significance is seen from day +3 as a positive anomaly in south, with the anomaly having its maximum amplitude at +4 days. In the north, a significant negative pressure anomaly peaks at +1 days.

Appendix C Figure 105 - 106 show the same method of sorting divided into 10-year periods, in addition to the solar maximum periods, respectively. As a general trend, either no significance is found around the keydate, or a significant anomaly peak show a negative lag to the peak value in the driver for the SH, except the period 1998-2002.

Targeting the potential seasonal dependence, Figure 54 shows the time evolution of the significant anomaly in the SH for January over the whole data period. As the analysis is restricted to a single month, the self replication of the response will be minimized at ± periodicity. Hence, a longer timescale is shown. By focusing only on the SH, a significant positive anomaly is seen at day 0. As for the other time periods, the positive response arises before the keydate. In this case the anomaly is seen to rise long before, with significance found at day -26, followed by a continuous positive response lasting till day +6. A signal

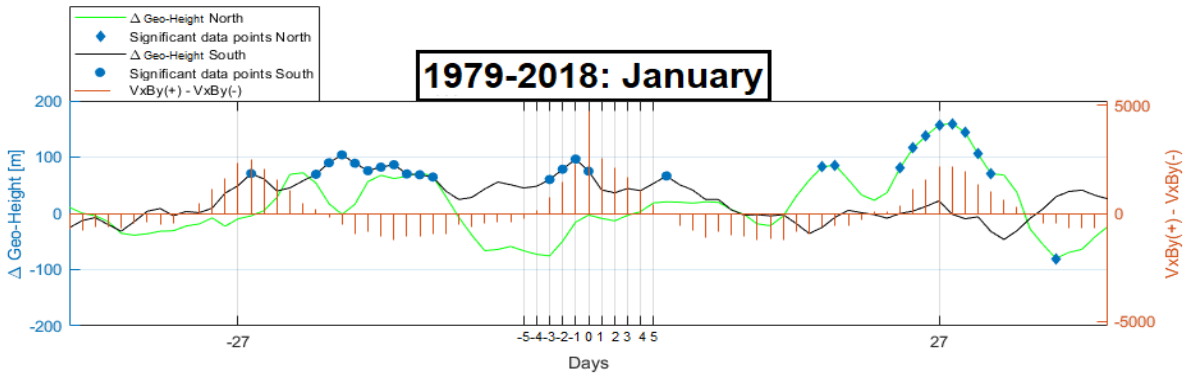

Figure 54: ΔGeo-Height[m] = high bin(>90th percentile V_xB_y) - low bin(<10th percentile V_xB_y) for January in the period 1979-2017. Significance is calculated through the t-test.

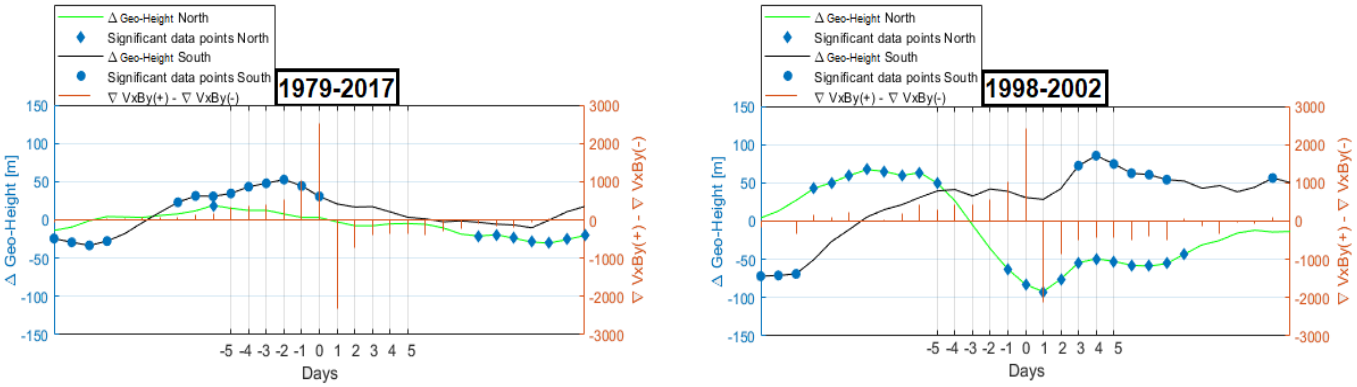

Figure 55: **Top panel:** ΔGeo-Height[m] = high bin(>90th percentile $\nabla V_x B_y$) - low bin(<10th percentile $\nabla V_x B_y$) for the period 1979-2017. **Bottom panel**: ΔGeo-Height[m] = high bin(>90th percentile $\nabla V_x B_y$) - low bin(<10th percentile $\nabla V_x B_y$) for the period 1998-2002. Significance is calculated through the t-test.

arising long before the keydate and the hypothesized driver, is unreasonable in terms of cause and effect. This raises questions regarding the actual significance of the response found in Figure 50.

The negative lag between the cause and the effect rises the question whether it could be change in the $V_x B_y$ and not the amplitude of $V_x B_y$ that is the real forcing agent. For both panels in Figure 53, the gradient of $\Delta V_x B_y$ is calculated, and shown in Figure 55. A constant gradient is assumed to attain a constant pressure response, with a gradient of zero equating to zero pressure response. In this perspective, the gradient ($\Delta \nabla V_x B_y$) show a better fit to the pressure response in the SH for the whole time period, compared to $\Delta V_x B_y$, as the beginning of the positive pressure anomaly correlates with a positive $\Delta \nabla V_x B_y$.

Another analysis is done that focuses on overcoming the limitations of the superposed epoch analysis. The goal is to investigate if there exists a real periodicity in the pressure in correlation with the $V_x B_y$. The method and results are summarized in Appendix C.2. No consistency in a 27-day periodicity is observed.

5.3 B3N/S: Aliasing through the gravitational pull of the Moon and the Sun

The -2 day lag, combined with the fact that the effect is only significant at certain times in the data period, raises some suspicion about the proposed mechanism. Potential aliasing effects have therefore been explored. Frequency analyses of V_xB_y and B_y are shown in Chapter 3.1.2 Figure 29. A dominant periodicity of approximately 27 days can be seen for both parameters, consistent with the rotation of the Sun as viewed from Earth. Although, it is not the most prominent signal, the geopotential height also exhibits this periodicity, as illustrated by Figure 56. In the SH geopotential height, a ∼29 days cycle is also evident.

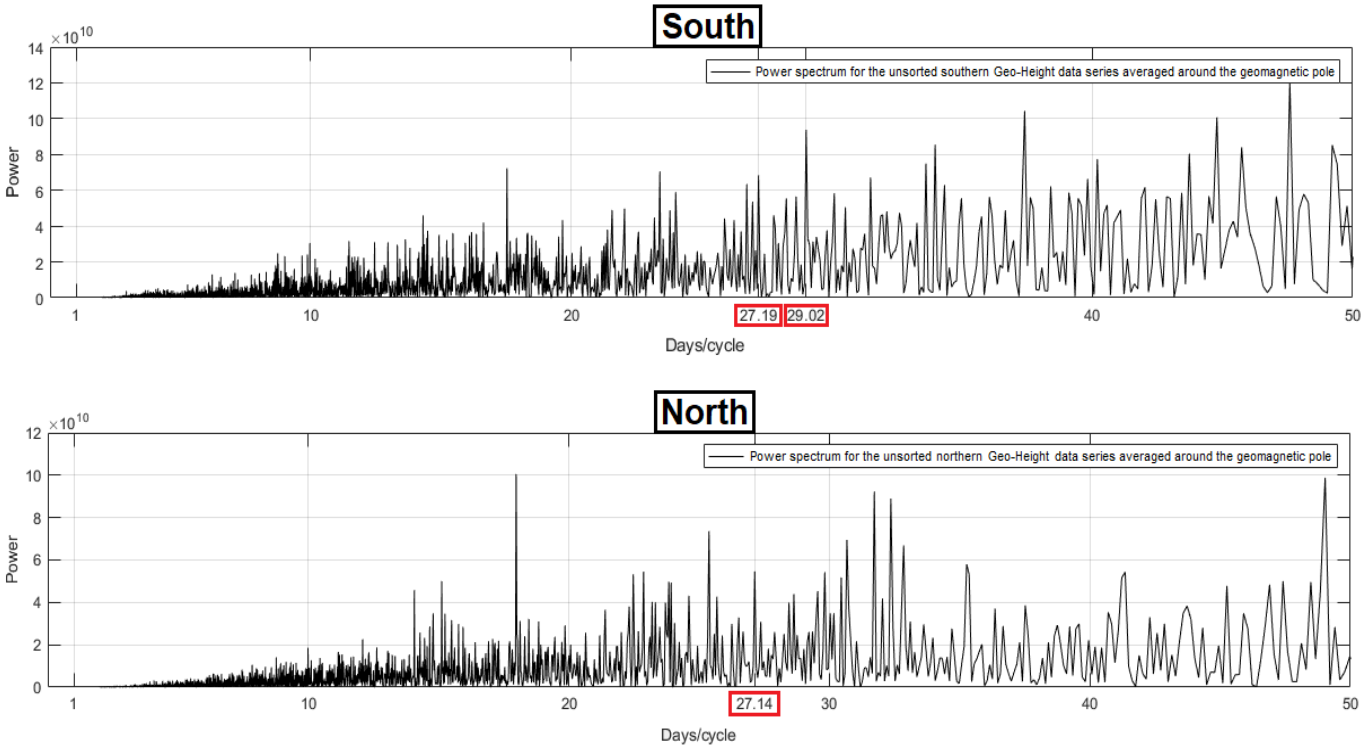

Figure 56: **Top panel:** Spectral analysis of the raw 1000 hPa geopotential height data for the NH averaged around the geomagnetic pole over the period 1979-2017. Although not the most prominent, peaks are found at 27.19 and 29.02 days per cycle. **Bottom panel:** Spectral analysis of the raw 1000 hPa geopotential height data for the SH averaged around the geomagnetic pole over the period 1979-2017. A peak is found at 27.14 days per cycle.

The orbit of the moon around the Earth follows a 27.2 day cycle, which is consistent with the average periodicity of the B_y-index. The synodic period, which is the time it takes from one full moon to the next, is approximately 29.5 days. This makes the hypothesized moon driver a candidate for a potential aliasing agent. For definitive proof of an aliasing mechanism operating through the gravitational pull of the moon, such a mechanism should be able to explain the significance seen in the period 1998-2002. It should also be consistent in the longer timer frame.

The moon might impact the surface pressure, both through the ocean and the atmosphere (Guoqing 2007; Malherbe et al. 2014; Kohyama and Wallace 2014). It is not readily evident how this will manifest itself at the 1000 hPa around the geomagnetic poles. As a first try, the potential impact by the moon's declination angle is explored. The angle varies from between 17° and 27° to -17° and -27° with a periodicity of 27.2 days. Through the gravitational pull, the first hypothesis is that a positive declination affect the pressure at a specific pole different then for a negative declination. This is thought to occur as a consequence of the reversed direction of the gravitational pull in both the horizontal and vertical direction. By focusing on the period 1998-2002, days with positive declination in the >50th percentile of the declination angles confined to the period is placed in the high(dec) bin. The corresponding low(dec) bin gathers the data points in the <50th percentile of the declination angle. The geopotential height response is then plotted through high(dec) bin - low(dec) bin. It is worth noting that because of the regularity of this cycle, a strong 'artificial' periodicity will be produced in the geopotential height response, as a consequence of the self replicating trait of the method. Therefore, it is con-

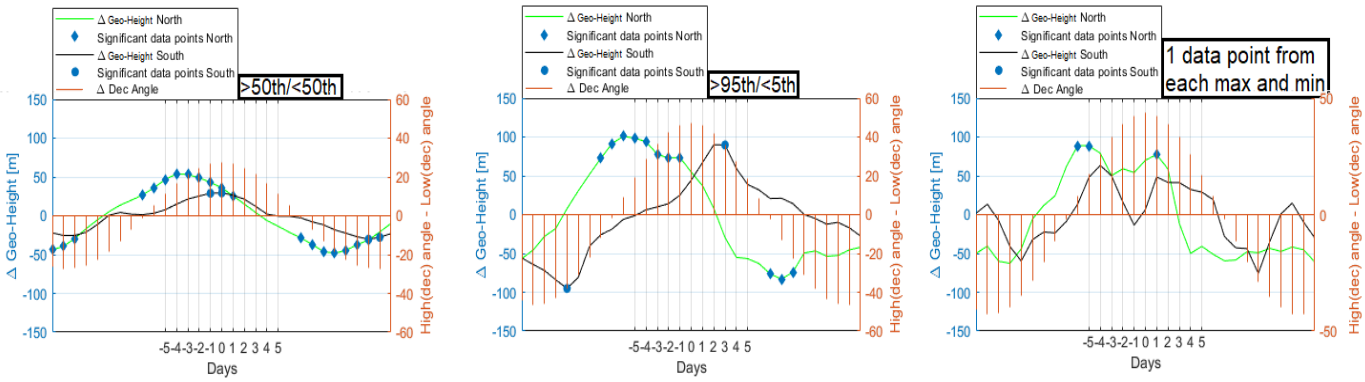

Figure 57: **Left panel:** ΔGeo-Height[m] = high(dec >50th) - low(dec <50th). **Middle panel:** ΔGeo-Height[m] = high(dec >95th) - low(dec <5th). **Right panel:** ΔGeo-Height[m] = high(1 data point per max) - low(1 data point per min). All plots are for the period 1998-2002. Significance is calculated through the t-test.

cluded that only the response seen from −half periodicity to +half periodicity can be treated as valid. Another binning is done at the >95th/<5th percentiles, as well as a binning only including one maximum for each cycle in the high(dec) bin, and one minima in the low(dec) bin. Figure 57 shows the results for the three different criteria. For the first binning, both hemispheres show a significant positive anomaly occurring at the peak difference between the declination angles. A slightly out of phase relationship between the NH and the SH is seen, with the SH lagging the NH by 4 days. In the second binning, the hemispheres are more out of phase, with the SH lagging the NH by approximately 9 days. Day 0 is still positive for both, but not at a significant level. Significance is seen at day +3 for the SH, and day +6 for the NH, manifesting as oppositely signed anomalies. The last binning method only show significance for the NH, as positive anomalies at day -6 and -5, and day +1.

For comparison with previous studies, which only used B_y and not V_xB_y, ΔGeo-Height[m] = high(>90th percentile of B_y) - low(<10th percentile of B_y) is plotted for the period 1998-2002 in Figure 58. In the figure, instead of showing the ΔB_y on the right y-axis, the associated declination of the moon according to the >90th/<10th percentiles of B_y is shown. The ΔB_y is shown as an illustrative red line scaled to fit the figure. The pressure anomalies in the NH clearly follows the Δdeclination of the moon. Note, however, that the declination angle sorted by the B_y criteria is only $\pm 7°$.

When looking at longer timescales for the declination sorting, an out of phase behaviour is observed between the NH and SH pressure response, as illustrated

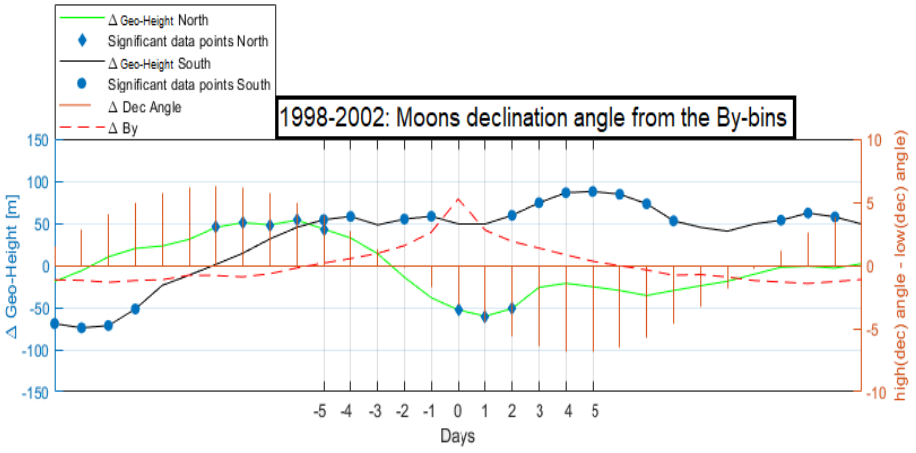

Figure 58: ΔGeo-Height[m] = high(B_y >90th) bin - low(B_y <10th) bin for the period 1998-2002. Angle on the right y-axis is calculated through declination from high(B_y >90th) bin - Declination from low(B_y <10th) bin. Red line show the behaviour of ΔB_y.

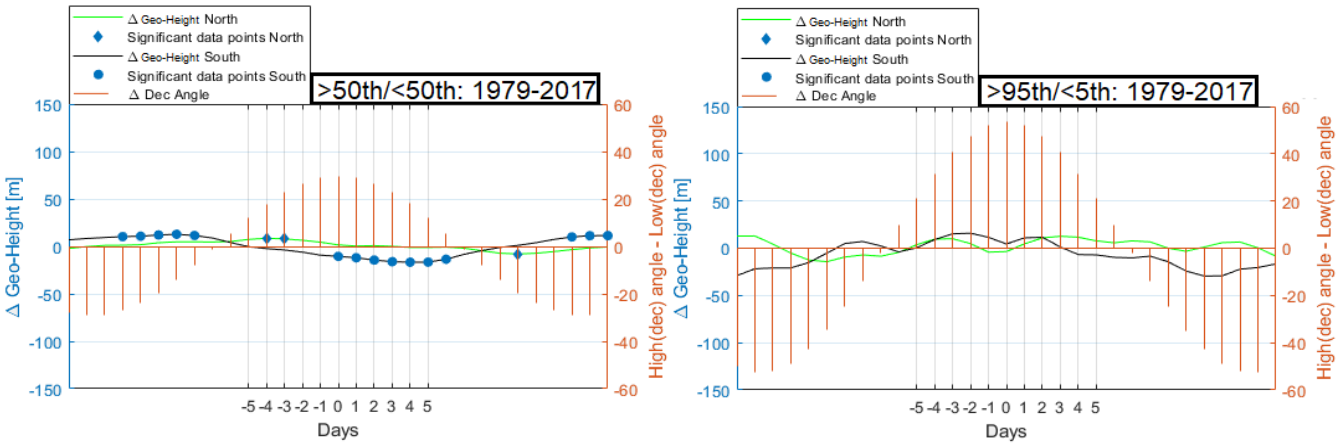

Figure 59: **Left panel:** ΔGeo-Height[m] = high(dec>95th) bin - low(dec<5th) bin. **Right panel:** ΔGeo-Height[m] = high(dec>50th) bin - low(dec<50th) bin.. Both analyses are for the full period 1979-2017. Significance is calculated through students t-test.

by the left panel in Figure 59. Here the full period 1979-2017 is plotted through the >95th/<5th and >50th/<50th percentile binning for the declination angle. The amplitude for both percentile criteria are weakened. Significance occur in the >50th/<50th criteria for the SH, manifesting as a negative anomaly from day 0 till day +6. Significance in the NH occur as positive anomalies at day -3 and -2, and as a negative anomaly at day +10. In the NH, the signature is similar to the one found in Figure 57, while the SH show an opposite response. The >95th/<5th percentile criteria show no significance over the whole data period.

The declination of the Moon is not the only parameter following a cyclic behaviour. If the gravitational pull has an effect on the atmosphere, the distance between the Moon and the Earth, as well as the contribution of the gravitational pull from the Sun, will also impact the response. As a next step, the combined radial gravitational acceleration from the Moon and the Sun is taken into account. A data sheet originally found on GitHub[6], and re-written to Python by Spencer Hatch, derives this variable for the specific locations geomagnetic North and South pole. As illustrated by Figure 60, the total gravitational pull also has periodicity of approximately 27 days.

With the aim of investigating if the geopotential height in each hemisphere responds differently to high and low gravitational acceleration, the analysis is firstly divided into two parts. One for the NH, and one for the SH. The 1000

[6] https://github.com/adienakhmad/Grav-TC

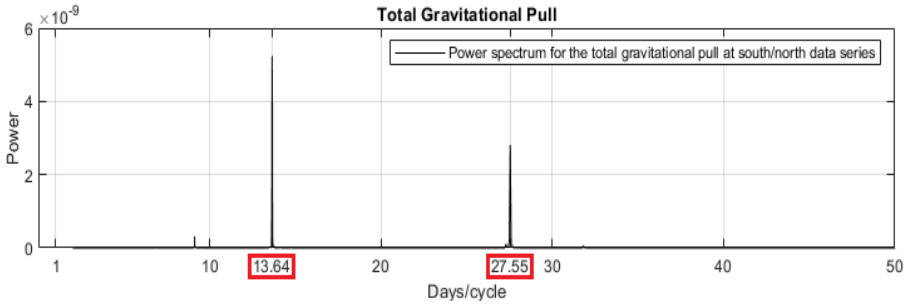

Figure 60: Spectral analysis of the total gravitational pull. The power spectrum is identical for total gravitational pull at north and south. Dominant periodicity's of 13.64 and 27.55 days per cycle are seen.

hPa geopotential height on the days with total gravitational acceleration in the >90th percentile from the chosen time period are subtracted the 1000 hPa geopotential height on the days in the <10th percentile. The top panels in Figure 61 depicts the situation for the period 1998-2002. As seen, it doesn't matter if the gravitational acceleration is focused on the NH or the SH, as both methods of sorting produces an approximately identical response. This can be reasoned for as the difference between the total radial acceleration at north and south are small. The geopotential height in both hemispheres show oppositely signed amplitudes at the keydate. However, significance is only obtained for the SH response. A shift for each hemisphere is also seen in the y-direction. The bottom panels give a visual impression of where the data points are gathered from. A disproportion can be seen, as a consequence of the data binning. More data points in the >90th percentile of the gravitational acceleration are located in the beginning of the period, while the majority in the <10th percentile are located at the end. This disproportion can explain the shift seen in the y-axis for both hemispheres, as slightly different time periods are compared against each other. Figure 62 illustrates the whole data period 1979-2017. The top left panel represents a >90th/<10th percentile sorting from the data series containing the acceleration at the geomagnetic south. Sorting by the acceleration at the geomagnetic north is not shown as it produces an approximately identical response. No significance is found at the keydate with this sorting. This could be a consequence of the shift on the y-axis, occurring as different time period are subtracted, as illustrated by the left bottom panel. The sensitivity of the t-test increases as anomalies peaks in value. With slightly shifted y-values, the peaks are displaced to either lower or higher values, thereby affecting the significance calculation. In the top right panel, the high and low pressure bins are sorted according to the single highest and single lowest value of acceleration at south per 27 days. Significance is found for the NH at +13 days, manifesting as a positive anomaly. By comparing the two methods of sorting, consistency is seen between the patterns formed. For the geopotential height in the SH, anomalies occur in phase with the acceleration driver. For the NH, a flattening is seen on

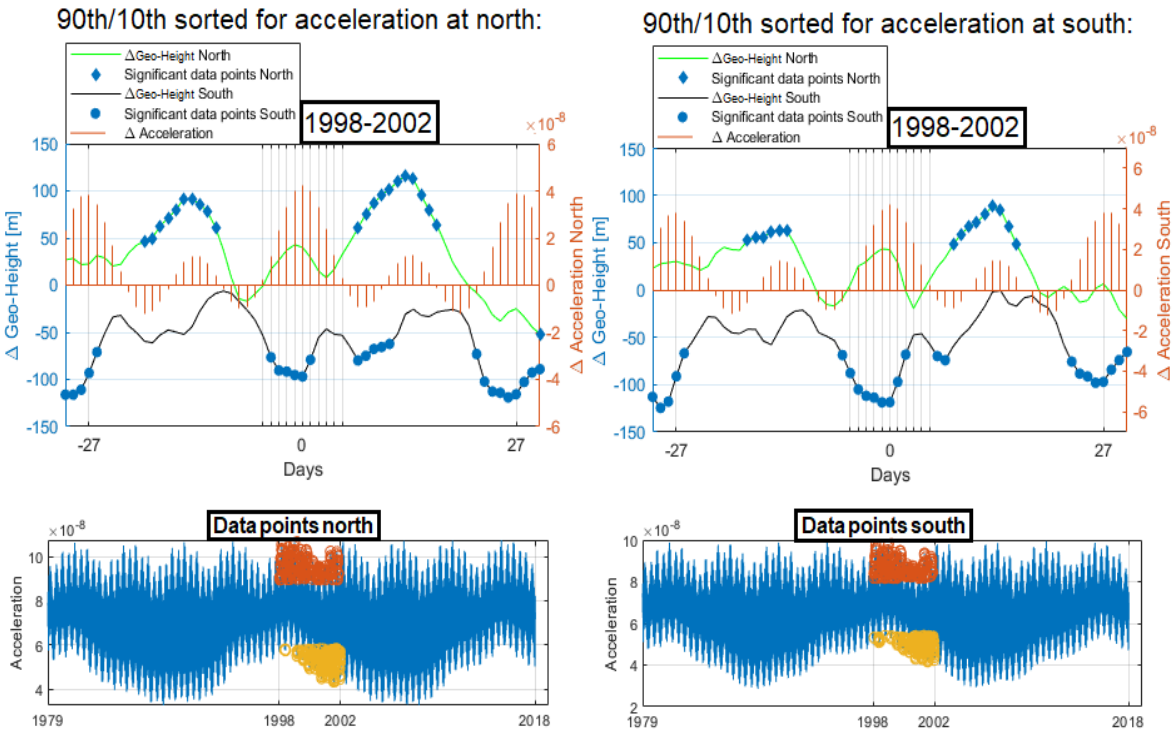

Figure 61: **Top left panel:** ΔGeo-Height[m] = high(acceleration at north >90th) bin - low(acceleration at north <10th) bin. **Top right panel:** ΔGeo-Height[m] = high(acceleration at south >90th) bin - low(acceleration at south <10th) bin. **Bottom panels:** Shows the gravitational pull at each pole over the whole data period. The orange and yellow dots indicate where the high and low datapoints are picked from. Significance is calculated through students t-test.

the keydate in both plots, with positive peaks at ±13 days in phase with the gravitational acceleration.

Over both time periods, a larger anomaly together with higher significance is seen in the NH at around day ±13. This period is correlated with a peak in the gravitational acceleration, but not the most prominent peak which occurs at day 0. It is evident that there are significant impact from the moon on the geopotential height in both hemispheres, but the current analysis might suffer from the lack of understanding of the complexity of the forcing. Hence, the moon driver remains a plausible candidate for further exploration of a potential aliasing mechanism.

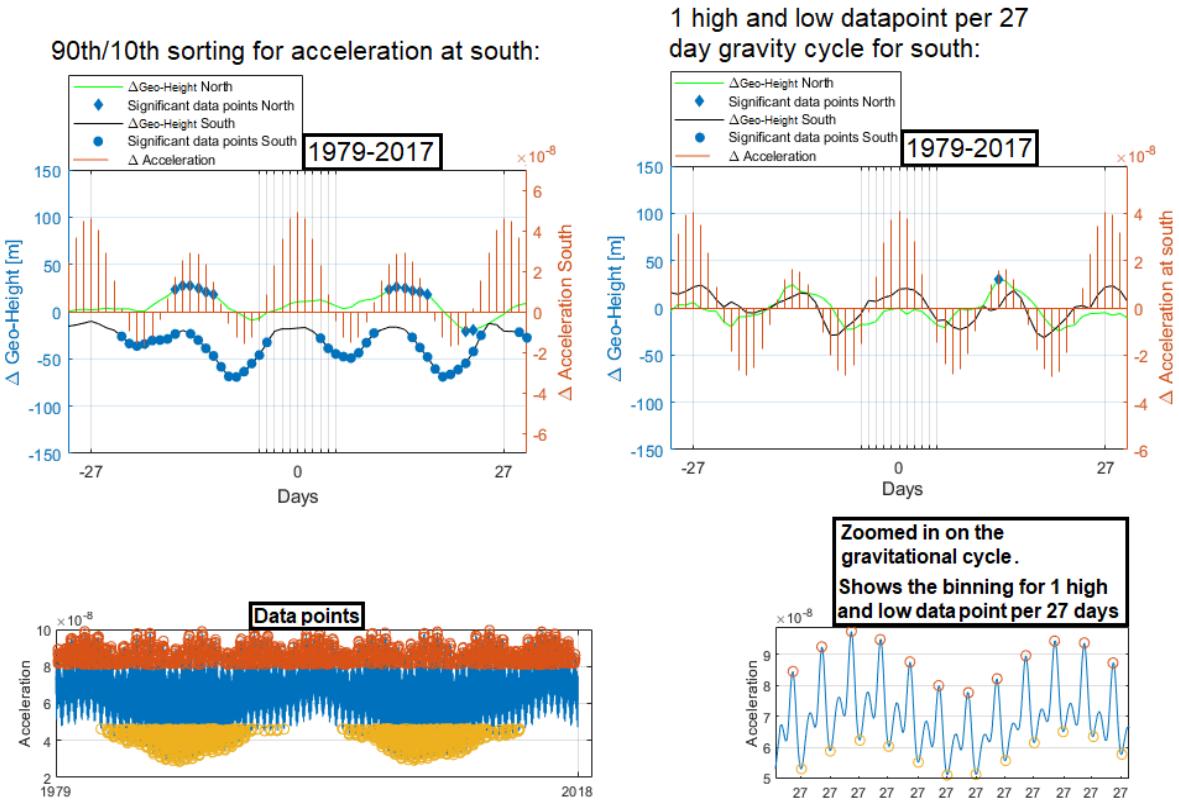

Figure 62: **Top left panel:** ΔGeo-Height[m] = high(acceleration at south >90th) bin - low(acceleration at south <10th) bin for the period 1979-2017. **Top right panel:** ΔGeo-Height[m] = high(only highest per 27 days) bin - low(only lowest per 27 days) bin for the period 1979-2017. **Left bottom panel:** Distribution of high (orange) and low (yellow) datapoints for the >90th/<10th percentile sorting. **Right bottom panel:** Illustrating how the datapoints are chosen when only the highest and lowest gravitational acceleration is the binning criteria. Significance is calculated through students t-test.

6 Discussion

This chapter will firstly discuss the results obtained for the Chemical-Dynamical coupling, before proceeding to the Mansurov effect. Further, the two main subjects will be divided into sections addressing the key questions of significant correlations, consistency with the hypothesized links, and potential aliasing effects.

6.1 The Chemical-Dynamical Coupling

6.1.1 Notion on the statistical significance of Seppälä et al. (2009)

The results of the thesis show statistical significant results at the 1000 hPa level in both hemispheres. Higher consistency is obtained in the NH, with similarities seen in the patterns for both the daily and monthly analyses. The findings also suggest that significant anomalies persist at the surface level, without significance obtained at higher atmospheric levels.

In re-analysis temperature data, Seppälä et al. (2009) found statistical significant temperature differences for winters with high A_p-index compared to winters with low A_p-index. These differences were enhanced in the NH when years with SSW events were excluded from the analysis. This is in part supported by Maliniemi et al. (2013) who found higher correlations between EPP and NAO when the two largest SSW events were excluded from the data. The manifestation of the response in the NH found by Seppälä et al. (2009) is seen as warming over Eurasia, and cooling over Greenland and polar latitudes, similar to that of a positive NAO. Included in the analysis, was the consideration and sorting after solar irradiance variations. The paper couldn't conclusively show a physical link between the temperature patterns and geomagnetic activity, but concluded that geomagnetic activity is likely to play a role in the modulation of wintertime surface air temperature. Further, they concluded that solar flux alone could not be responsible for the responses seen. Monte Carlo simulation or FDR was not used in the analysis.

Tartaglione et al. (2020) offers a more thorough statistical approach to the results obtained by Seppälä et al. (2009). By identical binning criteria of years, it was shown that the significance of the temperature differences vanish when the temporal and spatial auto correlation is handled in the proper manner. Still, the paper only handles the atmospheric range from 1 hPa to 200 hPa, while Seppälä et al. (2009) treats the 1000 hPa level. It is stated that for a possible surface impact associated with EPP, these levels must exhibit anomalies of statistical significance. However, the impact of the stratospheric pressure levels are expected to be more transient than the surface impact, which makes the dismissal of Seppälä et al. (2009) somewhat ambiguous. The exact same analysis should be carried out for clear evidence. Through the use of proper statistical approaches of the temporal and spatial auto-correlation, our results show

significant anomalies at the surface level, without significance seen at higher atmospheric pressure levels.

6.1.2 The exclusion of SSWs

While the results of Seppälä et al. (2009) showed enhancement of the surface response when SSW events were removed, Asikainen et al. (2020) found EPP-related enhancement of the polar vortex and other associated dynamical response only during winters having an occurrence of a SSW event. This enhancement was attributed the increased planetary wave activity into the stratosphere during times of SSW events, which acts to amplify the initial polar vortex enhancement caused by ozone loss. We do not, however, obtain any statistical significant results for the monthly analyses with or without the exclusion of SSW events in either hemisphere. When applying the t-test together with FDR, the exclusion of all SSW events show some statistical significant areas in the NH in January. Still, by proper statistical considerations, the significance drops, as illustrated by Figure 38.

Asikainen et al. (2020) showed the strong response 5-15 days preceding SSW events. Thus, one must note that similar consideration in our case is not possible when using only the average monthly data. The only statistically valid results for the monthly averaged pressure values correlating with periods of high A_p-index are found in the easterly QBO phase in the NH in March, when all SSW events are included (Figure 39). As for SSW events, the easterly phase of the QBO is attributed increased planetary activity into the polar stratosphere. Maliniemi et al. (2013) found a considerably stronger correlation between EPP and NAO in the easterly QBO_{30} phase, than the westerly. Holt et al. (2013) suggested that SSW events are correlated with an increase in NO_x in the stratosphere following the occurrence as a consequence of an increase in the descending branch of the residual circulation. The timing of the event was concluded to significantly affect the down welling, with earlier occurrences attributed more amounts of NO_x descending to the stratosphere.

For our results of March in the easterly QBO phase, the high A_p winter bin contains six SSW events in total. All events happen before March, with two events occurring in the early winter (early/mid December). Though not perfectly, the analysis of March in QBO-E fits the notion of increased planetary wave activity and increased down welling of NO_x into the stratosphere. The significance of the result only exists at 500 hPa, but remains so after proper statistical consideration. As these are the only significant results obtained for the monthly time scales, this favours a possible surface response from elevated EPP levels induced by increased planetary wave activity.

6.1.3 Daily scale analyses in the NH with SSWs removed

In the A2N case, all occurrences of SSW events are excluded. Days with high A_p-index restricted to a specific month are superposed, and subtracted the climatology. Anomalies of high significance appear in late December to early January for multiple different binning criteria. The response in this period manifests as negative pressure areas over polar latitudes and positive pressure areas over parts of Europe, as illustrated by Figure 40. All occurrences of SSW are excluded from this case analysis. The fact that the different keydate criteria all show significance for the same time period raises questions about the origin of the response seen. From the investigation of ΔA_p between the high bin and the climatology bin (Figure 41), a positive trend is seen throughout the whole autumn/winter period for each case. Considering the complex relationship be-

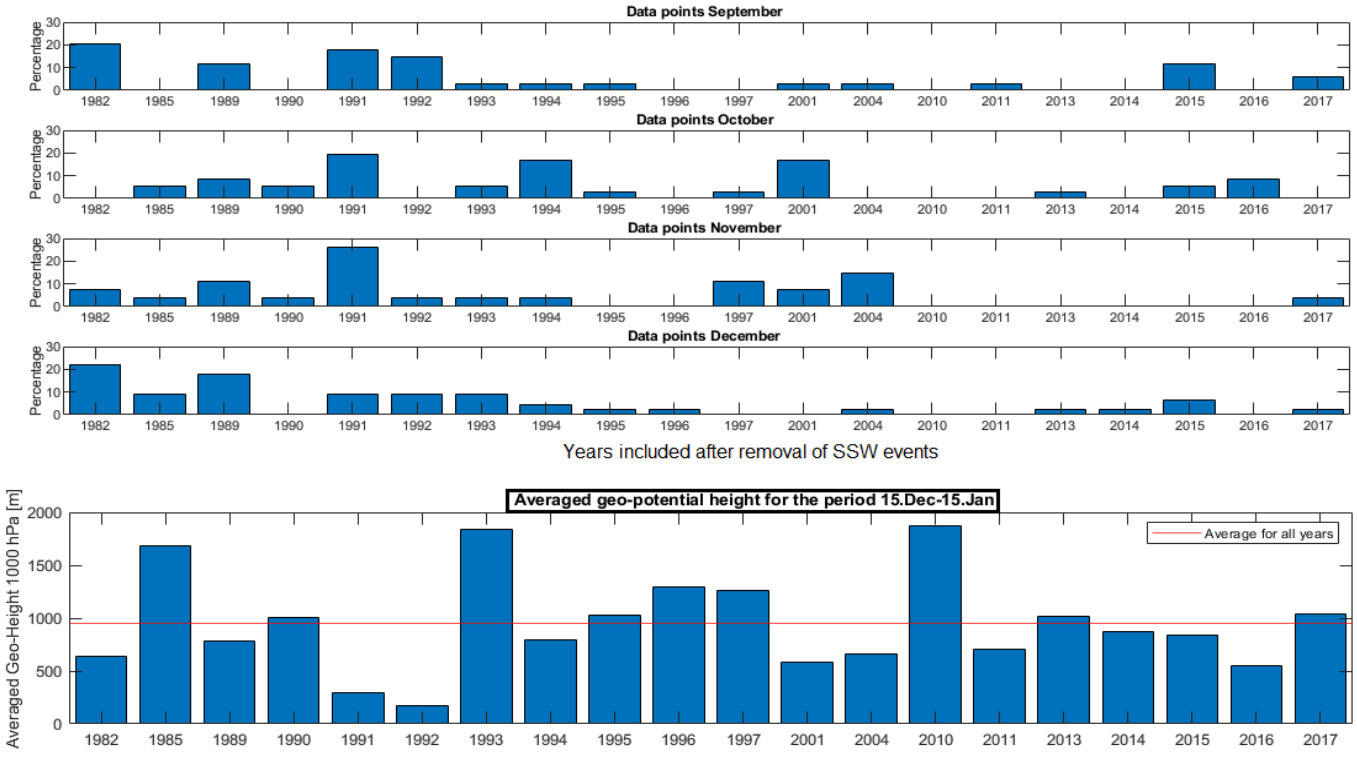

Figure 63: **Top panel:** Distribution of data points with the respect to the years included in the A2N case. Y-axis defines the percentage of data points in a particular year. Only the months producing a significant anomaly in the time period late December to early January are shown. **Bottom panel:** Averaged geopotential height for all the same years at the 1000 hPa level for the period 15.Dec-15.Jan. The year 1982 equates to the period 15.Dec 1982 to 15.Jan 1983 and so on. Red line specifies the average for the included years.

tween the effects of ozone depletion and planetary wave dynamics, which again depends on highly variable atmospheric parameters, it is unlikely that the effect should manifest itself at the same period independent of the key dates. The top panels in Figure 63 show the percentage of event per year with respect to the total distribution for September-December. A general trend of higher contribution from the earlier years in the time period is seen. Also, on average, roughly three individual years make up over 50% of the data bin in all cases. The year 1991 stands out as a particularly dominating year, with roughly 20% of the data points in the case for September, October and November, which are the months with the largest amplitude of the surface response seen in Figure 40. In 1991, a large eruption of the volcano Mount Pinatubo occurred, which contributed to significant cooling in global mean temperatures (Parker et al. 1996). The bottom panel in the figure show the averaged geopotential height for the period 15.Dec-15.Jan for the same years at the 1000 hPa level. As can be seen, the large majority of the dominating years have a pressure lower than the average for this period. Especially the year of 1991 and 1992 attributed to the post-volcanic conditions show particularly low geopotential heights at the 1000 hPa level. As 1991 dominate the data bins in all cases, the volcanic influence on the pressure will play a large role in the response seen. When looking at the other dominating years, there still exits a trend where these years correlate with lower than averaged geopotential height for the specific period. These dominating years are also correlated with high geomagnetic activity periods occurring at solar maximum and/or declining phase. Hence, the method of sorting will include many data points occurring at this time. The current analysis cannot confirm that the high geomagnetic activity are the cause of low pressure when disregarding the years 1991 and 1992. It can only be concluded at this point that the dominating years show a tendency of low geopotential height in this period, with some influence attributed to the volcanic eruption of 1991.

6.1.4 Daily scale analyses in the NH with SSWs and peak A_p years removed

The two top panels in Figure 64 are a reproduction of Figure 63, for the A2N: Peaks Excluded case when the keydate is restricted to September. The anomalies, which are illustrated in Appendix B Figure 92-93, also show significance for the period late December to early January manifesting as negative pressure areas over polar latitudes. Figure 64 shows the same pattern as the A2N case, where winters with low pressure in the time period 15.Dec-15.Jan are dominating the data set. Compared to the A2N case, the low pressure winters of 1982, 1991 and 1992 are not included in the A2N: Peaks Excluded analysis, as these years are ascribed as peak A_p years. This also means that the post volcanic conditions after Mount Pinatubo are excluded from the data. In the A2N analysis, these years make up about 50% of the high bin. The fact that the exclusion of these years still produces a similar pattern of significant pressure anomalies favour a surface impact caused by EPP, in opposition to generally lower pressure winters being caused by post-volcanic conditions. The major-

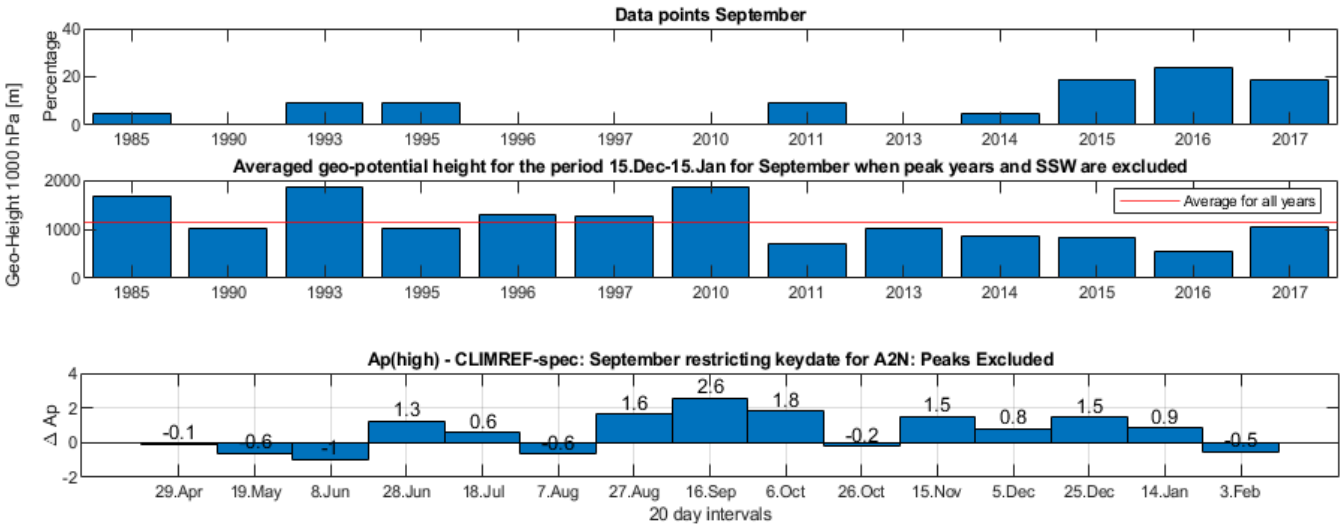

Figure 64: **Top panel:** Distribution of data points with the respect to the years included in the A2N: Peaks Excluded case for keydate restricted to September. Y-axis defines the percentage of data points in a particular year. **Middle panel:** Averaged geopotential height for all the same years at the 1000 hPa level for the period 15.Dec-15.Jan. Red line specifies the average for the included years. **Bottom panel:** ΔA_p calculated for the A_p high bin - CLIMREF-spec bin.

ity of NO_x produced in the thermo- and mesosphere this early in the winter will be destroyed by photolysis before reaching the stratosphere. The proposed accelerating effect on the down welling and the spatial confinement mechanism occurring as a consequence of the winter polar atmosphere dynamics are also not optimal at this time. However, from the perspective of an accumulative effect dependent on the integrated NO_x produced over the whole pre-winter/winter time, the analysis can be interpreted in a meaningful sense (This is equally valid for the A2N/S and the A2N: QBO case). The bottom panel in Figure 64 shows ΔA_p calculated through A_p(high) bin − CLIMREF-spec for A2N: Peaks Excluded for September. The difference between the bins producing the significant geopotential height anomalies has a general trend of positive ΔA_p in the time period before the anomalies are observed, which is required for an EPP-Pressure response to be physically realistic from the accumulative perspective.

6.1.5 Daily scale analyses in the NH with QBO phasing

For the A2N: QBO case, the same pattern at the same time period occurs for both QBO phases when keydate is set inside September. The selection of September as the most compatible month for comparison is made with the accumulative perspective in mind, as the data points picked for September in both phases show an approximately equal ΔA_p in the pre-winter/winter. Higher sig-

nificance and amplitudes are observed for the anomalies in the easterly QBO, especially at the 1000 hPa level. Nonetheless, both phases show significant patterns over similar time periods, with the westerly QBO phase showing higher significance at the upper atmospheric levels. It is emphasized how the splitting of the QBO-phases into separate analyses guarantees that no data point found in one of the analyses will be found in the other. Taken into account, this supports the hypothesis of a chemical-dynamical coupling able to penetrate a response to surface level in the NH.

6.1.6 A notion on the 15.Dec-15.Jan period

The combined results of A2N, A2N: Peaks Excluded and A2N: QBO (Figure 41, 46, 93-96 and 98) renders two plausible possibilities. The results could reflect real EPP related surface responses, or, a lowering of the polar surface pressure just happens to occur in the same time period, caused by external forcing or natural variability, which is partially seen in A2N. A larger fraction of the data points in the high A_p bin are consistently gathered from years when the following winter period 15.Dec-15.Jan have a lower than average pressure at the 1000 hPa level. These dominant A_p years are in general a consequence of the solar maximum/declining phase periods, attributed to overall elevated EPP fluxes. In these periods, the EPP fluxes will stay elevated for longer time periods than the single month restricting the specific analyses, which is partially reflected in the positive trends seen in ΔA_p. This states a relationship where higher A_p over extended time periods is correlated with negative polar pressure anomalies, even at the surface level.

Robustness of the response is seen through the consistency of the anomalies between the different sorting criteria. The results obtained for the A2N: Peaks Excluded case indicates that the most extreme geomagnetic activity years are not needed for a statistical significant correlation to be obtained at the surface. On the other hand, from the monthly averaged plots, no statistical significant response is seen in this time period. One reason for this could be attributed to the method of sorting. For the monthly analyses, high A_p years are compared to low A_p, with no further data manipulation. In the daily analyses, the signal is enhanced to a certain degree. CLIMREF-spec will contain equal proportions of all the years included by the criteria of the analysis, while the high A_p bin is dominated by the high geomagnetic activity years. An actual response occurring in these high activity periods will therefore also dominate the data bin, leading to an enhancement of the observed output response. An enhancement will also occur if any of the years dominating the data bin has an unrelated but large anomaly arising in the same time period for any given reason. This highlights the weakness of the method used, as it is not accustomed to determine the mechanism for the significant anomalies observed. The fact that the daily analyses are dominated by relatively few years, yields for caution as random

occurrences of pressure anomalies inside the dominating years would highly influence the result, possibly producing statistical significance.

No other public research have looked at the relation between EPP-Polar surface pressure on a daily scale. For a definite conclusion on the correlations obtained as a cause-effect relationship between EPP and atmospheric dynamics in the NH, research must verify the mechanism in play, and additionally comply with chemistry-climate models, where other elements affecting the variability of the pressure can be removed. Independent statistical significant and consistent results obtained for the period 15.Dec-15.Jan through other sorting criteria and methods would highly favour a cause and effect relation consistently occurring in this time period.

6.1.7 Response seen in early spring in the NH

When keydate for the A2N case is restricted to December, negative polar surface anomalies can be seen in middle March, with little to no disturbances in the middle atmospheric levels, and strong positive anomalies in the upper atmosphere, as illustrated by Figure 88 in Appendix B. These results resembles the pattern at the 500 hPa and 1000 hPa level obtained for March in the monthly analysis in the easterly QBO phase, but with deviations in the upper atmospheric levels. The amplitudes are also weaker than for the pure QBO-E phasing in the lower levels. The results could indicate the pervasiveness of stronger amplitudes originating mainly from the QBO easterly phase and manifesting in the composite of both phases as a slightly weaker response. It also shows that a surface response may persist far longer than in the upper atmospheric levels.

For the same analysis, with the keydate restricted to January, a significant anomaly is seen in middle April, resembling the results obtained by Seppälä et al. (2009). The results are compared in Figure 65. It must be noted that

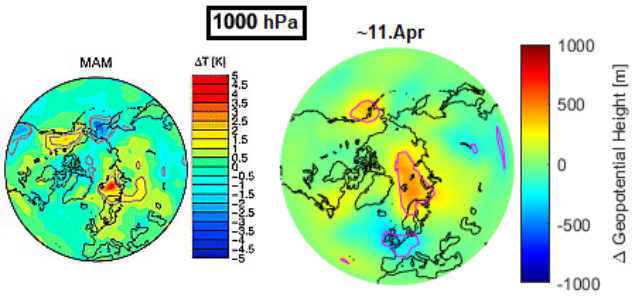

Figure 65: **Left map:** All SSW events are excluded, where high A_p is subtracted low A_p for the averaged temperature in MAM. Full details found in Seppälä et al. (2009). **Right map:** Anomaly at the 1000 hPa level from Figure 42 when keydate is restricted to January for the A2N-case.

two different variables are compared, temperature (Seppälä et al. (2009)) and geopotential height/pressure. As of this, the signature for the same response will not be identical, and the comparison is only treated as an indication. The left map illustrates the case by Seppälä et al. (2009), which is a three-month average over March-April-May (MAM), where solar flux variability is taken into account, and SSW events are removed. Our analysis only removes the SSW events, and does not account for the solar flux variations. These results indicate that statistical significance is obtained through two independent and differently set up analyses, with a consistent pattern in the same time period when internal atmospheric variability and external forcing are handled in an approximately equal matter. Figure 42 shows, however, that the higher levels are not necessarily representable of the surface response.

6.1.8 Weighted climatology

The A3N case, which use weighted climatology, is an effort to mitigate the over representation of certain years when analysing climatological data on a daily scale. It ensures equal representation of the years independent of the number of key dates. A criteria for the method to work, is a fairly consistent time lag between the cause and response, or else the response will be smoothed out. Figure 66 shows the distribution of data points among the available winters for the A3N case when keydate is restricted by October and March, respectively. The data point are collected from roughly the same periods, attributed to high geomagnetic activity. This could in turn influence the results seen in March

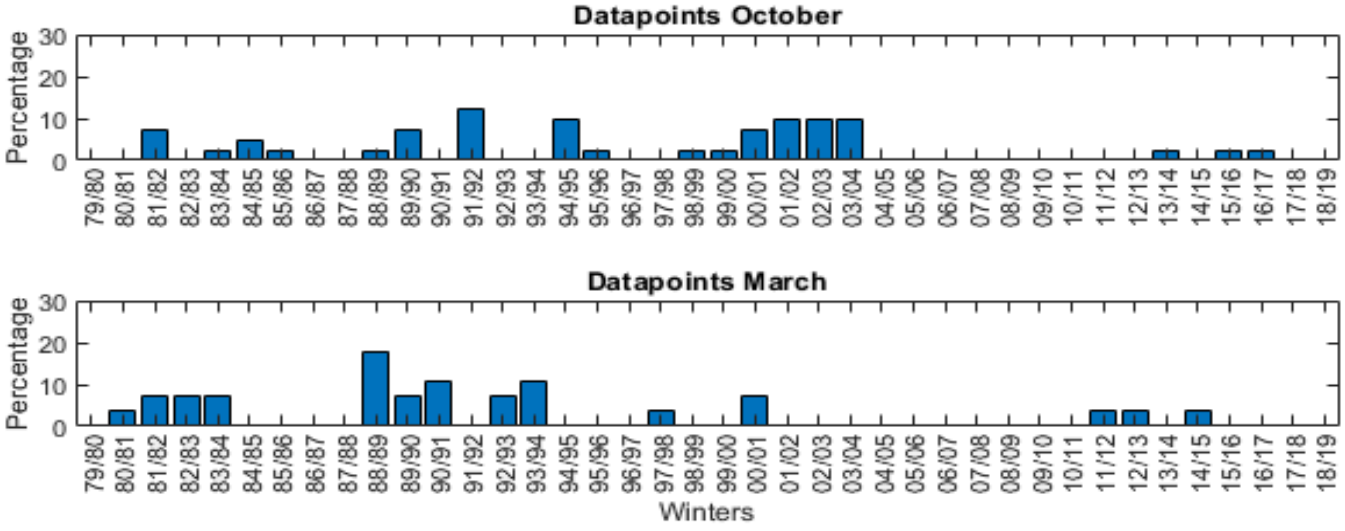

Figure 66: **Top panel:** Data points obtained for October when A_p >50 for the A3N case. **Bottom panel:** Data points obtained for March when A_p >50 for the A3N case.

before the keydate, as illustrated by Figure 47. Still, large response before the keydate without preexisting peaks in ΔA_p cannot be attributed to the forcing, as no cause is present. This hints at large atmospheric variability, or noise, occurring at equal amplitudes as the response seen in October in Figure 46. Therefore, the significant anomalies seen for October cannot be interpreted as a significant result.

6.1.9 Differences between the NH and SH response

From the perspective of the EPP-forcing, both hemispheres should yield fairly equal responses. Hence, differences could be attributed to either atmospheric dynamics or aliasing effects. Findings from Funke et al. (2014) indicates a 2-5 times larger downward transport of EPP-induces NO_x in the SH compared to the NH. The SH also has a more stable polar vortex, which helps to confine the molecules to polar latitudes. Strong down welling in the NH could, however, occur after SSW events in the NH. On the other hand, while the SH favours the down welling of NO_x, the dynamical coupling and a possible surface response could be highly influenced by the topology and planetary wave activity, which is favoured in the NH.

Although the analysis presented in this thesis do not show an indisputable impact, it hints of a stronger impact in the NH compared to SH in both the monthly and daily scale analyses. Based on previous studies, few research papers confirm a lower atmospheric response from EPP in the SH compared to NH. Seppälä et al. (2009) found a dipole like response of positive and negative temperatures attributed to high A_p-index occurring in June-July-August (JJA) in the SH. Though slightly different groupings of years, where the solar variability is not accounted for, the A1S analysis finds no significant results for the monthly averages in the SH.

Tomikawa (2917) found highly significant negative temperature anomalies in the southern midlatitude upper stratosphere attributed to EPP related effects in July. For the A2S case, as a general trend, a diffuse pattern is seen composed of both positive and negative anomalies, occurring mostly at the lower atmospheric levels. The strongest and largest negative anomaly do occur in July when keydate is restricted to March, as illustrated by the left panel in Figure 43. It is still difficult to establish the real significance of the response seen, as very little consistency is found between the different analyses for the SH.

The fact that the A2N patterns are reproduced when years are distributed into the QBO-phases, and when peak A_p years are excluded (which helps to exclude the effects of the volcanic eruption in 1991), strengthens the evidence of an actual response seen in the NH. This is further supported by statistical significant results found in the monthly analysis for March in the easterly QBO phase in the NH. The westerly QBO phase, which is attributed stable vortex conditions, also produces significant anomalies in the A2N: QBO case, though

slightly less than the easterly QBO phase at the surface level.

On the other hand, as the results are not conclusive in the terms of a mechanism, the possibility of an aliasing mechanism being responsible for the asymmetric behaviour cannot be ruled out.

6.2 The Mansurov effect

6.2.1 Dependence of the solar cycle

Though not stated directly in the literature, it is indirectly implied that the solar maximum is the reason for the significance found for the Mansurov effect in the period 1998-2002 (Burns et al. 2007; Burns et al. 2008; Lam et al. 2013; Lam et al. 2014; Lam et al. 2018). Figure 51 shows that the larger absolute values of V_xB_y occur during solar maximum. For a small but significant forcing, those time periods are ideal for an enhanced effect of the hypothesized mechanism. However, the results for all the other solar maximums in the period 1979-2017 show no statistical significant relationship.

6.2.2 The 1998-2002 period

Lam et al. (2014) concludes that the response seen in Antarctica for the period 1999-2002 originates in the troposhere, where it propagates upward to a maximum height of the tropopause on the order of days. As illustrated by Figure 52, which show the results for the period 1998-2002 for both hemisphere, the SH response seem to be consistent with these results. In the NH, a large negative anomaly is present at the 1 hPa level. Negative anomalies remaining statistically significant after t-test is applied together with FDR are also seen at all intermediate levels between 1-1000 hPa for the >90th/<10th percentile sorting. Even though proper Monte Carlo simulations are not carried out for any level except the 1000 hPa, the results still indicates an atmospheric anomaly extending far above the tropopause. This is not in accordance with the findings of Lam et al. (2014). Considering the lack of significance in the remaining 30-year period, the possibility of aliasing phenomena for the 1998-2002 period needs to be evaluated.

In the following, a thorough investigation of the time period 1998-2002 is conducted. Figure 67 illustrates the period separated into individual years for the >90th/<10th percentile sorting, with the 1000 hPa level for both hemispheres shown. The aim of this division is to reveal if the response is consistent throughout the period, or if it's dominated by a specific year, which would increase the probability of aliasing. However, as seen from the figure, a negative anomaly over Greenland and the surrounding area in the NH persists throughout the time period. For the SH, a positive anomaly persist over the Antarctic plateau to some extent for the period 1999-2002. Note, however, that proper statistical considerations are not conducted. Table 13 summarizes the atmospheric variability attributed to this time period. The time period is heavily dominated by

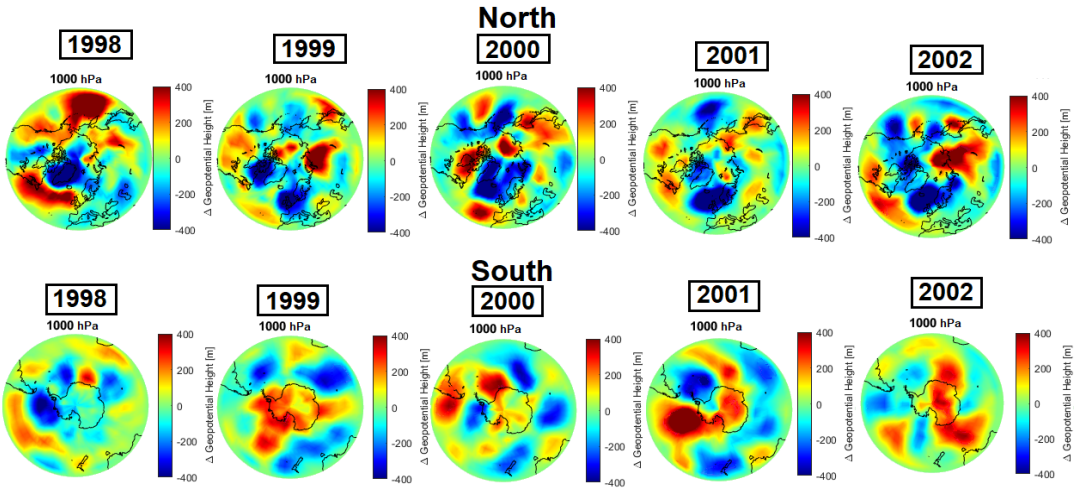

Figure 67: ΔGeo-Height[m] = high(V_xB_y >90th) - low(V_xB_y <10th) plotted for the years 1998, 1999, 2000, 2001 and 2002. The 1000 hPa level for both hemispheres are shown. Significance have not been treated.

SSWs in the NH. The only occurrence of SSW in the SH also appear in this time period. The QBO phases are distributed in roughly equal amounts. For the ENSO, the oceanic cooling phase, known as La Niña, is slightly dominating the time period. If some internal atmospheric mode is overrepresented in the bins, the response seen will be aliased by the mode itself. When looking back at Figure 67, the overall hemispheric patterns seen are not consistent throughout the years for either hemisphere. However, it is evident that the 5-year average suggests a negative anomaly over Greenland in the NH. In the SH, 1998 is the only majorly deviating year, with no apparent warming over the Antarctic plateau. As of this, no single year can be attributed as the sole consequence of the 1998-2002 anomaly. An investigation of the distribution of SSW events in the data points for the NH is done, with no apparent aliasing between the high

Table 13: Internal atmospheric variability in the period 1998-2002

Year	**SSW**	**QBO**	**ENSO**
1998	December(NH)	Easterly	Warm and Cold
1999	February(NH)	Westerly	Cold
2000	March(NH)	Westerly and Easterly	Cold
2001	February(NH) and December(NH)	Easterly	Cold and Neutral
2002	September(SH)	Westerly	Neutral and Warm

ENSO divided into warm, neutral and cold phase according to the Multivariate ENSO Index Version 2. The index can be found from https://psl.noaa.gov/enso/mei/.

and low bin. Shown in Appendix C.3 Figure 109, is a division of the period into winter and summer for both hemispheres. A negative anomaly occur over Greenland for both seasons in the NH, which is also the case for the positive anomaly over the Antarctic plateau at the 1000 hPa level. As of this, the possibility of SSWs causing the observed response diminishes. Noted, however, is a disappearance of the negative 1 hPa anomaly in the NH when the summer is chosen. In general, this underlines how the 5-year averaged plot is not a fair representation of the actual response. Even though some consistency is seen over Greenland and the Antarctic plateau for the individual years, a potential aliasing effect should not be overlooked without a thoroughly investigation of the distribution of the remaining atmospheric modes between the data points.

6.2.3 Seasonal dependence

Considering the seasonal dependence of the Mansurov effect, the month of January exhibits high significance for the whole time period in the SH. Freeman and Lam (2019) determined a seasonal dependence for temperature changes related to the Mansurov effect when looking at the limited time period 1999-2002. The Autumn and Winter are regarded as the highest response times, with an observed 3.2° and 2.4° Celsius temperature change correlating with the B_y-index. Spring and summer is regarded as the smallest response period, with an attributed temperature change of 1.6° and 0.9°, respectively. In contrast, the analysis restricted to January finds the largest response, which is the the local summer time. On the other hand, the geopotential height of a certain level do not correlate perfectly with the temperature. From the division into summer and winter referenced in the last sub section, no clear seasonal dependence is seen if the response is spatially restricted to Greenland in the NH. In the SH, slightly higher amplitudes are observed over the Antarctic plateau for Apr-Sep, which is in line with the findings of Freeman and Lam (2019). However, the limitations of such a small time period doesn't necessarily give an accurate depiction of the real seasonal dependence if the Mansurov effect is thought of as having a continuous but small impact.

Figure 54 shows the time evolution of the anomaly in January at the 1000 hPa level. A positive anomaly in the southern pressure starts as early as day -26, and remains mostly significant until day 0. Day 0, which marks the peak for the $\Delta V_x B_y$, does not affect or contribute to an amplification of the anomaly. Hence, it is possible that the apparent anomaly found in Figure 54 is a consequence of the data handling, and not a consequence of the forcing driven by the IMF. An overweight of data points being chosen in generally warmer (colder) Januaries and placed in the high (low) bin could result in a response of a prolonged time period of positive pressure anomalies when the low bin is subtracted from the high bin.

6.2.4 Time lag

Burns et al. (2008) found a -2 day lag between the forcing and the surface pressure response at mlat >83°S through a linear regression coefficient analysis for the period 1995-2005. The lag was justified to be within the statistical uncertainty limits of a zero lag value. Figure 53 shows, however, that this feature is statistically valid over the whole data period 1979-2018. The negative lag still holds when the length between each picking of data points are increased to >28 days and >55 days for the whole data period, which can be seen in Appendix C.2 Figure 107. A reconstruction of Figure 49 is made for the SH, where the results are plotted for a -2 day lag. Illustrated by Figure 68, the whole data period now show statistical significant areas over the Antarctic plateau, as well as in the South-Pacific and South-Indian oceans. The results remain

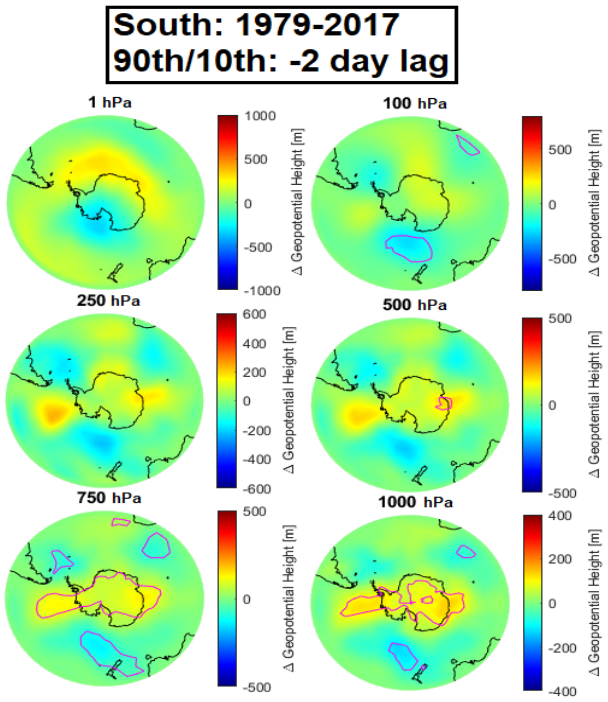

Figure 68: ΔGeo-Height[m] = high(V_xB_y) - low(V_xB_y) is plotted with the criteria of choosing all datapoints happening 2 days before the data points in the >90th percentile for the high bin and <10th percentile for the low bin. The results are shown for the time period 1979-2017 in the SH. A significant positive anomaly is seen at the 1000 hp level covering the Antarctic plateau, with minor negative anomalies in the South-Pacific and South-Indian oceans. Monte Carlo simulations and FDR are only applied to the 1000 hPa level. Other levels have significance calculated by students t-test combined with FDR.

significant after the Monte Carlo method combined with FDR is applied to the 1000 hPa level. For the Antarctic plateau, the same analysis provided by Burns et al. (2008) yields a positive lag for the response. They argue that a slightly negative lag could be physically realistic if the pressure response is nonlinear, or reaches a saturation level where the effect reverses with a further increased forcing. Assuming that a negative lag is a feature of the Mansurov effect, Figure 68 provides evidence for a statistical significant correlation for the whole period from 1979 to 2018. As the action of the mechanism is not concluded upon, a non-linear or saturated response could be feasible in explaining the consistency and significance observed for a -2 day lag.

6.2.5 Potential aliasing effects/The 27 day cycle

Another suggestion explaining the -2 day lag is the aliasing effect of a forcing slightly out of phase with the periodicity of the B_y-component. On average, V_xB_y has a periodicity closely following the rotational period of the Sun as view from Earth, which is approximately 27 days. The orbit of the Moon and the combined gravitational pull of the Moon and the Sun has a periodicity of 27.2 days. To determine if the correlation observed as the Mansurov effect in 1998-2002 are aliased with the gravitational pull by the moon, the following criteria need to be valid:

1) A significant correlation, with opposite signs, between the moon's orbit and the surface pressure

2) The impact from the moon should be observable for the whole time period 1979-2017

3) If the mechanism behind the moons surface pressure impact is known, it must be evident that the B_y data series is distributed in a way that favours this mechanism

As the tidal forcing from the moon occurs on a global scale, it is not readily evident how it will impact the polar surface specifically. The tidal waves in both the sea and atmosphere, and their associated feedback mechanism, forms a complex non-linear system. Guoqing (2007) finds a close relationship between the atmospheric circulation and the lunar cycle, with a 27.3 day and 13.6 day oscillating feature. The declination during the lunar orbit is ascribed as the dominating feature producing such oscillation. A maximum tidal forcing occurring at 0° declination angle is correlated with an increase in global zonal wind speed. While when the maximum declination of Moon occurs global zonal wind speed decrease.

The dependency of maximum atmospheric influence for 0° declination is also supported by Malherbe et al. (2014). The SAM (southern annular mode) index is plotted against a Tidal SAM index, as illustrated by Figure 69. The Tidal SAM Index is calculated by linear combinations of variables of tidal potential associated with certain characteristics of the lunar cycle occurring through middle

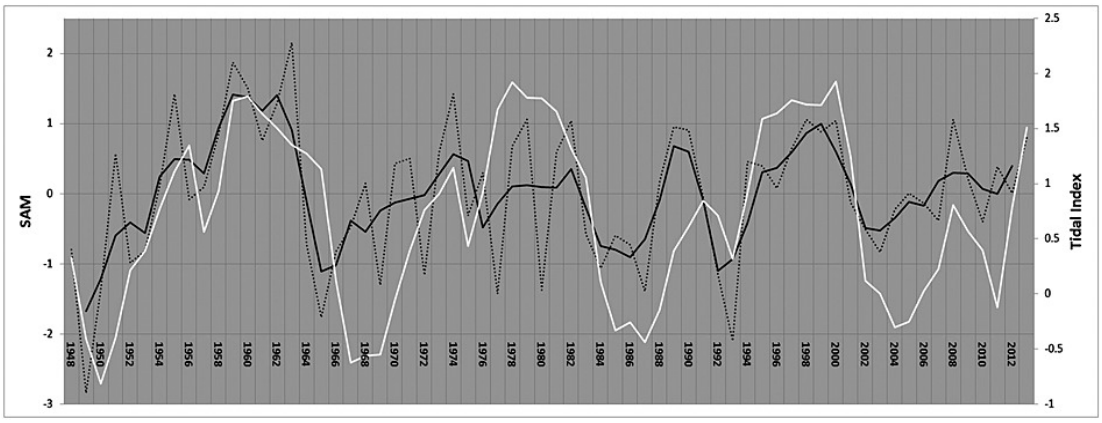

Figure 69: Observed detrended JFM SAM (broken black line) per year for 1948–2013 with 3 year moving average (solid black line). The Tidal SAM Index (solid white line) is also indicated. Full details about the indices and the analysis done can be obtained by Malherbe et al. (2014).

to late summer, shown to cause reactions in the SAM. For the period 1998-2002, highly correlating behaviour between the indices are seen. The analysis done in this thesis is not ideally set up for a measure of this forcing having a maximum at 0° declination. However, the significance found still supports the findings of some cyclic atmospheric response to the lunar declination. In particular, Malherbe et al. (2014) finds an increased significance in the period 1998-2002.

In this thesis we have examined two forcing components associated with the moon's orbit: the declination angle and the combined radial acceleration from both the moon and sun.

Figure 59 examines the relationship between the declination angle and the surface pressure at the poles for the whole time period. In general, this displays a significant but weak dependence in the south, but no significance in the north. The pressure dependence in the south is an order of magnitude smaller than the apparent pressure impact by the Mansurov effect for the period 1998-2002. Similar to the findings of Malherbe et al. (2014), Figure 57 shows that the apparent impact from the moon increases for the 1998-2002 period. Figure 58 demonstrates that the Δ declination angle distributed among the data points obtained for the B_y percentile criteria are in phase with the northern pressure response. However, a deviation from the in phase relationship is observed for the southern response. The highly correlating Tidal SAM Index for the period 1998-2002 incorporates multiple lunar parameters with the declination angle only being one of them. As we do not understand how the moon impacts the surface pressure at the poles, such a quantification of only one parameter will not tell the full story. However, from the limited evidence of the Mansurov effect

in the NH, together with the lack of a mechanism, it is therefore equally evident a response exits as a consequence of the change in lunar declination cycle. More investigation is necessary to understand the full aspects of how the moon cycle will impact the polar surface pressure.

In Figure 61 and 62, pressure variations in both hemispheres correlate with the total gravitational acceleration from the Moon and the Sun driver in a fairly consistent manner for both the period 1998-2002, and the whole data period 1979-2017. In particular, when the data is binned as only 1 high and low data point per 27 days, as illustrated by the left top panel in Figure 62, a rather odd feature occurs, where significance and the largest anomaly is found at day +13, which marks a minor positive peak for the gravitational acceleration driver. This feature is replicated in all the other plots for the total acceleration. It reveals that the relationship between the gravitational forcing and the pressure response is a more complex process than extreme values equating to the largest response. Nonetheless, the observed significance, consistency and in phase behaviour makes it evident that further investigations, with a more precise handling of the total gravitational acceleration, could potentially provide evidence of an aliasing mechanism being the origin of the Mansurov effect.

6.2.6 Differences between the NH and SH response

In the SH geopotential height response, a fairly consistent response is seen over the whole data period 1979-2017, as the -2 day lag produce significant anomalies. This consistency is not reproduced in the NH. In the NH, the continent-ocean contrast is high compared to the SH, which also induces higher atmospheric variability. This contrast favours the generation of Rossby waves able to penetrate into the stratosphere and disturb the polar vortex. The oceans are also fairly symmetrically placed around Antarctica, compared to the Arctic areas consisting of irregular ice caps, land masses and oceans. This difference in topology can effect both an aliasing mechanism, and the unknown mechanism of the V_xB_y driver. For a more stable climate and symmetrical topology, it can be argued that depending on the mechanism, the SH provides better conditions for a stable response throughout an extended time period. If true for the mechanism driving the correlations seen for the Mansurov effect, this could help explain the difference between the observed consistency in the SH, and the lack of it in the NH.

6.2.7 A notion on the geomagnetic centering

From the map plots, the geomagnetic centering for the averaged geopotential height at the 1000 hPa level seem unnecessary for the SH. When statistical significance is found, it is seen as an anomaly fully extending over the mainland of Antarctica, and not specifically located over the geomagnetic South pole. However, in the NH, the only significant map plot show significance close to the geomagnetic pole. The hypothesized mechanism is dependent on the chang-

ing current density J_z in fair weather regions, which is proposed to modulate cloud generation processes. The spatial occurrences of fair weather regions are variable in itself, and the modulation of cloud generation processes are not well understood. A study by Laken et al. (2012) found no robust evidence of solar/and or cosmic ray modulation of clouds through the GEC. Together, this induces large uncertainties in terms of spatial extent and location. As seen from our figures, the spatial distribution of the southern pressure response exhibit large uncertainties in terms of a specific fixed location. On the other hand, the northern response is obedient to a fixed location close to the geomagnetic pole. However, the significance in the NH is only found in the period 1998-2002, where other significant pressure anomalies are found in the higher atmosphere. As discussed in section 6.2.2, the anomaly in the higher atmosphere disappears when the period is divided into summer and winter, with the surface anomaly over Greenland persisting. Still, without a thoroughly investigation into all modes of atmospheric variability, the small time period of significant response emphasizes the possibility of an aliasing mechanism being responsible for the anomalies observed.

Together with the short time period of significance, the localization of the supposed pressure response in the NH remains a quest for further investigation. From the perspective of a definite aliasing mechanism occurring as a consequence of the total gravitational pull provided by the Moon and the Sun, the epicenter of the response occurring at the geomagnetic poles are unlikely. The method of forcing is also not determined in this case, but a mechanism acting through both the oceans and the atmosphere is likely (Guoqing 2007; Malherbe et al. 2014; Kohyama and Wallace 2014). This would imply a larger scale response, possibly notifiable on the scale of a hemisphere, and certainly not restricted to the geomagnetic poles.

7 Conclusion

Here a concise conclusion, giving the answers to the three key questions of the thesis, is presented.

1. Is there a statistical significant correlation between polar surface pressure and the geomagnetic activity index A_p and/or the IMF B_y?
For the Chemical-Dynamical coupling, statistical significant correlations are found in the NH in terms of significant geopotential height changes at the 1000 hPa level. The anomalies show consistency in the obtained surface responses through multiple different methods of sorting and with different distribution of years over the time period 1979-2017. Statistical significant correlations are also found in the SH in terms of significant geopotential height changes at the 1000 hPa level, but without the same consistency. Possible reasons for this asymmetry have been discussed.
For the Mansurov effect, statistical significant correlation is observed in the NH in terms of significant geopotential height changes at the 1000 hPa level, but for a very limited time period. Statistical significant correlations are observed in the SH for the whole time period 1979-2017 when a -2 day lag is added between the response and the hypothesised driver.

2. Are there deviations between the hypotheses and the findings (e.g. unphysical relationship, dependence on season, atmospheric state etc.)?
For the Chemical-Dynamical coupling, multiple theories still exists for the driving mechanism for a possible surface response. The analyses done have neither proved any of them right, nor disproved any, as limitations on such insight are imposed by the methods used. However, the first links in the mechanism are dependent on the winter season according to the hypothesis. A consistent pattern of anomalies are found for the time period 15.Dec-15.Jan over the whole data period for the NH. Significant surface anomalies are also found in the late winter when the whole data period is used. For the SH, some statistical significant correlations are found occurring sporadic throughout the winter time. For the combined analyses in the NH, a slight favouring of the eastern QBO phase is observed, with higher statistical significance acquired for different binning criteria. However, statistical significant results are also obtained in one analysis for the westerly QBO phase, as well as for the combined phases when SSW events are included on a daily scale. On this basis, no solid conclusive evidence exists from the analyses of an absolute dependence on a particular atmospheric state. The results in the SH are insubstantial, with no clear evidence. If the sporadic responses seen in the SH, and the responses seen in the period 15.Dec-15.Jan in the NH can be attributed a viable mechanism with EPP as the driver, this would suggest an effect occurring without the help of SSW events.
For the Mansurov effect, there is lack of explanations for the last link that leads to the observed pressure response. A major deviation is found, attributed to the -2 day lag observed over the whole data period 1979-2018, and also refer-

enced in the literature. Such a response is unphysical, perhaps occurring as a consequence of statistical errors when reanalysis data is used together with other sources of sampled data. It could also indicate a misunderstanding of the driver, and inherently the mechanism. Significant correlations are found in both hemispheres for the period 1998-2002, which is a solar maximum period. No other solar maximum is correlating at a significant level, therefore no solar maximum dependency is concluded. In the SH, a significant correlation is found for January over the whole data period. The signature of the response is inconsistent with the other correlations obtained, and no seasonal dependency is concluded on behalf of the response.

3. Are there any potential aliasing effects associated with the two mechanisms?

For the Chemical-Dynamical coupling, the responses in the NH for the period 15.Dec-15.Mar have the potential of being biased by an aliasing mechanism. As the distribution of data point show, a few years dominate the distribution, which would amplify any potential aliasing response appearing in one of them. This is true for the A2N analysis, where 20% of the data points are influenced by the 1991 volcanic eruption, which likely enhances the negative anomalies seen. Sparking for further investigation, is the fact that the other analyses produces a similar response in the same time period, when the effects of the post volcanic years are excluded from the analysis.

For the Mansurov effect, a probable suggestion for an aliasing mechanism are the effects of the lunar orbit, manifesting as pressure responses driven by atmospheric and oceanic tidal changes. Statistical significance is observed for different lunar positions related to declination angle in the same period producing the highest significance for the Mansurov effect. Significance is also observed for differences in total gravitational acceleration originating from the Moon and the Sun. With closely matching periodicity's, only a part of the data points being biased by an in-phase relationship between the moon driver and the B_y index could yield erroneous conclusions between the relationship of the IMF and surface polar pressure. Therefore, the Moon remains a viable target for further investigations.

8 Future work

For the Chemical-Dynamical coupling, further investigation into the planetary wave activity dependence of a response is important. Asymmetry between the NH and SH is observed, where the initial NO_x down welling indicates better condition for a response in the SH. This is not observed, possibly suggesting a low altitude atmospheric response dependent on disturbed polar vortex condition, which is favoured in the NH. Investigations determining the mechanism involved in the wave-mean flow interactions between the heating originating from the ozone depletion and the atmospheric dynamics are of great importance for advancement in the research area. Different criteria for the period 15.Dec-15.Jan in the NH should also be investigated further. Here, a proposal is a more specific sorting in terms of solar flux, pre-volcanic conditions and SSW events through use of multiple reanalysis data set. All years contributing to the anomaly seen in this period needs to be evaluated on the basis of all known external forcing and internal atmospheric variability for further knowledge about the origin. In the SH, a study on the two occurrences of SSW in regards to EPP related effects could help to determine the importance of disturbed conditions for a surface response to occur.

For the Mansurov effect, a thoroughly investigation dealing with the combined acceleration of the Moon and the Sun is needed. Firstly, the parameters yielding the most extreme forcing needs to be determined. As our analyses show, a minor peak in the gravitational acceleration at day ± 13 show the largest amplitudes and significance for the pressure, indicating that the extreme values in the acceleration is not the full story. Secondly, with the correct parameters, the proof of an aliasing mechanism is a straight forward process. Further investigations through multiple reanalysis data set could also reveal if the -2 day lag in the southern pressure is just a statistical anomaly or a consistent reoccurring feature. Investigations and measurements of the current density J_z regarding atmospheric responses are also highly important for determining a viable mechanism of the Mansurov effect. This would significantly increase the certainty on behalf of a solar wind driven response, or an aliasing mechanism.

9 Dictionary

Definitions according to *Wikipedia*:

- **Adiabatic cooling**: The process of reducing heat through a change in air pressure caused by volume expansion.
- **Blackbody**: An idealized physical body that absorbs all incident electromagnetic radiation, regardless of frequency or angle of incidence. (It does not only absorb radiation, but can also emit radiation). The radiation emitted by a blackbody is emitted according to Planck's law, meaning that it has a spectrum that is determined by the temperature alone, not by the body's shape or composition.
- **Climatology**: Weather conditions averaged over a period of time.
- **Conjugate geomagnetic points**: Two points on Earth are geomagnetically conjugate if they are on opposite ends of the same field line.
- **Easterly wind**: Wind coming from east.
- **Eddy**: The swirling of a fluid and the reverse current created when the fluid is in a turbulent flow regime.
- **Equilibrium**: The condition of a system in which all competing influences are balanced.
- **Equipotential**: Refers to a region in space where every point in it is at the same potential (e.g. in terms of field strength).
- **Geoeffective**: Capable of causing a geomagnetic disturbance
- **Heliosphere**: The vast, bubble-like region of space which surrounds and is created by the Sun. In plasma physics terms, this is the cavity formed by the Sun in the surrounding interstellar medium.
- **Interstellar medium**: The matter and radiation that exists in the space between the star systems in a galaxy.
- **Opacity**: Describes the absorption and scattering of radiation in a medium. Higher opacity accounts for more absorption and scattering in the medium.
- **Perturbation**: A small change in a physical system.
- **Plasma**: A state of matter happening in a gas if the temperature is so high that electrons can not be bound to the atoms nucleus. Plasma is then defined as a gas consisting of ions and electrons, contrary to a normal gas consisting of neutral atoms.

- **Proxy**: An indirect association with a physical phenomenon. The phenomenon itself is usually difficult to quantify and/or measure.
- **Reciprocal**: A mutual relationship/connection between two or more components. A relationship/connection going both ways, where each of the participants affects each other.
- **Stochastic**: A randomly determined process.
- **Westerly wind**: Wind coming from west.

10 Abbreviation

AAO	Antarctic Oscillation
AO	Arctic Oscillation
CLIMREF-spec	Specific Climatology Frame of Reference
CIR	Corotating Interaction Region
CME	Coronal Mass Ejection
EF	External Forcing
EPP	Energetic Particle Precipitation
ECMWF	European Center for Medium-range Weather Forecast
EMIC	Electromagnetic Ion Cyclotron (waves)
ERA	European center for medium-range weather forecast Re-Analysis
FDR	False Detection Rate
ENSO	El Niño-Southern Oscillation
GCR	Galactic Cosmic Ray
GEC	Global Electric Circuit
GSM	Geocentric Solar Magnetic (coordinate system)
HCS	Heliospheric Current Sheet
HEPPA	High Energy Particle Precipitation in the Atmosphere
HSSWS	High Speed Solar Wind Streams
IMF	Interplanetary Magnetic Field
IPCC	The International Panel on Climate Change
IR	Infrared Radiation
LOSU	Level Of Scientific Understanding
MLT	Mesosphere-Lower-Thermosphere
NAM	Northern Annular Mode
NAO	North Atlantic Oscillation
NH	Northern Hemisphere
NOAA	National Oceanic and Atmospheric Administration
OMNI	Operating Missions as a Node on the Internet
QBO	Quasi-Biennial Oscillation
SH	Southern Hemisphere

SOURCE SIM	Solar Radiation and Climate Experiment Spectral Irradiance Monitor
SPE	Solar Proton Event
SSI	Spectral Solar Irradiance
SSW	Sudden Stratospheric Warming
TSI	Total Solar Irradiance
ULF	Ultra Low Frequency
UV	Ultra Violet
VLF	Very Low Frequency
WPI	Wave Particle Interaction

11 References

[1] Akasofu, S.I. (1977), Magnetospheric Substorms: Introduction. In: Physics of Magnetospheric Substorms. Astrophysics and Space Science Library (A Series of Books on the Recent Developments of Space Science and of General Geophysics and Astrophysics Published in Connection with the Journal Space Science Reviews), vol 47. *Springer*, Dordrecht

[2] Alfvén, H. (1942), Existence of Electromagnetic-Hydrodynamic Waves. *Nature*. 150, 405–406

[3] Allen, C.W. (1944), Relation between Magnetic Storms and Solar Activity. *Month.Not.Roy.Astron.Soc.* 104(1):13-21

[4] Allen, C.W. (1964), M-regions. *Planet. Space Sci.* 12(5):487-494

[5] Alves, M.V., Echer, E. & Gonzalez, W.D. (2006), Geoeffectiveness of corotating interaction regions as measured by Dst index, *J. Geophys. Res.*, 111, A07S05

[6] Ambaum, M.H., Hoskins, B.J. & Stephenson, D.B. (2001), Arctic Oscillation or North Atlantic Oscillation?. *J. Climate*, 14, 3495–3507

[7] Andersson, M.E., Verronen, P.T., Rodger, C.J., Clilverd, M.A. & Wang, S. (2014a), Longitudinal hotspots in the mesospheric OH variations due to energetic electron precipitation. *Atmospheric Chemistry and Physics*. 14. 1095-1105

[8] Andersson, M.E., Verronen, P.T., Rodger, C.J., Clilverd, M.A. & Seppälä, A. (2014b), Missing driver in the Sun–Earth connection from energetic electron precipitation impacts mesospheric ozone, *Nat. Commun.*, 5, 5197

[9] Antiochos, S.K., Mikić, Z., Titov, V. S., Lionello, R. & Linker, J. A. (2011), A Model for the Sources of the Slow Solar Wind. *The Astrophysical Journal*. 731 (2): 112

[10] Asikainen, T., & Ruopsa, M. (2016), Solar wind drivers of energetic electron precipitation, *J. Geophys. Res. Space Physics*. 121. 2209– 2225

[11] Asikainen, T., Salminen, A., Maliniemi, V. & Mursula, K. (2020). Influence of enhanced planetary wave activity on the polar vortex enhancement related to energetic electron precipitation. *Journal Geophysical Research: Atmospheres*. 125

[12] Babcock, H.W. (1961), The topology of the Sun's magnetic field and the 22-year cycle. *Astrophys. J.* 133. 572-587

[13] Baker, D.N., Mason, G.M. & Mazur, J.E. (2012), A small spacecraft mission with large accomplishments. *Eos*. 93, 325–32

[14] Baldwin, M.P. & Dunkerton, T. (2001), Stratospheric harbingers of anomalous weather regimes, *Science*, 294, 581–584

[15] Baldwin, M.P., Gray, L.J., Dunkerton, T.J., Hamilton,K., Haynes, P.H., Randel, W.J., Holton, J.R., Alexander, M.J., Hirota, I., Horinouchi, T. & Jones, D.B.A. (2001). The quasi-biennial oscillation. *Reviews of Geophysics*, 39(2), 179– 229

[16] Bartels, J. (1932), Terrestrial-magnetic activity and its relations to solar phenomena, Terr. Magn. *Atmos. Electr.*, 37(1), 1–52

[17] Bates, D.R. & Nicolet, M. (1950), Atmospheric hydrogen. *Publ. Astron. Soc. Pac.* 62, 106 –110

[18] Baumgaertner, A.J.G., Seppälä, A., Jöckel, P. & Clilverd, M.A. (2011), Geomagnetic activity related NOx enhancements and polar surface air temperature variability in a chemistry climate model: modulation of the NAM index, *Atmos. Chem. Phys.*, 11, 4521–4531

[19] Belov, A.V. (2017), Flares, ejections, proton events. *Geomagn. Aeron.* 57, 727–737

[20] Billings, D.E. & Roberts, W.O. (1964). The origin of M-region geomagnetic storms. *Astrophysica Norvegica*, 9

[21] Blanc, M. (1988), Magnetosphere-ionosphere coupling, *Computer Physics Communications*, Volume 49, Issue 1, 103-118

[22] Borovsky, J. (2016) Relativity and the Solar Wind: The Maxwell-Equation Origins of the Solar-Wind Motional Electric Field. *Journal of Electromagnetic Analysis and Applications*, 8, 133-151

[23] Borovsky, J.E. & Denton, M.H. (2009), Relativistic-electron dropouts and recovery: A superposed epoch study of the magnetosphere and the solar wind, *J. Geophys. Res.*, 114, A02201

[24] Brasseur, G. & Jacob, D. (2017). Chemical Processes in the Atmosphere. In Modeling of Atmospheric Chemistry. *Cambridge University Press*, 54-83

[25] Brewer, A.W. (1949), Evidence for a world circulation provided by the measurements of helium and water vapour distribution in the stratosphere. *Quart. J. Roy. Meteor. Soc.*, 75, 351–363

[26] Burns, G.B., Tinsley, B.A., Frank-Kamenetsky, A.V. & Bering, E.A. (2007), Interplanetary magnetic field and atmospheric electric circuit influences on ground-level pressure at Vostok, *J. Geophys. Res.*, 112, D04103

[27] Burns, G.B., Tinsley, B.A., French, W.J.R., Troshichev, O.A. & Frank-Kamenetsky, A.V. (2008), Atmospheric circuit influences on ground-level pressure in the Antarctic and Arctic, *J. Geophys. Res.*, 113, D15112

[28] Butchart, N. (2014), The Brewer-Dobson circulation. *Rev. Geophys.* 52, 157–184

[29] Butler, A.H., Sjoberg, J.P., Seidel, D.J. & Rosenlof, K. H. (2017), A sudden stratospheric warming compendium, *Earth Syst. Sci. Data*, 9, 63–76

[30] Carmen, J.N. (2002), 6 - Waves and Turbulence. *International Geophysics. Academic Press.* Volume 85, 125-154

[31] Case, N. (2014), Solar Wind-Magnetosphere Interactions: A Statistical Analysis of Spacecraft Measurements

[32] Chaston, C.C., Bonnell, J.W., Wygant, J. R., Reeves, G.D., Baker, D.N., Melrose, D.B. & Cairns, I.H. (2017), Radial transport of radiation belt electrons in kinetic field-line resonances, *Geophys. Res.* Lett., 44, 8140–8148

[33] Cliver, E.W. & Dietrich W.F. (2013), The 1859 space weather event revisited: limits of extreme activity. *J. Space WeatherSpace Clim.*,3, A31

[34] Cohen, N.Y., Gerber, E.P. & Bühler, O. (2014), What Drives the Brewer–Dobson Circulation?. *J. Atmos. Sci.*, 71, 3837–3855

[35] Cowley, S.W.H. (2000). Magnetosphere-ionosphere interactions: A tutorial review. In S.-I. Ohtani, R. Fujii, M. Hesse, & R. L. Lysak (Eds.), Magnetospheric current systems, *Geophysical Monograph Series.* American Geophysical Union. 118, 91–106

[36] Cramer, E.S., Briggs, M.S., Liu, N., Mailyan, B., Dwyer, J.R. & Rassoul, H.K. (2017), The impact on the ozone layer from NOx produced by terrestrial gamma ray flashes, *Geophys. Res. Lett.*, 44, 5240– 5245

[37] Crutzen, P.J. (1970) The influence of nitrogen oxide on the atmospheric ozone content. *Q. J. R. Meteorol. Soc.*96, 320–327

[38] Davey, M.K., Brookshaw, A. & Ineson, S. (2014), The probability of the impact of ENSO on precipitation and near-surface temperature, *Climate Risk Management*, Volume 1, 5-24

[39] Dobson, G.M.B. (1956), Origin and distribution of the polyatomic molecules in the atmosphere. *Proc. Roy. Soc.* 236A, 187–193

[40] Duewer, W.H., Wuebbles, D.J., Ellsaesser, H.W. & Chang, J.S. (1977), NOx catalytic ozone destruction: Sensitivity to rate coefficients, *J. Geophys. Res.*, 82(6), 935– 942

[41] Dungey, J.W. (1961), Interplanetary magnetic fields and the auroral zones, *Phys. Rev. Lett.*, 6, 47–48

[42] Dungey, J.W. (1963), The structure of the exosphere or adventures in velocity space, *Geophysics*, The Earth's Environment, edited by C. De Witt, J. Hieblot, and L. Le Beau, 503

[43] Eguchi, N. & Kodera, K. (2007), Impact of the 2002, Southern Hemisphere, stratospheric warming on the tropical cirrus clouds and convective activity, *Geophys. Res. Lett.*, 34, L05819

[44] Espy, P.J., Jones, G.O.L., Swenson, G.R., Tang, J. & Taylor, M.J. (2004), Seasonal variations of the gravity wavemomentum flux in the Antarctic mesosphere and lower thermosphere, *J. Geophys. Res.*, 109, D23109

[45] Fairfield, D.H. & Cahill, L.G. (1966), Transition region magnetic field and polar magnetic disturbances, *J. Geophys. Res.*, 71, 155–169

[46] Feldman, W.C., Asbridge, J.R., Bame, S.J., Fenimore, E.E. & Gosling, J.T. (1981) , Origin of solar wind interstream flows: Near Equitorial coronal streamers, *J. Geophys. Res.*, 86, 5408

[47] Ford, E.A.K., Hibbins, R.E. & Jarvis, M.J. (2009), QBO effects on Antarctic mesospheric winds and polar vortex dynamics, *Geophys. Res. Lett.*, 36, L20801

[48] Frank-Kamenetsky, A.V., Troshichev, O.A., Burns, G.B. & Papitashvili, V.O. (2001), Variations of the atmospheric electric field in the near-pole region related to the interplanetary magnetic field, *J. Geophys. Res.*, 106, 179–190

[49] Freeman, M.P. & Lam, M.M. (2019), Regional, seasonal, and inter-annual variations of Antarctic and sub-Antarctic temperature anomalies related to the Mansurov effect. *Environmental Research Communications*. vol. 1, 11, 111007

[50] Fritts, D.C. & Alexander, M.J. (2003), Gravity wave dynamics and effects in the middle atmosphere, *Rev. Geophys*. Volume 41, 1944-9208

[51] Fumio, M. (2016), The solar activity by wavelet-based multifractal analysis, *NRIAG Journal of Astronomy and Geophysics*, Volume 5, Issue 2, 301-305

[52] Funke, B., López-Puertas, M., Holt, L., Randall, C.E., Stiller, G.P. & Clarmann, T.von. (2014), Hemispheric distributions and interannual variability of NOy produced by energetic particle precipitation in 2002–2012, *J. Geophys. Res. Atmos.*, 119, 13,565–582

[53] Graf, H.-F., Kirchner, I. & Perlwitz, J. (1998), Changing lower stratospheric circulation: The role of ozone and greenhouse gases, *J. Geophys. Res.-Atmos.*, 103, 11251–11261

[54] Gray, L.J., Anstey, J.A., Kawatani, Y., Lu, H., Osprey, S. & Schenzinger, V. (2018), Surface impacts of the quasi biennial oscillation. *Atmospheric Chemistry and Physics*, 18(11), 8227–8247

[55] Gray, L.J., et al. (2010), Solar influences on climate, *Rev. Geophys.*, 48, RG4001

[56] Guoqing, L. (2007), 27.3-day and 13.6-day atmospheric tide and lunar forcing on atmospheric circulation. *Adv. Atmos. Sci.* 22. 359–374

[57] Haigh, J.D., Blackburn, M. & Day, R. (2005), The response of tropospheric circulation to perturbations in lower-stratospheric temperature. *J. Clim.* 18, 3672–3685

[58] Harder, J.W., Fontenla, J.M., Pilewskie, P., Richard, E.C. & Woods, T.N. (2009), Trends in solar spectral irradiance variability in the visible and infrared. *Geophys. Res. Lett.*, 36, L07801

[59] Hardiman, S.C. & Haynes, P.H. (2008), Dynamical sensitivity of the stratospheric circulation and downward influence of upper level perturbations. *J. Geophys. Res.* 113, D23103

[60] Harrison, R.G. (2004). The Global Atmospheric Electrical Circuit and Climate. *Surveys in Geophysics*, 25, 441-484

[61] Harrison, R.G. (2011), Fair weather atmospheric electricity, *J. Phys.*: Conf. Ser.301 012001

[62] Hartley, D.E., Villarin, J.T., Black, R.X. & Davis, C.A. (1998), A new perspective on the dynamical link between the stratosphere and troposphere. *Nature.* 391, 471–474

[63] Hauglustaine, D., Emmons, L., Newchurch, M., Brasseur, G., Takao, T., Matsubara, K., Johnson, J., Ridley, B. & Stith, J. (2001), On the Role of Lightning NOx in the Formation of Tropospheric Ozone Plumes: A Global Model Perspective. *Journal of Atmospheric Chemistry.* 38 (3). 277–294

[64] Haynes, P.H. (2005), Stratospheric dynamics. *Annu. Rev. Fluid Mech.* 37, 263–293

[65] Haynes, P.H., Marks, C.J., McIntyre, M.E., Shepherd, T.G. & Shine, K.P. (1991), On the "downward control" of extratropical diabatic circulations by eddy-induced mean zonal forces. *J. Atmos. Sci.*, 48, 651–678

[66] Heppner, J.P. (1972), Polar-cap electric field distributions related to the interplanetary magnetic field direction, *J. Geophys. Res.* 77, 4877–4887

[67] Hiraga, R. & Omura, Y. (2020), Acceleration mechanism of radiation belt electrons through interaction with multi-subpacket chorus waves. *Earth Planets Space.* 72, 21

[68] Hoeksema, J.T., Wilcox, J.M. & Scherrer, P.H. (1983), The structure of the heliospheric current sheet: 1978–1982, *J. Geophys. Res.*, 88(A12), 9910–9918

[69] Holt, L.A., Randall, C.E., Peck, E.D., Marsh, D.R., Smith, A.K. & Harvey, V.L. (2013), The influence of major sudden stratospheric warming and elevated stratopause events on the effects of energetic particle precipitation in WACCM, *J. Geophys. Res. Atmos.*, 118, 11, 636–646

[70] Holton, J.R. (1983), The influence of gravity wave breaking on the general circulation of the middle atmosphere, *J. Atmos. Sci.*, 40, 2497–2507

[71] Holton, J.R. & Lindzen, R.S. (1972), An updated theory for the quasi-biennial cycle of the tropical stratosphere, *J. Atmos. Sci.*, 29, 1076 – 1080

[72] Holton, J.R., Haynes, P.H., McIntyre, M.E., Douglass, A.R., Rood, R.B. & Pfister, L. (1995), Stratosphere–troposphere exchange. *Rev. Geophys.*, 33, 403–439

[73] Holton, J.R. & Alexander, M.J. (2013), The Role of Waves in the Transport Circulation of the Middle Atmosphere. *Geophysical Monograph Series*, 123. 21-35

[74] Hu, J.G., Ren, R.C. & Xu, H.M. (2014), Occurrence of winter stratospheric sudden warming events and the seasonal timing of spring stratospheric final warming. *J. Atmos. Sci.*, 71, 2319–2334

[75] Hudson, M.K. et al. (2000), Increase in relativistic electron flux in the inner magnetosphere: ULF wave mode structure. *Adv. Space Res.* 25, 2327–2337

[76] Hudson, M.K., Baker, D.N., Goldstein, J., Kress, B.T., Paral, J., Toffoletto, F.R. & Wiltberger, M (2014), Simulated magnetopause losses and Van Allen Probe flux dropouts, *Geophys. Res. Lett.*, 41, 1113–1118

[77] Hurrell, J.W. (1995), Decadal Trends in the North Atlantic Oscillation: Regional Temperatures and Precipitation. *Science*. 269 (5224). 676–679

[78] Hurrell, J.W., Kushnir, Y., Ottersen, G. & Visbeck, M. (2013), An Overview of the North Atlantic Oscillation. In The North Atlantic Oscillation: Climatic Significance and Environmental Impact (eds J.W. Hurrell, Y. Kushnir, G. Ottersen and M. Visbeck)

[79] Ivy, D.J., Solomon, S. & Rieder, H.E. 2016: Radiative and Dynamical Influences on Polar Stratospheric Temperature Trends. *J. Climate*, 29, 4927–4938

[80] Jing, P., Banerjee, S. & Barrera, M. (2019), Impact of Rossby wave breaking on ozone variation in the upper troposphere and lower stratosphere, 1985–2015, *Atmospheric Environment*, 117122

[81] Johnston, H.S. (1971), Reduction of stratospheric ozone by nitrogen oxide catalysts from supersonic transport exhaust. *Science*. 173, 517 –522.

[82] Jovanović, G., Reljin, I. & Reljin, B. (2008), The influence of Arctic and North Atlantic Oscillation on precipitation regime in Serbia. IOP Conference Series: Earth and Environmental Science. 4. 012025

[83] Kabin, K., Rankin, R., Marchand, R., Gombosi, T.I., Clauer, C.R., Ridley, A.J., Papitashvili, V.O. & DeZeeuwk, D.L. (2003), Dynamic response of Earth's magnetosphere to By reversals, *J. Geophys. Res.*, 108, 1–13

[84] Kessel, R.L., Chen, S.-H., Green, J.L., Fung, S.F., Boarden, S.A., Tan, L.C., Eastman, T.E., Craven, J.D. & Frank, L.A. (1996), Evidence of high latitude reconnecting during northward IMF: Hawkeye observations, *Geophys. Res. Lett.*, 23, 583

[85] Kidston, J., Scaife, A., Hardiman, S., et al. (2015), Stratospheric influence on tropospheric jet streams, storm tracks and surface weather. *Nature Geosci.* 8, 433–440

[86] Kleinknecht, N.H., Espy, P.J. & Hibbins, R.E. (2014), The climatology of zonal wave numbers 1 and 2 planetary wave structure in the MLT using a chain of Northern Hemisphere SuperDARN radars, *J.Geophys. Res. Atmos.*, 119, 1292–1307

[87] Kohyama, T. & Wallace, J.M. (2014), Lunar gravitational atmospheric tide, surface to 50 km in a global, gridded data set, *Geophys. Res. Lett.* 41. 8660–8665

[88] Krieger, A.S., Timothy, A.F. & Roelof, E.C. (1973). A coronal hole and its identification as the source of a high velocity solar wind stream. *Solar Physics.*

[89] Laken, B.A., Pallé, E., Čalogović, J. & Dunne, E.M. (2012), A cosmic ray-climate link and cloud observations, *J. Space Weather Space Clim.* 2. A18

[90] Lam, M.M., Chisham, G. & Freeman, M. (2013). The interplanetary magnetic field influences mid-latitude surface atmospheric pressure. *Environmental Research Letters.* 8.

[91] Lam, M.M., Chisham, G. & Freeman, M.P. (2014), Solar-wind-driven geopotential height anomalies originate in the Antarctic lower troposphere. *Geophys. Res. Lett.* 41

[92] Lam, M.M. & Tinsley, B.A. (2016). Solar wind-atmospheric electricity-cloud microphysics connections to weather and climate. *Journal of Atmospheric and Solar-Terrestrial Physics*, ISSN: 1364-6826, Vol: 149, 277-290

[93] Lam, M.M., Freeman, M. & Chisham, G. (2018). IMF-driven change to the Antarctic tropospheric temperature due to the global atmospheric electric circuit. *Journal of Atmospheric and Solar-Terrestrial Physics.* 180, 148-152

[94] Langematz, U., Kunze, M., Krüger, K., Labitzke, K. & Roff, G. L. (2003), Thermal and dynamical changes of the stratosphere since 1979 and their link to ozone and CO2 changes, *J. Geophys. Res.-Atmos.*, 108, 4027

[95] Lary, D.J. (1997), Catalytic destruction of stratospheric ozone, *J. Geophys. Res.*, 102(D17), 21515–21526

[96] Lean, J.L. & DeLand, M.T. (2012), How Does the Sun's Spectrum Vary?. *J. Climate*, 25, 2555–2560,

[97] Leverington, D. (2003), Babylon to Voyager and beyond: a history of planetary astronomy. *Cambridge University Press.* 6–7

[98] Li, X. & Temerin, M. (2001). The Electron Radiation Belt. *Space Science Reviews.* 95. 569-580

[99] Li, Y. & Lau, N. (2013), Influences of ENSO on Stratospheric Variability, and the Descent of Stratospheric Perturbations into the Lower Troposphere. *J. Climate*, 26, 4725–4748

[100] Lin, C.-H., Gallagher, P. & Raftery, C. (2010), Investigating the driving mechanisms of coronal mass ejections.

[101] Lindblad, B.A. (1990). Coronal sources of high-speed plasma streams in the solar wind during the declining phase of solar cycle 20. *Astrophys Space Sci* 170, 55–61

[102] Lindzen, R.S. & Holton, J.R. (1968), A theory of the quasi-biennial oscillation, *J. Atmos. Sci.*, 25, 1095 – 1107

[103] Lingri, D., Mavromichalaki, H., Belov, A., Eroshenko, E., Yanke, V., Abunin, A. & Abunina, M. (2016). Forbush Decreases during the Deep Min and Mini Max of Solar Cycle 24

[104] Loewe, C.A. & Prölss, G.W. (1997), Classification and mean behavior of magnetic storms, *J. Geophys. Res.*, 102(A7), 14209– 14213

[105] Lu, H., Clilverd, M.A., Seppälä, A. & Hood, L.L. (2008), Geomagnetic perturbations on stratospheric circulation in late winter and spring, *J. Geophys. Res.* 113(D12), D16106

[106] MacAlester, M.H. & Murtagh, W. (2014), Extreme Space Weather Impact: An Emergency Management Perspective, *Space Weather.* 12, 530– 537

[107] Malherbe, J., Engelbrecht, F.A. & Landman, W.A. (2014), Response of the Southern Annular Mode to tidal forcing and the bidecadal rainfall cycle over subtropical southern Africa, *J. Geophys. Res. Atmos.* 119. 2032– 2049

[108] Maliniemi, V., Asikainen, T., Mursula, K. & Seppälä, A. (2013), QBO-dependent relation between electron precipitation and wintertime surface temperature, J. Geophys. Res. Atmos., 118, 6302– 6310

[109] Maliniemi, V., Asikainen, T. & Mursula, K. (2016), Effect of geomagnetic activity on the northern annular mode: QBO dependence and the Holton-Tan relationship, *J. Geophys. Res. Atmos.* 121

[110] Mansurov, S.M. (1969), New evidence of a relationship between magnetic fields in space and on earth, Geomagn. Aeron., Engl. Transl., 9, 622

[111] Mansurov, S.M., Mansurova, L.G., Mansurov, G.S., Mikhnevich, V.V. & Visotsky, A.M. (1974), North-south asymmetry of geomagnetic and tropospheric events. *Journal of Atmospheric and Terrestrial Physics.* 36(11), 1957-1962

[112] Marchenko, S.V., DeLand, M.T. & Lean, J.L. (2016), Solar spectral irradiance variability in cycle 24: observations and models, *J. Space Weather Space Clim.* 6 A40

[113] Marshall, A.G. & Scaife, A.A. (2009), Impact of the QBO on surface winter climate, *J. Geophys. Res.* 114, D18110

[114] Matsuno, T. (1971), A Dynamical Model of the Stratospheric Sudden Warming. *J. Atmos. Sci.* 28, 1479–1494

[115] Mertens, C., Wilson, J., Blattnig, S., Kress, B., Norbury, J., Wiltberger, M., Solomon, S. & Tobiska, W.K. (2008), Influence of Space Weather on Aircraft Ionizing Radiation Exposure. 46th AIAA Aerospace Sciences Meeting and Exhibit.

[116] Milan, S.E., Provan, G. & Hubert, B. (2007), Magnetic flux transport in the Dungey cycle: A survey of dayside and nightside reconnection rates, *J. Geophys. Res.*, 112, A01209

[117] Millan, R. et al. (2007), Observation of relativistic electron precipitation during a rapid decrease of trapped relativistic electron flux. *Geophys. Res. Lett.* 34, L10101

[118] Misios, S., Mitchell, D.M., Gray, L.J., Tourpali, K., Matthes, K., Hood, L., Schmidt, H., Chiodo, G., Thiéblemont, R., Rozanov, E. & Krivolutsky, A. (2016), Solar signals in CMIP-5 simulations: effects of atmosphere–ocean coupling. *Q.J.R. Meteorol. Soc.* 142: 928-941

[119] Norton, W.A. (2003), Sensitivity of Northern Hemisphere surface climate to simulation of the stratospheric polar vortex. *Geophys. Res. Lett.* 30, 1627

[120] Ormes, J.F. (2018), Cosmic rays and climate, *Advances in Space Research*, Volume 62, Issue 10, 2880-2891

[121] Osprey, S.M. et al. (2010), The climatology of the middle atmosphere in a vertically extended version of the Met Office's climate model. Part II: variability. *J. Atmos. Sci.* 67, 3637–3651

[122] Ossó, A., Sola, Y., Rosenlof, K., Hassler, B., Bech, J. & Lorente, J. (2015), How Robust Are Trends in the Brewer–Dobson Circulation Derived from Observed Stratospheric Temperatures?. *J. Climate*, 28, 3024–3040

[123] O'Callaghan, A., Joshi, M., Stevens, D. & Mitchell, D. (2014), The effects of different sudden stratospheric warm-ing type on the ocean, *Geophys. Res.Lett.*,41

[124] Parker, D., Wilson, H., Jones, P., Christy, J. & Folland, C. (1996). The Impact of Mount Pinatubo on World-Wide Temperatures. *International Journal of Climatology*. 16. 487-497

[125] Parker, E.N. (1965), Dynamical Theory of the Solar Wind, *Space Science Reviews*, Volume 4, Issue 5-6, 666-708

[126] Pavia, E.G. (2017), Changes in the ENSO–rainfall relationship in the Mediterranean California border region. *Atmos. Sci. Lett.*, 18: 183-186

[127] Pettigrew, E.D., Shepherd, S.G. & Ruohoniemi, J.M. (2010), Climatological patterns of high-latitude convection in the Northern and Southern hemispheres: Dipole tilt dependencies and interhemispheric comparisons, *J. Geophys. Res.*, 115, A07305

[128] Portmann, R., Daniel, J. & Ravishankara, A. (2012). Stratospheric ozone depletion due to nitrous oxide: Influences of other gases. *Philosophical Transactions: Biological Sciences*, 367(1593), 1256-1264

[129] Potgieter, M.S. (2008), Solar cycle variations and cosmic rays, *Journal of Atmospheric and Solar-Terrestrial Physics*, Volume 70, Issues 2–4, 207-218

[130] Randall, C.E. et al. (2005), Stratospheric effects of energetic particle precipitation in 2003–2004, *Geophys. Res. Lett.*,32, L05802

[131] Randall, C.E., Harvey, V.L., Holt, L.A., Marsh, D.R., Kinnison, D., Funke, B. & Bernath, P.F. (2015), Simulation of energetic particle precipitation effects during the 2003–2004 Arctic winter, *J. Geophys.Res. Space Physics*, 120, 5035–5048

[132] Randall, C.E., Harvey, V.L., Siskind, D.E., France, J., Bernath, P.F., Boone, C.D. & Walker, K.A. (2009), NO_x descent in the Arctic middle atmosphere in early 2009. *Geophys, Res, Lett.* 36:18811

[133] Randall, C.E., Lumpe, J., Bevilacqua, R., Hoppel, K., Shettle, E., Rusch, D., Gordley, L., Kreher, K., Pfeilsticker, K., Boesch, H., Toon, G., Goutail, F. & Pommereau, J.-P. (2002), Validation of POAM III NO2 measurements, *J. Geophys. Res.* 107(D20), 4432

[134] Rasmusson, E.M. & Carpenter, T. H. (1982), Variations in tropical sea surface temperature and surface wind fields associated with the Southern Oscillation/El Niño. *Mon. Wea. Rev.*,110, 354–384

[135] Reeves, G.D., McAdams, K.L., Friedel, R.H.W. & O'Brien, T.P. (2003), Acceleration and loss of relativistic electrons during geomagnetic storms, *Geophys. Res. Lett.*, 30(10), 1529

[136] Reeves, G., Spence, H., Henderson, M., Morley, S., Friedel, R., Funsten, H., Baker, D., Kanekal, S., Blake, J., Fennell, J., Claudepierre, S., Thorne, R., Turner, D., Kletzing, C., Kurth, W., Larsen, B. & Niehof, J. (2013), Electron Acceleration in the Heart of the Van Allen Radiation Belts. *Science*, Vol.341(6149), 991-994

[137] Rhines, P.B. (2002), ROSSBY WAVES. *Encyclopedia of Atmospheric Sciences*, School of Oceanography, Holton, Pyle and Curry Eds. Academic Press, London.

[138] Richardson, I.G (2013), What in the Solar Wind Does the Earth React to?. AIP Conf. Proc.. 1539. 370-375

[139] Richardson, I.G. (2018) Solar wind stream interaction regions throughout the heliosphere. *Living Rev Sol Phys.* 15, 1

[140] Richardson, I.G., Cliver, E.W. & Cane, H.V. (2000), Sources of geomagnetic activity over the solar cycle: Relative importance of coronal mass ejections, high-speed streams, and slow solar wind, *J. Geophys. Res.*, 105(A8), 18203– 18213

[141] Richardson, I.G. & Cane, H.V. (2012), Near-earth solar wind flows and related geomagnetic activity during more than four solar cycles (1963–2011), *J. Space Weather Space Clim.* 2 A02

[142] Robock, A. & Mao. J. (1995), The Volcanic Signal in Surface Temperature Observations. *J. Climate*, 8, 1086–1103

[143] Rodas, C. & Pulido, M. (2017), A climatology of Rossby wave generation in the middle atmosphere of the Southern hemisphere from MERRA reanalysis, *J. Geophys. Res. Atmos.*, 122, 8982– 8997

[144] Rosenlof, H.K. (1995), Seasonal cycle of the residual mean meridional circulation in the stratosphere. *J. Geophys. Res.*, 100, 5173–5191

[145] Rossby, C.-G. (1939), "Relation between variations in the intensity of the zonal circulation of the atmosphere and the displacements of the semi-permanent centers of action". *Journal of Marine Research.* 2: 38–55

[146] Rozanov, E., Calisto, M., Egorova, T., Peter, T. & Schmutz, W. (2012), Influence of the precipitating energetic particles on atmospheric chemistry and climate. *Surv. Geophys.* 33, 483–501

[147] Rozanov, E., Callis, L., Schlesinger, M., Yang, F., Andronova, N. & Zubov, V. (2005), Atmospheric response to NOy source due to energetic electron precipitation, *Geophys. Res. Lett.*, 32, L14811

[148] Russell, C.T. & Jian, Lan. (2008). Flows and obstacles in the solar wind. *Advances in Space Research.* 41. 1177-1187

[149] Salby, M.L. & Callaghan, P.F. (2002),: Interannual Changes of the Stratospheric Circulation: Relationship to Ozone and Tropospheric Structure. *J. Climate*, 15, 3673–3685

[150] Salminen, A., Asikainen, T., Maliniemi, V. & Mursula, K. (2019). Effect of energetic electron precipitation on the northern polar vortex: Explaining the QBO modulation via control of meridional circulation. *Journal of Geophysical Research: Atmospheres*, 124, 5807– 5821

[151] Saxena, V.K., Shaocai, Y. & Anderson, J. (1997), Impact of stratospheric volcanic aerosols on climate: Evidence for aerosol shortwave and longwave forcing in the Southeastern U.S., *Atmospheric Environment*, Volume 31, Issue 24, 4211-4221

[152] Scaife, A.A. & Knight, J.R. (2008), Ensemble simulations of the cold European winter of 2005–2006. *Q. J. R. Meteorol. Soc.* 134, 1647–1659

[153] Scaife, A.A., Knight, J.R., Vallis, G.K. & Folland, C.K. (2005), A stratospheric influence on the winter NAO and North Atlantic surface climate. *Geophys. Res. Lett.* 32, 1–5

[154] Seppala, A., Clilverd, M.A. & Rodger, C.J. (2007) NOx enhancements in the middle atmosphere during 2003–2004 polar winter: Relative significance of solar proton events and the aurora as a source. *J Geophys Res.* 112:D23303

[155] Seppala, A., Matthes, K., Randall, C.E. & Mironova, I.A. (2014) What is the solar influence on climate? Overview of activities during CAWSES-II. *Progress Earth Planet Science.* 1-24

[156] Seppälä, A., Lu, H., Clilverd, M.A. & Rodger, C.J. (2013), Geomagnetic activity signatures in wintertime stratosphere wind, temperature, and wave response, *J. Geophys. Res. Atmos.*, 118, 2169– 2183

[157] Seppälä, A., Randall, C.E., Clilverd, M.A., Rozanov, E. & Rodger, C.J. (2009), Geomagnetic activity and polar surface air temperature variability, *J. Geophys. Res.*, 114, A10312

[158] Shen, B., Lian, Y., ZHANG, S. & Li, S. (2012), Impacts of Arctic Oscillation and Polar Vortex Anomalies on Winter Temperature over Eurasian Continent. *Advances in Climate Change Research.* 8. 434-439

[159] Shprits, Y.Y., et al. (2006), Outward radial diffusion driven by losses at magnetopause. *J. Geophys. Res.*111, A11214

[160] Sider, D. (1973). "Anaxagoras on the Size of the Sun". *Classical Philology.* 68 (2): 128–129

[161] Siingh, D, Singh, R.P., Kamra, A.K., Gupta, P.N., Singh, R., Gopalakrishnan, V. & Singh, A.K. (2005), Review of electromagnetic coupling between the Earth's atmosphere and the space environment. *J. Atmos. SolarTerr. Phys.* 67, 637-658

[162] Siingh, D., Gopalakrishnan, V., Singh, R.P., Kamra, A.K., Singh, S., Pant, V., Singh, R. & Singh, A.K. (2007), The atmospheric global electric circuit: An overview. *Atmospheric Research*, 84 (2). 91-110

[163] Singh, D.K., Singh, R.P. & Kamra, A.K. (2004). The electrical environment of the Earth's atmosphere: A review. *Space Sci. Rev.* 113, 375-408

[164] Singh, A. & Bhargawa, A. (2019), Prediction of declining solar activity trends during solar cycles 25 and 26 and indication of other solar minimum. *Astrophysics and Space Science.*

[165] Sinnhuber, M., Nieder, H. & Wieters, N. (2012), Energetic Particle Precipitation and the Chemistry of the Mesosphere/Lower Thermosphere. *Surveys in Geophysics.* 33.

[166] Sinnhuber, M., Berger, U., Funke, B., Nieder, H., Reddmann, T., Stiller, G., Versick, S., von Clarmann, T. & Wissing, J.M. (2018), NO_y production, ozone loss and changes in net radiative heating due to energetic particle precipitation in 2002–2010, *Atmos. Chem. Phys.*, 18, 1115–1147

[167] Smith, E.J. (2001), The heliospheric current sheet, *J. Geophys. Res.*, 106(A8), 15819– 15831

[168] Smith-Johnsen, C., Nesse Tyssøy, H., Hendrickx, K., Orsolini, Y., Kishore Kumar, G., Ødegaard, L.-K. G., Sandanger, M.I., Stordal, F. & Megner, L. (2017), Direct and indirect electron precipitation effect on nitric oxide in the polar middle atmosphere, using a full-range energy spectrum, *J. Geophys. Res.Space Physics*,122, 8679–8693

[169] Soden, B.J., Wetherald, R. T., Stenchikov, G. L. & Robock, A. (2002), Global cooling after the eruption of Mount Pinatubo: A test of climate feedback by water vapor, *Science*, 296(5568), 727– 730

[170] Solanki, S., Krivova, N. & Haigh, J. (2013). Solar Irradiance Variability and Climate. *Astronomische Nachrichten*. 323.

[171] Stadsnes, J. Kompendium, Det nære verdensrom, PHYS251

[172] Suess, S. (1999), Overview and Current Knowledge of the Solar Wind and the Corona. The Solar Probe. NASA/Marshall Space Flight Center.

[173] Svalgaard, L. (1968), Sector structure of the inter- planetary magnetic field and daily variations of the geomagnetic field at high latitudes, *Geophys. Pap.* R-6, Dan. Meteorol. Inst.

[174] Tartaglione, N., Toniazzo, T., Orsolini, Y.J. & Otterå, O.H. (2020), A note on the statistical evidence for an influence of geomagnetic activity on Northern Hemisphere seasonal-mean stratospheric temperatures using the Japanese 55-year Reanalysis. 545-555

[175] Thorne, R.M., et al. (2013), Rapid acceleration of relativistic radiation belt electrons by magnetospheric chorus, *Nature*, 504, 411–414,

[176] Thorne, R., Ni, B., Tao, X., Horne, R. & Meredith, N. (2010). Scattering by chorus waves as the dominant cause of diffuse aurora precipitation. *Nature*. 467. 943-6

[177] Thorne, R.M. (1980), The importance of energetic particle precipitation on the chemical composition of the middle atmosphere. *PAGEOPH* 118, 128–151

[178] Tinsley, B.A. (2000). Influence of Solar Wind on the Global Electric Circuit, and Inferred Effects on Cloud Microphysics, Temperature, and Dynamics in the Troposphere. *Space Science Reviews*, 94, 231-258

[179] Tinsley, B.A. (2008). The global atmospheric electric circuit and its effect on cloud microphysics. *REPORTS ON PROGRESS IN PHYSICS*. 71. 66801-31.

[180] Tokumaru, M., Kojima, M. & Fujiki, K. (2010), Solar cycle evolution of the solar wind speed distribution from 1985 to 2008, *J. Geophys. Res.* 115, A04102

[181] Tomikawa, Y. (2017), Response of the Middle Atmosphere in the Southern Hemisphere to Energetic Particle Precipitation in the Latest Reanalysis Data. *Scientific online letters on the atmosphere: SOLA*. 13A. 1-7

[182] Torsti, J., Kocharov, L.G., Teittinen, M. & Thompson, B.J. (1999), Injection of 10 MeV Protons in Association with a Coronal Moreton Wave, *The Astrophysical Journal*, 510(1):460-465

[183] Tribble, A. (2003, The Space Environment, Implications for Spacecraft Design. *Princeton University Press*. 15–18.

[184] Tsurutani, B.T., et al. (2006), Corotating solar wind streams and recurrent geomagnetic activity: A review, *J. Geophys. Res.*, 111, A07S01

[185] Turner, D.L., et al. (2014), Competing source and loss mechanisms due to wave-particle interactions in Earth's outer radiation belt during the 30 September to 3 October 2012 geomagnetic storm, *J. Geophys. Res. Space Physics*, 119, 1960– 1979

[186] Turner, D., Shprits, Y., Hartinger, M. et al. (2012), Explaining sudden losses of outer radiation belt electrons during geomagnetic storms. *Nature Phys* 8, 208–212

[187] Turunen, E, Verronen, P.T., Seppala, A., Rodger C.J., Clilverd, M.A., Tamminen, J., Enell, C.F. & Ulich, T. (2009), Impact of different energies of precipitating particles on NOx generation in the middle and upper atmosphere during geomagnetic storms. *J Atmos Sol Terr Phy.* 71:1176–1189

[188] Ukhorskiy, A.Y. et al. (2006), Storm time evolution of the outer radiation belt: Transport and losses. *J. Geophys. Res.* 111, A11S03

[189] Van Allen, J.A. & Frank, L.A. (1959), Radiation around the Earth to a radial distance of 107,400 km. *Nature* 183, 430–434

[190] Vincent, R.A. (2015), The dynamics of the mesosphere and lower thermosphere: a brief review. *Prog. in Earth and Planet Sci.* 2, 4.

[191] Vokhmyanin, M.V., Stepanov, N.A. & Sergeev, V.A. (2019), On the evaluation of data quality in the OMNI interplanetary magnetic field database. *Space Weather*, 17, 476– 486

[192] Walker, G. (1933). Seasonal Weather and its Prediction. *Nature* . 132(3343), 805-808

[193] Walt, M. (1971), The radial diffusion of trapped particles induced by fluctuating magnetospheric fields. *Space Sci Rev* 12, 446–485

[194] Wang C., et al (2019), Relationship of Halo CMEs and Solar Proton Events, Chinese *Astronomy and Astrophysics*, Volume 43, Issue 1, 34-46

[195] Webb, D.F. & Howard, T.A. (2012), Coronal Mass Ejections: Observations. Living Rev. *Solar Physics.* 9, 3.

[196] Whiteway, J.A. & Duck T.J. (1996), Evidence for critical level filtering of atmospheric gravity waves. *Geophysical Research Letters.* vol 23. Issue 2

[197] Wilks, D.S. (2016), "The Stippling Shows Statistically Significant Grid Points": How Research Results are Routinely Overstated and Over interpreted, and What to Do about It. *Bulletin of the American Meteorological Society.* 97

[198] Williams, E.R. (2005), Lightning and climate: a review. *Atmos. Res.* 76, 272–287

[199] Willson, R.C. & Hudson, H.S. (1991). The Sun's luminosity over a complete solar cycle. *Nature*. 351 (6321): 42–4

[200] Woods, T.N., Snow, M., Harder, J., Chapman, G. & Cookson, A. (2015). A Different View of Solar Spectral Irradiance Variations: Modeling Total Energy over Six-Month Intervals. *Solar physics*, 290, 2649–2676

[201] Yulaeva, E., Holton, J. & Wallace, J.M. (1994), On the cause of the annual cycle in tropical lower-stratospheric temperatures. *J. Atmos. Sci.*, 51, 169–174

[202] Zhang, Y., Fan, J., Chen, X., Ashkenazy, Y. & Havlin, S. (2019). Significant impact of Rossby waves on air pollution detected by network analysis. *Geophysical Research Letters*, 46, 12476– 12485

[203] Zhu, H., Chen, L., Claudepierre, S. G. & Zheng, L. (2020). Direct evidence of the pitch angle scattering of relativistic electrons induced by EMIC waves. *Geophysical Research Letters*, 47

[204] Zirker, J.B. (1977), Coronal holes and high-speed wind streams, *Reviews of Geophysics*, 15(3), 257–269

[205] http://acmg.seas.harvard.edu/people/faculty/djj/book/bookchap10.html

[206] http://kejian1.cmatc.cn/vod/comet/oceans/radio_waves/print.php.htm

[207] http://www.astrosurf.com/luxorion/qsl-hf-tutorial-nm7m3.htm

[208] https://ase.tufts.edu/cosmos/view_picture.asp?id=638

[209] https://commons.wikimedia.org/wiki/File:Solar_spectrum_en.svg

[210] https://en.wikipedia.org/wiki/Atmospheric_circulation

[211] https://en.wikipedia.org/wiki/Birkeland_current#/media/File:Schematic-of-combined-FACs-and-ionospheric-current-systems.png

[212] https://en.wikipedia.org/wiki/Coronal_hole

[213] https://en.wikipedia.org/wiki/Listoflargevolcaniceruptionsinthe21stcentury

[214] https://en.wikipedia.org/wiki/Listoflargevolcaniceruptionsofthe20thcentury

[215] https://en.wikipedia.org/wiki/Sun

[216] https://en.wikipedia.org/wiki/VolcanicExplosivityIndex

[217] https://forcetoknow.com/space/influence-solar-wind-earth.html

[218] https://no.wikipedia.org/wiki/William

[219] https://poleshift.ning.com/profiles/blogs/real-time-magnetosphere-data-reading-between-the-lines?overrideMobileRedirect=1

[220] https://solarsystem.nasa.gov/resources/754/what-is-a-lagrange-point/

[221] https://studylib.net/doc/18352779/the-standard-model-of-the-solar-flares

[222] https://www.climate.gov/news-features/event-tracker/how-polar-vortex-related-arctic-oscillation

[223] https://www.internetgeography.net/topics/what-is-global-atmospheric-circulation/

[224] https://www.ipcc.ch/

[225] https://www.ipcc.ch/site/assets/uploads/2018/02/ar4_syr_full_report.pdf

[226] https://www.sciencephoto.com/media/946558/view/heliospheric-current-sheet-illustration

[227] https://www.shutterstock.com/search/earth+magnetic+field

[228] https://www.uio.no/studier/emner/matnat/geofag/nedlagte-emner/GEO1030/h17/undervisningsmateriale/forelesninger/aguado7_lecture_ch_08_fs.pdf

12 Appendices

12.1 Appendix A: Supplement theory

12.1.1 A.1 Sunspots

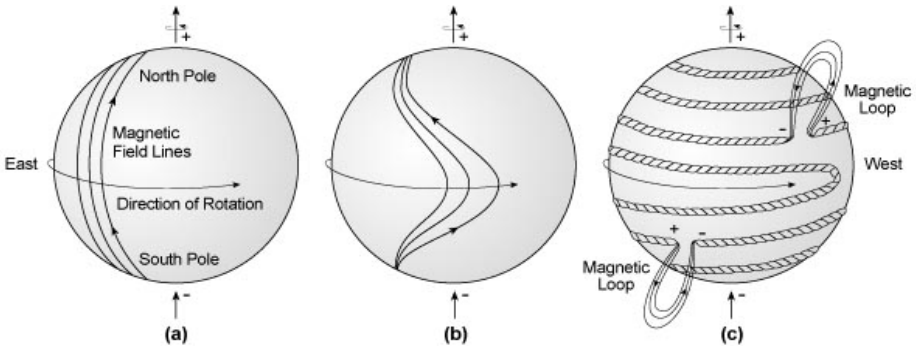

Figure 70: Creation of sunspots according to Babcocks mechanism (Figure taken from ase.tufts.edu)

Babcock (1961) proposed a simple model for the generation mechanisms behind sunspots, linking them to the solar magnetic field. In this model sunspots are created as a consequence of the difference in the rotational period between the equator and the poles. This causes magnetic field lines to twist near the surface. The magnetic field strength will increase the more twisted the field lines get. As the sum of the magnetic pressure and particle pressure is constant, the temperature and density in the same area will decrease with increasing magnetic field strength:

$$\mathrm{P_B} + \frac{\mathrm{T}\rho\mathrm{k_B}}{\mathrm{m}} = \mathrm{p_{total}} \tag{21}$$

The decrease in particle density in the specific area creates an upward force according to Archimedes principle, ultimately forcing the twisted magnetic field line to penetrate the surface and thereby creating an extended arch as shown in Figure 70c, with different magnetic polarities at each intersection between the field lines and the Sun's surface. The dark color of the sunspots can then be explained by the decrease in temperature at the intersection.

12.1.2 A.2 Three types of particle motion

Figure 71 shows three basic types of particles trapped in Earths magnetic field. Firstly, a charged particle moving in a homogeneous electromagnetic field will experience a force perpendicular to both the magnetic field direction and the

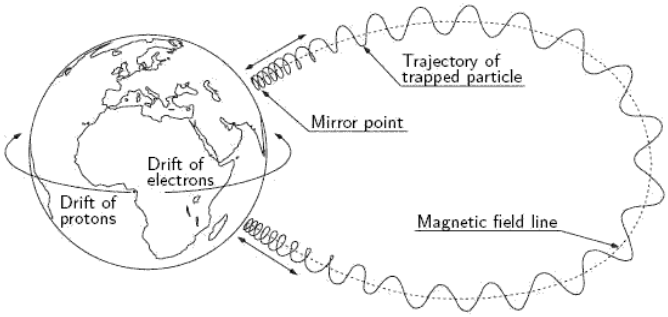

Figure 71: Charged particle motion on closed field lines (Figure taken from European Space Agency (ESA)).

velocity direction. This force, known as the Lorentz force, is given by:

$$\mathrm{m}\frac{\mathrm{d}\mathbf{v}}{\mathrm{dt}} = q(\mathbf{E} + \mathbf{v} \text{ x } \mathbf{B}) \tag{22}$$

In an inertial frame of reference where the electrical field is zero, the charged particle will move in a circular gyromotion, with a radius and period given by:

$$\mathrm{r} = \frac{\mathrm{m}\mathbf{v}_{\perp}}{\mathrm{qB}} \tag{23}$$

$$\omega_{\mathrm{g}} = \frac{\mathrm{qB}}{\mathrm{m}} \tag{24}$$

Secondly, particles bounce between geomagnetic conjugate mirror points, where the pitch angle $\alpha = 90°$ (Appendix A.3). Finally, the charged particles show a drift motion, with electrons drifting eastward and protons drifting westward, thereby creating the ring current. An increased ring current decreases the strength of the horizontal component of the terrestrial field. Although the perturbation is small, it is still measurable in the equatorial region (Dst-index is measure of the strength of the ring current).

12.1.3 A.3 Pitch angle, mirror point and loss cone

When particles move along magnetic field lines towards the poles, the magnetic field converges. An illustration of a converging magnetic field, with the decomposed components of the Lorentz force is given in Figure 73. As the field is converging, it would have a magnetic component, B_2 pointing towards the center of the circular path traced out by the gyromotion. The cross product between the perpendicular velocity and the B_1-component would trace out this regular gyromotion ($\mathbf{v}_{\perp}$ x $\mathbf{B}_1$). It can be shown that the parallel velocity and

the B_2-component, by taking the cross product ($\mathbf{v}_{\parallel}$ x $\mathbf{B_2}$) would give a forcing accelerating the perpendicular velocity component, $v_{\perp}$. There will also be a force along the magnetic field line in the opposite direction of the parallel velocity ($\mathbf{v}_{\perp}$ x $\mathbf{B_2}$). This force is called the mirror force, as it acts to decelerate the parallel speed of the gyrating particle. With a strong enough B_2-component (large convergence), the mirror force would be strong enough to reverse the $v_{\parallel}$ direction. By expressing the velocity vectors as:

$$v_{\perp} = v \sin \alpha \tag{25}$$

$$v_{\parallel} = v \cos \alpha \tag{26}$$

Where α on a certain point at the magnetic field line is defined as the pitch

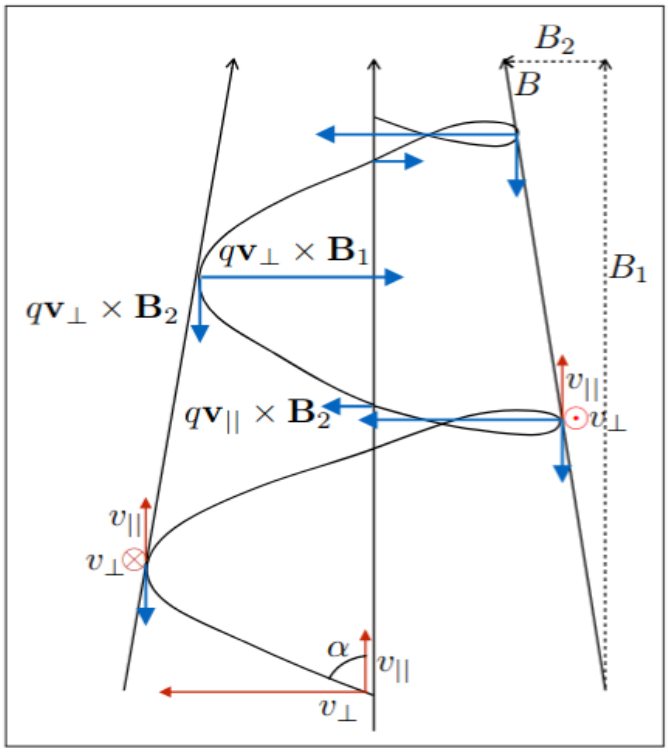

Figure 72: Motion of a charged particle in a converging magnetic field. The Lorentz force have been decomposed into a parallel and perpendicular component, derived from the parallel and perpendicular velocity and magnetic field. [PHYS 251 compendium]

angle at that point. When $\alpha = 90°$, the particle reaches the mirror point, as $v_{\parallel} = 0$. From the same equations $v_{\perp}$ reaches maximum at the same point, thereby conserving the velocity (momentum). The magnetic field cannot change the

total velocity of the particle, only the direction, as the magnetic force is always perpendicular to the velocity.

Together with the attribute that the magnetic dipole moment is conserved when a gyrating particle moves along a magnetic field line:

$$\mu = \frac{\mathrm{m}{v_\perp}^2}{2B} = \frac{\mathrm{m}v^2 \sin^2 \alpha}{2B} = \text{constant} \tag{27}$$

As the mass and the total speed are constant, the pitch angle and the magnetic field are the only variables, giving:

$$\frac{\sin^2 \alpha}{B} = \text{constant} \tag{28}$$

For a pitch angle of 90°, which would be the mirror point, the equation would look like:

$$\frac{\sin^2 (\alpha = 90°)}{B} = \frac{1}{B_{\text{Strength at } \alpha = 90°}} \tag{29}$$

The pitch angle can then be defined as:

$$\sin \alpha_0 = \sqrt{\frac{B_0}{B_1}} \tag{30}$$

Where B_0 represents the field strength at the location of the particle, and B_1 represents the field strength at the point where the particle 'mirrors'. By setting B_1 equal to the magnetic field near the surface of the Earth (<100km from the surface), one get a pitch angle varying in size dependent on the location of the particle and hence B_0, which traces out a cone around the magnetic field. All particles with a pitch angle falling inside this cone, defined as the loss cone, at a specified point will in this case be lost to the atmosphere. The smaller the pitch angle, the deeper into the atmosphere before reaching the mirror point, hence a higher chance of interaction between the particle and the atmosphere before it is mirrored back.

12.1.4 A.4 Adiabatic invariants

Adiabatic invariants are physical quantities that change slowly enough within a system to be considered constants of motion. In plasma physics all three types of charged particle motion described in Appendix A.2 have their respective adiabatic invariants, which are conserved for slowly changing magnetic fields. The first invariant is the magnetic dipole moment of a gyrating particle given by:

$$\mu = \frac{\mathrm{m}{v_\perp}^2}{2B} \tag{31}$$

For 'slow' temporal variations with respect to one gyroperiod, the perpendicular velocity of a particle varies as the square root of the magnetic field.

The second invariant is the longitudinal invariant of a trapped particles parallel momentum which bounce off mirror points. The trajectory of the guiding center can be regarded as being approximately closed, even though there is a small azimuthal drift component, hence the invariant is expressed as:

$$\mathrm{J} = \oint \mathrm{p}_{\parallel} \mathrm{ds} \tag{32}$$

The path of integration is along a field line and back, and ds represents arch length along the field line. Provided that the magnetic field varies on time scales much longer than the bounce time between the mirror points, the invariant assures that charged particles mirroring always returns to the same line of force.

The third invariant is associated with the azimuthal drift motion, and is defined as the conservation of magnetic flux Φ enclosed by a drift surface. Simplified, it conserves the magnetic flux through a particles drift orbit. The sufficient conditions require magnetic field variations on time scales longer than the drift period, which can be on the time scale of an hour, conserving the invariant only under relatively quiet geomagnetic conditions.

12.1.5 A.5 L-value

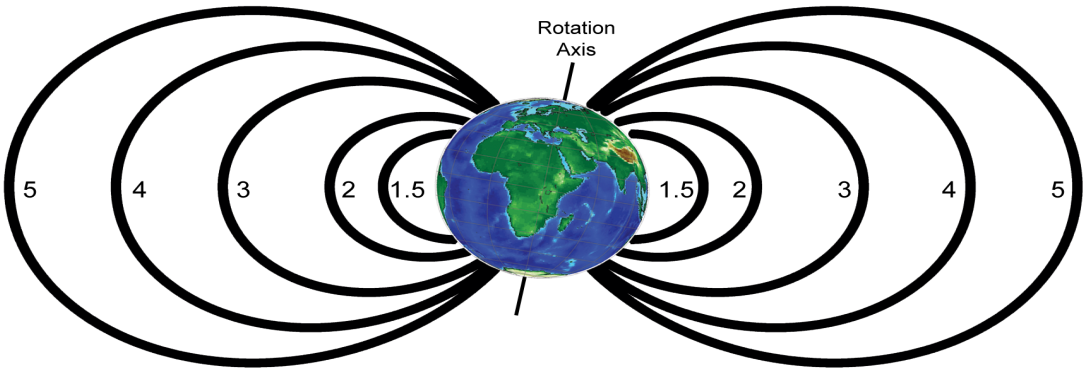

Figure 73: Drawing of multiple distinct L-shells. (wikipedia)

The maximum distance of a field line from the Earth, divided by the Earth radius, defines the L-value. This happens in the magnetic equatorial plane, and the equation is given by:

$$\mathrm{L} = \frac{1}{\sin^2 \theta_{\mathrm{E}}} \tag{33}$$

where θ_{E} represents the point of intersection between the Earth and the magnetic field line, given in polar coordinates.

12.2 Appendix B: Supplement figures for the Chemical-Dynamical coupling results

Plots for the chemical dynamical coupling. All plots are described in the thesis.

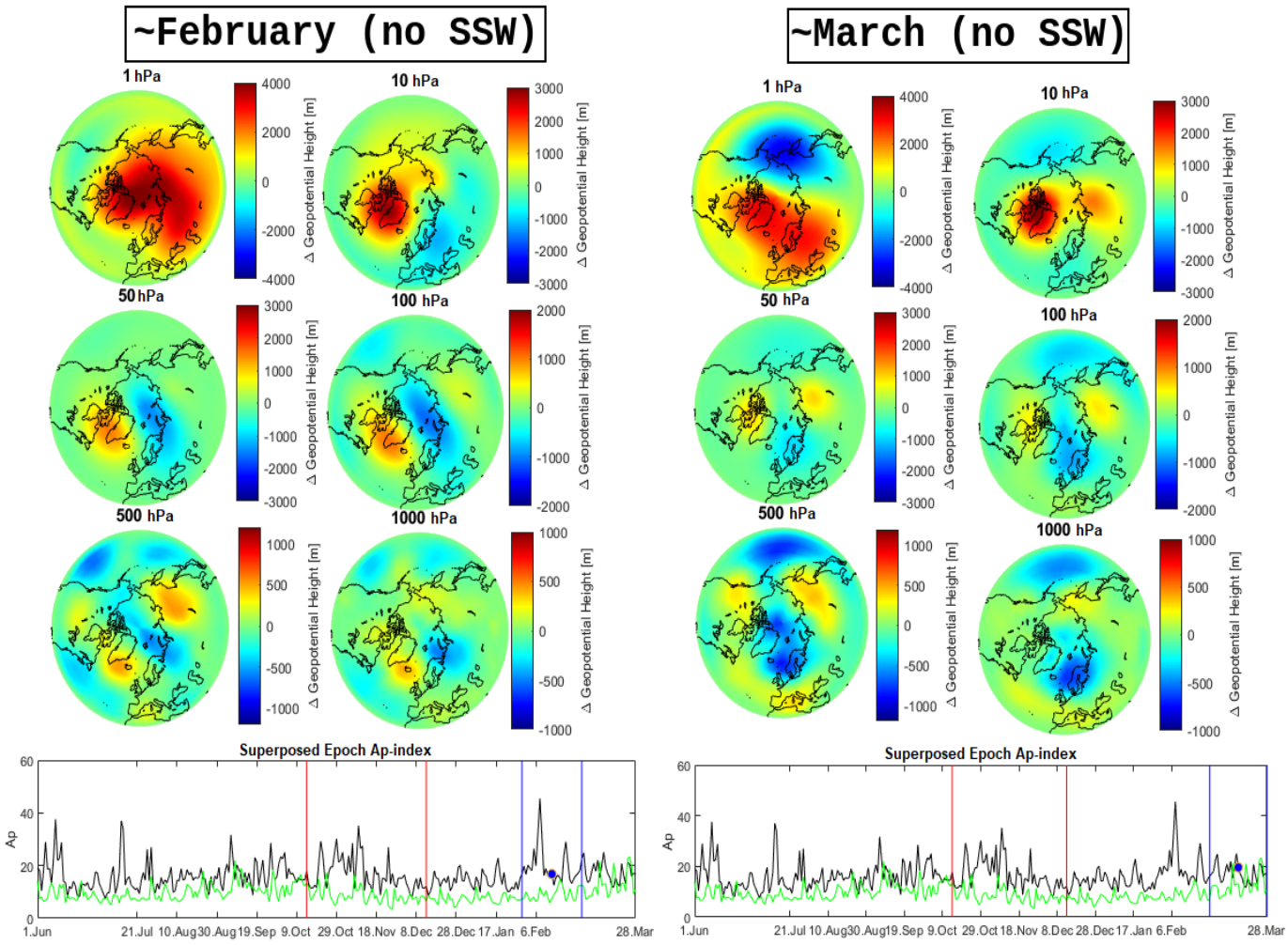

Figure 74: **Top panels:** Δ Geo-Height[m] = A_p(high) - A_p(low) for February and March (A1N: SSW). **Bottom Panels:** Black (green) line represents the averaged Ap-index from the high (low) bin.

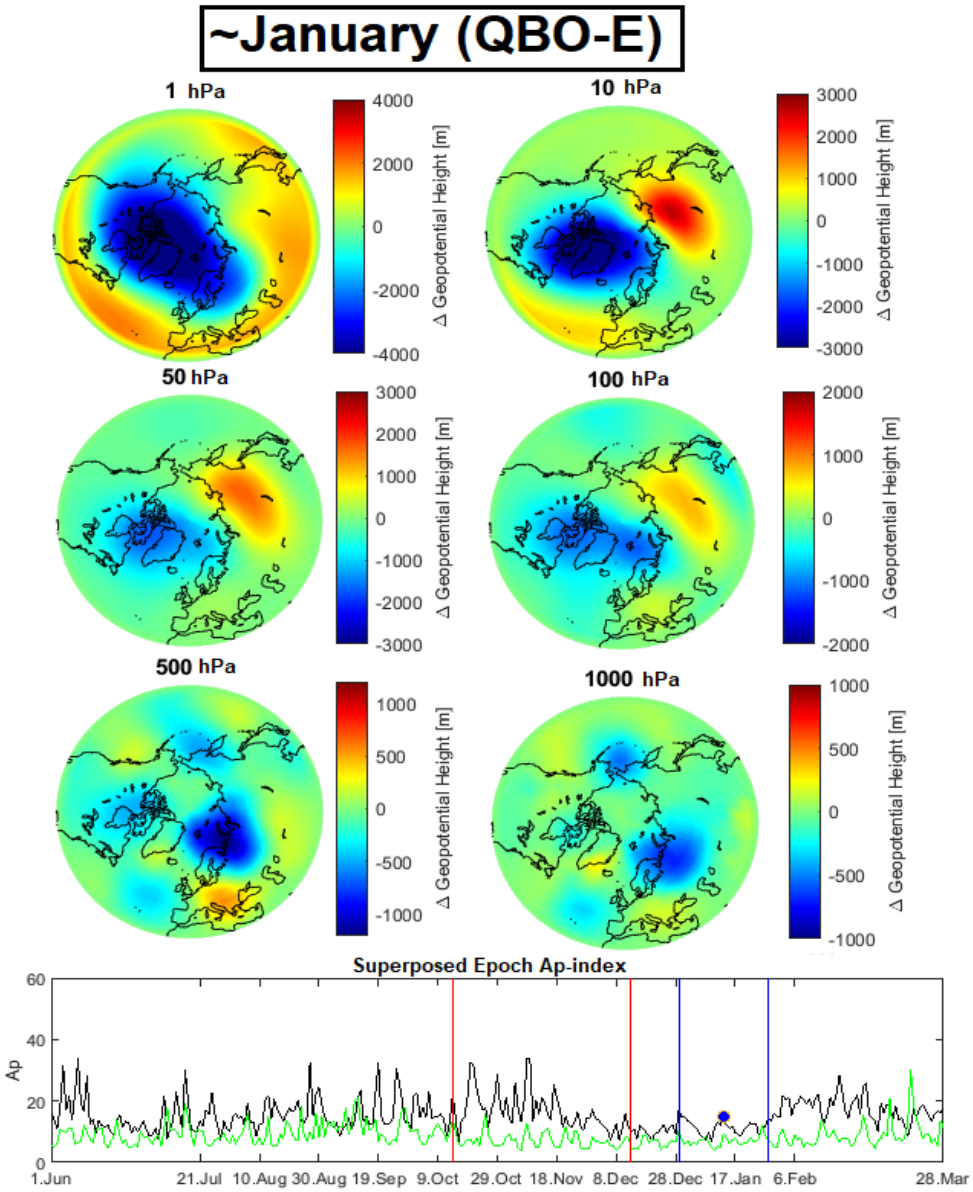

Figure 75: **Top panel:** Δ Geo-Height[m] = A_p QBO-(E)(high) - A_p QBO-(E)(low) for January (A1N: QBO). No statistical significance is found. **Bottom Panel:** Black (green) line represents the averaged Ap-index from the high (low) bin.

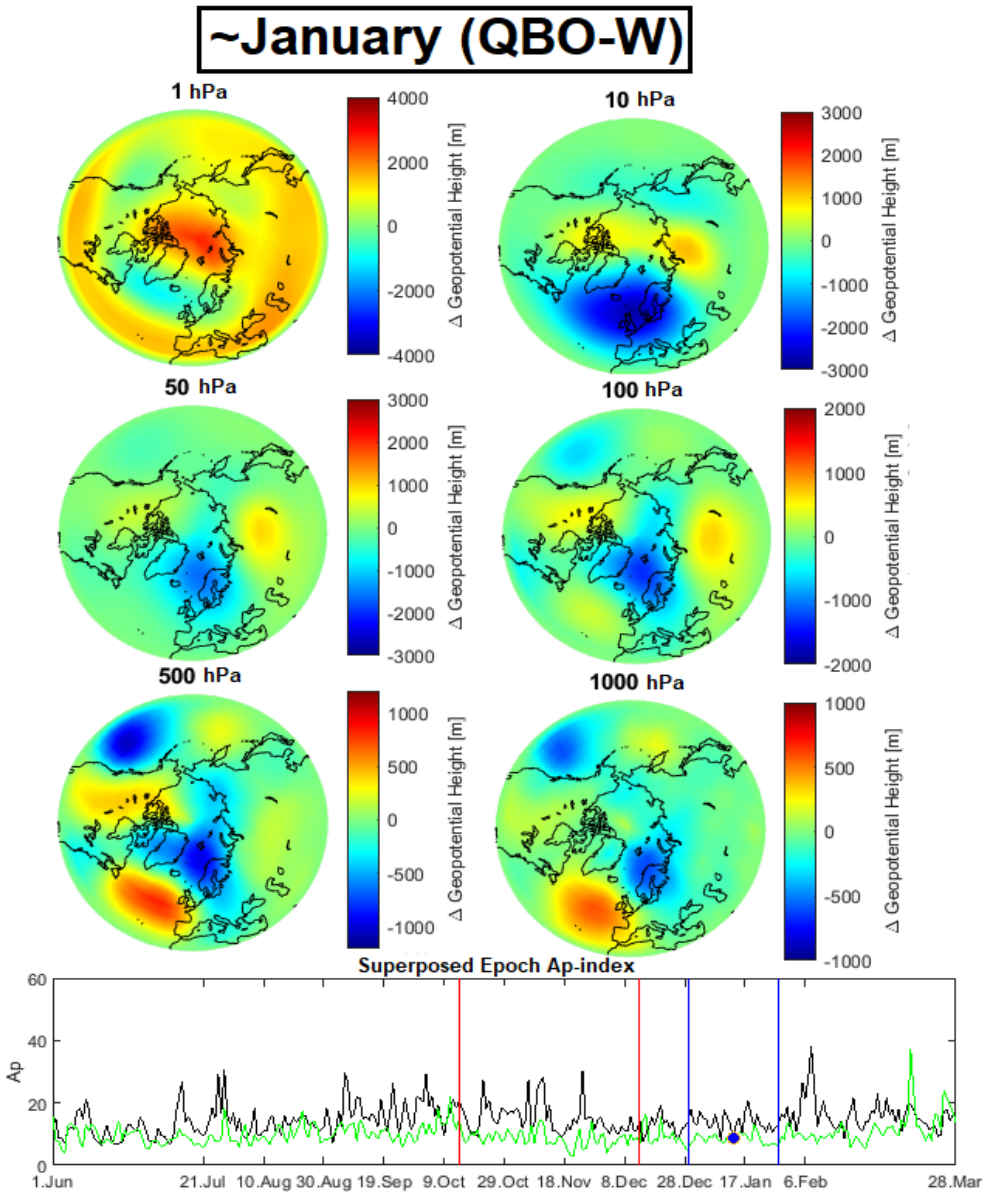

Figure 76: **Top panel:** Δ Geo-Height[m] = A_p QBO-(W)(high) - A_p QBO-(W)(low) for January (A1N: QBO). No statistical significance is found. **Bottom Panel:** Black (green) line represents the averaged Ap-index from the high (low) bin.

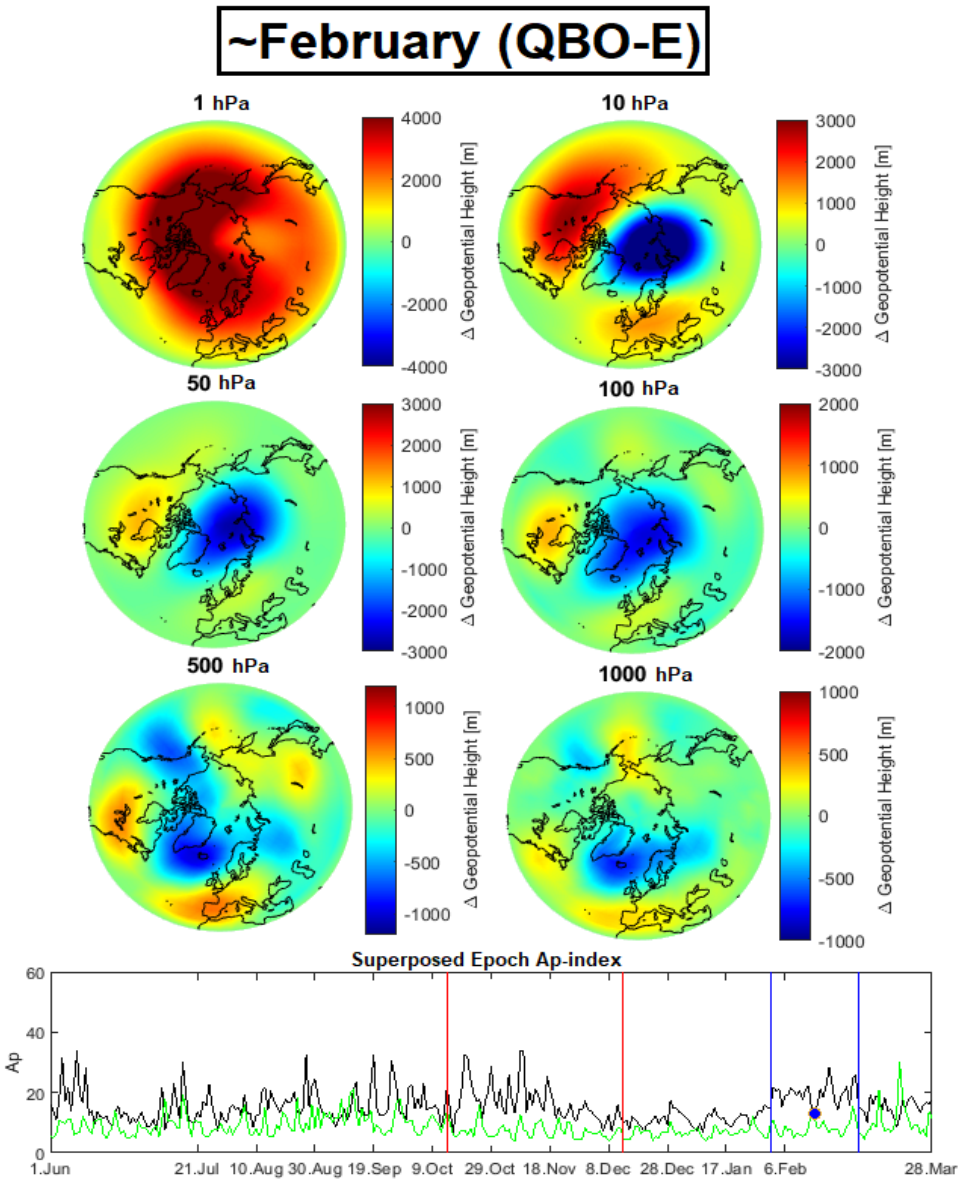

Figure 77: **Top panel:** Δ Geo-Height[m] = A_p QBO-(E)(high) - A_p QBO-(E)(low) for February (A1N: QBO). No statistical significance is found. **Bottom Panel:** Black (green) line represents the averaged Ap-index from the high (low) bin.

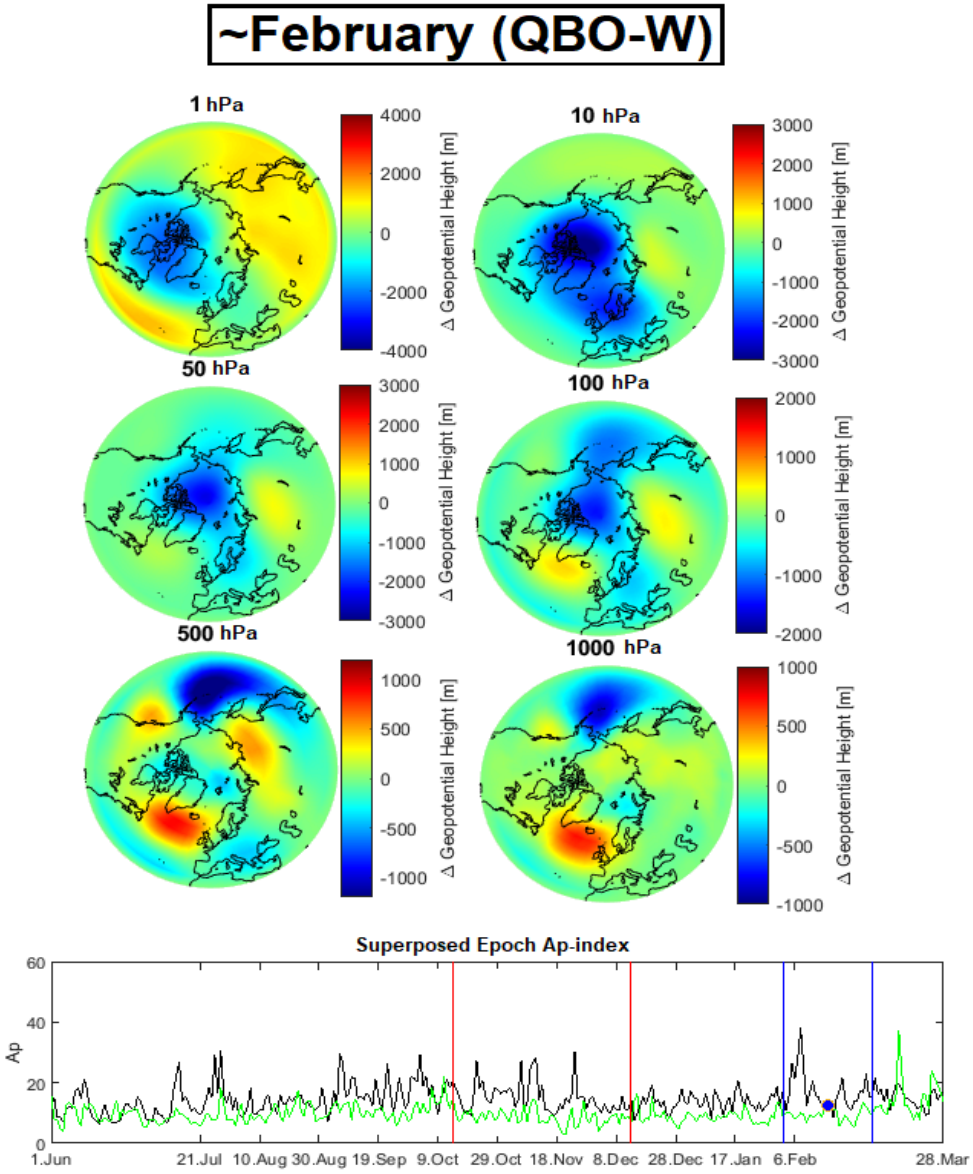

Figure 78: **Top panel:** Δ Geo-Height[m] = A_p QBO-(W)(high) - A_p QBO-(W)(low) for February (A1N: QBO). No statistical significance is found. **Bottom Panel:** Black (green) line represents the averaged Ap-index from the high (low) bin.

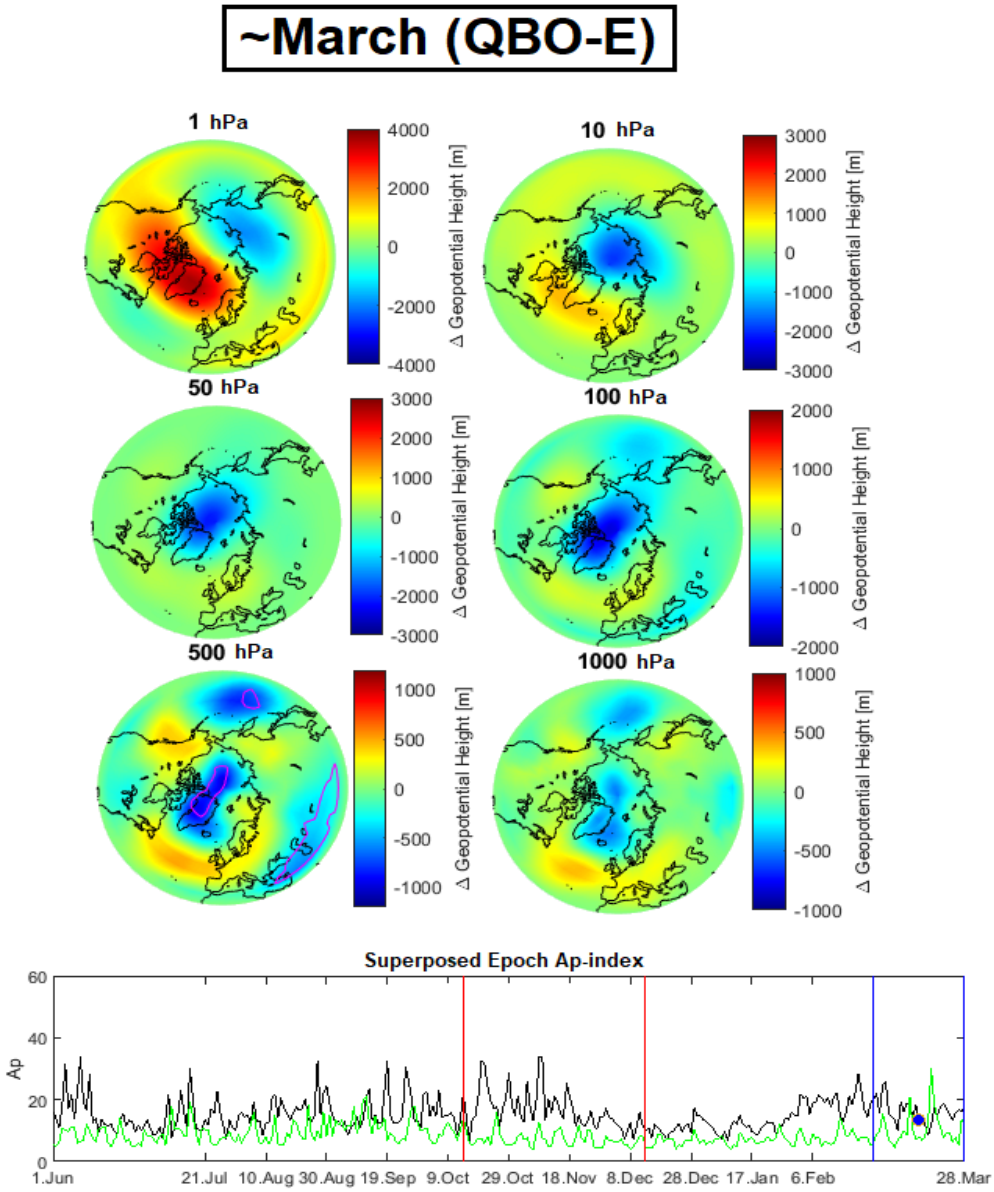

Figure 79: **Top panel:** Δ Geo-Height[m] = A_p QBO-(E)(high) - A_p QBO-(E)(low) for March (A1N: QBO). Statistical significance found at the 500 hPa level. **Bottom Panel:** Black (green) line represents the averaged Ap-index from the high (low) bin.

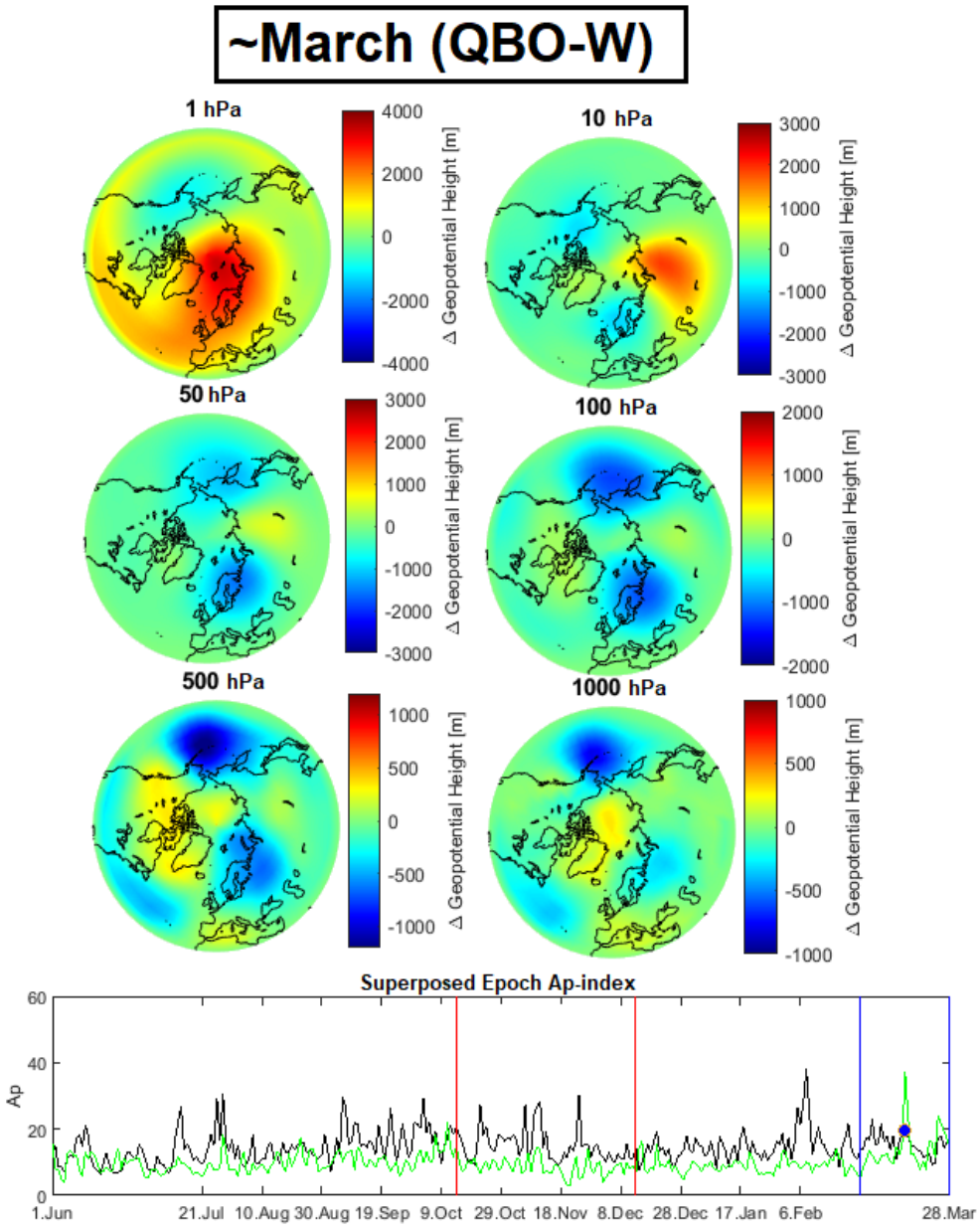

Figure 80: **Top panel:** Δ Geo-Height[m] = A_p QBO-(W)(high) - A_p QBO-(W)(low) for March (A1N: QBO). No statistical significance is found. **Bottom Panel:** Black (green) line represents the averaged Ap-index from the high (low) bin.

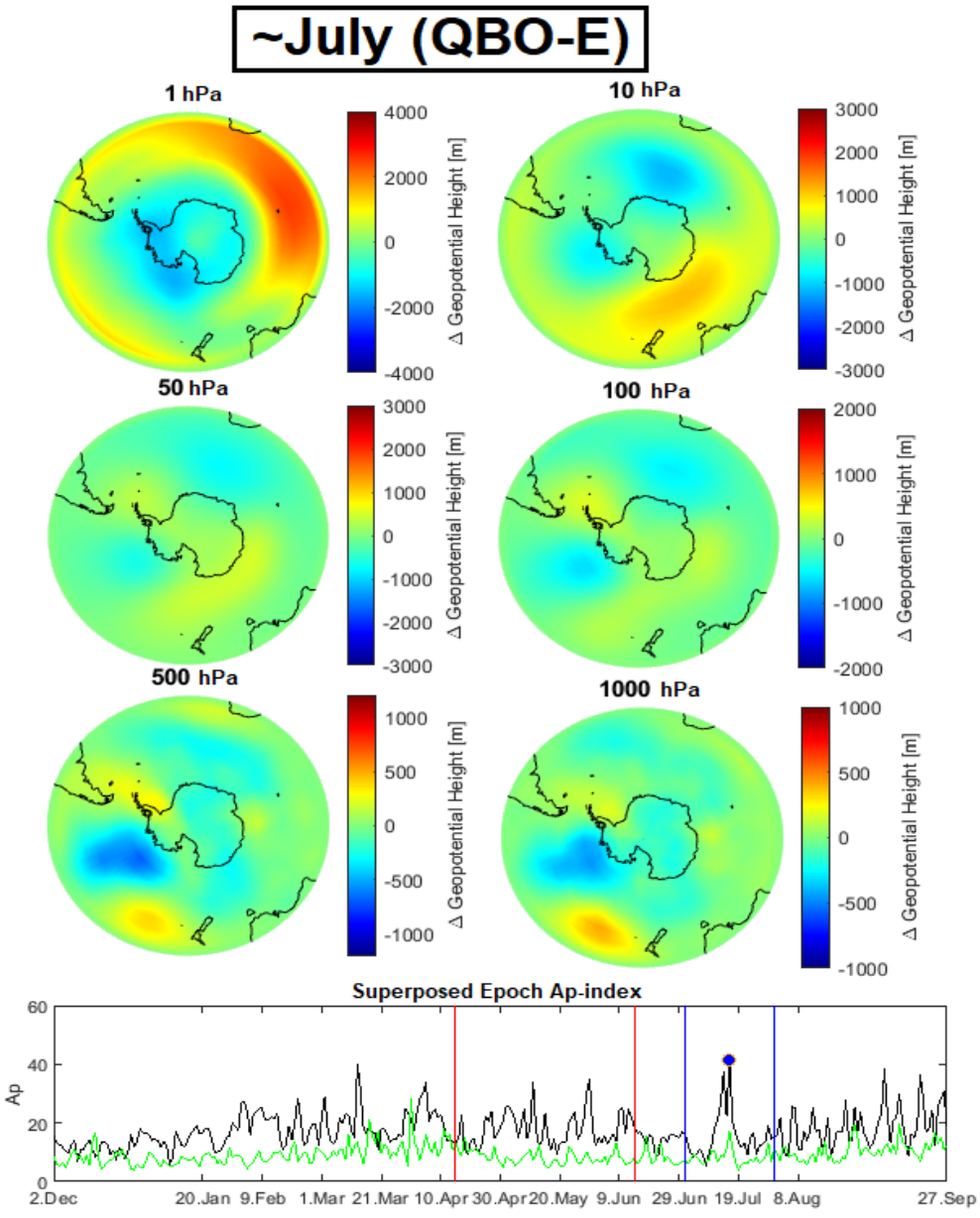

Figure 81: **Top panel:** Δ Geo-Height[m] = A_p QBO-(E)(high) - A_p QBO-(E)(low) for July (A1S: QBO). No statistical significance is found. **Bottom Panel:** Black (green) line represents the averaged Ap-index from the high (low) bin.

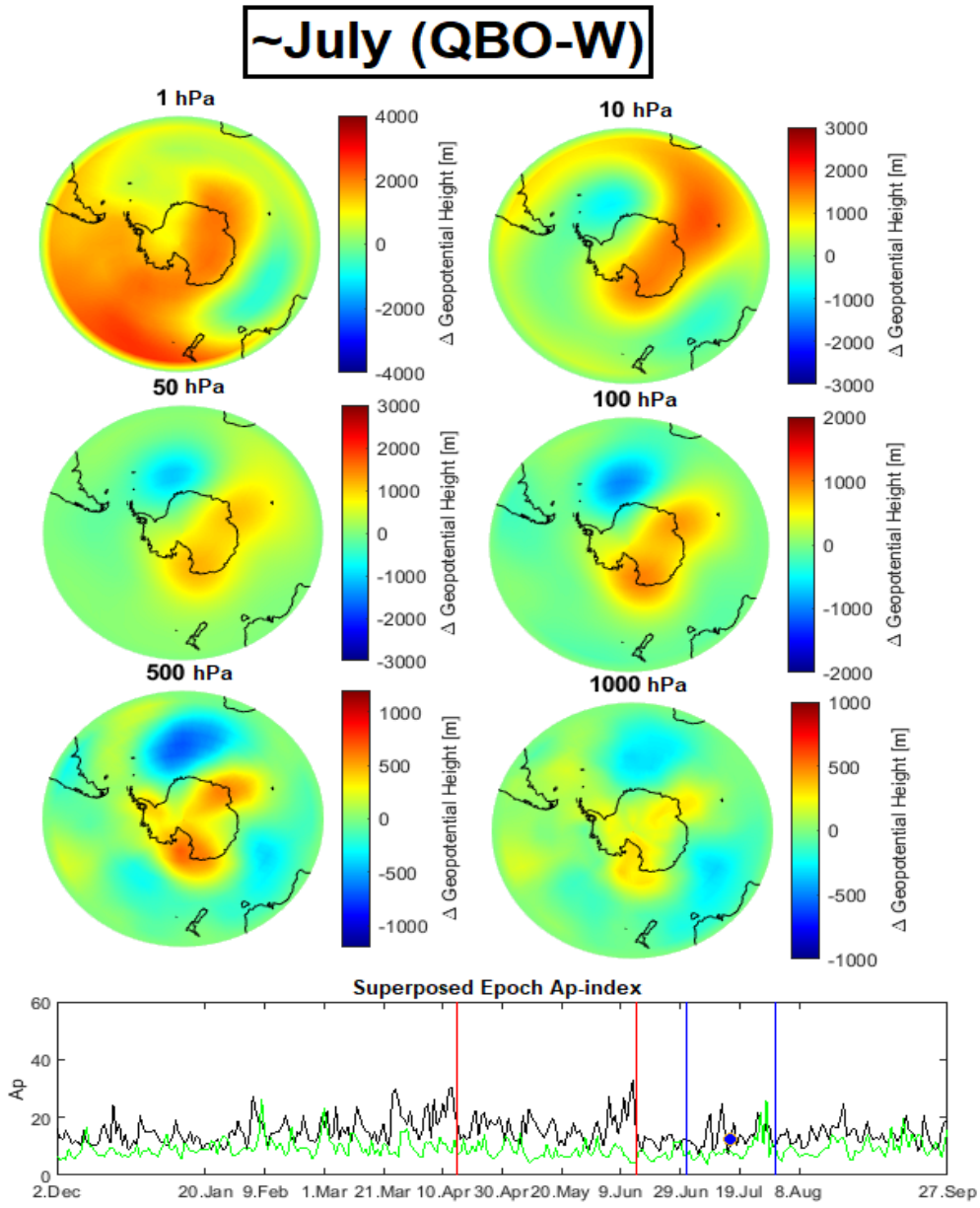

Figure 82: **Top panel:** Δ Geo-Height[m] = A_p QBO-(W)(high) - A_p QBO-(W)(low) for July (A1S: QBO). No statistical significance is found. **Bottom Panel:** Black (green) line represents the averaged Ap-index from the high (low) bin.

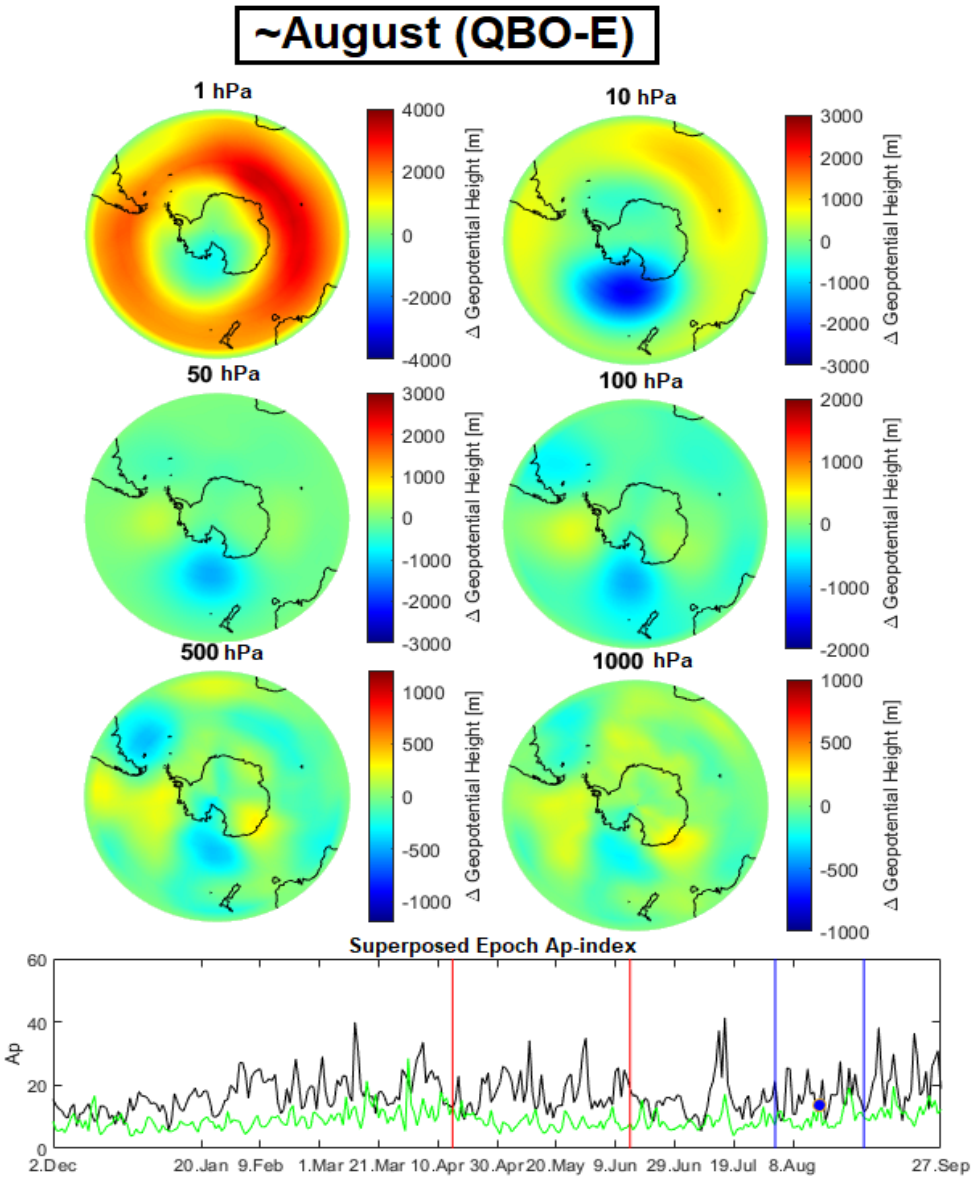

Figure 83: **Top panel:** Δ Geo-Height[m] = A_p QBO-(E)(high) - A_p QBO-(E)(low) for August (A1S: QBO). No statistical significance is found. **Bottom Panel:** Black (green) line represents the averaged Ap-index from the high (low) bin.

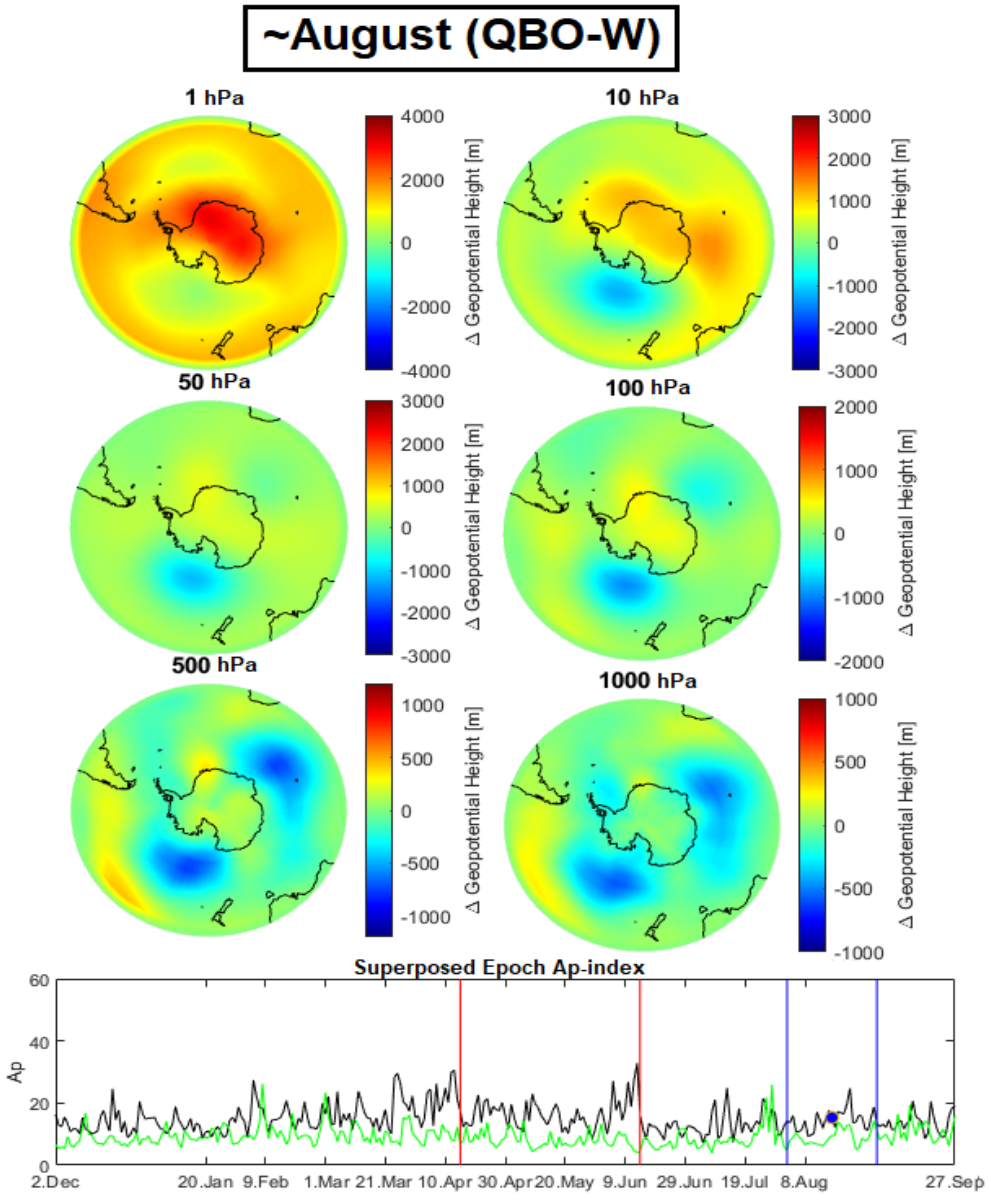

Figure 84: **Top panel:** Δ Geo-Height[m] = A_p QBO-(W)(high) - A_p QBO-(W)(low) for August (A1S: QBO). A statistically significant anomaly is seen at the 500 hp and 1000 hp level. **Bottom Panel:** Black (green) line represents the averaged Ap-index from the high (low) bin.

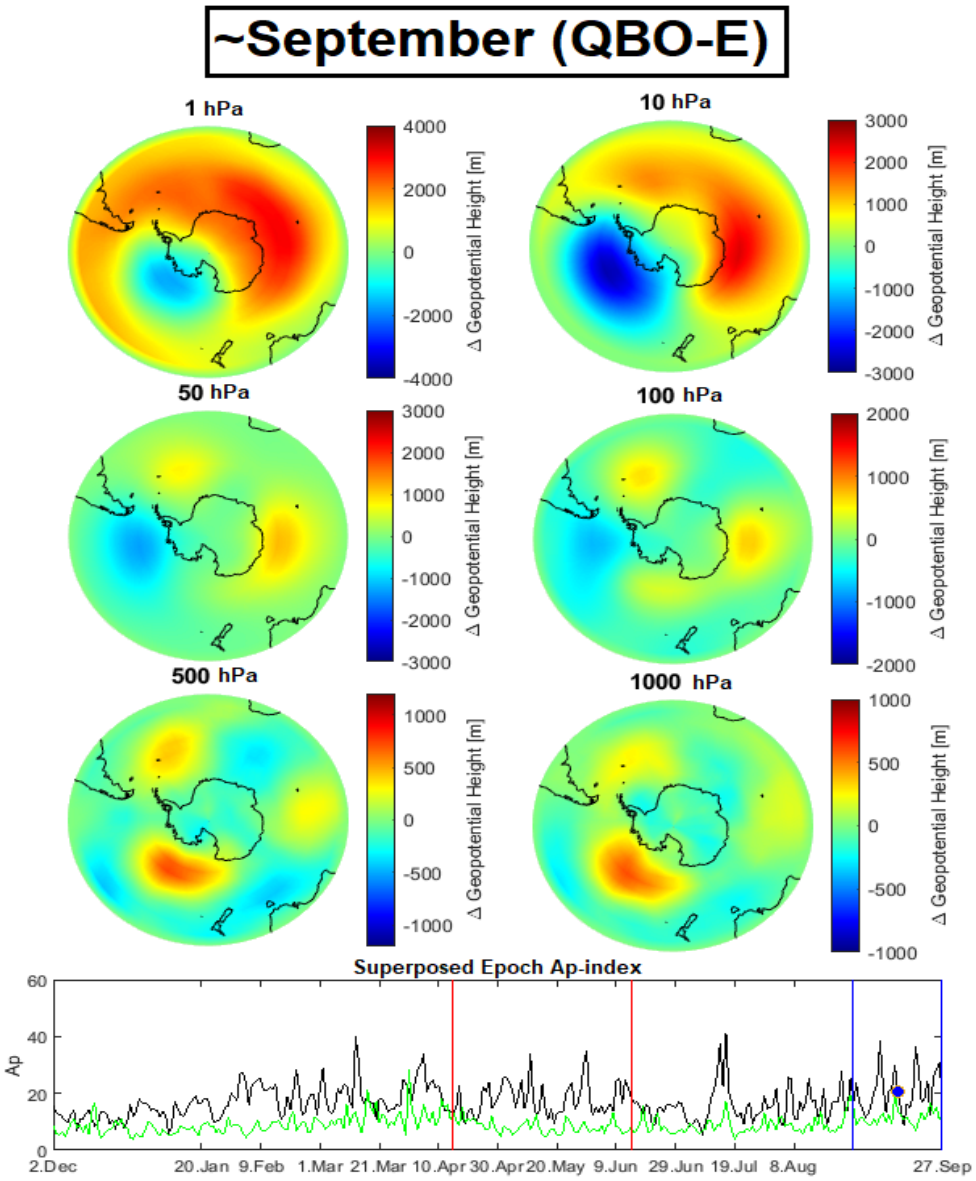

Figure 85: **Top panel:** Δ Geo-Height[m] = A_p QBO-(E)(high) - A_p QBO-(E)(low) for September (A1S: QBO). No statistical significance is found. **Bottom Panel:** Black (green) line represents the averaged Ap-index from the high (low) bin.

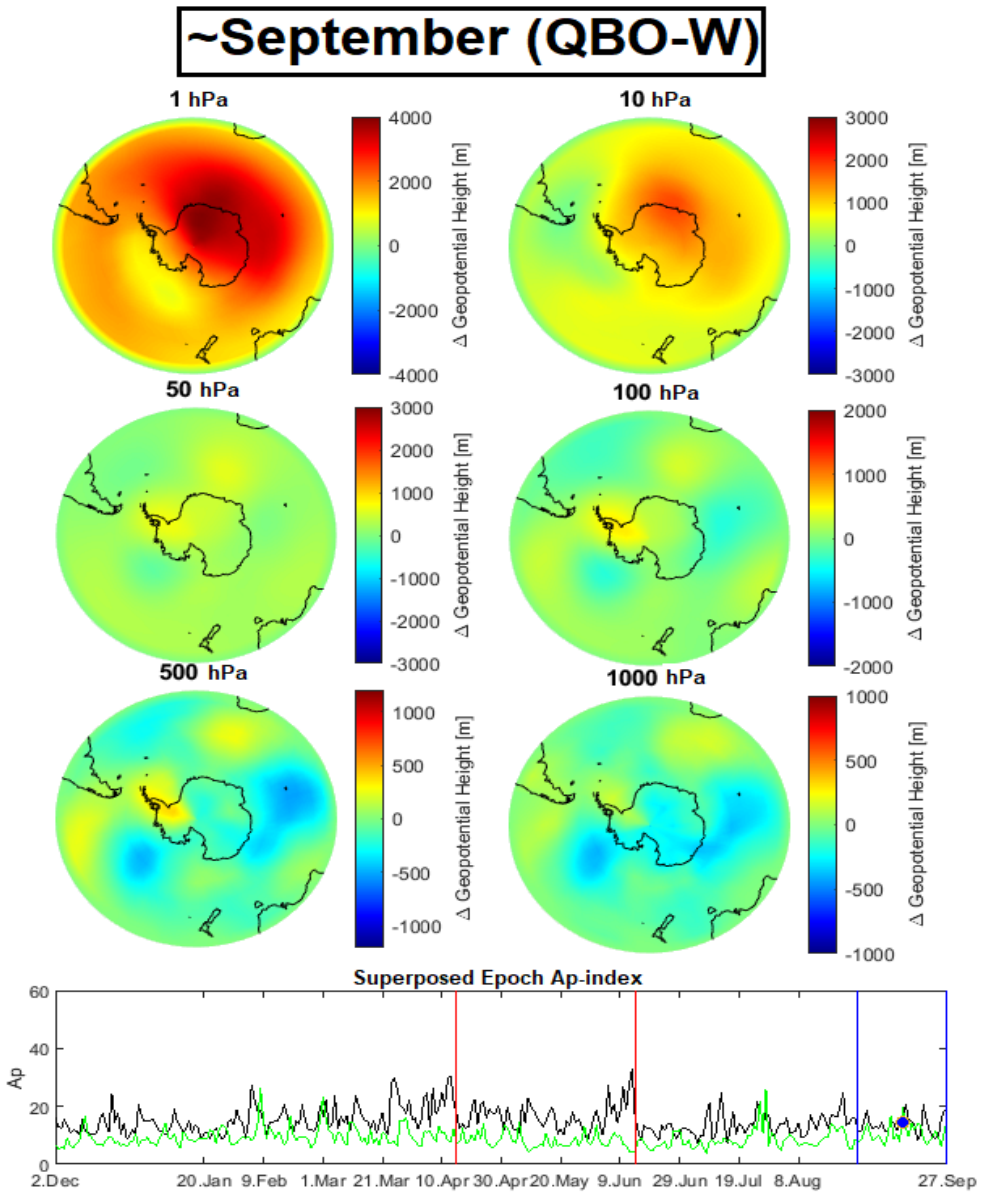

Figure 86: **Top panel:** Δ Geo-Height[m] = A_p QBO-(W)(high) - A_p QBO-(W)(low) for September (A1S: QBO). No statistical significance is found. **Bottom Panel:** Black (green) line represents the averaged Ap-index from the high (low) bin.

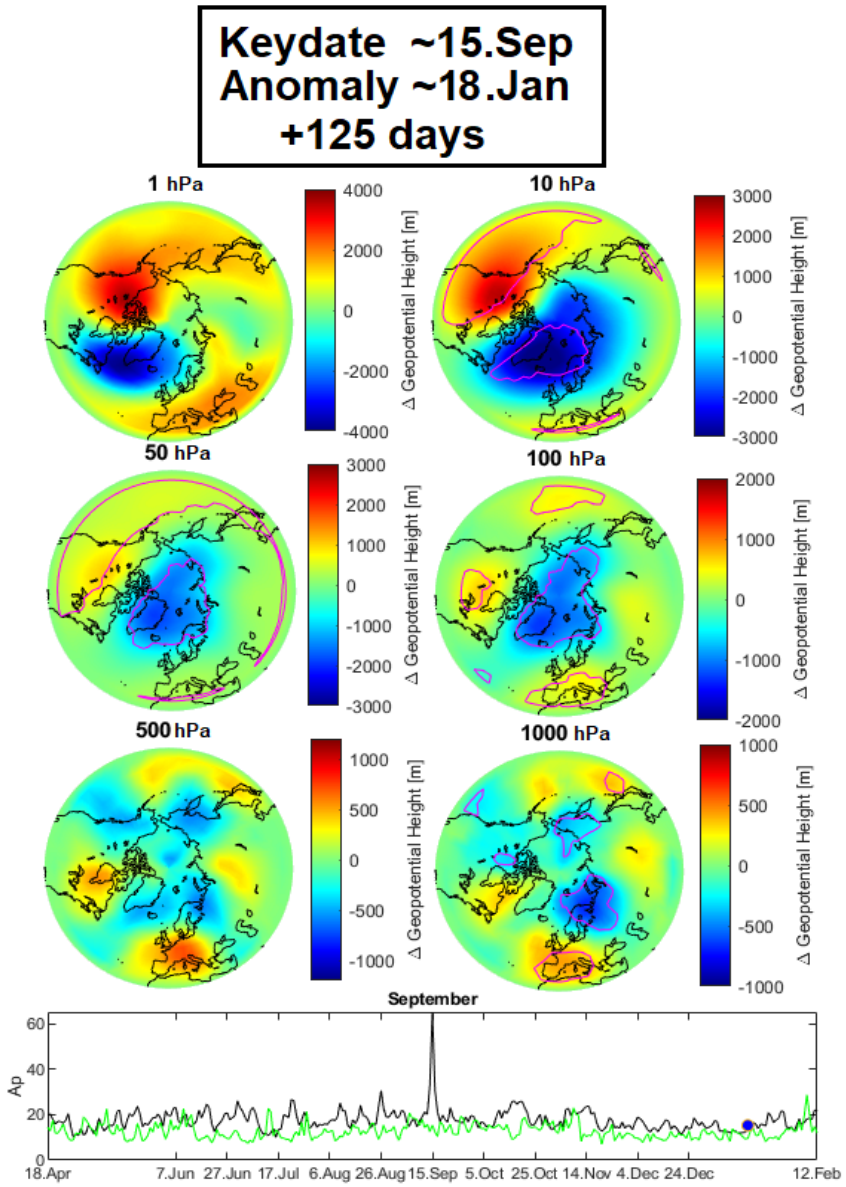

Figure 87: **Top panel:** Anomaly occurring in middle January for keydate inside September (A2N). Purple lines indicate statistical significance. **Bottom panel:** Black (green) line represents the averaged Ap-index from the high (CLIMREF-spec) bin.

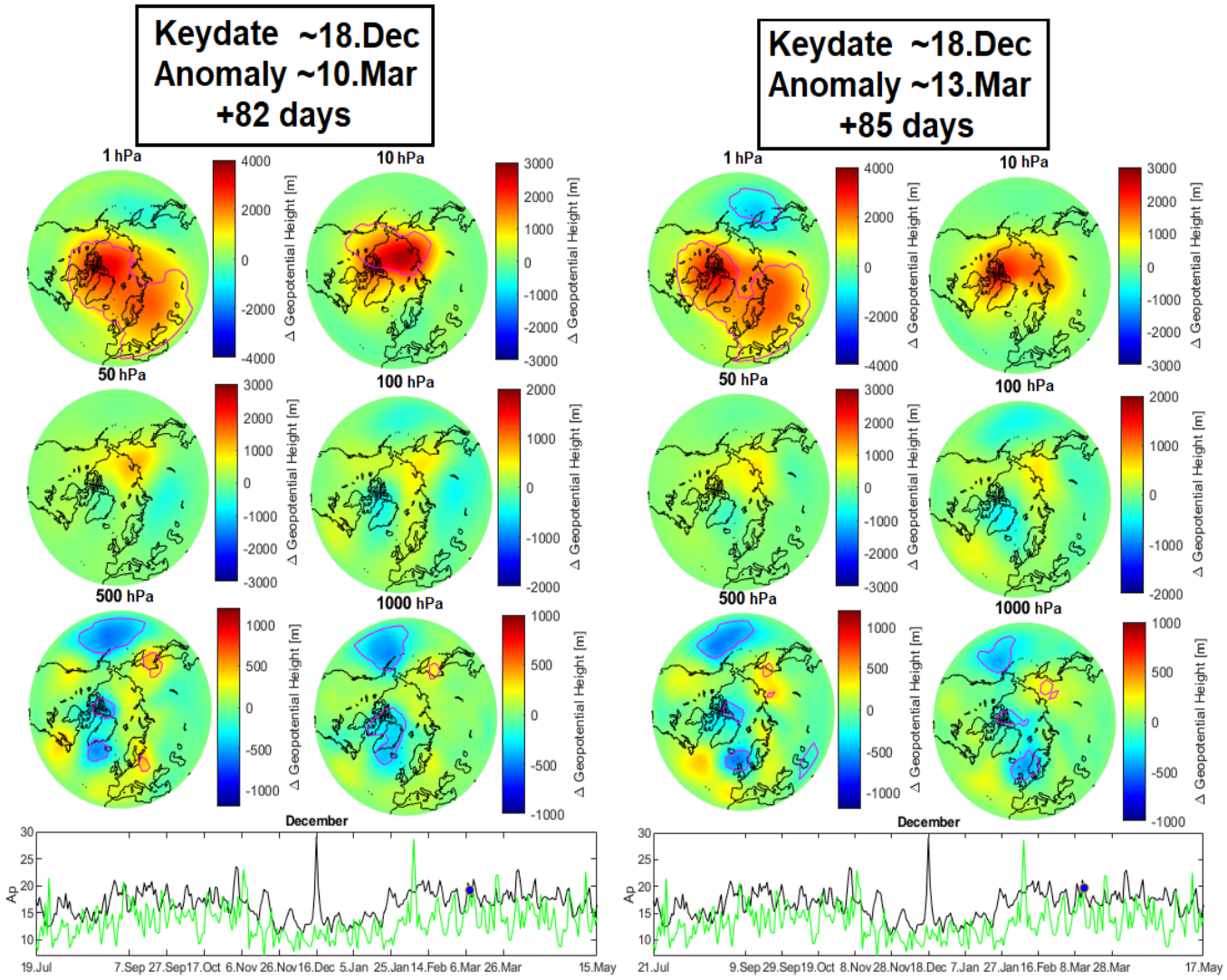

Figure 88: **Top panels:** Anomaly occurring in middle March for keydate inside December (A2N). Purple lines indicate statistical significance. **Bottom panels:** Black (green) line represents the averaged Ap-index from the high (CLIMREF-spec) bin.

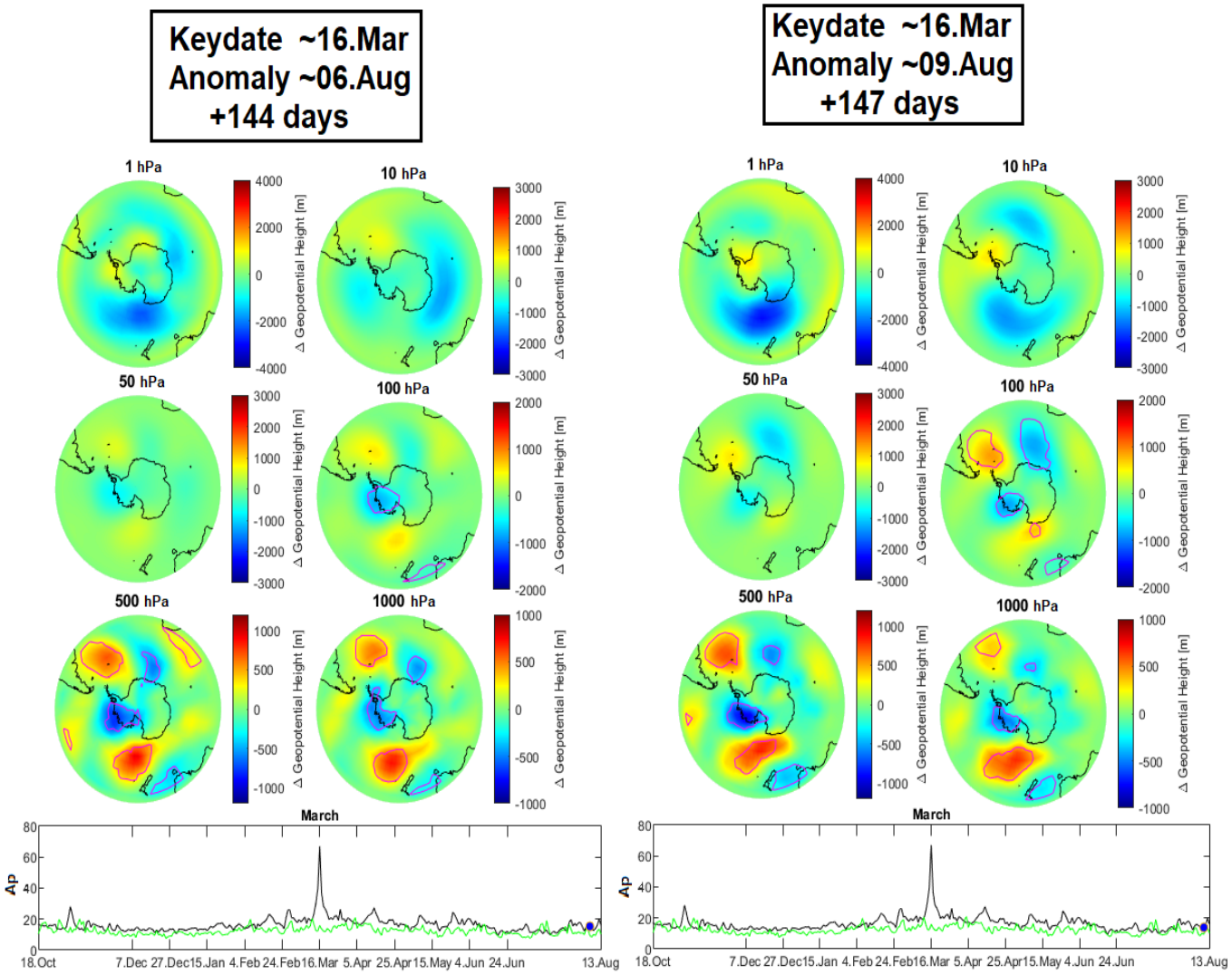

Figure 89: **Top panels:** Anomaly occurring in early August for keydate inside March (A2S). Purple lines indicate statistical significance. **Bottom panels:** Black (green) line represents the averaged Ap-index from the high (CLIMREF-spec) bin.

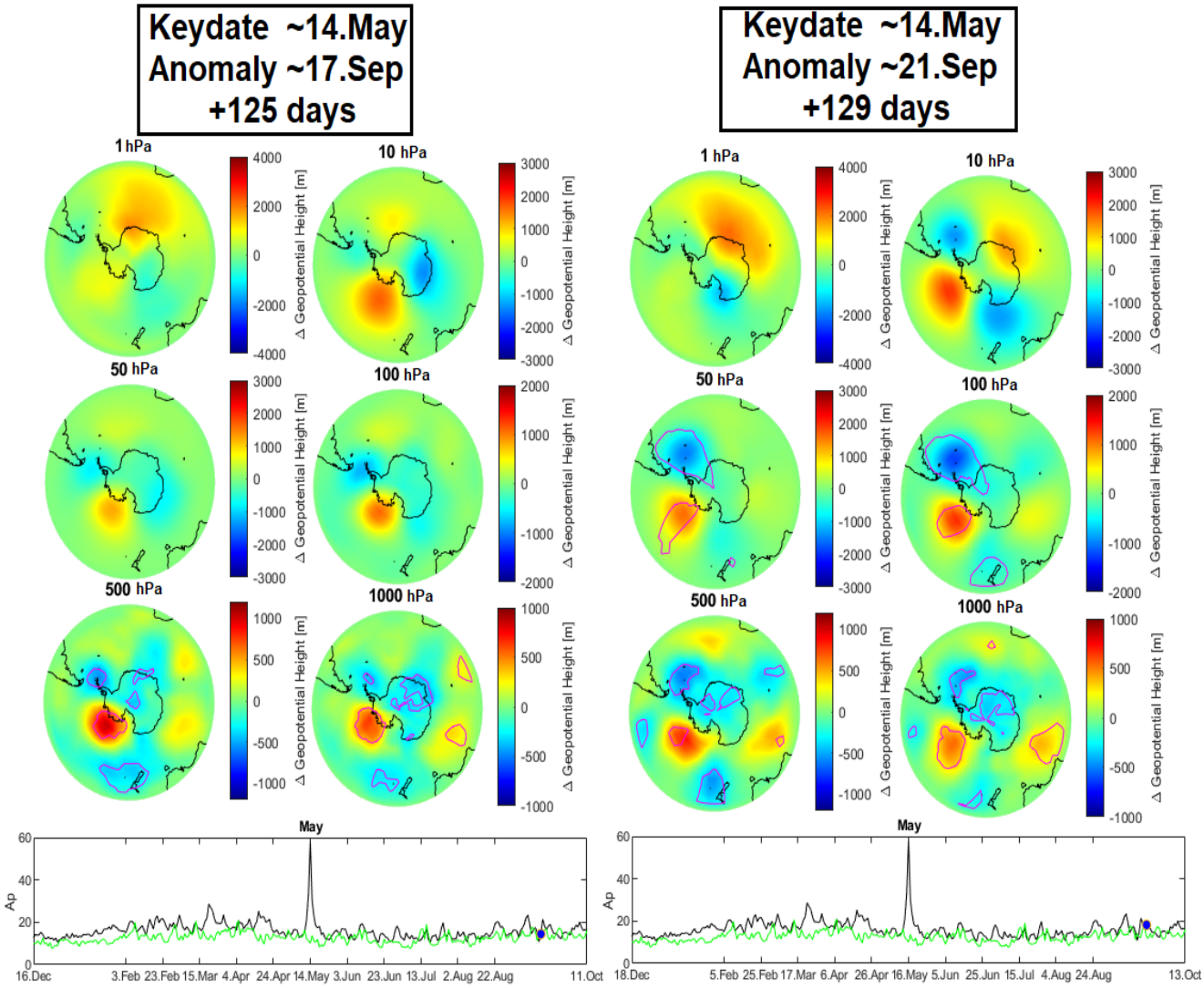

Figure 90: **Top panels:** Anomaly occurring in middle September for keydate inside May (A2S). Purple lines indicate statistical significance. **Bottom panels:** Black (green) line represents the averaged Ap-index from the high (CLIMREF-spec) bin.

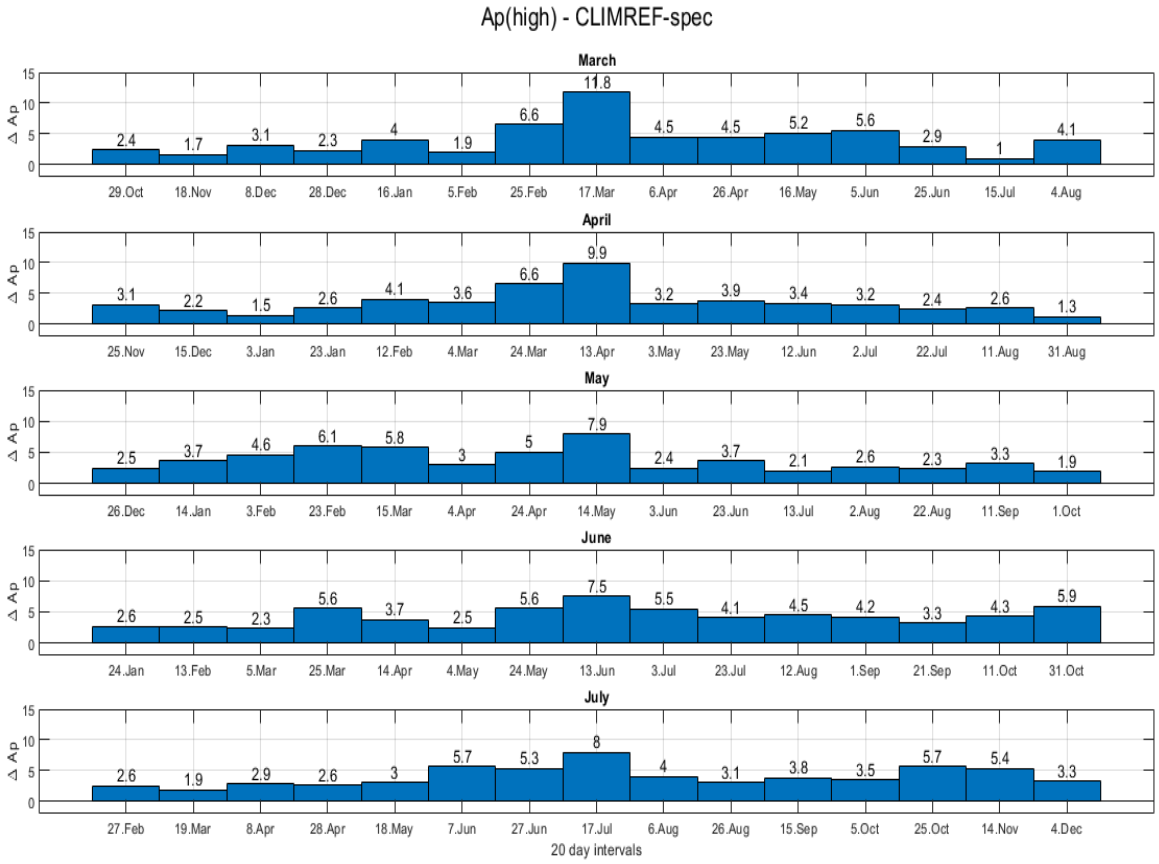

Figure 91: ΔA_p calculated through A_p(high)-CLIMREF-spec at 20 day intervals from the data series used in the A2S-case.

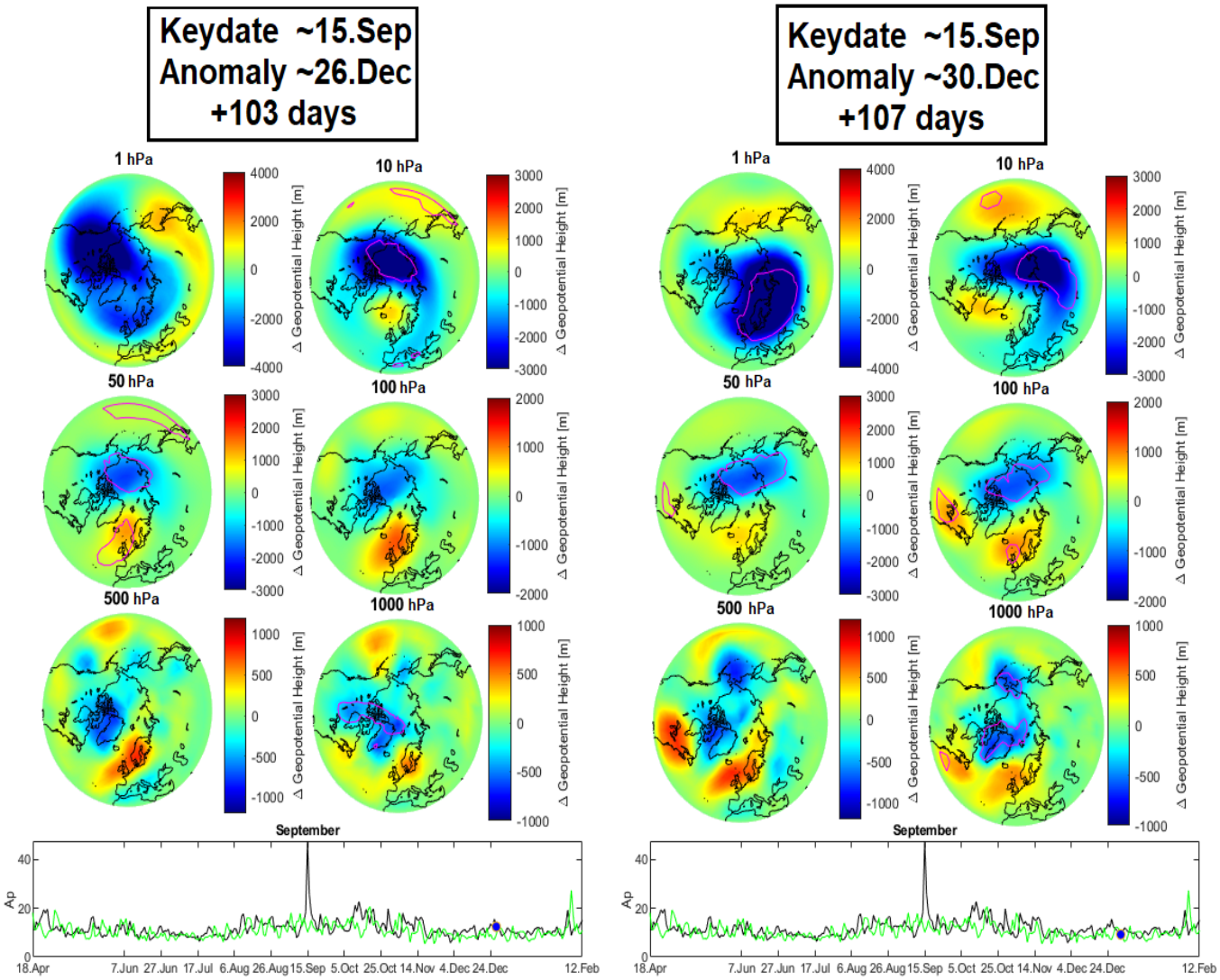

Figure 92: **Top panels:** Anomaly occurring in late December for keydate inside September (A2N: Peaks excluded). Purple lines indicate statistical significance. **Bottom panels:** Black (green) line represents the averaged Ap-index from the high (CLIMREF-spec) bin.

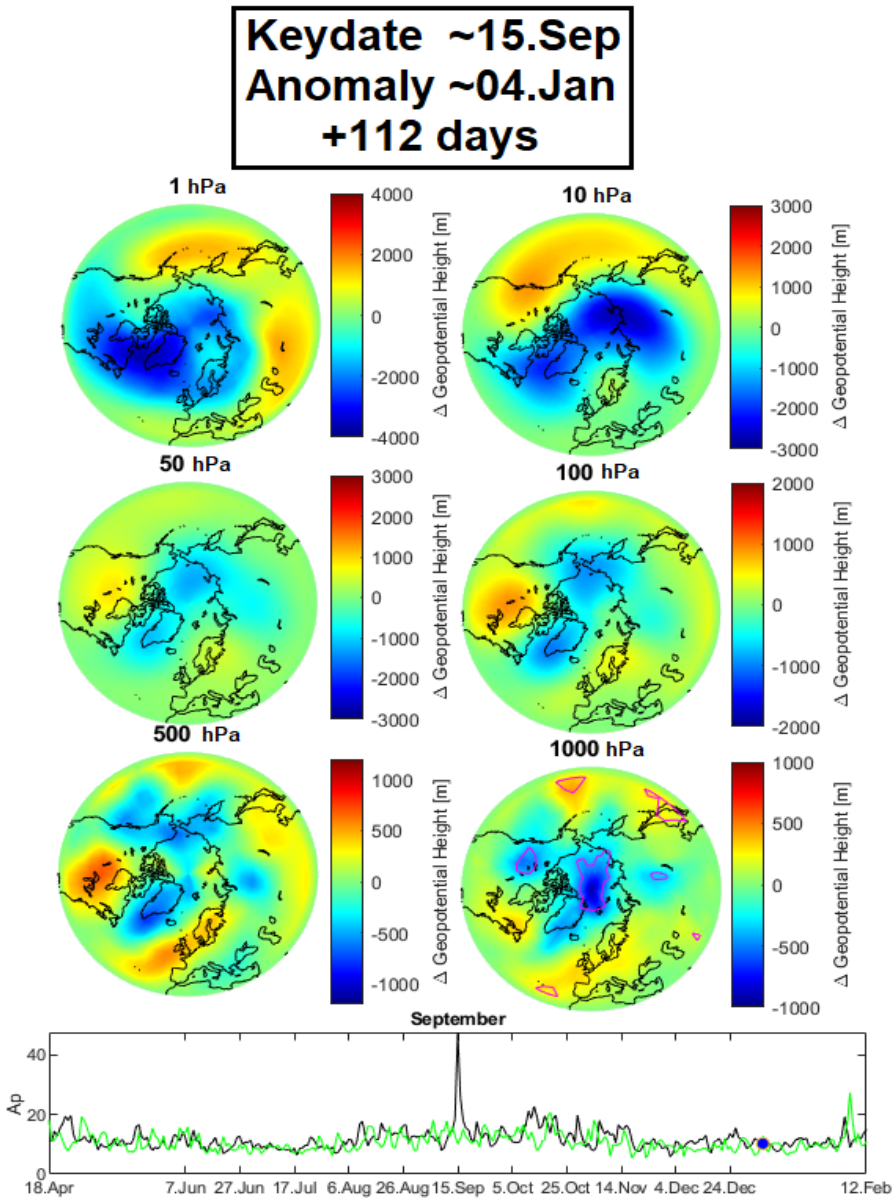

Figure 93: **Top panels:** Anomaly occurring in early January for keydate inside September (A2N: Peaks excluded). Purple lines indicate statistical significance. **Bottom panels:** Black (green) line represents the averaged Ap-index from the high (CLIMREF-spec) bin.

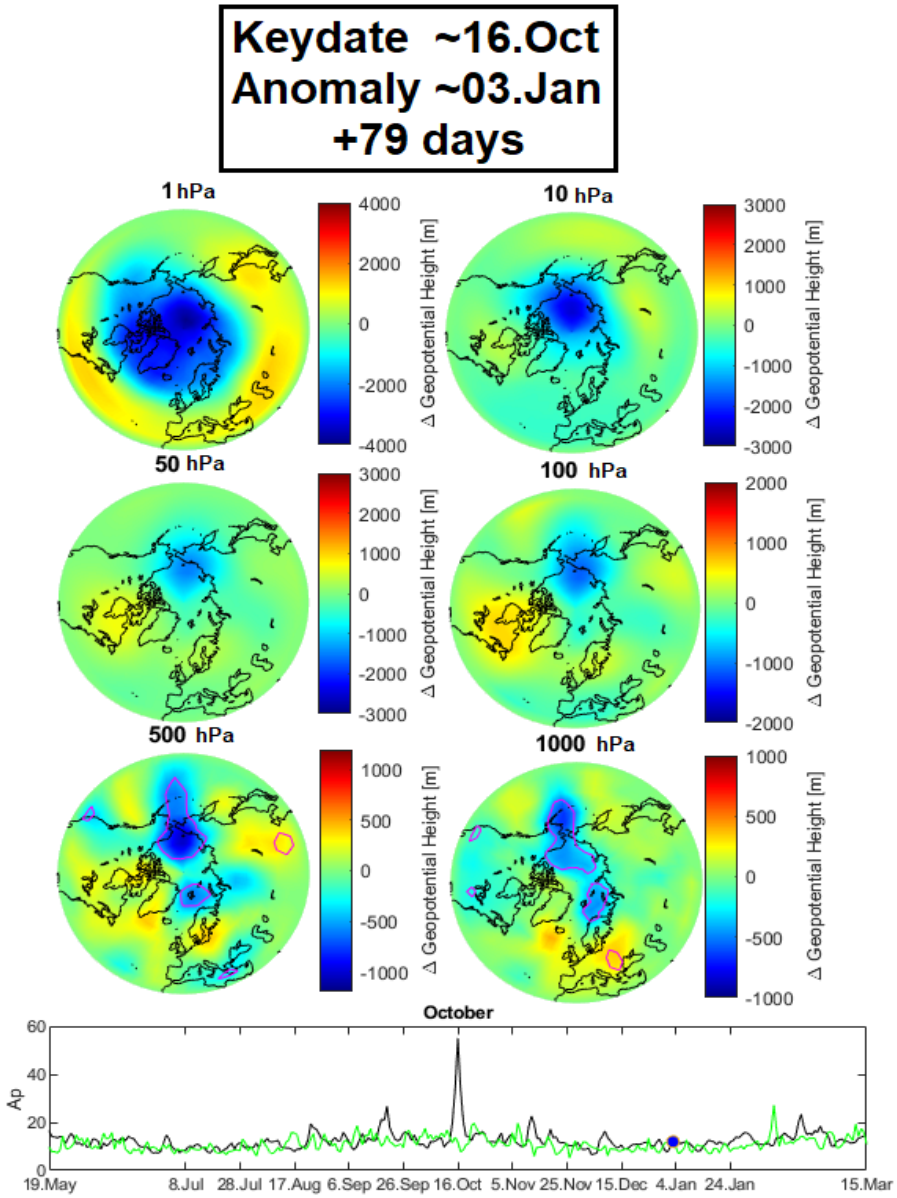

Figure 94: **Top panels:** Anomaly occurring in early January for keydate inside October (A2N: Peaks excluded). Purple lines indicate statistical significance. **Bottom panels:** Black (green) line represents the averaged Ap-index from the high (CLIMREF-spec) bin.

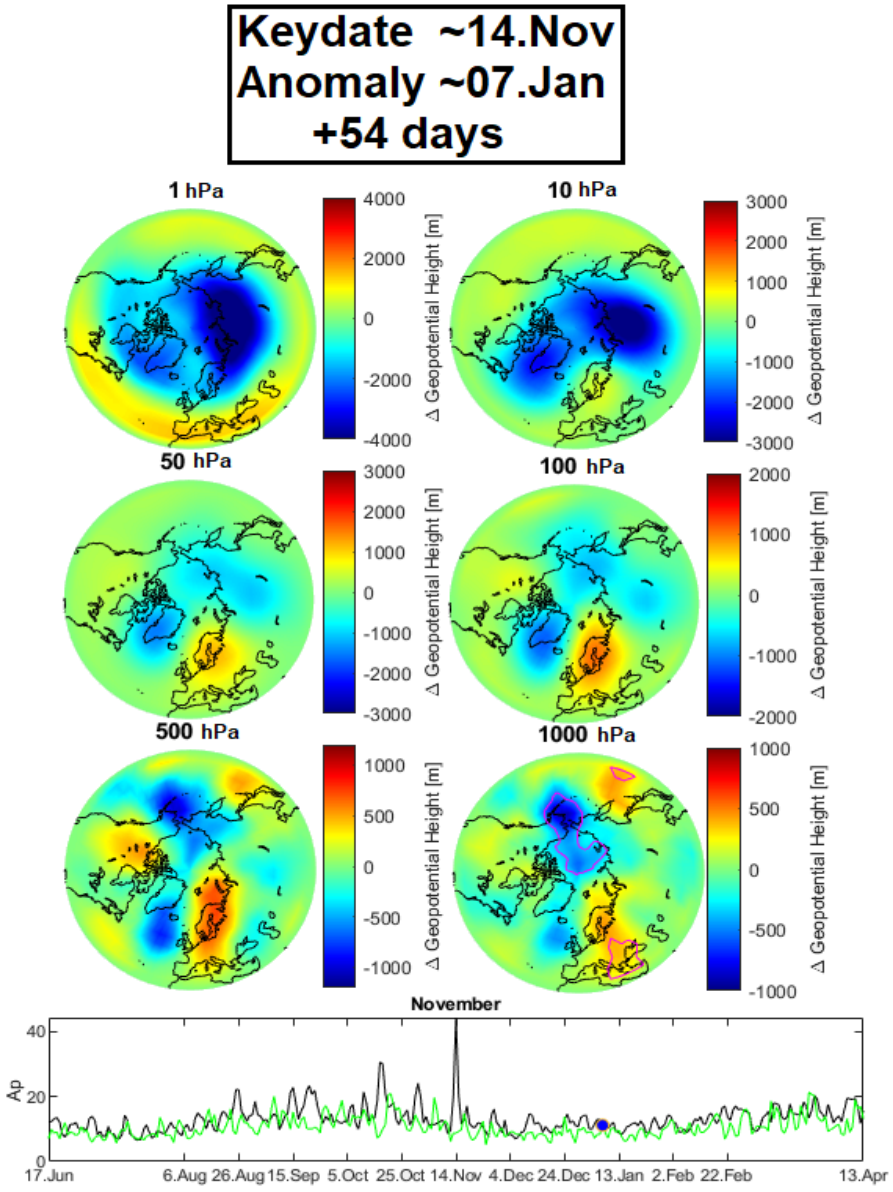

Figure 95: **Top panels:** Anomaly occurring in early January for keydate inside November (A2N: Peaks excluded). Purple lines indicate statistical significance. **Bottom panels:** Black (green) line represents the averaged Ap-index from the high (CLIMREF-spec) bin.

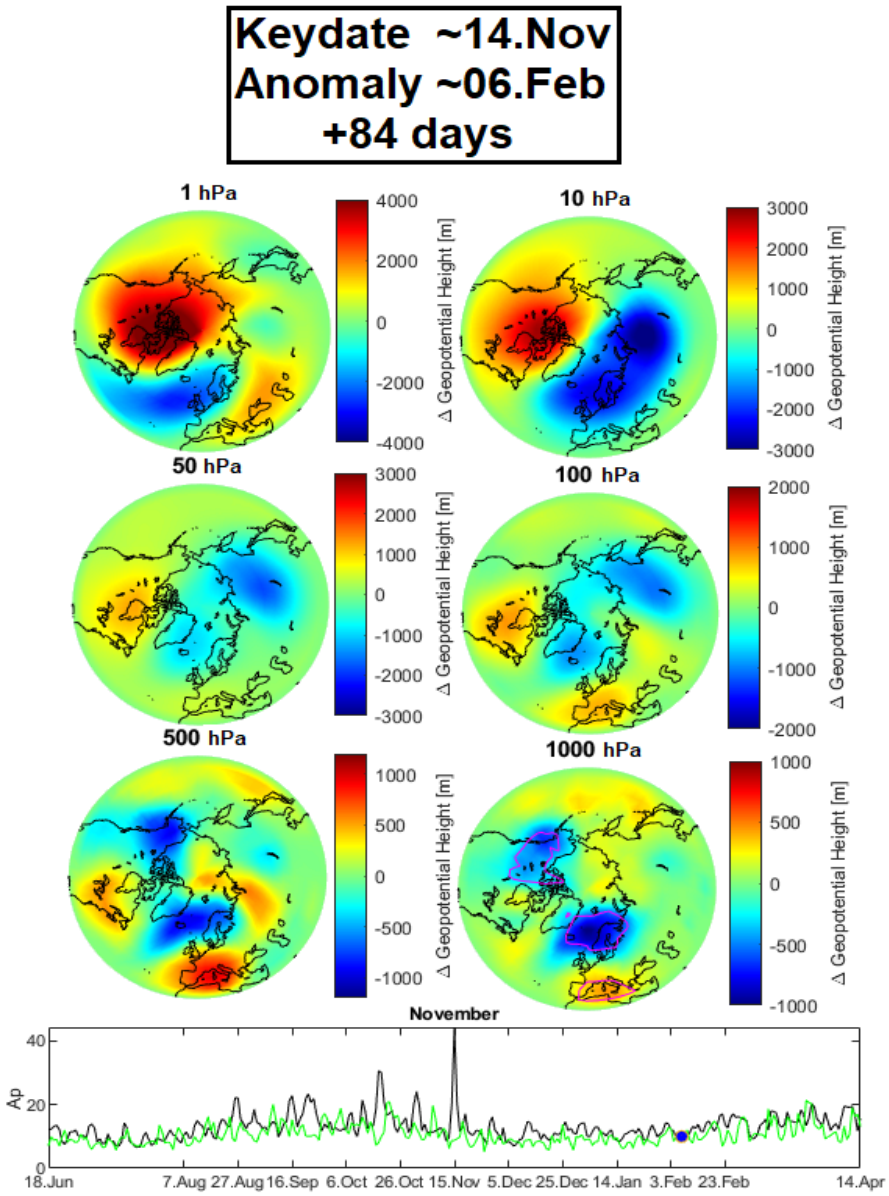

Figure 96: **Top panels:** Anomaly occurring in early February for keydate inside November (A2N: Peaks excluded). Purple lines indicate statistical significance. **Bottom panels:** Black (green) line represents the averaged Ap-index from the high (CLIMREF-spec) bin.

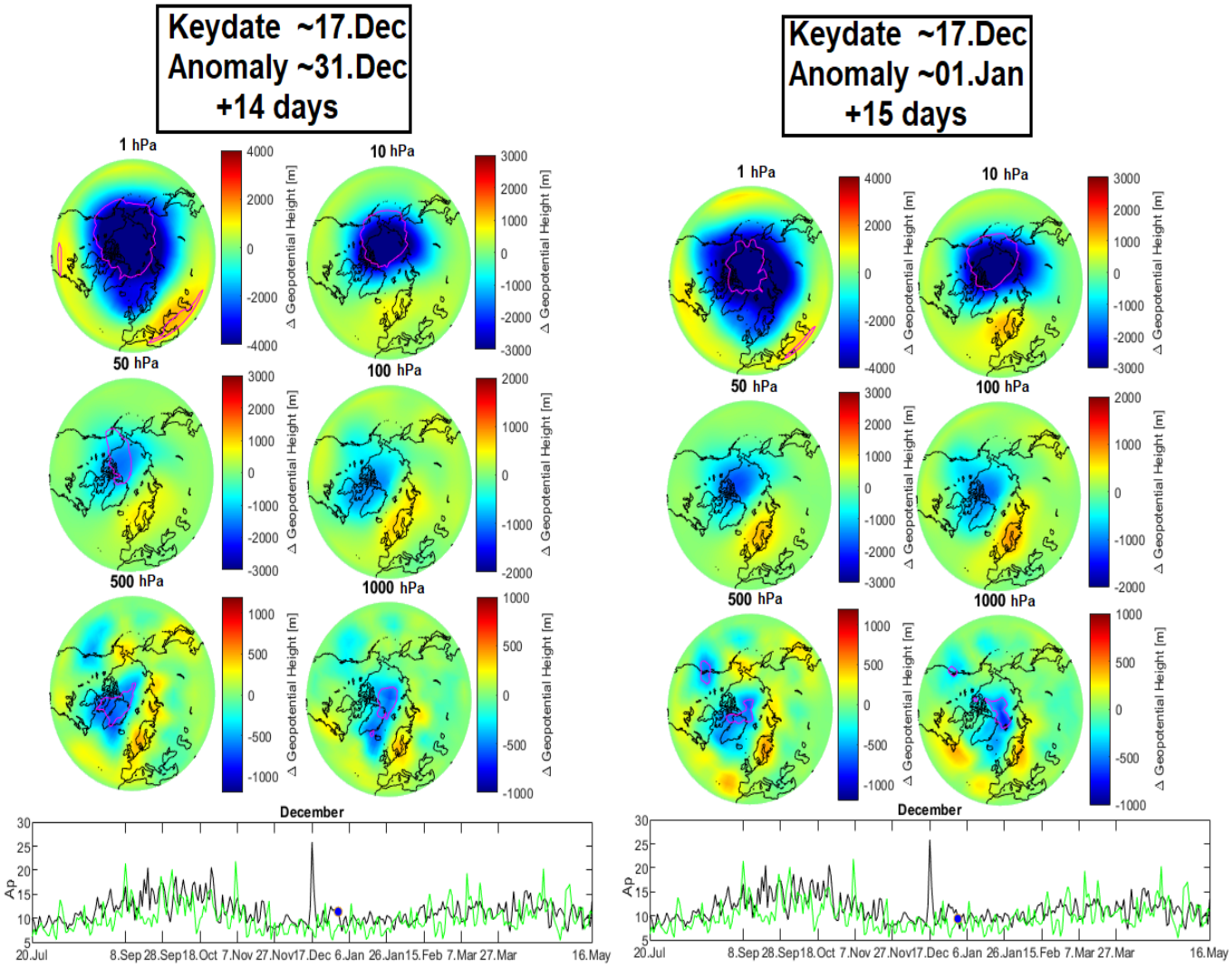

Figure 97: **Top panels:** Anomaly occurring in late December/early January for keydate inside December (A2N: Peaks excluded). Purple lines indicate statistical significance. **Bottom panels:** Black (green) line represents the averaged Ap-index from the high (CLIMREF-spec) bin.

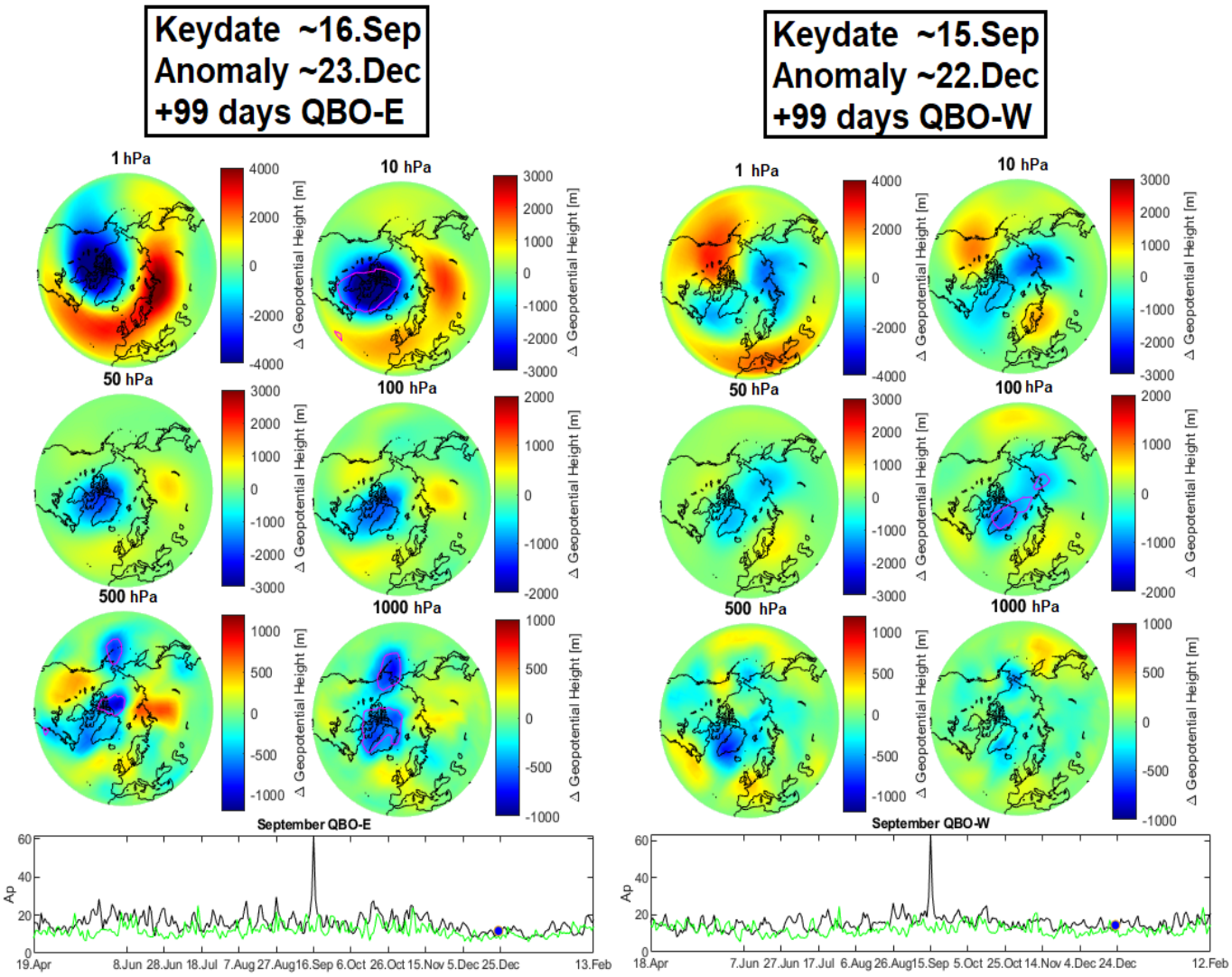

Figure 98: **Top panels:** Anomaly occurring at +99 days for keydate inside September for both QBO-phases (A2N: QBO). Purple lines indicate statistical significance. **Bottom panels:** Black (green) line represents the averaged Ap-index from the high (CLIMREF-spec) bin.

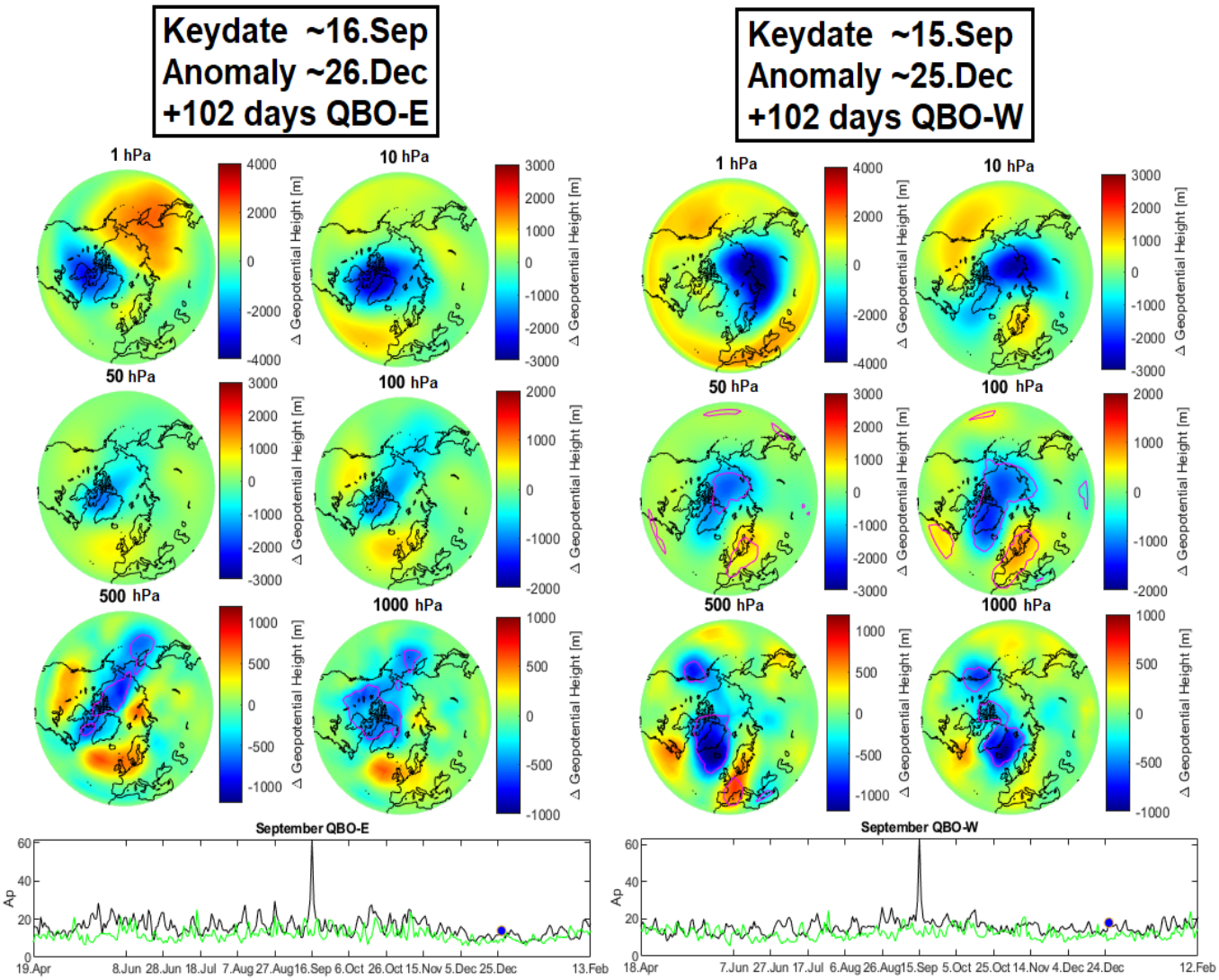

Figure 99: **Top panels:** Anomaly occurring at +102 days for keydate inside September for both QBO-phases (A2N: QBO). Purple lines indicate statistical significance. **Bottom panels:** Black (green) line represents the averaged Ap-index from the high (CLIMREF-spec) bin.

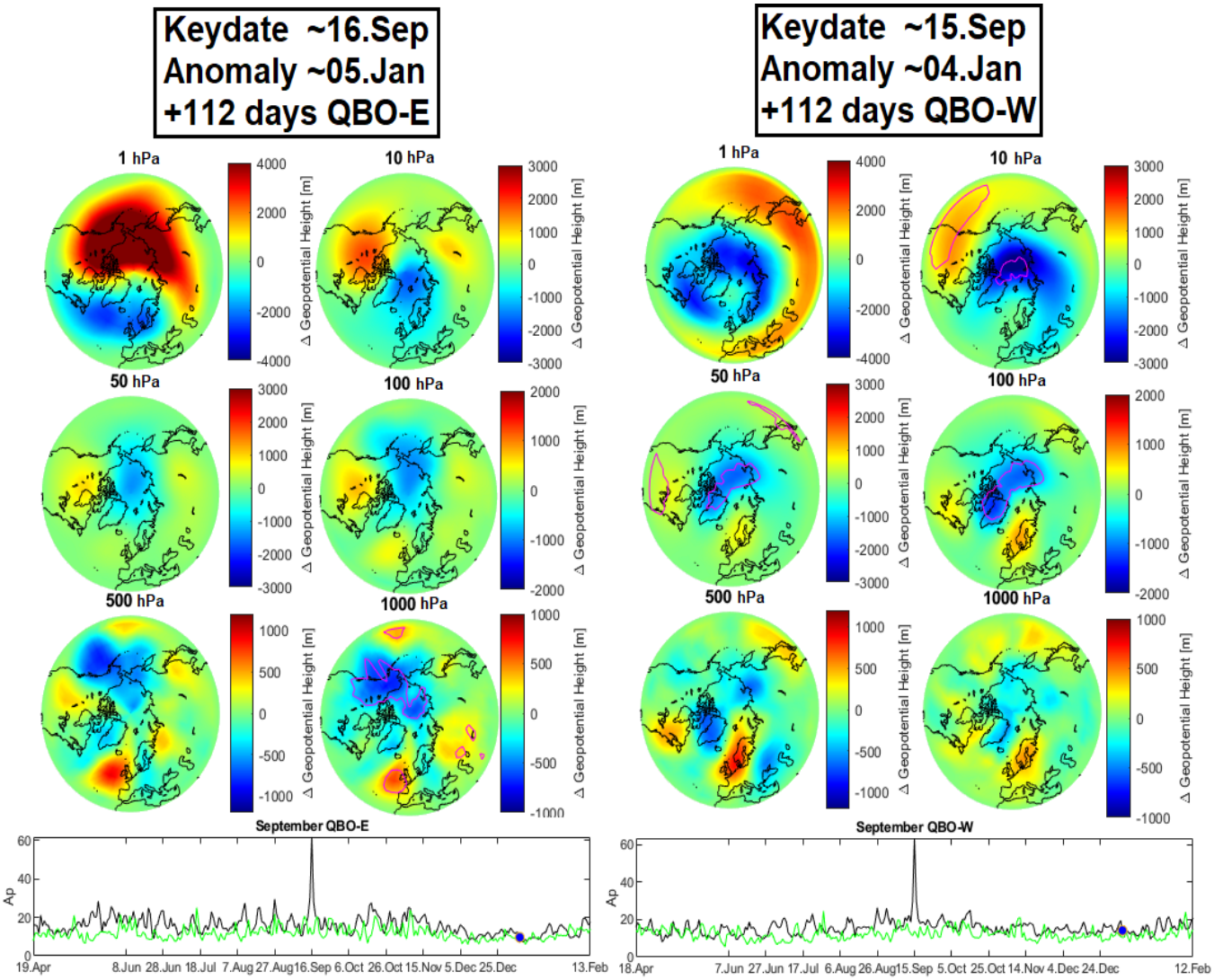

Figure 100: **Top panels:** Anomaly occurring at +112 days for keydate inside September for both QBO-phases (A2N: QBO). Purple lines indicate statistical significance. **Bottom panels:** Black (green) line represents the averaged Ap-index from the high (CLIMREF-spec) bin.

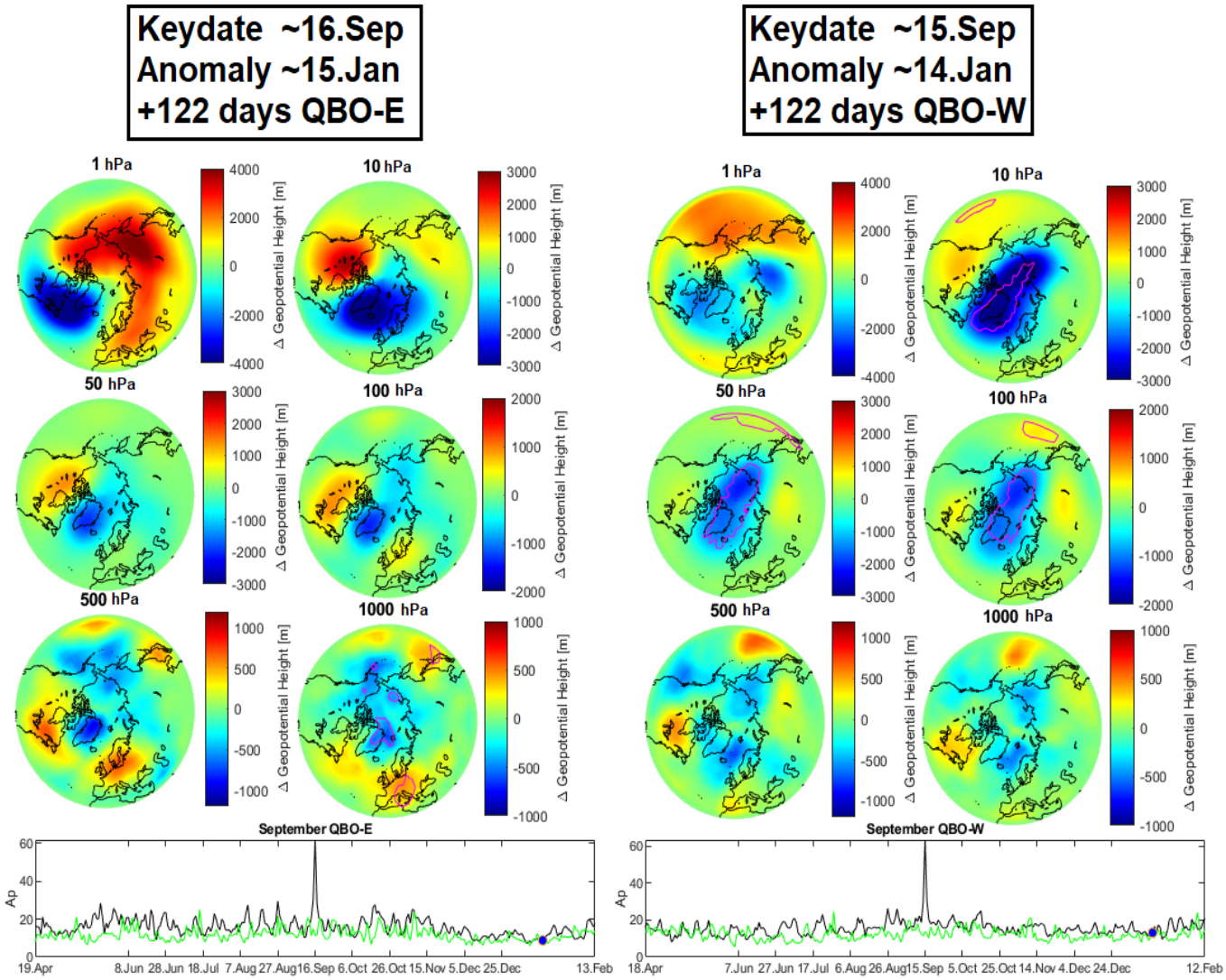

Figure 101: **Top panels:** Anomaly occurring at +122 days for keydate inside September for both QBO-phases (A2N: QBO). Purple lines indicate statistical significance. **Bottom panels:** Black (green) line represents the averaged Ap-index from the high (CLIMREF-spec) bin.

12.3 Appendix C: Supplement figures/analyses for the Mansurov effect results

12.3.1 Appendix C.1

This section is devoted to figures regarding the Mansurov effect. All figures shown are described in the text.

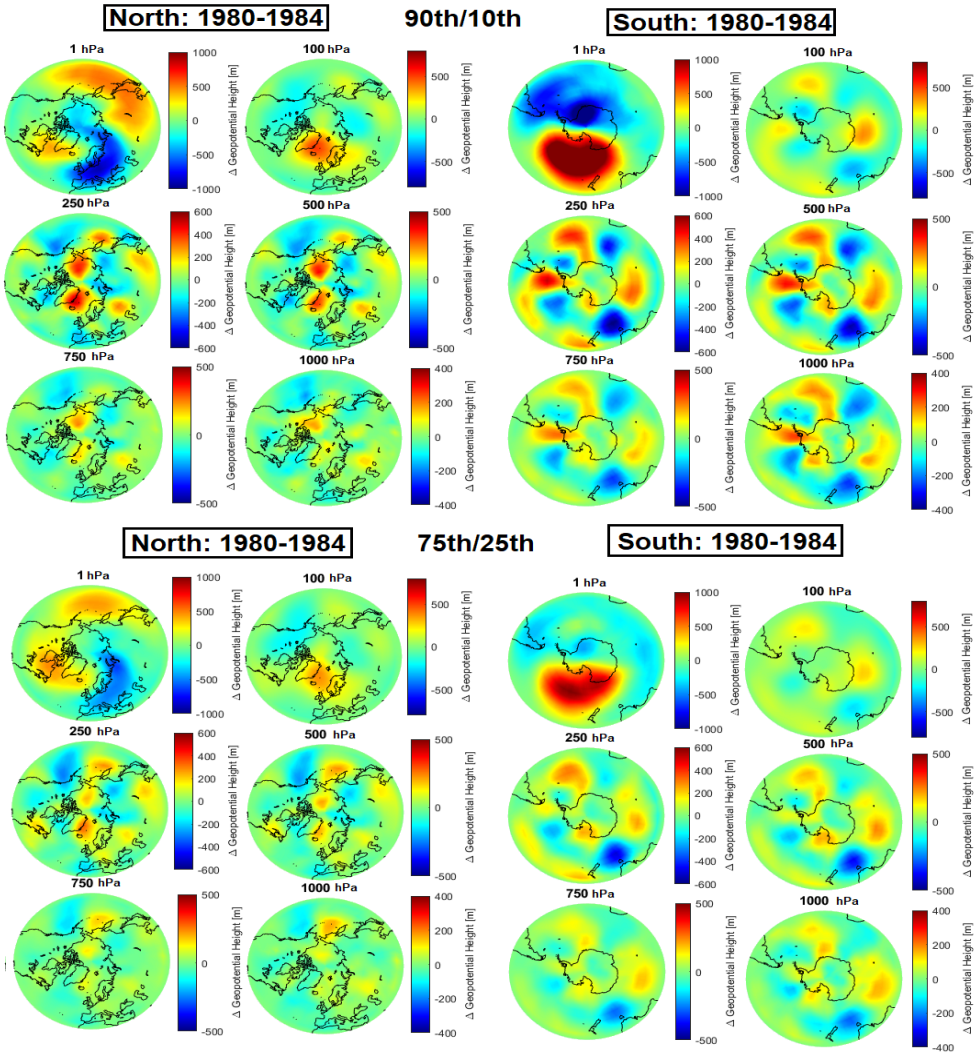

Figure 102: Solar maximum from 1980-1984 (B1N/S). Binning according to the >90th/<10th and >75th/<25th percentile of the V_xB_y values are shown. No significance is found.

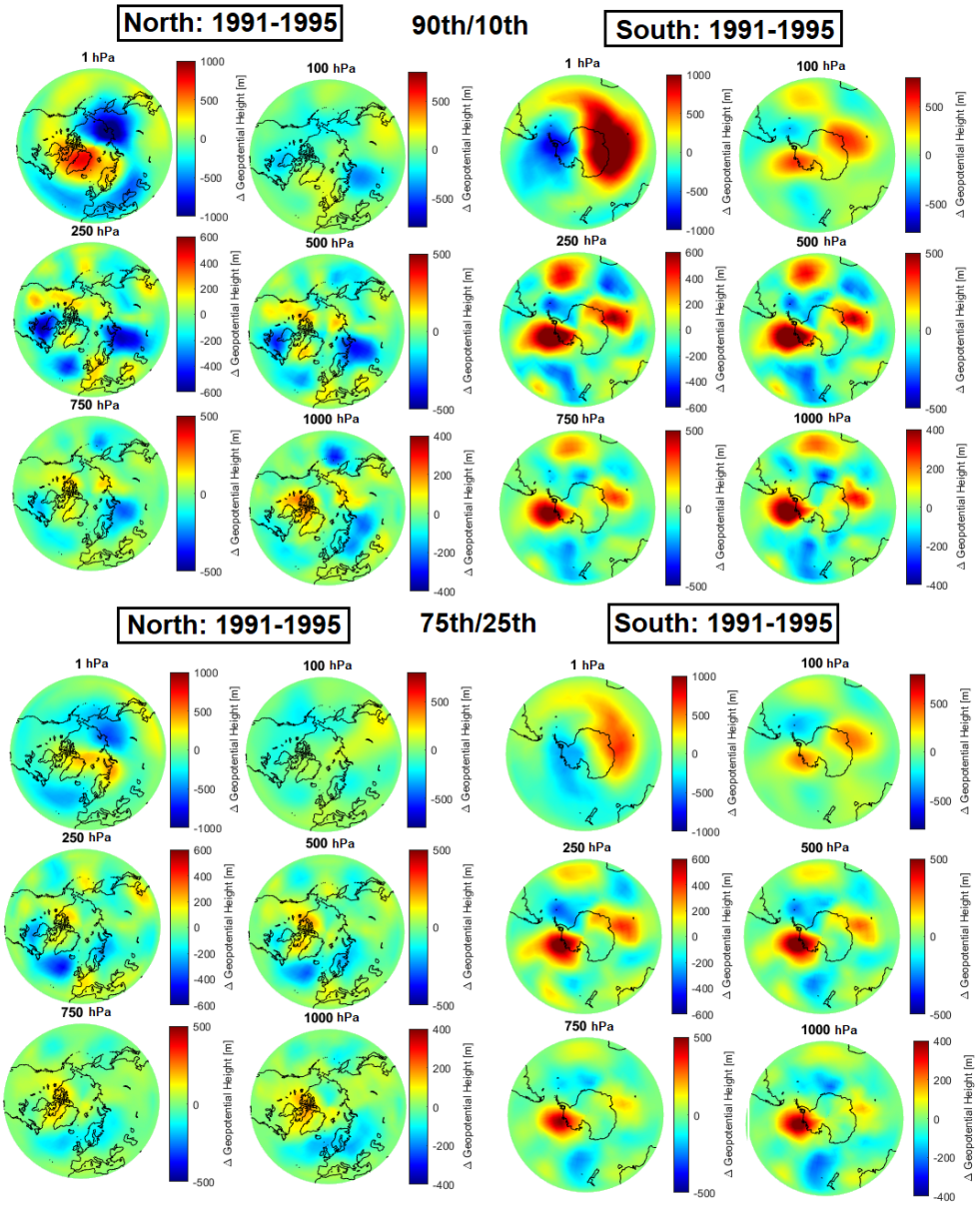

Figure 103: Solar maximum from 1991-1995 (B1N/S). Binning according to the >90th/<10th and >75th/<25th percentile of the V_xB_y values are shown. No significance is found.

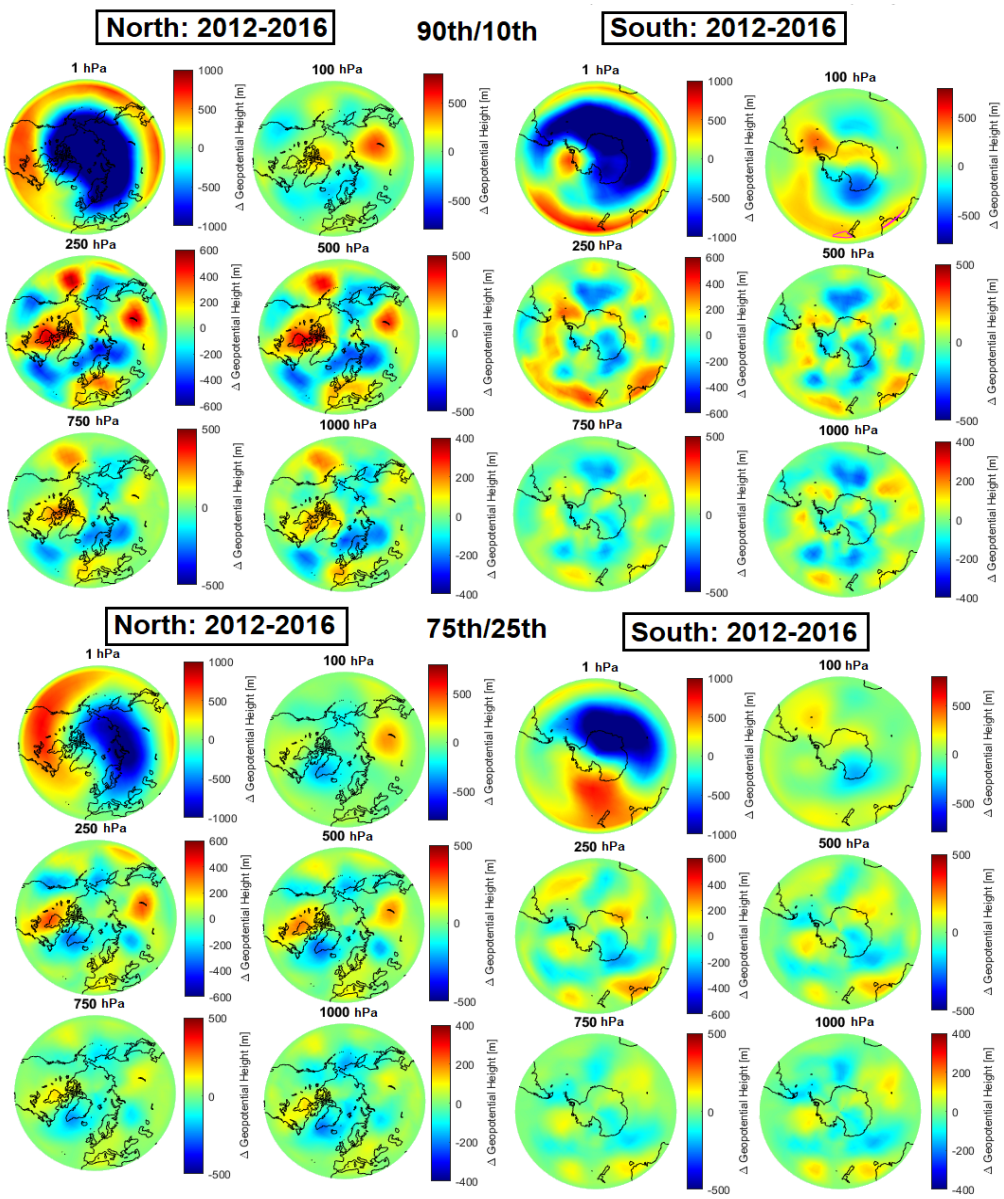

Figure 104: Solar maximum from 2012-2016 (B1N/S). Binning according to the >90th/<10th and >75th/<25th percentile of the V_xB_y values are shown. No significance is found.

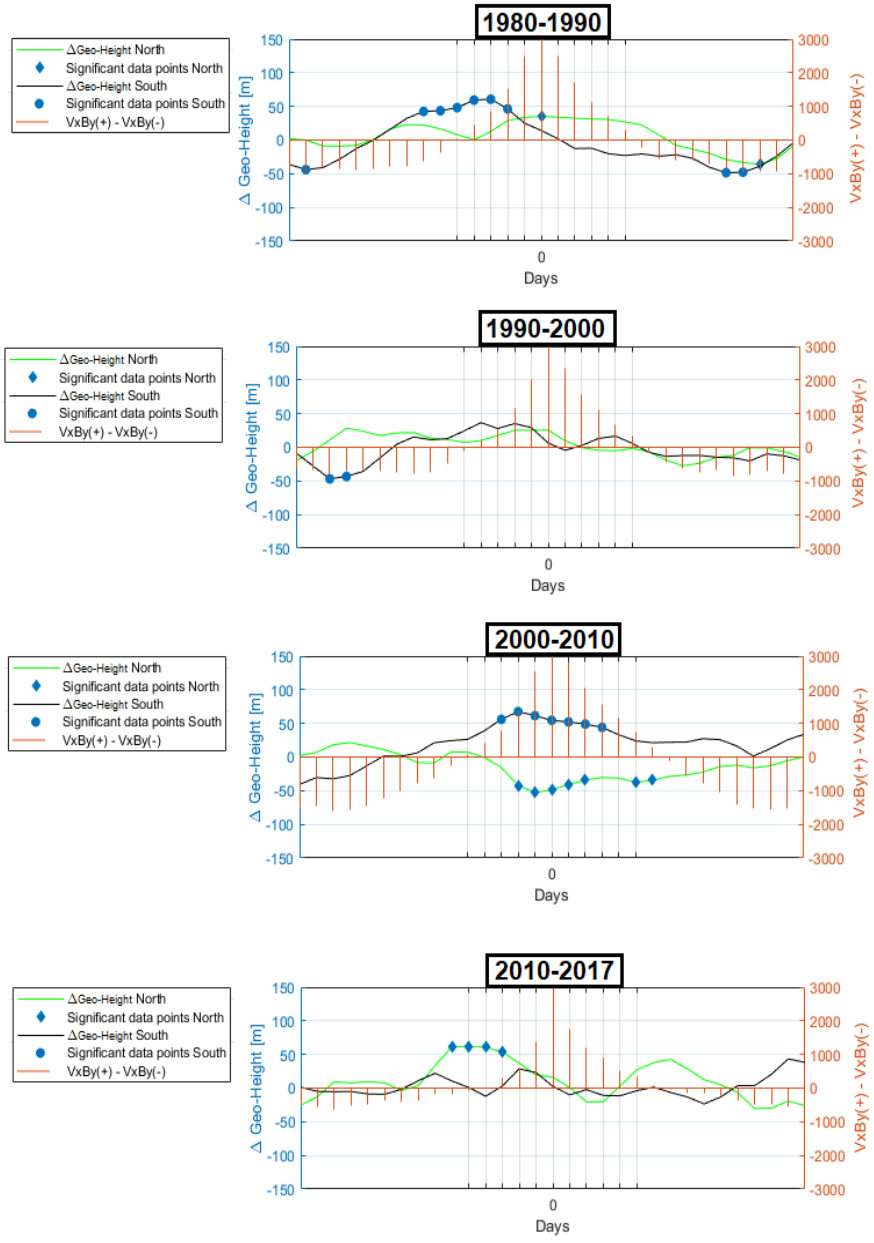

Figure 105: ΔGeo-Height[m] = high (>90th percentile V_xB_y) bin - low (<10th percentile V_xB_y) bin (B2N/S). 10 year periods are shown, with a 7 year period in the last panel. Significance is calculated through the t-test.

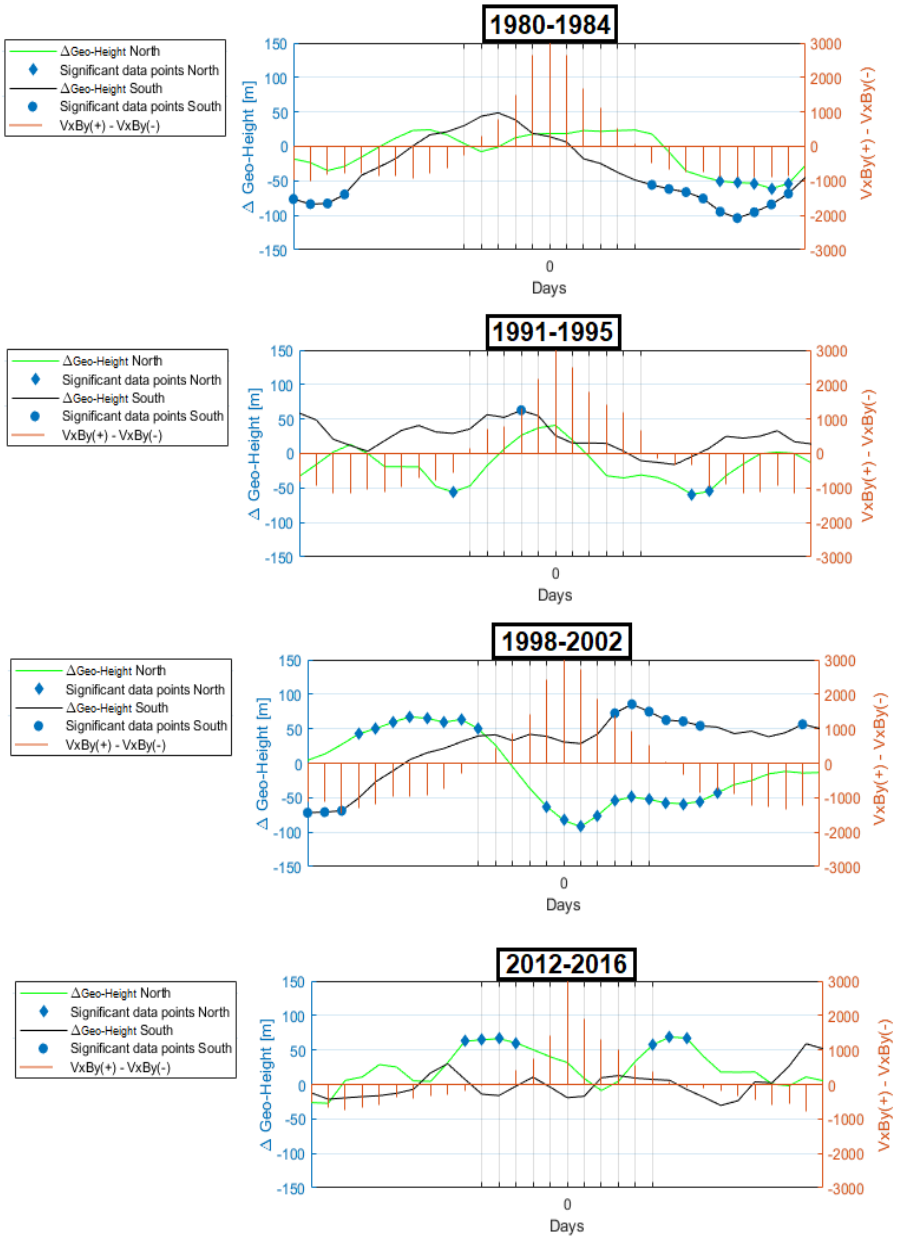

Figure 106: ΔGeo-Height[m] = high (>90th percentile V_xB_y) bin - low (<10th percentile V_xB_y) bin (B2N/S). Solar maximum periods are shown. Significance is calculated through the t-test.

12.3.2 Appendix C.2

This analysis focuses on overcoming the limitations of the Super Epoch analysis (Ref: Chapter 3.4). Criteria are introduced in the analysis to ensure that the data points contributing at day 0 will not contribute to day ±periodicity. Firstly, data points going in the high (low) bin has to be the maximum (minimum) value within a 4-day period, ensuring it is an absolute peak value. Secondly, this data point also has to be above (below) the percentile distribution of the V_xB_y values defined by the analysis. Thirdly, from this data point there has to be a minimum time period T before the next data point fulfilling the two other criteria is picked. Figure 107 shows the results when sorting by the >95th/<5th percentile and the >75th/<25th percentile for the whole data period. T equals 28, 55, 82 and 110. The plots are restricted to three solar rotations. A significant positive anomaly occur a couple of days before the keydate in three of the cases for the SH response. Significance around the keydate is lost as T between each data pick increases. In the northern response, no consistent significance is found. The same procedure is done for the highly significant period of 1998-2002, illustrated by Figure 108. Only the >95th/<5th percentile sorting with T = 55 show significance for the southern response near day 0. Here significance is also seen at day +27 as a positive anomaly, and day -24 as a negative anomaly. In the NH, significant positive response is seen for the >75th/<25th sorting for the same T. Other periods show some sporadic significance, but no consistent response. No cyclic behaviour is concluded on the basis of the analyses, as little consistency and significance are obtained.

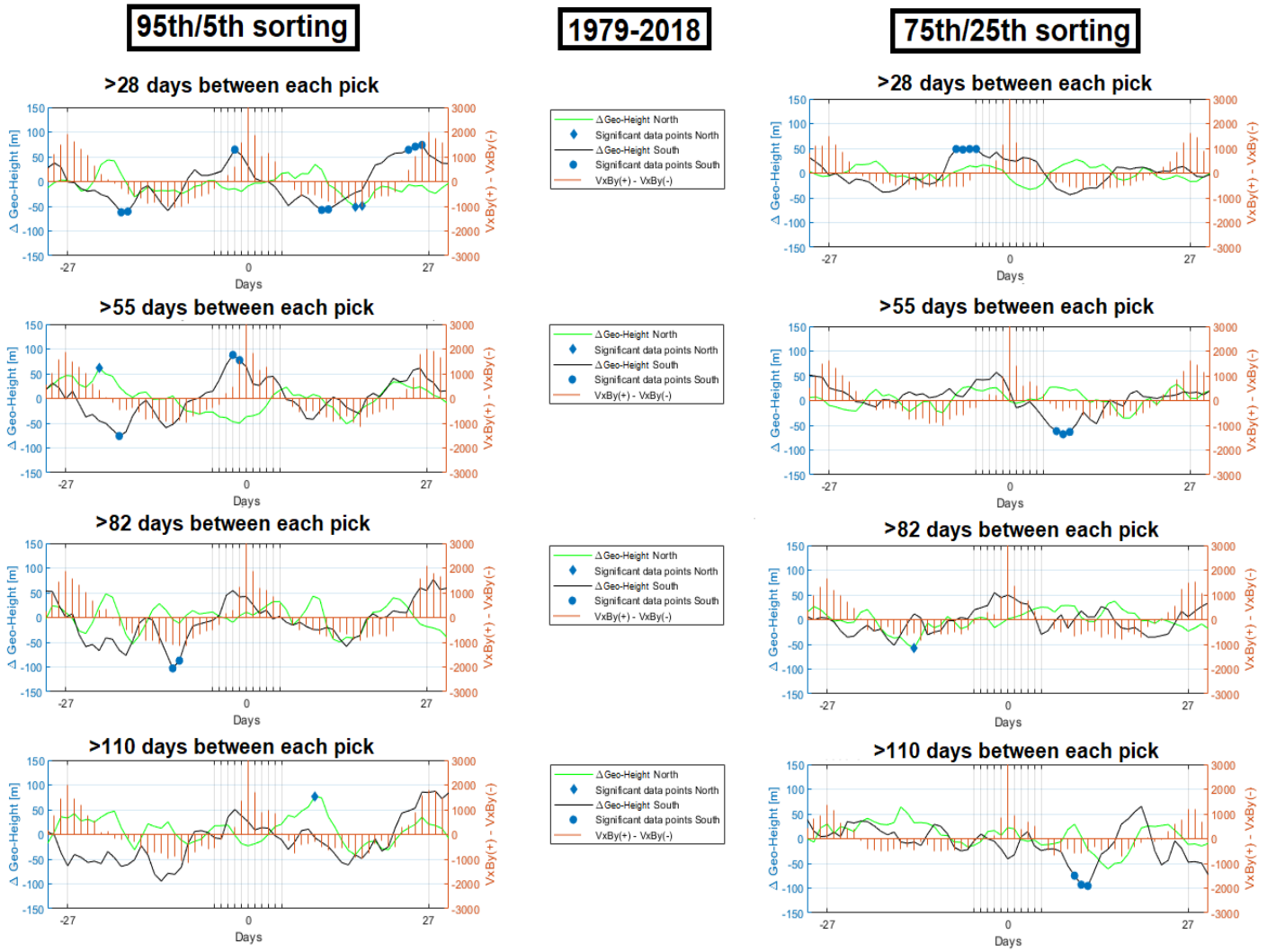

Figure 107: 1979-2017. Significance is calculated through the t-test. Time period between each data point obtained are increased with 27+1 for each downward panel to suppress the self replication of the response at ± periodicity.

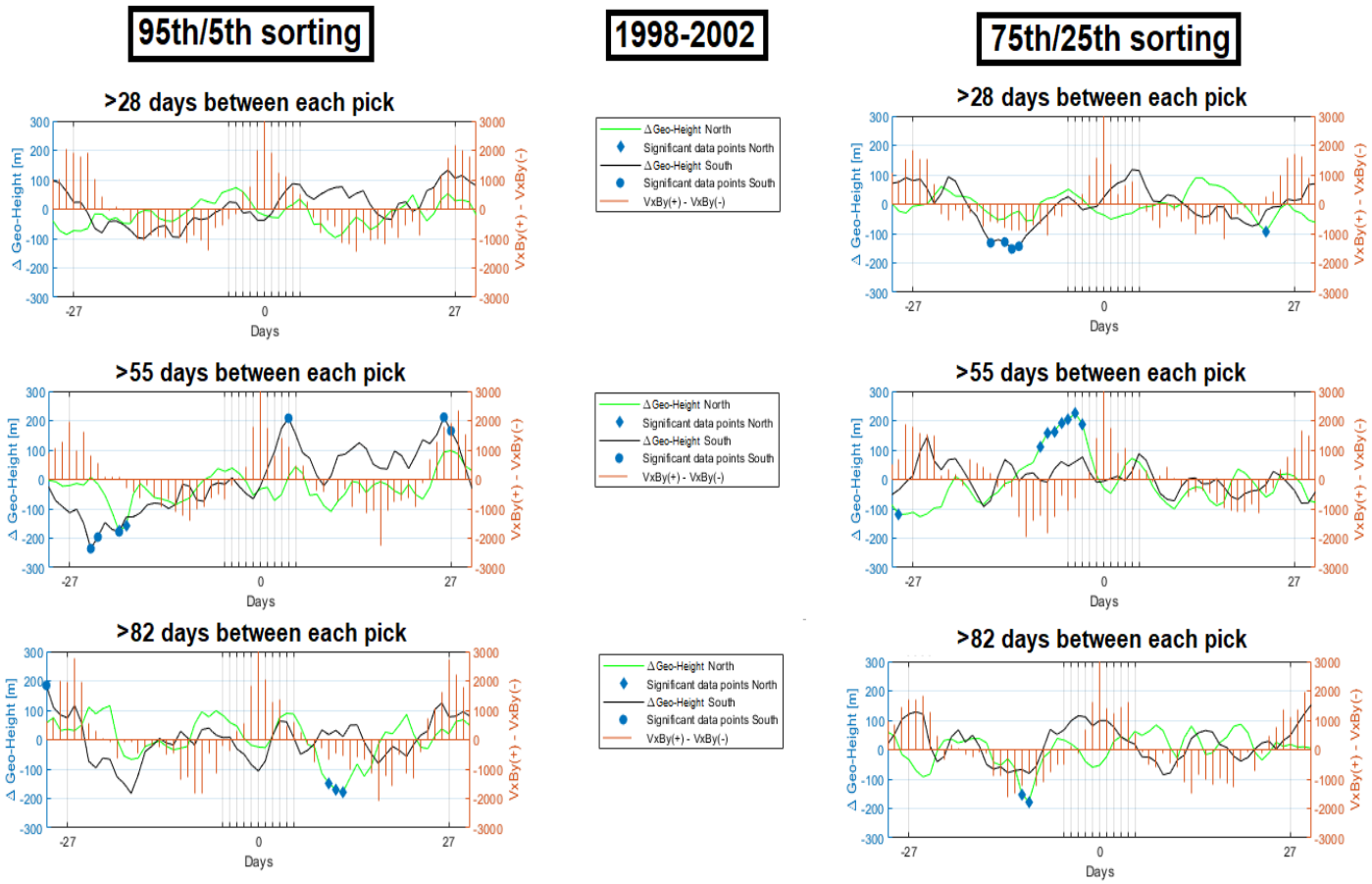

Figure 108: 1998-2002. Significance is calculated through the t-test. Time period between each data point obtained are increased with 27+1 for each downward panel to suppress the self replication of the response at ± periodicity.

12.3.3 Appendix C.3

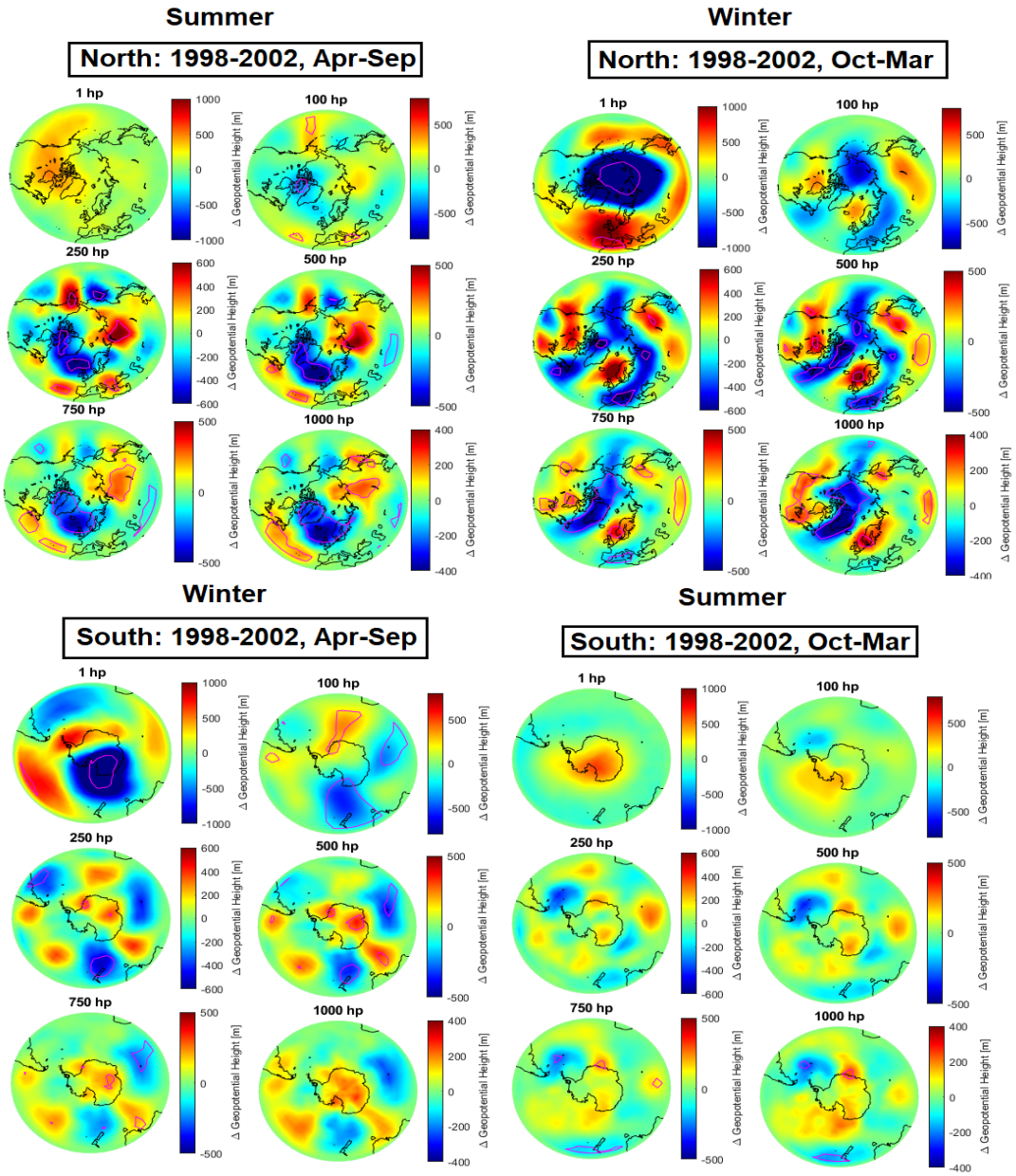

Figure 109: ΔGeo-Height[m] = high (>90th percentile V_xB_y) bin - low (<10th percentile V_xB_y) bin for NH and SH in the period 1998-2002 divided into winter (Oct-Mar) and summer (Apr-Sep). Significance is calculated through the t-test.